DOCTOR OF PHILOSOPHY

A Numerical Study of the Internal Tide in Upper Loch Linnhe

Riley, Graeme

Award date:
2007

Awarding institution:
University of Wales, Bangor

A Numerical Study of the Internal Tide in Upper Loch Linnhe

Graeme Riley
March 2007

A thesis submitted to the University of Wales in candidature for the degree of Doctor of Philosophy

Abstract

Data has been analysed from two independent investigations into the dynamics of Upper Loch Linnhe. The first data set, collected between February 1991 and February 1992 by Fisheries Research Services (FRS), was made available by the British Oceanographic Data Centre. The second set of data was collected between November 1992 and June 1993 by G. Allen. Comparison with the earlier data backs up the original conclusions of Allen (1995) that an energetic mode 1 internal tide is present in the basin. Further the residual flows during a renewal event have also been found to compare favorably with those taken from the current meter moorings of the earlier FRS data during a similar renewal event.

The dynamics of the mode 1 internal tide have been simulated using two differing numerical models. The hydrostatic model of Gillibrand (1993) has been compared with a model developed for this study based around the non-hydrostatic model presented in Bourgault and Kelley (2004). The hydrostatic model fails to reproduce the phase of the internal tide, in error by approximately 180°. The non-hydrostatic model reproduces this internal tidal stream within the error bounds of the harmonic analysis at the surface and bed. The errors in the middle of the water column were larger, at 60m the disagreement was 33° ±15. The gross lack of agreement of the hydrostatic model with the data was found to be due to its inability to simulate flow separation from the lee of the sill.

Subsequently the non-hydrostatic model was used to investigate the flows during renewal events. The deep depression in the isopycnals, attributed by Allen and Simpson (2002) to a baroclinic adjustment to the density gradients at slack water, has been reproduced by this model, showing its generation is due to several flood streams advecting dense water over the sill.

Further analysis of this model output is suggestive of three processes that can lead to the formation of an internal tidal response in a jet fjord. Firstly Bernoulli forcing involves a low pressure created in the lee of the sill drawing deep waters seaward during a flood. The second process is the vertical advection of the density gradient up the slope at the northern end of the basin. This has been termed aspirational forcing. The third and most significant mechanism has been identified as time variant density, caused by density variations over the tidal cycle in the waters overflowing the Corran sill.

It is proposed that these processes go someway to explaining the conundrum posed by Stigebrandt (1999b); how can a jet fjord create an internal tide?

Acknowledgements

The initial application of the hydrostatic model to another system was funded by the Procurement Agency of the MoD to whom I am grateful for their financial support. Further financial help and encouragement came from my family. The opportunities given to me by Dave Barnes and so many others have enabled me to work in North Wales for several years while completing this work.

For technical advice and support in the development of the non-hydrostatic model code I am indebted to Graham Worley whose involvement in this project went far beyond his job description. The comments of my supervisor, John Simpson and Dave Bowers have encouraged the investigation of the data and improved this final document. I would also like to thank Kevin Horsbourgh, for without his involvement in the early stages, this project could never have been completed.

Daniel Bourgault and Mark Inall have both made work awaiting publication available; their generosity, along with that of Graham Allen who provided his processed data, has enabled this work to build upon a firm foundation of their scientific work.

There are too many people for me to thank for their input and encouragement here. Tragically there are those whom I can no longer thank in person. This work is dedicated to Ray Delahunty, Steve Pearce and Pat McArthy.

Contents

List of Figures

List of Tables

List of Symbols

a_0	Amplitude of the vertical rise and fall of the tide (m)
A	Cross sectional area (m^2)
A_i	Surface Area landward (m^2)
A_s	Cross sectional area at sill (m^2)
A_h	Horizontal and vertical components of kinematic eddy viscosity (m^2s^{-1})
A_0	Vertical eddy viscosity in neutral conditions (m^2s^{-1})
B	Channel width (m)
C	Wave speed in chapter 1 (ms^{-1}) or Chézy Coefficient in Appendix 1
E	Energy flux (Wm^{-2})
E_a	Energy loss to barotropic form drag (J)
E_f	Energy loss to bottom friction (J)
E_w	Energy loss to baroclinic wave drag (J)
f	Coriolis parameter
Fr	Internal Froude number
g	Acceleration due to gravity (m^2s^{-1})
g'	Reduced acceleration due to gravity = $(\Delta\rho/\rho)\times g$ (m^2s^{-1})
G	Composite Froude number
h	Layer thickness (m)
H	Water depth relative to Mean Sea Level (m)
K_h	Horizontal and vertical components of kinematic eddy diffusivity (m^2s^{-1})
L	Length, of sill (m)
R	Hydraulic radius of a channel (m)
S	Salinity (*Practical Salinity Units*)
t	Time (s)
T	Temperature (℃)
u	Horizontal flow speed (ms^{-1})
U	Depth or layer averaged flow speed (ms^{-1})
U_0	Amplitude of the barotropic tidal current (ms^{-1})
U_s	Depth averaged velocity at sill (ms^{-1})
w	Vertical flow speed (ms^{-1})
x	Horizontal along loch direction (m)
z	Vertical direction (m)
η	Surface elevation (m)
ρ	Density (kgm^{-3})
ϕ	Phase shift in equation 1.1 (rad) or represents any scalar in chapter 3
ω	Frequency ($rads^{-1}$)
Ω	Angular frequency of the Earth ($rads^{-1}$)

Chapter 1 – Review of previous study & thesis aims

1.1 Introduction

1.1.1 The origin of Lochs

The word '*loch*' is a Celtic expression for what is termed a '*fjord*' in Scandinavia. This in turn comes from the Norse word '*fjorthr*' used to describe all types of marine inlet and sometimes associated with fresh water. The words '*loch*' and '*fjord*' are both used here, reflecting the terminology used by the original authors. The marine inlets seen today are the products of glacial retreat and sea level changes that have occurred since 10,000 years before present.

A loch can be formed by the retreat of ice and inundation by the sea into the valley previously carved out by the glacier. It has been suggested that lochs can be formed in valleys eroded by flowing water alone. However lochs are only found in high latitudes that have been previously subject to glaciation; the characteristic '*U*' shaped valley created by glaciers matches with their cross sections.

Lochs and fjords are found at high latitudes beyond 42° South and 56° North. Among the most widely studied areas having fjordic coastlines are those in Scandinavia, Canada and Scotland. Fjords have also been studied in the Southern Hemisphere, in Chile and New Zealand.

1.1.2 Classification

An ideal loch is deep, narrow, has freshwater input at the head and a shallow sill at the mouth. There are many variations but they are all types of estuary. A topographic definition outlined by Dyer (1996) is that they have a width to depth ratio of approximately 10:1 and only a thin bottom sediment layer. Fresh water flow is considered small compared to the total volume of enclosed water, but it can be large compared with the tidal prism. This latter point is a consequence of most research into lochs emanating from Norway, (hence the term *fjord* is more common in scientific literature) where tidal ranges are small. Tidal ranges in Scottish lochs can be large, for example 4.5m in Loch Torridon and Loch Carron located in the NW. There are also lochs with smaller tidal amplitudes of less than 1m, found to the south of the Scottish West Coast, near the Sound of Jura (Syvitski *et al.*, 1987).

A commonly used classification of the stratification and circulation is the Hansen-Rattray (HR) diagram (Hansen and Rattray, 1966). It consists of a two dimensional representation of stratification on the *y*-axis, and circulation on the *x*-axis (figure 1.1). The stratification parameter is the ratio of the vertical salinity difference over the entire water depth to the mean salinity; the circulation parameter is the ratio of the surface and net fluxes (U_s/U_f).The longitudinal time-mean velocity at the surface (U_s) can be measured directly. The net flux (U_f) is defined as the river discharge per unit area of cross section of the estuary. This circulation parameter can also be derived from other measurements of the velocity profile so long as the vertical gradient of the streamfunction is known (see section 3.3 for a definition of the streamfunction).

Based on this system fjords generally occupy type 3b of the diagram; high stratification, however they can change classification to type 3a due to changes of fresh water flow (Farmer and Freeland, 1983). This classification system differentiates fjords from the other types of estuary (table 1.1).

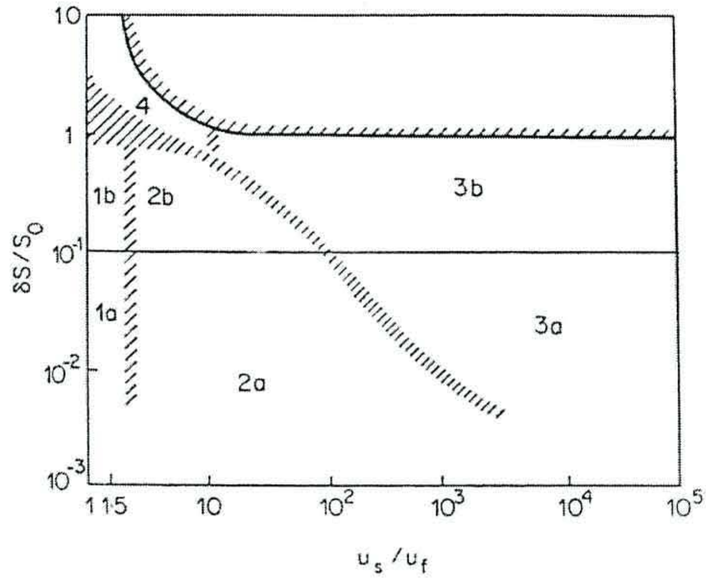

Figure 1.1 – The Hansen Rattray diagram

Table 1.1 – Summary of the Hansen Rattray estuarine classification after Dyer (1996)

Type	Name	Description	Salt Transfer Mechanism
1a / 1b	Well Mixed	Net flow seawards at all depths. Stratification in type b.	Diffusion
2a / 2b	Partially Mixed	Flow reversed at depth.	Advection and Diffusion
3a	Fjord (weak stratification)		Advection
3b	Fjord (stratified)	Lower layer so deep that circulation does not extend to the seabed.	Advection
4	Salt Wedge	Greatest stratification.	

The HR classification demonstrates the typical 2-layer flow associated with fjords and lochs. They can, however, exhibit other types of estuarine classification as seasonal changes alter fresh water run-off and mixing mechanisms. Syvitski *et al.* (1987) explain that temperate fjords may be 2-layer systems during the spring, summer and autumn due to large fresh water flow from precipitation and ice-melt. During the winter mixing may dominate creating a vertically well-mixed estuary.

Sills are shallow areas often found at the mouth of a loch, or at the junction of two lochs. The definition of a sill used by Edwards and Sharples (1986) is a shallow region, ⅔ the depth of the basin it bounds. It can appear to be arbitrary in deep water where a 'sill' may not have any of the dynamics normally associated with them, and the term should be applied cautiously.

The sill of a basin serves to separate the deeper waters from the adjacent coastal water. Above this sill level the circulation can be thought to be estuarine; a brackish surface layer moving seaward over a more saline landward flowing layer. The landward flowing layer is forced by entrainment of the saline water upwards into the outflow. The two layer circulation is described by the scheme of Hansen and Rattray. Fjords also have another circulation system in the deeper, isolated water below sill depth. When the inflowing water is denser than that at depth the deep water is lifted and can exit the basin in the seaward flowing surface layer.

If the two vertical circulation systems interfere with one another the basin can be described as overmixed by the classification of Stigebrandt (1981). Basins that exhibit an intermediate layer between the two systems were regarded as 'normal' fjords (N-type), as opposed to the overmixed (O-type) fjords. The mathematical division of the two relies upon the depth of the lower layer over the entrance sill. Therefore it cannot distinguish lochs and fjords that have a fully mixed water column over the sill.

A further classification was introduced by Stigebrandt and Aure (1989) to differentiate between fjords by reference to their tidal forcing. It was found that fjords with weak tidal forcing over the sill exhibited stronger internal tides than those with strong tidal forcing. The difference was attributed to the formation of jets in those fjords where tidal forcing was strongest. In these cases the inflowing stream separates from the bottom topography and forms a high speed jet in the upper part of the water column. The inflow in the cases with weaker forcing follows the topography; water is advected vertically causing an internal tide. The quantitative definition of these types involved the ratio of the inflowing tidal velocity to the speed of internal waves. This *Froude* number is discussed further in the following section.

1.2 Tides

1.2.1 Barotropic Tides

The tidal ranges for ports in the areas where lochs are most studied are shown in table 1.2. This demonstrates the larger tidal ranges generally found in the Scottish Lochs compared against those in Scandanavia and North America. The tidal range in Oslo is remarkably small due to its position landward of several shallow sills. Data for the North American ports is not directly comparable as the tidal regime there is mixed diurnal / semidiurnal. Therefore the mean ranges have been given.

While the tidal forcing in the Norwegian fjords is the smallest of those covered in table 1.2, the Norwegian Hydrographic Service also give the maximum and minimum water levels recorded at their ports. For Oslo the greatest observed high water is 2.6m above chart datum. This clearly demonstrates that non-tidal forcing can be at times far more significant than tidal forcing alone.

Table 1.2 – Tidal ranges (m) near fjordic studies

	Location	MSR	MR	MNR	Source
Scandinavia					
	Byfjorden	0.35			Luingman *et al* (2001)
	Oslo	0.36		0.2	NHS
	Bergen	1.3		0.5	ATT
	Trondheim	2.5		1.2	NHS
	Narvik	2.7		1.3	ATT
North America					
	Port Townsend (Admiralty Inlet)		1.63		NOAA
	Neah Bay (Strait of Juan de Fuca)		1.68		NOAA
	Seattle		2.3		NOAA
Scotland					
	Oban	3.3		1.1	ATT
	Ullapool	4.5		1.8	ATT

MSR – Mean Spring Range, MR – Mean Range, MNR – Mean Neap Range.
NHS – Norwegian Hydrographic Service, ATT – Admiralty Tide Tables,
NOAA – National Oceanic and Atmospheric Administration (USA).

If the phases of the surface elevation and horizontal velocities at a point are in direct quadrature then the surface tidal wave is reflected and there is no removal of energy from the barotropic tide. Any deviation from this 90° relationship suggests a progressive component to the flow and that energy is being lost from the barotropic tide. Two independent methods of estimating the loss of energy from the barotropic tidal wave at a sill have been used by Inall *et al* (2004) in loch Etive. The first method uses the phase difference of the barotropic tide (ϕ_1) either side of the sill (equation 1.1) to estimate the energy loss from the surface tidal wave. The second method relates the phase shift from quadrature (ϕ_2) to the energy flux from the barotropic tide (equation 1.2).

$$E_1 = \frac{1}{4}\rho g A_l \omega a_0^2 \sin(2\phi_1) \qquad [1.1]$$

$$E_2 = \frac{1}{2}\rho g A_s a_0 U_0 \cos(\phi_2) \qquad [1.2]$$

A_l is the surface area landward

A_s the cross sectional area of the sill

a_0 the amplitude of the vertical tide

U_0 the amplitude of the barotropic current

The fate of this energy taken from the barotropic tide is discussed in section 1.5. In general the larger proportion of energy extracted from the barotropic tide, the more progressive the tidal wave will be. Manifested as the lag of the time of high water at the head of a loch, the progressive wave will contribute to asymmetry in the tide.

1.2.2 Baroclinic Tides

While studying the influence of the wind upon the thickness of the brackish surface layer found in Alberini Inlet (British Columbia), Farmer and Osborne (1976) found a semi-diurnal change in thickness. The semi-diurnal changes in the layer thicknesses were only apparent at the station nearest the head of the loch and it was suggested that it was forcing of the stratification over a slope that led to the formation of the internal response.

The 2-layer circulation regime, a brackish seaward flowing upper layer over a saline lower layer, is not confined to sealochs. All types of estuary (except fully mixed) show two (or more) layers of differing density often flowing in different ways. In the case of a sealoch fresh water flows into a stagnant basin of seawater, the acceleration due to surface slope is balanced by entrainment of stagnant water into the upper layer. Entrainment draws water in at depth (+ve estuarine circulation). Such circulation is shown in figure 1.2. The difference between this and the ideal estuarine circulation system is that the lower layer is far deeper than the salt wedge found in classic estuaries.

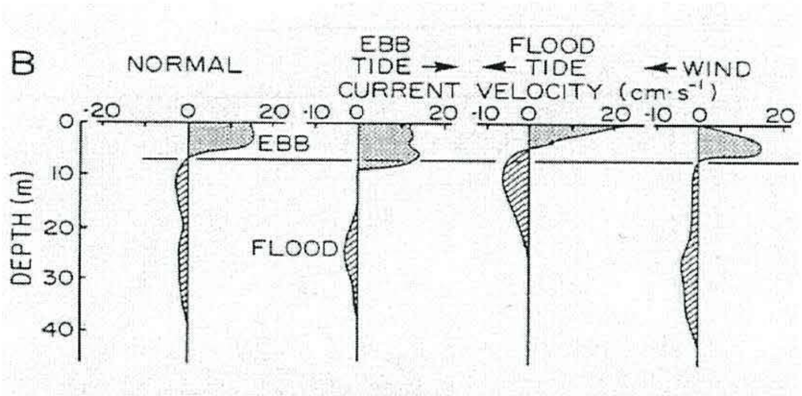

Figure 1.2 – Ideal 2-layer fjord circulation (Syvitski et al. 1987)

It was 3 years after the publication of a theoretical description of internal tidal forcing in fjords (Stigebrandt 1976) that observations were presented to confirm the presence of a progressive M2 internal response in the Oslofjord (Stigebrandt 1979).

These observations were based around current meters located at the Dröbak sill and some 10km landward. The internal tide was inferred from the fact that the amplitude of the M2 signal was greater at the location farther from the sill. This would not be true for a barotropic flow in which the flow would be reduced at the location with the greater cross sectional area; thus the M2 response must be baroclinic in nature. The phase lag of the observed M2 signals was shown to be consistent with a progressive baroclinic tidal wave. A barotropic signal with a large phase lag cannot exist over such a small horizontal separation.

More recent observations of the M2 internal tide have been presented in Ellis (2001) for the Gareloch. This is a small Scottish sealoch 8km in length, approximately 35m deep with a 15m deep sill connecting it to the Clyde Sea. At a location approximately half way up the loch the upper layer thickness was observed from ADCP data to be at approximately 10m. The current meter records from 3 and 15m depth are presented in figure 1.3 and ADCP data for a shorter time period shown in figure 1.4.

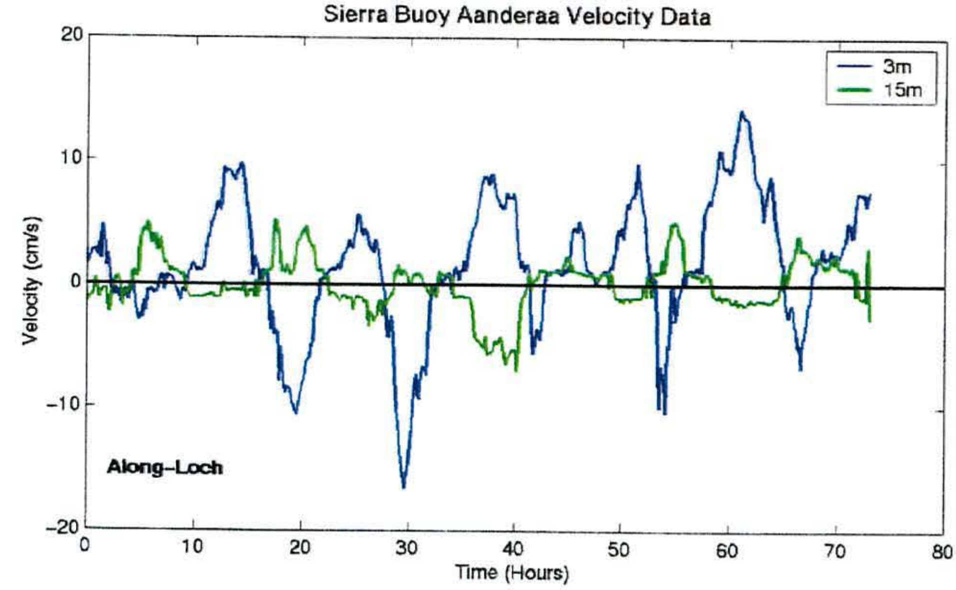

Figure 1.3 – Current meter data from the Gareloch (Ellis 2001)

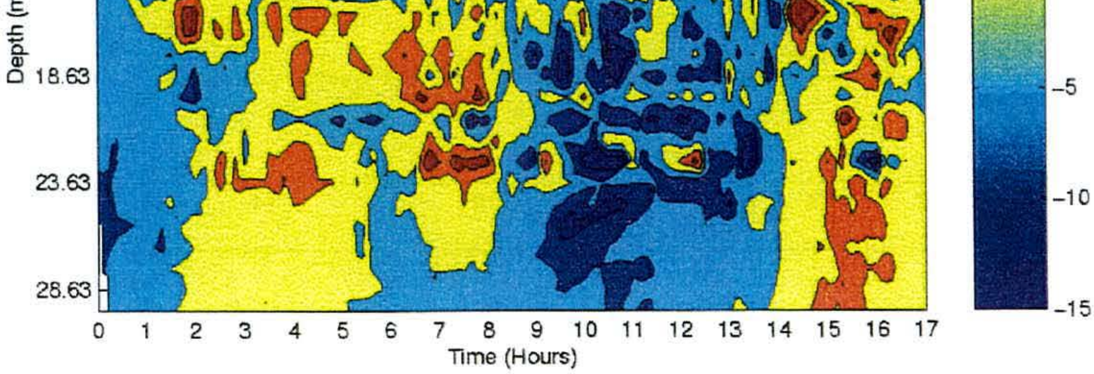

Figure 1.4 – ADCP data from the Gareloch (Ellis 2001)

A more quantitative investigation of the M2 internal tide was taken by Allen and Simpson (1998b) on the data set used in the current study. Comparison was made between harmonic analysis of the along loch components of velocity and the theoretical internal waves from fitting normal modes.

The 7 months of data were split into 6 periods of similar stratification before analysis was undertaken. There were significant differences in the behaviour of the internal tide between these periods. The best agreement between the mooring data and the normal mode derived from theory was found in the centre of the loch. These results are shown in figure 1.5.

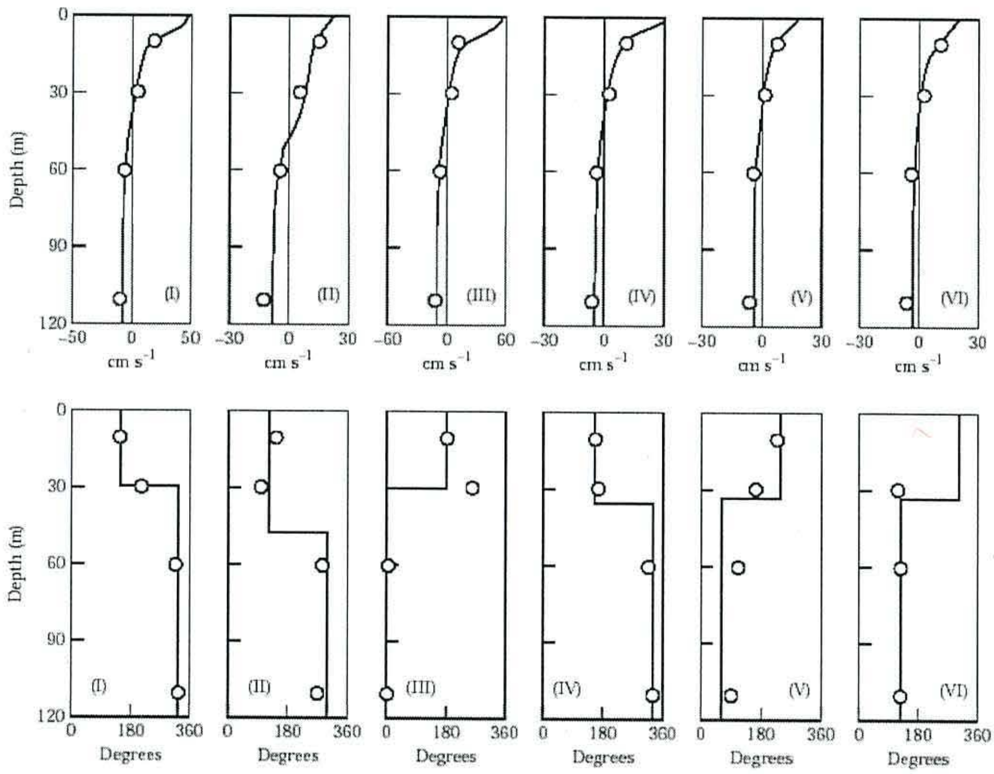

Figure 1.5 – Amplitudes (A) and phases (B) of the M2 velocity, circles observations, line normal mode theory (Allen and Simpson 1998b)

As can be seen in figure 1.5 the depth at which there is minimum amplitude the phase changes abruptly in both the observations and the theoretical wave. This is the classic mode 1 response.

1.3 Renewal

Should the water flowing into a basin over a sill become denser than the ambient waters in the basin the inflow will initially sink. The importance of this process in sealochs cannot be overstated as it controls the major exchange of deeper waters. Broadly there are 3 factors controlling the density of water at a sill, wind, freshwater runoff and tidal range.

Onshore winds and storms can pile water up against the coast, increasing the sealevel at the entrance to a loch and encouraging landward flow at the surface. When the sealoch is connected via an intermediate stretch of water to the open ocean then the simple picture is complicated. Evidence is presented (Cannon *et al.* 1990) that salinity variations outside Puget Sound are statistically related to changes in the mean sea level lagged 6½ days. These changes in mean surface level are shown to be the result of winter storm activity, thus this gives seasonality to the process of renewal. The same paper attributes a period without such intrusions to a lack of horizontal density gradients following storms and increased mixing.

While modelling the same data set Lavelle *et al.* (1991) showed that during these winter renewal events there was a corresponding net outflow at the surface of Puget Sound.

The assessment of flushing in Loch Ailort (Gillibrand *et al.* 1996) compares the flushing characteristics of Lochs Etive and Sunnart. Loch Etive has a flushing frequency of 16 months and Loch Sunnart 3 weeks. The difference is caused by the variability of fresh water inflows. Fresh water flows into Loch Etive via the freshwater Loch Awe and so the supply of fresh water is buffered against periods of low flow. This is not the case in Loch Sunnart where fresh water flows are more variable. It was proposed that periods of low freshwater input are required for renewal to take place.

Using statistical arguments Allen and Simpson (1998a) show that of the three factors (fresh water input, tidal range and along-loch windspeed) the fresh water input via the River Lochy accounted for 71% of the variance of the horizontal density gradient in Loch Linnhe. It was stated that the river flow must be below $180m^3s^{-1}$ for a renewal event to take place. It was also noted that during the spring months inflows occurred on a fortnightly basis, although none of these inflows were sufficient to completely renew the deep basin waters. This suggests a relationship with tidal range, in that larger tides advect more dense water from further seaward and from a greater depth by aspiration. This process involves strong flows over sills drawing water up from depth; water from twice the sill depth has been observed crossing the sill in Loch Etive (Inall *et al.* 2004).

The strait separating Vancouver Island from the mainland of British Columbia, the Juan de Fuca Strait, has been studied extensively. This body of water is the seaward end of many of the well studied North American fjords. A summary of previous studies (Masson and Cummins 2000) indicates that a fortnightly modulation of surface salinity exists. During springs there was an increase in surface salinity, attributed to an increase in mixing over the many sills.

The relationship between the spring neap cycle and dense water inflows was shown to be reversed in Puget Sound. The flow over the sill was stratified; therefore at spring tides more vertical mixing took place between the brackish surface layer and the bottom water reducing its salinity. Dense water intrusions were therefore associated with neap tides when mixing was less intense (Cannon *et al.* 1990).

The near-sill process of renewal has been measured in the Gareloch by Ellis (2001). ADCP data were collected showing a negatively buoyant jet flowing down the lee side of the 15m deep sill to a depth of approximately 25m. A gravity driven component to the flow was estimated to enhance the flood speed of the jet by 50% above the barotropic estimate.

To say that deep water renewal is simply the exchange of the dense deep water for juvenile dense water that has crossed the sill is to simplify matters. Luingman *et al* (2001) use the concentrations of oxygen in the deep water prior and following renewal, to estimate that the deep basin water after renewal was made up of equal measures of juvenile and existing basin waters. The density of the inflowing water was greater than that at depth during the entire period of the inflow, suggesting that 'total renewal' had taken place. The main mechanism for this mixing was shown to be entrainment of old 'basin' water into the plume of juvenile water as it flows down the slope from the sill to the depths of the basin. It was estimated that the volume of the plume grew by a factor of between 2 or 3 due to entrainment.

Edwards and Edelsten (1977) used data from Loch Etive to quantify entrainment in an analytical model. This study also relied on dissolved oxygen concentrations as a tracer to indicate the mixing of juvenile water with stagnated basin water. Mixing was related to empirical constants derived from the observations which successfully hindcasted other renewal events.

1.4 Mixing by internal waves

1.4.1 Theoretical Description

Where the internal Froude number changes from less than unity (sub-critical flow) to greater than unity (super-critical flow) a hydraulic jump is said to occur; conversely a change from super-critical to sub-critical flow causes a hydraulic drop. Both situations are characterised by a change in layer thickness and a breaking internal wave. The internal Froude number is the ratio of the flow speed (u) to the speed of interfacial waves in the undisturbed system (upstream of any obstacle). This Froude number (F) can be given for each layer in a 2-layer system for the upper layer (Baines 1984, Armi 1986) where the lower layer is considered to be static and infinitely deep.

$$Fr = \frac{u_1}{\left(g\frac{\Delta\rho}{\rho}h_1\right)^{\frac{1}{2}}} \qquad [1.3]$$

u_1 is the flow speed of the upper layer
h_1 is the thickness of that layer

The density difference ($\Delta\rho$) and the density of the lower layer (ρ) multiplied by the acceleration due to gravity give the 'reduced' gravity (g'). This does however use a simplification to the expression for the speed of a wave in a two-layer system. There are two simplified expressions for the speed of a wave on an interface, both are shown in table 1.3 (Pond and Pickard 1998).

Table 1.3 – Expressions for wave speeds in a two-layer system

Expression for wave speed	Applicable
$C = \left(g'\frac{h_1 h_2}{h_1 + h_2}\right)^{\frac{1}{2}}$ [A]	Both layers are considered to be shallow with respect to the wavelength (λ) of the interfacial wave ($\lambda > 20h_1$ and $\lambda > 20h_2$)
$C = (g'h_1)^{\frac{1}{2}}$ [B]	Upper layer is shallow and the lower layer is infinitely deep

Expression A for the speed of internal waves has been used by Armi (1986) in relation to flume tank experiments and by Stigebrandt (1976) where the interfacial wave under consideration was the M_2 internal tide, with a wavelength far greater than 20 times the layer depths.

Expression B was originally put forward by Ekman and used to describe observations in the deep ocean from the research vessel the *Fram*. Its use in coastal oceanography, although ubiquitous, should be qualified by its overestimate of wave speed when the lower layer is not infinite. When applied to Froude number calculations this underestimates the Froude number and so the threshold of critical flow would occur at $Fr < 1$.

Comparing the flow speed to the speed of long internal waves may not fully describe the flow conditions. (Farmer and Smith, 1980) introduced the concept of comparing speeds against the wave speeds for different modes of internal waves. They showed through observations that differing flow characteristics were observed when the flow changes from critical to supercritical with respect to the mode 2 internal wave speed, as well as the faster mode 1 wave.

The composite Froude number (Farmer and Armi, 1986) describes the situation for an interface between two fluids moving with differing speeds. The Froude number is calculated in each layer separately, and then combined according to;

$$G^2 = F_1^2 + F_2^2 \qquad [1.4]$$

If the lower layer is considered to be stationary, F_2^2 becomes zero and the composite Froude number reduces to the expression given previously corresponding to an infinitely deep ocean (equation 1.3). Less intuitively, if the velocities in the two layers are equal ($u = u_1 = u_2$), it can be shown that the composite Froude number reduces to the ratio of the flow speed to the expression for interfacial wave speed where both layers are considered shallow (equation A in table 1.3), as shown below.

$$G^2 = F_1^2 + F_2^2 = \frac{u^2}{g'h_1} + \frac{u^2}{g'h_2} = \frac{u^2}{g'\left[\frac{h_1 h_2}{h_1 + h_2}\right]} \qquad [1.5]$$

The undular internal bore was found in laboratory experiments in a two layer system upstream of an obstacle. It also marks a change in layer depth and a transition from sub to super critical flows (Lane-Serff, 2002).

Where the stratification is found to be a continuous change of density with depth rather than the simple 2-layer case internal waves can propagate at an angle to the horizontal. The changing stratification can be described by the buoyancy frequency (*N*) which is a measure of the natural frequency of oscillation of such a stratified system (equation 1.6). It is also referred to as the Brunt – Väisälä frequency and can be approximated by ignoring the term containing the speed of sound (*C*) through the system (Pond and Pickard, 1998).

$$N^2 = g\left[-\frac{1}{\rho}\frac{\partial \rho}{\partial z} - \frac{g}{C^2}\right] \approx g\left[-\frac{1}{\rho}\frac{\partial \rho}{\partial z}\right] \qquad [1.6]$$

The slope of the phase velocity vector of such an internal wave is given by equation 1.7 assuming a fixed frequency (ω) and a fixed buoyancy frequency (*N*) and ignoring the effects of the Coriolis force. Internal waves are called transverse waves, in that the group velocity is perpendicular to the phase velocity, therefore the direction of propagation is perpendicular to the slope defined in equation 1.7. Therefore for a small frequency (tidal frequency) the group velocity will be nearly horizontal. However higher frequency waves, can propagate at appreciable slopes to the horizontal (α), especially in situations of weak stratification (large values of *N*).

$$\alpha = \pm\left[\frac{\varpi^2}{N^2 - \varpi^2}\right]^{1/2} \qquad [1.7]$$

Where internal waves can propagate at an angle to the horizontal a comparison of their slope (α) with that of the bottom topography ($\partial H/\partial x$) can be used to distinguish two types of wave that show distinct characteristics.

The review of Vlasenko *et al.* (2005) describes the case where $\alpha > \partial H/\partial x$ as having a subcritical topographic slope with respect to the slope of the internal wave rays. The situation where $\alpha < \partial H/\partial x$ is described as having a slope supercritical to the internal wave rays. This creates a wave beam where the internal waves propagate vertically, reflecting from the surface and seabed. An overview of the mechanisms for the creation of internal waves under a variety of conditions is presented in figure 1.6, reproduced from Vlasenko *et al.* (2005). The latitude (φ) is included as these generation regimes are also applicable to shelf edge scales where the Coriolis parameter can become significant. The region where the frequency of the internal waves is less than the Coriolis parameter ($f = 2\Omega.sin(\varphi)$, where Ω is the frequency of the Earth's rotation) is above the critical latitude. This modification of internal waves by the Coriolis force is unlikely in fjords and lochs due to the narrow channels and high latitudes. The generation regime pertinent to Upper Loch Linnhe is that in the bottom right of figure 1.6.

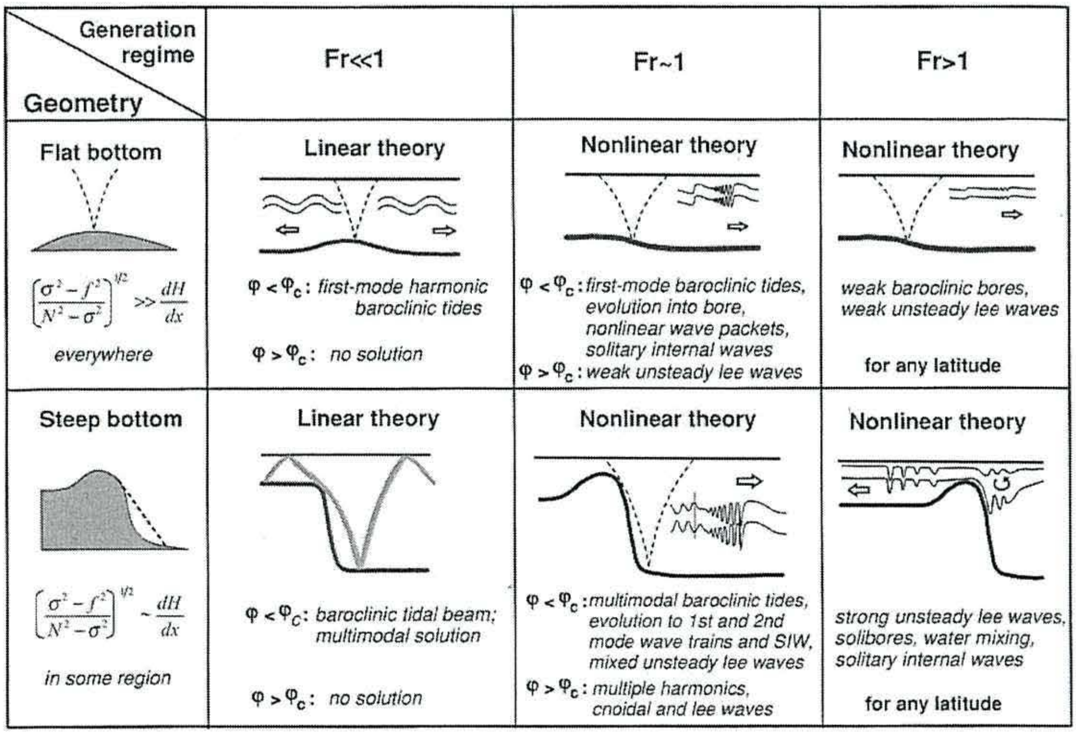

Figure 1.6 – Scheme of generation mechanisms of tidally induced internal waves for different oceanic conditions (Vlasenko et al., 2005)

1.4.2 Internal wave observations

Observations of these phenomena in oceanography have benefited greatly from the increasing spatial resolution offered by modern instruments. Acoustics allow the water column to be sampled from a moving vessel, giving both spatial and temporal coverage. Initially echo sounder images illustrated the presence of lee waves using the amplitude of backscatter.

More recently ADCP's have been used, both frame mounted on the seabed (Inall *et al,* 2004) and vessel mounted (Farmer and Armi, 1999), to give high resolution velocity data. The high spatial resolution enables features such as leewaves and jets to be eluded.

Perhaps the observations to have generated the most study are those taken in Knight Inlet by Farmer and Armi (1999). The flows over this sill have previously been studied (Farmer and Smith, 1980), however never with the high resolution that was afforded by the use of simultaneous vessel mounted ADCP, sonar images and undulating CTD. The ADCP and CTD data gave velocity components and density profiles respectively. The sonar image gave an indication of the density interfaces. Scatterers were thought to concentrate at these locations, and the plots of backscatter show lee waves on the density interface (figure 1.7).

The use of vessel mounted ADCP to measure flows over sills has also revealed the spatial extent of the jet generated downstream of the sill in loch Etive (Figure 1.8). This data set also shows lee waves, along with flow separation and a reverse flow at depth.

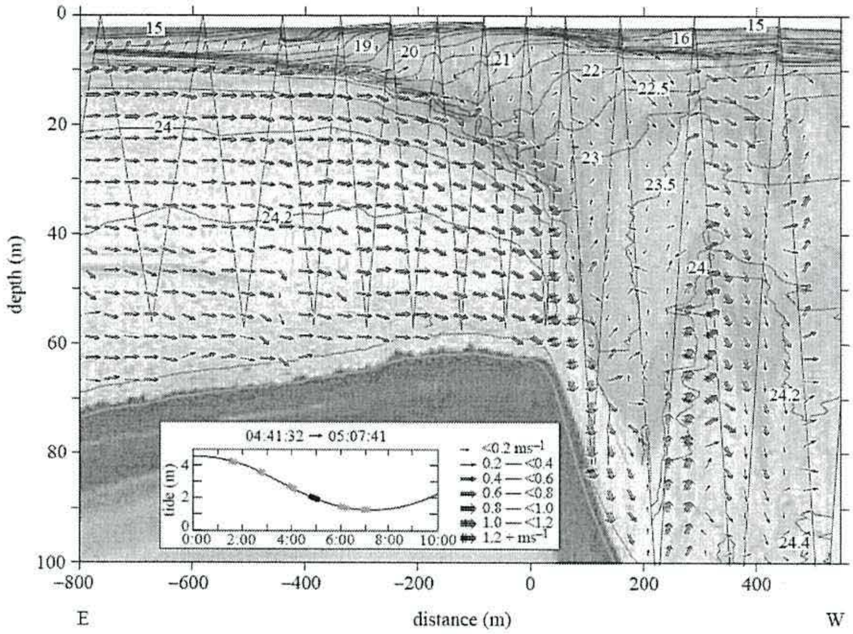

Figure 1.7 – Flow over a sill in Knight Inlet (Farmer and Armi, 1999)

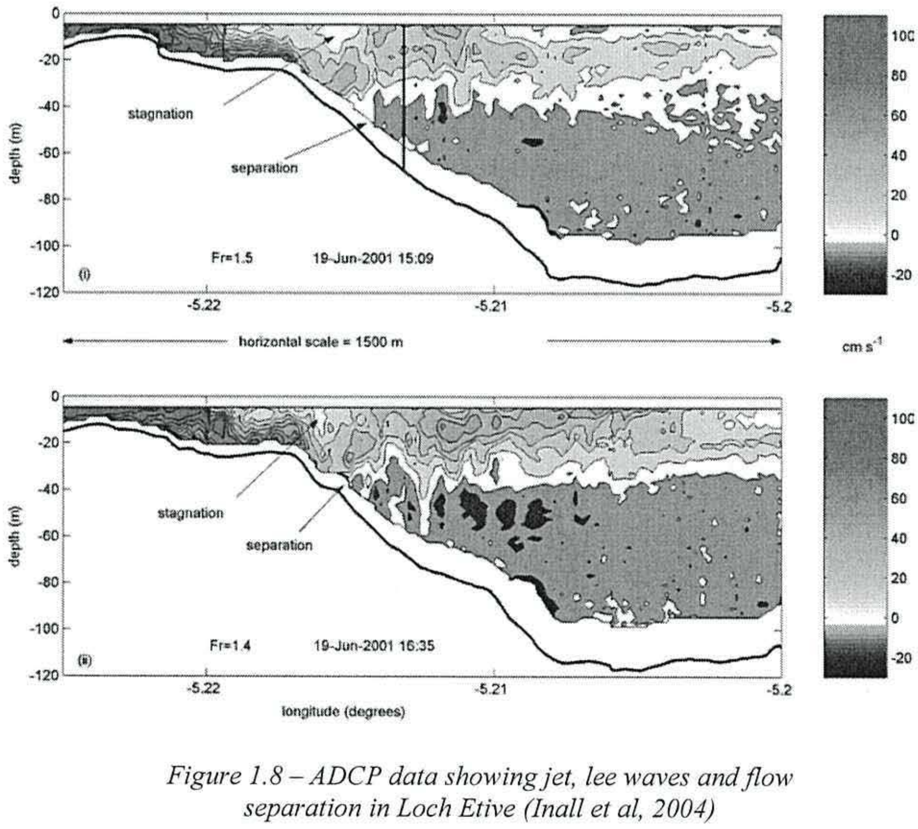

Figure 1.8 – ADCP data showing jet, lee waves and flow separation in Loch Etive (Inall et al, 2004)

The ability to make measurements over large areas enabled Allen (1995) to show the presence of a basin scale internal tide in the study area. Each section along the axis of Upper Loch Linnhe took approximately 1 hour; therefore a time series of current observations, covering most of the water column and the entire length of the basin, was constructed at hourly intervals. The analysis by Allen and Simpson (1998b) of these observations compares the ADCP data to current meter data collected at the same time, thus giving two independent observations of an internal tide.

1.4.3 Mixing by the internal tide

The most significant contribution to the theoretical understanding of internal tides comes from work by Stigebrandt (1976) applied to the Oslofjord in Sweden. Conceptually the model was of a 2-layer system with the pycnocline at sill depth. The current over the sill produces an internal wave on either side 180° out of phase. The period of the waves is assumed to be equal to the tidal forcing frequency. The speed of propagation uses case A from table 1.1 under the assumption that the wavelength of the tide is far greater than the depth of either layer. The flow over the sill is assumed to be subcritical, i.e. the Froude number is less than 1 and no hydraulic jump or jet is produced. Later work by Stigebrandt and Aure (1989) suggests that the demarcation between jet and wave fjords should be approximately $F_i = \frac{2}{3}$.

The internal tide thus generated is assumed to decay to turbulence at the edges of the basin via internal wave steepening and breaking. In this way the energy supplied by the cross-sill barotropic tide is transferred to internal tide and subsequently to mixing. This simple energy pathway was used to estimate the flux Richardson number in the Oslofjord, which is comparable with other estimates.

Building upon his earlier theory of barotropic to baroclinic energy transfer, Stigebrandt (1999b) summarises other work since published to relate the removal of energy from the barotropic tide to a phase shift of the barotropic tide over the sill. Here frictional losses due to the interaction of a boundary layer with the seabed are included. It is stated that these only become important when the length of the sill becomes significant.

The concept of barotropic form drag is also described in Stigebrandt (1999b). The flow is considered to accelerate into the sill constriction and therefore there is a reduction of pressure and hence sea level. The down sill flow separates from the seabed and therefore the deceleration is less rapid so the pressure drop is not entirely reversed. This results in a net loss of energy. This process is thought to be dominant in supercritical (jet type) fjords. It is suggested that baroclinic wave drag, the process by which an M2 internal tide was seen to be generated in the Oslofjord, is the dominant energy pathway in subcritical (wave type) fjords.

1.5 Energy pathways

Using the above theory of energy pathways, Inall *et al.* (2004) simplify matters for Loch Etive to give the ratio of the energy lost by bottom friction (E_f), barotropic form drag (E_a) and baroclinic wave drag (E_w) to be given by equation 1.6:

$$E_f : E_a : E_w = C_D L : h/2 : \frac{dhC_g}{(d+h)U} \qquad [1.8]$$

The first two energy pathways in equation 1.8 are fixed by the topography. It is only baroclinic wave drag that is a function of the stratification and the tidal forcing. It was shown by Inall *et al.* (2004) that over the spring / neap cycle dominant pathways of energy changed from being almost exclusively barotropic form drag at springs, to a combination of barotropic form drag and baroclinic wave drag at neaps. Thus the classification of jet and wave basins cannot be considered fixed in time or a straight forward distinction.

Work by Tinis and Pond (2001) in Sechelt Inlet, a Canadian jet-type fjord, showed that most of the incident tidal energy was removed by friction at the sill. The second largest energy loss (5%) suffered by the barotropic tide was due to the formation of the jet in the lee of the sill. Approximately ½% was lost to the progressive internal tide via the mechanism described by Stigebrandt (1976).

Recently similar techniques have been used (Stacey, 2005; Stacey and Valle-Levinson, 2006) to compare the pathways of energy losses in a review of North American Fjords, and in the Paso Galvarino in Chile. The comparison enabled a distinction to be made between deep silled fjords such as Knight Inlet, and shallow silled fjords (Sechelt Inlet and el Paso Galvarino) based on the processes extracting energy from the tidal forcing. The internal tide was the largest sink of energy in Knight Inlet; the shallower silled fjords extracted most energy via friction at the sill.

Work by Inall *et al* (2005) has sought to investigate the energy dissipated by turbulence in a jet produced in the lee of a shallow sill. Their revised energy budget for the Loch Etive sill showed that the internal hydraulic jump accounted for only 10% of the energy extracted from the barotropic tide. The greatest sources were found to be internal wave radiation and horizontal eddy formation.

These energy pathways to mixing from barotropic tides play an important role in the global balance of mixing surface and deep waters. Similar processes are played out at the shelf edges and over seamounts in the deep ocean. Thus the study of these isolated basins at high latitudes has global implications.

1.6 Consequences of the oceanography of sealochs

Given the sheltered nature of sealochs, they make ideal areas to study vertical mixing processes relevant to general oceanography. During periods where wind stirring can be ignored, and when no cross sill density exchanges take place, the tidal stirring and its resultant mixing of the stratification can be quantitatively studied. Such work was the ultimate goal of the initial work of Stigebrandt (1976). The assumptions involved are that all of the energy passed to the internal tide via baroclinic wave drag is converted to turbulent mixing in the lower layer. It was proposed that this mixing occurs at the edges of the fjord where internal waves break against the boundary. Therefore horizontally integrated stratification needs to be used to assess how much mixing has taken place in the entire system. Once the vertical exchange co-efficient (K) has been estimated from observations over time, an estimate of the Flux Richardson number (R_f) can be obtained from equation 1.9.

$$R_f = \int_V \frac{KN^2 dV}{\sum_{\omega} \varepsilon_i(\omega)} \qquad [1.9]$$

The exchange co-efficient (K) and the buoyancy frequency (N) are integrated over the volume of the basin (V) and the internal wave energy (ε_i) is summed over all the frequencies of interest (ω).

Applying the above theory to the Oslofjord an estimate of the Flux Richardson number was found to be 0.05. An extensive investigation by Stigebrandt and Aure (1989) yielded estimates from 35 fjords on the Norwegian coast, encompassing both jet and wave type basins. While there are differences between the total energy put into each type of system, the values for Flux Richardson number for each were shown to be in good agreement, and with the estimate for the Oslofjord previously published.

Long periods between renewal events can lead to a loss of oxygen from deeper waters due to the biological demand exceeding the mixing down of oxygen rich surface waters. In the absence of oxygen H_2S can be formed which is detrimental to the health of virtually all marine organisms.

The tidal flows in Scottish sealochs and exchanges with the open sea are of concern for the study of pollutant pathways, most notably in the form of fish farm waste. Along with decomposition of excess food and excretion products from the fish themselves, the most serious pollutant from the fish farming industry is Diclorvos (DDVP). Parasitic crustaceans often infect farmed salmon and this organophosphate is used to irradiate them. Concerns about using such a chemical in large quantities in the environment have lead to studies of its pathways and effects. Mixing studies in Scottish sealochs have been undertaken (Gillibrand and Turrell, 1997) to assess if safe limits are likely to be exceeded.

Excess nutrients in sealochs give rise to plankton blooms (Watts *et al.* 1998) that can interfere with the shellfish cultivation and fish farms. Silicates are added to the Loch Linnhe system via fresh water runoff at the northern end of the basin. Phosphates and Nitrates were found to be in the greatest concentrations in the inflowing seawater. Therefore the mixing of these nutrients by physical processes will influence the nature and timing of phytoplankton blooms. With the addition of nutrients by commercial fish farming there is a mechanism for conflicting interests between the fish farms and the existing shell fish industry. It is therefore vital to be able to accurately predict the impacts of new and existing fish farms on nutrient levels inside the lochs.

The study of our sealochs has great significance to industry, and to pure science. In addition, the ecological importance of our sealochs cannot be overstated. The Knoydart peninsular, between Lochs Hourn and Nevis, is the largest area of wilderness left in the British Isles, and among the largest left in Western Europe.

1.7 The study area

1.7.1 Location

Firth of Lorne is a large wide opening on the West Coast of Scotland formed by the Great Glen Fault which runs from the South West to the North East of Scotland, bisecting the Scottish mainland forming the Caledonian Canal. It is approximately 25km long, the North Eastern end joins Loch Linnhe where it is 5km wide; at the southern end where it joins the North Atlantic it is approximately 10km wide. The North Western shore is formed by the Isle of Mull, the opposite shore is mainland Scotland. The land surrounding the Firth of Lorne, and the rest of the study area is the Scottish County of Argyle and Bute. The locations are shown in figures 1.9 and 1.10.

Taken together by Edwards and Sharples (1986) Upper Loch Linnhe and Loch Eil contain 5 sills. The two important sills for this study are those at Corran Narrows and Annat Narrows. These two shallow sills (18m and 5m deep at LW respectively) form the ends of the Upper Loch Linnhe basin which has a maximum depth of 155m. The surface area of the two lochs together is nearly 36 km^2 at HW. Joining the system at the landward end of Upper Loch Linnhe is the river Lochy, the major local source of fresh water. Bio-chemical studies in this basin have been reported in Overnell and Young (1995), Overnell *et al* (1995) and Watts *et al* (1998). Dynamical investigations, resulting from the second data set used in this study, are reported in Allen (1995), Allen and Simpson (1998a), Allen and Simpson (1998b) and Allen and Simpson (2002).

Other lochs mentioned in this study are Lochs Etive and Creran. The former joins the Firth of Lorne at Dunstaffnage and the later is joined to Loch Linnhe, further north. Loch Etive is close to 30km in length and has 6 sills (Edwards and Sharples 1986). The only sill relevant to this study is the most landward, enclosing the upper basin from the lower reaches of the loch. It has a depth of 13m and a width at LW of 200m. Due to the isolation of this upper basin from the coastal waters it undergoes renewal of the deep water on average every 16 months (Gillibrand *et al.* 1996). This has made it the subject of many recent studies, both into the chemistry (Overnell 2002) and the dynamics of the system (Inall *et al.*, 2004, Inall *et al.*, 2005 & Stashchuk *et al.* In Press).

Loch Creran is the smallest of the Lochs mentioned here, being 12.8 km long and containing 2 basins. These are separated by an extremely shallow sill of 3m depth. It is the flood stream over this sill, and the tidal intrusion front generated in the upper basin that has formed the only dynamical study in this loch (Booth 1987).

Loch Leven joins Loch Linnhe's Eastern Shore just south of Corran narrows. Its length, 13.4km, is slightly longer than Loch Creran. It has 5 sills; the most seaward consists of 2 sills of 6m depth separating a small basin 36m deep. The total length of this sill system is 2.5 km. Towards the landward end of the loch a 4m deep sill separates the upper, 47m deep 4km long basin from the rest of the loch. Recent investigations into the mussel culture in this loch have found them to be contaminated with polycyclic aromatic hydrocarbons thought to emanate from an aluminum smelter (McIntosh *et al.* 2004).

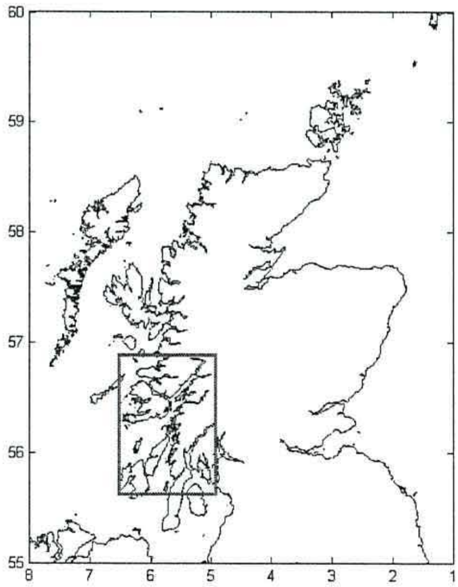

Figure 1.8 – Scotland showing the extent of figure 1.9.

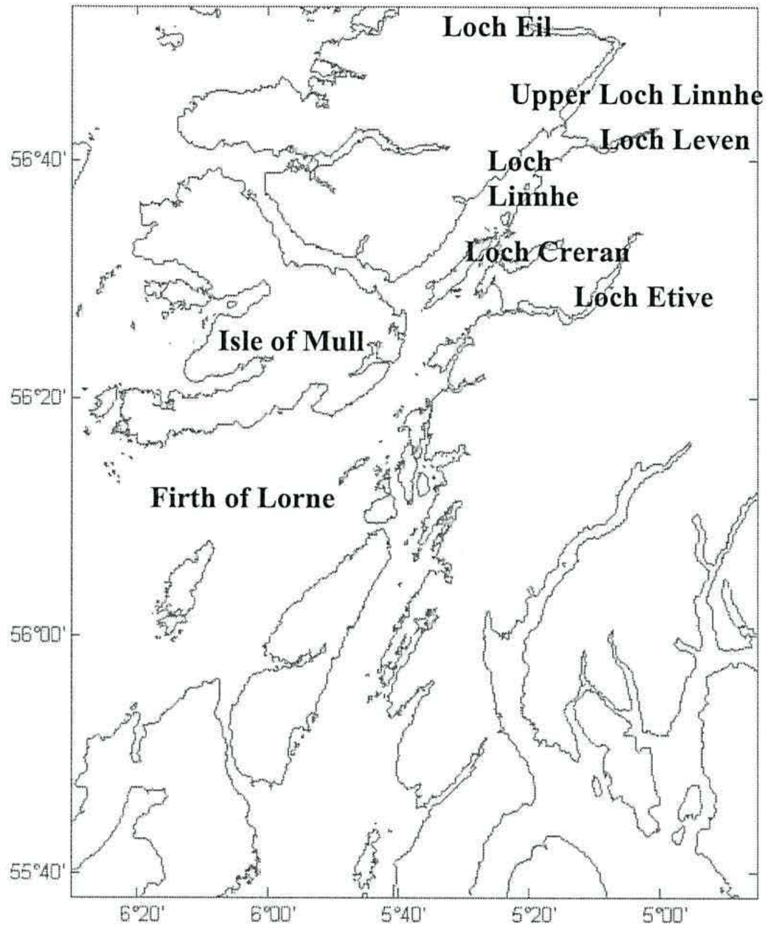

Figure 1.10 – The Firth of Lorne and the sea lochs

1.7.2 Ecological importance

The region around the Firth of Lorne is a European Special Area of Conservation and a designated site of National Scenic Beauty. The Northern shore of Loch Etive is a Special Area of Conservation due to the deciduous woodlands found there. There are in total 116 Sites of Special Scientific Interest (SSSI) in Argyll and Bute, (approximately 8% of the total in Scotland) covering a total area of 62,000 ha (roughly 6 % of the total area of all SSSI's in Scotland)[1].

[1] Scottish Natural Heritage – Facts and Figures 2004 - 2005

1.7.3 Economic factors

The farmed salmon industry has grown significantly on the West Coast of Scotland. Estimated by the Scottish Executive to be worth £260 million in 1998, makes it worth more than Highland beef and lamb sales put together. Over the decade 1988 to 1998 the quantity of Scottish farmed salmon rose 10 fold[2]. Recently the WWF Scotland have put forward a possible link between high levels of nutrients in the water, thought to be associated with the fish farming industry, and toxic phytoplankton blooms that adversely affect oyster fisheries[3]. The aquaculture industry in Scotland, in total, accounts for 90% of the total in the United Kingdom[4], which means its importance in the locality cannot be overstated.

1.7.4 Tourism

The ecotourism industry is active on the West Coast of Scotland. Cetacean and shark observing has become popular and is reportedly worth £1.7 million annually[5]. Numerous other forms of marine tourism such as recreational pleasure boating and diving take place in the study area. Although not in this locality, in the Highlands and Islands region of Scotland the marine wildlife tourism industry accounted for £57 million in 2004, involving more than 2,670 jobs[4].

---

[2] Friends of the Earth Scotland - Salmon farming - The One That Got Away

[3] World Wildlife Fund - Scotland's Secret? Aquaculture, nutrient pollution eutrophication and toxic blooms

[4] The Scottish Executive - Developing a Strategic Framework for Scotland's Marine Environment (2004 – 2006)

[5] Hebridean Whale and Dolphin Trust annual report 2005

1.8 Aims and Objectives

The Shellfish Waters Directive covers 104 sites in Scotland and lays down in law the levels of pollutants and measures to control them at each location[6]. This is due to end in 2013 when full implementation of the EU Water Framework Directive replaces the current regulations. Currently the major designated sites in the study area include most of Loch Etive, Loch Creran (from Port Appin to the narrows) and Loch Leven. There are currently 6 smaller sites in Loch Linnhe north of Oban[7]. When the legislative control of these areas changes there are plans by the Scottish Executive to increase the number of such sites[8].

Initiated in March 2003, the Strategic Framework for Scottish Aquaculture set out to enable a sustainable industry to be achieved. The goal was to identify research priorities to assist the industry. Their document titled 'Recommendations on Research Priorities Consultation - May 2004' has as its first statement '*Improving the specific modelling tools used to assess the cumulative impact of nutrient inputs to a defined area of sea.*'

The simulation of the short-term pathways of pollutants is of considerable interest in the management of port and naval operations around the West Coast of Scotland. In the review article of the state-of-the-art in oil spill models, Reed *et al.* (1999) suggest that future work would involve the simulation of processes at scales of 10 – 1000m. The same review begins with the assertion that oil, having a density similar in magnitude to that of seawater, requires 3 dimensional models to predict its movement. Tkalich (2006) shows that the treatment of the advection is critical to the success of any spill code; both in terms of the advection of the slick itself, or advection in the water column. With the extensive use of the West Coast sealochs

---

[6] European Community Shellfish Waters Directive (79/923/EEC)
[7] Scottish Environmental Protection Agency - Designated Shellfish Waters in Scotland
[8] Scottish Executive Environment Group – Developing a Strategic Framework for Scotland's Marine Environment – 2004 -06

by the Royal Navy both for berthing and testing vessels, there is a considerable need to accurately simulate the water movements over timescales of hours in order to manage a response to any spill.

In a broader context, the simulation of ever more complex geophysical fluid dynamics is becoming possible with advances in computer technology. The simulation of turbulent atmospheric flow in the lee of mountains (Smith, 1985) has challenged numerical methods in a similar fashion to the observations of jets and lee waves in the lee of sills in Knight Inlet (Farmer and Armi, 1999). Numerical techniques must therefore advance, both to take advantage of the increased computational power available, and to accurately simulate observations of new phenomena.

It is with these goals in mind that the non-hydrostatic model has been developed. The intention is to outline a sea loch model capable of answering the needs of environmental planners and managers.

Firstly it will be validated against laboratory experiments and against existing data from Scottish lochs. There will then be a comparison against the slice model previously applied to Scottish lochs by Gillibrand (1993) to investigate the consequences of the different treatment of the pressure fields.

The validation of the non-hydrostatic model with the data of Allen (1995) will enable some of the complex oceanographic processes to be described, processes fundamental to the mixing and circulation of these waters. The simulation of the internal tide in the Upper Loch Linnhe basin will identify the processes important in its creation. This has been the subject of discussion since these data were first published a decade ago.

Chapter 2 –Loch Linnhe Data Analysis

Two data sets have been made available for this study. They both used similar deployments of current meter moorings and have been examined together with rainfall and riverflow data. The seasonal variations of density structure are shown to influence the nature of the internal currents. In particular two responses of the basin are shown; firstly a mode 1 internal tide and secondly a more complex flow regime associated with a renewal event.

2.1 Cruises and Data Overview

2.1.1 FRS data set

Research undertaken by the Fisheries Research Services (Aberdeen) into the physical processes in several sea lochs yields the first data set used in this study. These data were then made available by the British Oceanographic Data Centre. A wide area was covered with current meter moorings in Upper Loch Linnhe as well as the basin seaward, Loch Linnhe. The three stations shown in figure 2.1 are the most northerly of a larger data set extending seaward to the Firth of Lorne and also into Loch Etive. The mooring deployments lasted from 23rd February 1991 to 12th February 1992. During deployment the mooring design varied and including the inevitable effects of instrument failure yields a patchy data set yet exceptionally long and with high temporal resolution. This data set has been used in a description of the bio-chemical processes in the loch by Watts *et al* (1998).

Stations 1 and 3 consisted of current meters also recording temperature and conductivity. The depths of the instruments are shown in table 2.1, however data does not exist at every depth for the entire deployment period. Station 2 consisted of a temperature and conductivity sensor mounted on the seabed. All data were averaged over a period of 10 minutes, except that recorded after 14th December 1991 which was every 30 minutes.

Table 2.1 – Temporal data coverage of the FRS data set

	Station 1	Station 3
5m	05/10/91 to 10/10/91	11/08/91 to 15/08/91 09/11/91 to 14/11/91
13 to 15m	12/03/91 to 09/11/91 14/12/91 to 12/02/92	23/02/91 to 11/02/92
40 to 42m	24/02/91 to 02/05/91 18/05/91 to 15/06/91 13/07/91 to 12/02/92	23/02/91 to 14/07/91 11/08/91 to 11/02/92
80 to 84m	22/03/91 to 06/04/91 20/04/91 to 30/04/91	23/02/91 to 11/02/92
100m	18/05/91 to 15/06/91 13/07/91 to 05/10/91 09/11/91 to 12/02/92	No deployment
140m	15/06/91 to 27/06/91	No deployment

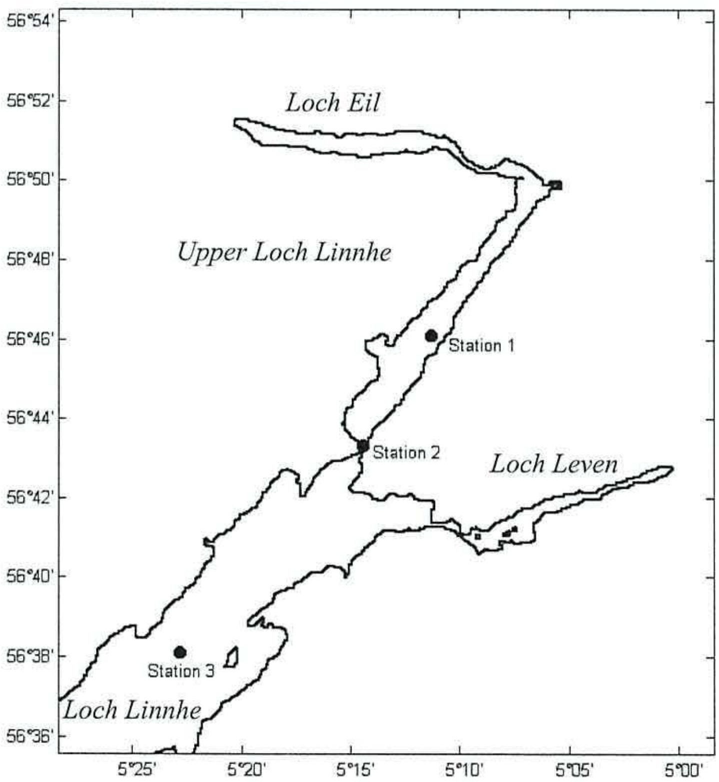

Figure 2.1 – Spatial coverage of the selected portion of the FRS data set

2.1.2 Allen data set

Subsequently collaboration between University of Wales, Bangor and Dunstafnage Marine Laboratories yielded a further data set concentrating just on the Upper Loch Linnhe basin. Much of this data and subsequent analysis are published in Allen and Simpson (1998a), Allen and Simpson (1998b) and Allen and Simpson (2002) along with the thesis of Allen (1995). Moorings were laid between November 1992 and June 1993 at the two locations (LL14 and LL04) shown in figure 2.2. The LL14 mooring is approximately co-incident with station 1 from the FRS data set. There are gaps in the data caused by instrument failure and the monthly retrieval and re-deployment. 4 Aanderaa RCM-7's were deployed at each site at depths of 10, 30, 60 and 110m. Current, temperature and conductivity data were averaged over 1-hour time bins.

Tide gauges were also deployed at two locations, one close to the LL14 mooring and the other 12km south of Corran Narrows in Loch Linnhe itself. A CTD sensor was also deployed on the seabed close to the shore in Corran Narrows, in a similar fashion to station 2 in the FRS data set.

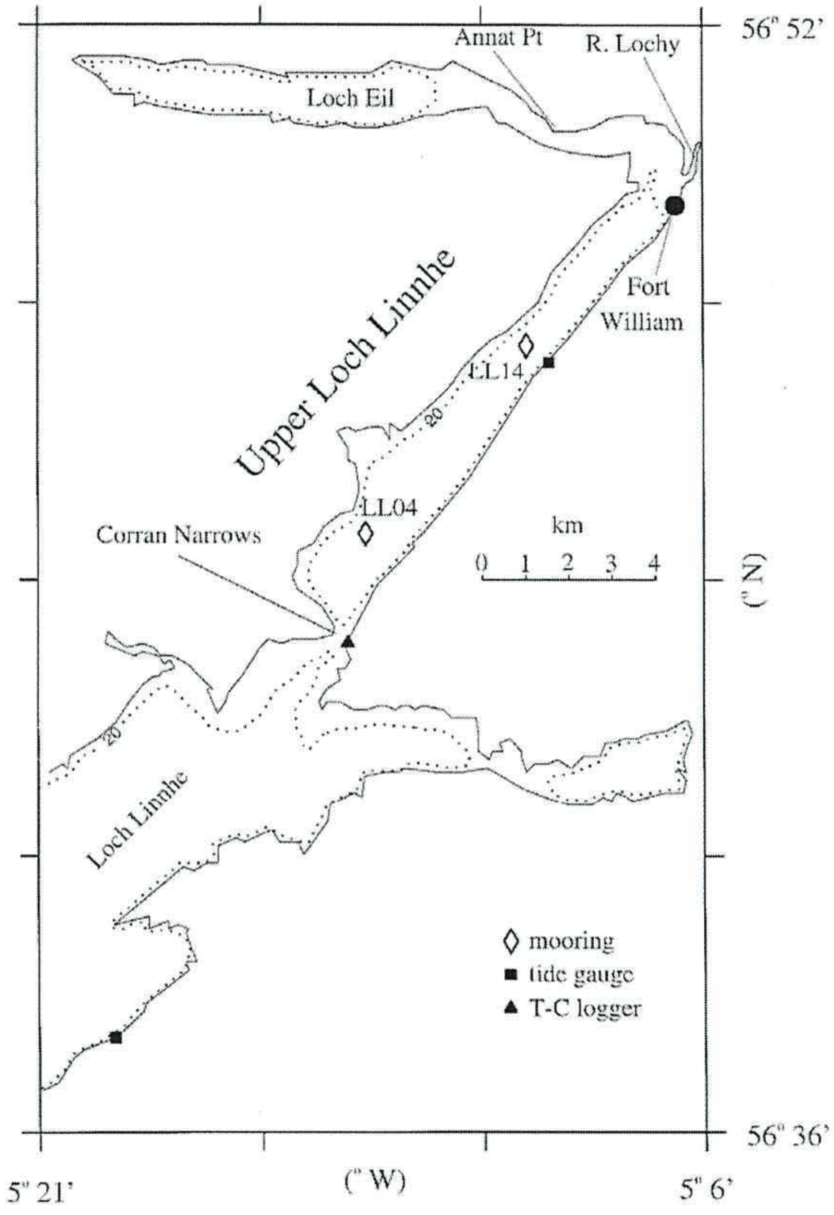

Figure 2.2 – Moored instruments of Allen (1995)

In addition to the moored instruments an undulating CTD and Ship-Mounted ADCP survey was undertaken over one tidal cycle on the 3rd June 1993. Repeated runs were made along the axis of the basin at approximately hourly intervals, commencing at 05:45 at the seaward end until 19:10, just short of the seaward end. The track of the ship is shown in figure 2.3.

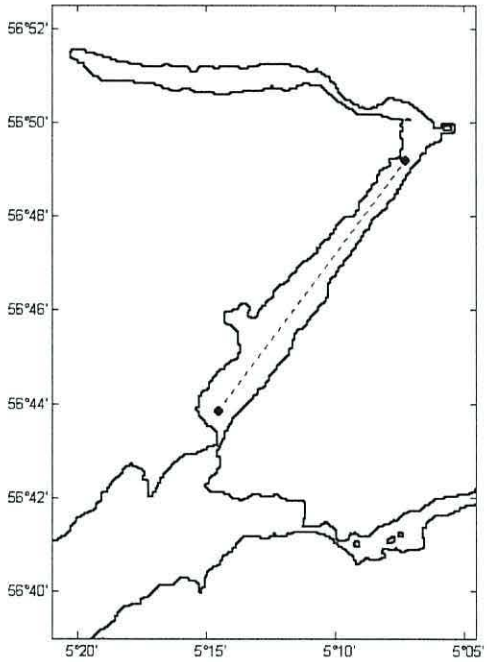

Figure 2.3 – Track of ADCP and Searover CTD survey

In addition to the oceanographic data, other environmental data has been obtained for this study. The closest rainfall station in the MIDAS Land Surface Observation dataset is at the Mucomir generating station (figure 2.4) location (56°54.6' N, 004°59.1'W). This Met. Office data was made available via the British Atmospheric Data Centre. Data exists from Jan 1961 to December 1998.

River flow data for the River Lochy was distributed by the Centre for Ecology and Hydrology Wallingford. The data represent average daily flow over the period September 1980 to December 2003. The gauging station is at Camisky (56°52.7' N, 005°02.7'W), also shown in figure 2.4.

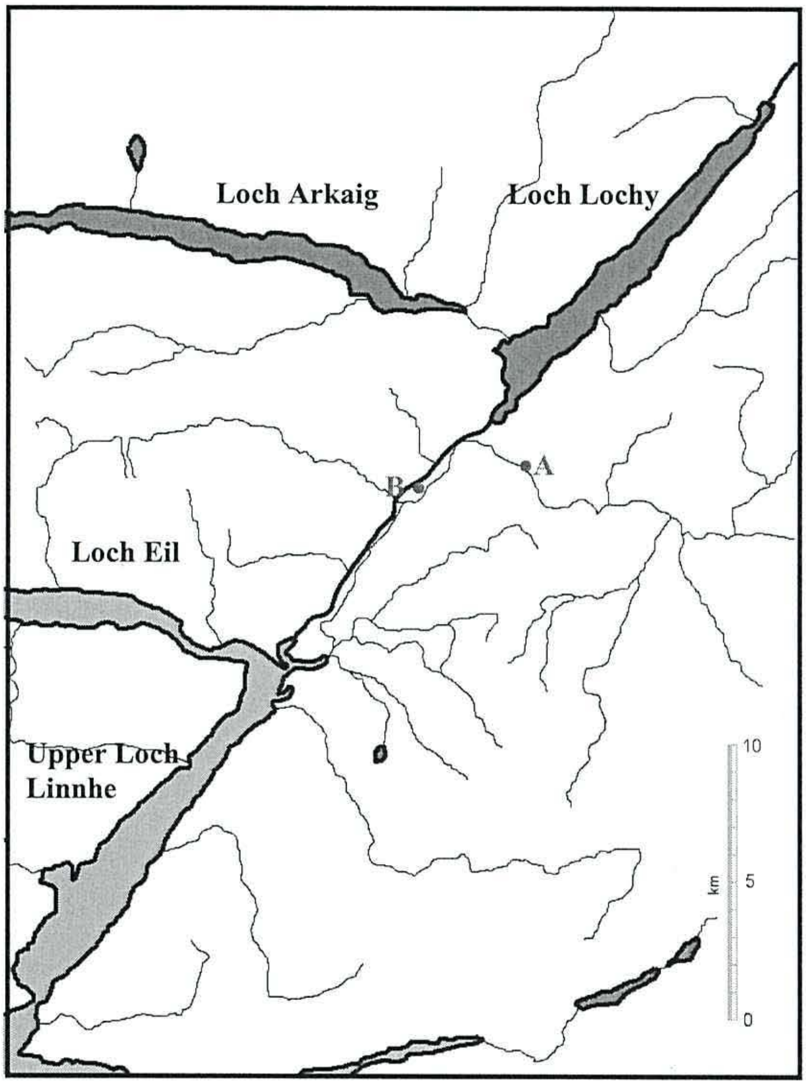

Figure 2.4 – Location of rainfall (A) and riverflow (B) data sites with significant surface drainage features

2.2 Annual Cycles

2.2.1 Fresh Water Addition

The rainfall data for 1991 and 1993 are presented in figure 2.5. Red areas show where data is missing and do not represent zero rainfall.

1991 – Prior to day 100 the two largest amounts of rain to fall in one day occurred, 65 and 83mm. There are also periods during this time when no rainfall was recorded, the longest such event being between days 30 and 45. Subsequently between day 100 and 240 the maximum peaks are generally less than 20mm per day, with the mean daily rainfall of 2.8mm per day.

1993 - Between days 1 and 30 the average daily rainfall was 13.5mm. This represents the largest amount of rain falling over a sustained period where data exists. From days 100 to 175 rainfall was less sustained but with peaks of up to 20mm per day. The mean daily rainfall for this period was 2.4mm per day.

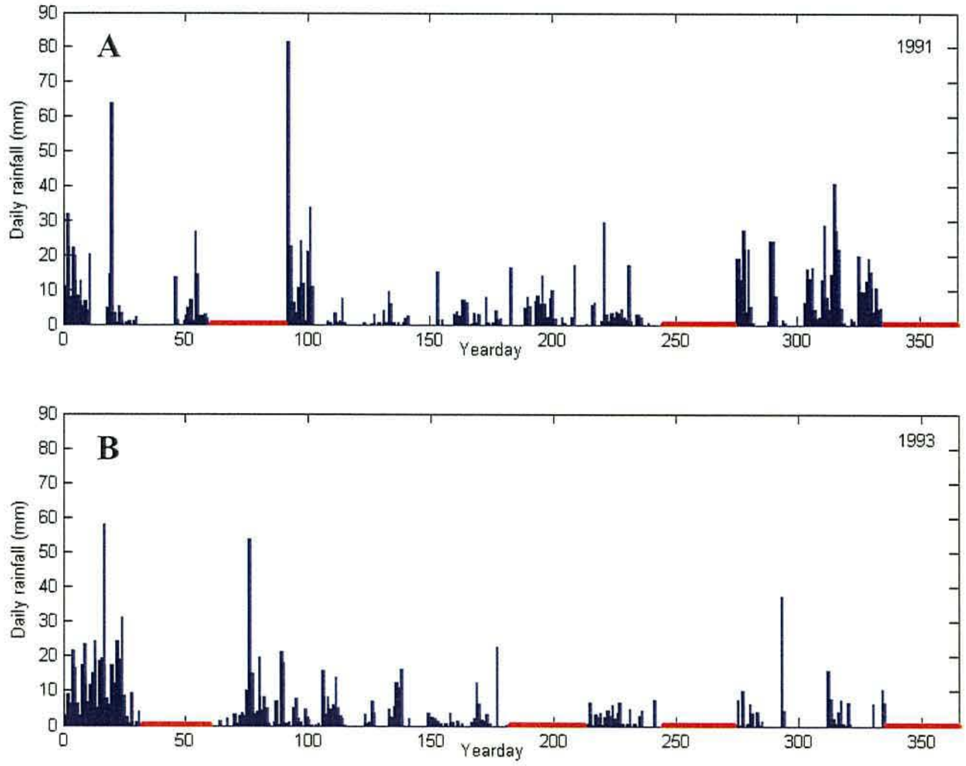

Figure 2.5 – Daily Rainfall at Mucomir generating station 1991(A), 1993(B)

A comparison of figures 2.5 and 2.6 shows that a relationship certainly exists between rainfall and river flow, however with such a large amount of data missing over the two years presented a statistical relationship may suffer.

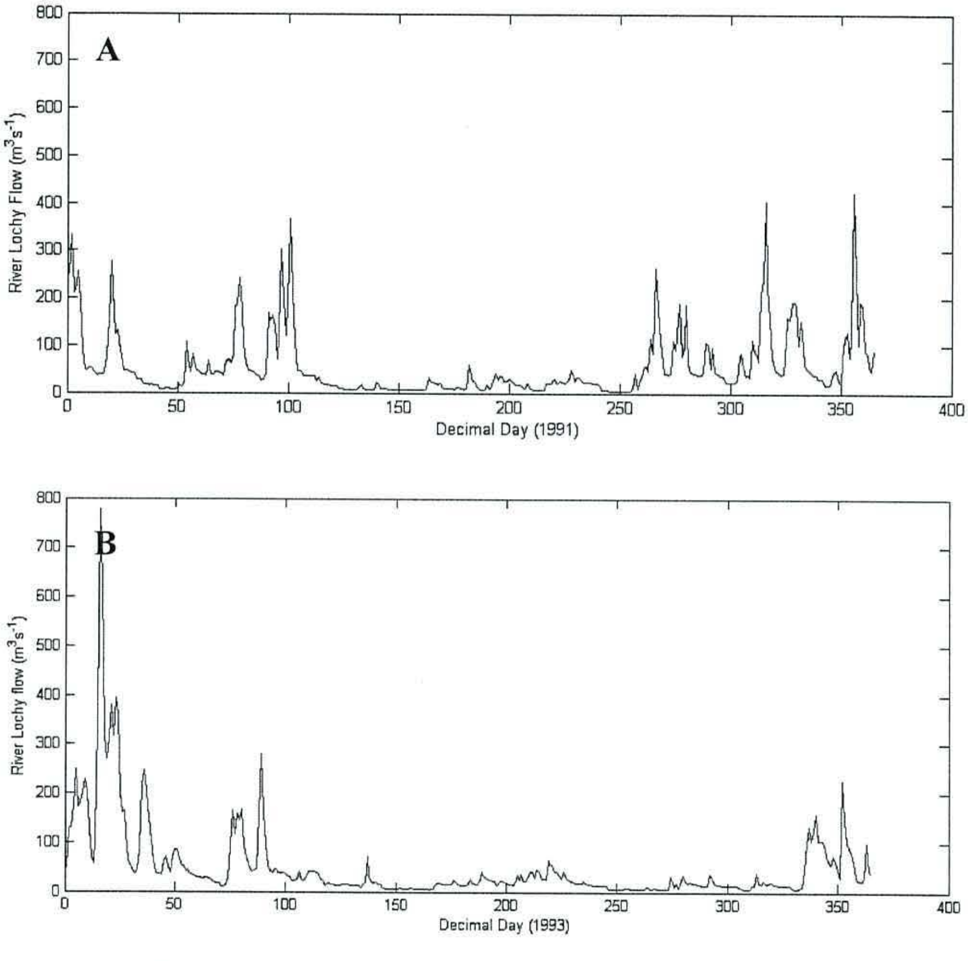

Figure 2.6 – River Loch River Discharge 1991 (A) and 1993 (B)

During 1991 the River Lochy flow rarely exceeded $400m^3s^{-1}$. From day 1 to 105 there were episodic peak flows of over 250 m^3s^{-1}. Following this, the summer period extended from day 106 to day 255. This was characterised by low flows, a peak of $61m^3s^{-1}$ with $30m^3s^{-1}$ only exceeded on 4 occasions. The autumn saw flows increase to similar levels observed at the start of the year with two peaks of over $400m^3s^{-1}$.

By contrast in 1993 the summer period of low flow extended between days 100 and 340, approximately 90 days longer than in 1991. During this time the river flow was generally below 40 m^3s^{-1} only exceeding this level between days 100 and 120 and then on two occasions, day 140 and days 220 to 225. The situation before day 100 and after day 340 was that the flow peaked at $700m^3s^{-1}$ and rarely fell below $100m^3s^{-1}$.

Table 2.2 – Mean river discharge and variation during 1993

Period	**Yearday**	**Mean Flow (m^3s^{-1})**	**95% confidence interval**
2	3 to 34	217.8	167.4
3	29 to 59	73.4	56.0
4	60 to 109	58.3	55.8
5	109 to 145	21.2	13.6
6	140 to 172	8.6	4.8

2.2.2 Salinity Gradient from Timeseries

The time series of temperature and salinity at the sill can be used to construct a spatial density gradient. Neglecting diffusion and assuming that only horizontal motions and gradients are important allows the advection equation (2.1) to be re-arranged to give a spatial gradient in terms of a timeseries (2.2).

$$\frac{\partial S}{\partial t} = -u\frac{\partial S}{\partial x} \qquad [2.1]$$

$$\frac{\partial S}{\partial x} = -\frac{1}{u}\frac{\partial S}{\partial t} \qquad [2.2]$$

In this case the time period chosen has been the flood stream (approx 6.2 hours). The salinity difference taken has been the two extreme values from the measurements at Corran sill during each event.

The flood stream speed shown is taken from the 1D channel model outlined in appendix 1. To obtain a time averaged velocity for the duration of the flood the maximum value (U_{max}) has been multiplied by $\frac{2}{\pi}$. This factor arises from the integration of the function sin(t) over the limits 0 to π.

Table 2.3 - Estimates of spatial salinity gradient

Event	Date	ΔS	U_{max} $\mathrm{ms^{-1}}$	$\partial S/\partial x$ $\mathrm{m^{-1}}$
1	09/12/1992	15	1.50	-7.291×10^{-04}
2	29/12/1992	-	-	-
3	08/02/1993	17	1.75	-7.082×10^{-04}
4	16/02/1993	4	0.90	-3.240×10^{-04}
5	27/02/1993	8	1.00	-5.833×10^{-04}
6	11/03/1993	3.5	1.60	-1.595×10^{-04}
7	11/04/1993	5.5	1.50	-2.673×10^{-04}
8	29/04/1993	-	-	-
9	09/05/1993	-	-	-
10	25/05/1993	-	-	-
11	11/06/1993	3.5	1.00	-2.552×10^{-04}
SeaRover	03/06/1993	1.5	1.50	-7.291×10^{-05}

The salinity gradients for the renewal events shown in table 2.3 are plotted in figure 2.7. The time axis is measured in days from 1st Jan 1993 so event 1 occurring on the 9th December 1992 is shown at day –22.

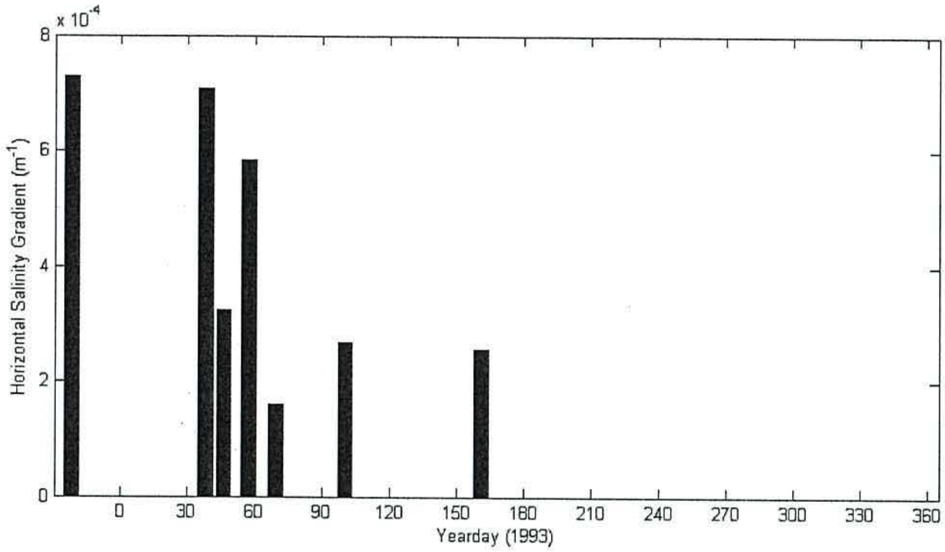

Figure 2.7 – Derived horizontal salinity gradients for renewal events

2.2.3 Salinity Gradient from Spatial Measurements

Data from the FRS dataset can be used to form a comparison with the gradients derived in the previous section. Salinity from stations 1 and 3 (figure 2.1) have been used to arrive at a salinity gradient between the centre of the Upper Loch Linnhe basin and a point 18km to the south in Loch Linnhe. The two moorings differed in design (the depths are 13m and 15m, 41m and 42m), however an approximate comparison can be made between salinity at 14m and 41.5m depth over the period 24th Feb 1991 to 15th Dec 1991. Assuming a constant linear gradient between the two stations over a distance of 18.87 km the gradients are shown in figure 2.8.

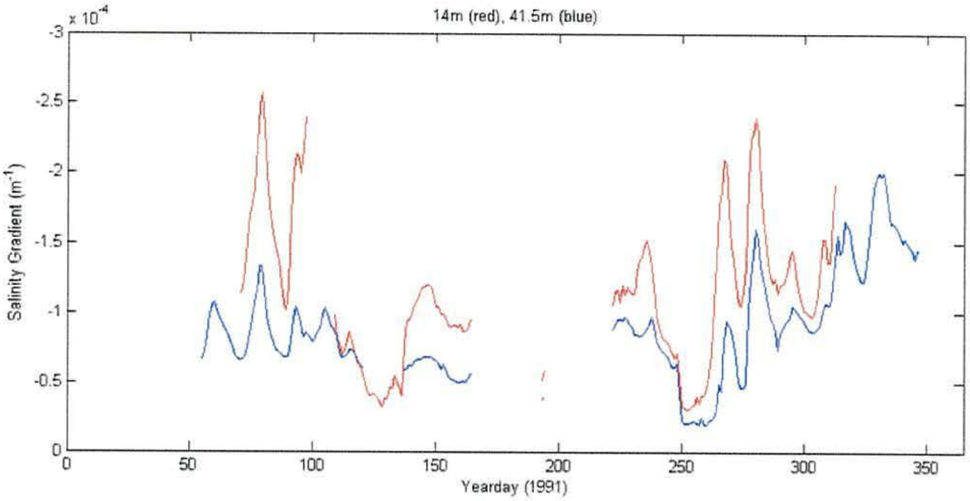

Figure 2.8 – Horizontal density gradients in 1991

The measurements from 1991 between the two moorings show in general a greater gradient at 14m than at 41½m depth. There is also a larger variability in the shallower gradient. Both timeseries show a larger gradient and larger variability before day 100 and after day 250. This matches the river flow data for the River Lochy (figure 2.6a), which was greatest during these periods.

2.2.4 Stratification and the Internal Tide

The changing stratification over the year influences the way in which the internal tide behaves. Calculations of the wavelengths of the internal tide were undertaken by Allen (1995) and are presented in table 2.4. The naming of the time periods has been altered to match the later publications of Allen and Simpson (1998a & b).

Table 2.4 – Wavelength of the Internal Tide (Allen, 1995)

Period	**Yearday**	**Wavelength (km)**			
		M2		**S2**	
		Mode 1	**Mode 2**	**Mode 1**	**Mode 2**
All		24.58	14.68	23.75	14.18
1	329 to 1	32.29	18.40	31.82	17.78
2	3 to 34	30.51	17.04	29.48	16.47
3	29 to 59	32.29	18.40	31.82	17.78
4	60 to 109	19.43	11.63	18.77	11.24
5	109 to 145	17.21	9.67	16.24	9.34
6	140 to 172	13.40	7.37	12.95	7.12

The variation of the internal tide is evident from the large spread of values in table 2.4. The length of the Upper Loch Linnhe basin is approximately 15km in length; the exact position of the northern end being indeterminate as the Annat sill is preceded by another shoal near McLean's rock. A comparison of this length with the values of internal tide wavelength would suggest that during periods 5 and 6 there is the possibility of resonance and a mode-1 internal seiche developing. It is also of interest, but not explored further, that during period 2 there is the possibility of a mode-2 internal seiche becoming resonant.

2.2.5 Tidal range

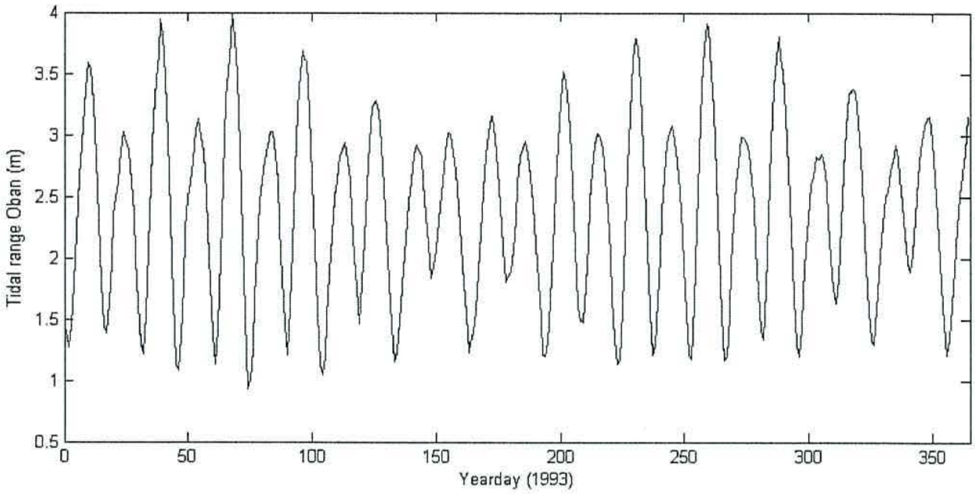

Figure 2.9 – Tidal range at Oban 1993

As shown in figure 2.9, the difference between the spring and neap ranges at this location (Oban) is large. During 1993 the greatest difference between the tidal range over the spring – neap cycle occurred between days prior to day 100 and around day 250. Of the standard ports on this coast the ratio of the mean spring range (MSR) to mean neap range (MNR) is the largest (see table 2.5).

Table 2.5 – Spring and Neap ranges for Standard Ports in NW Britain

Location	Tidal Ranges (m)		MSR:MNR
	Spring	Neap	
Lerwick	1.6	0.7	2.28
Ullapool	4.5	1.8	2.50
Oban	3.3	1.1	3.00
Greenock	3.1	1.8	1.72
Barrow	8.2	4.1	2.00
Liverpool	8.4	4.5	1.86

Source: Admiralty Tide Tables

2.2.6 Density and tidal range

The depth mean density of the water recorded at the Corran Sill is plotted with tidal range for 1991 (figure 2.10) and 1993 (figure 2.11).

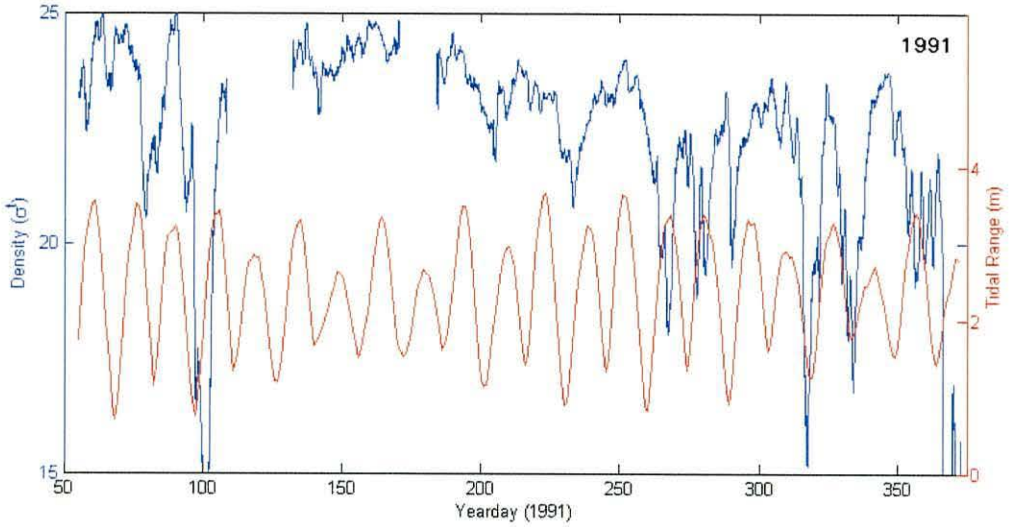

Figure 2.10 – Tidal range and sill density (1991, data from FRS)

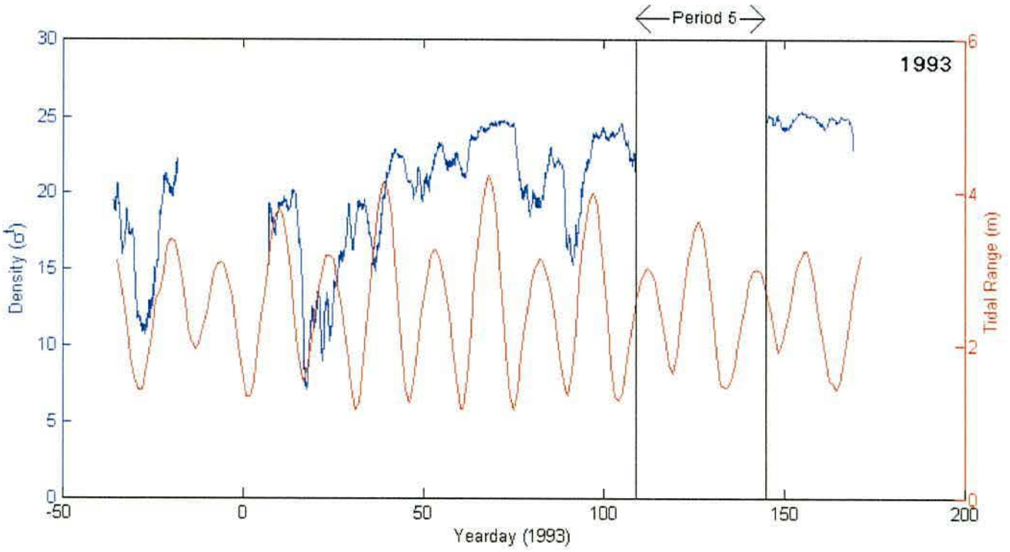

Figure 2.11– Tidal range and sill density (1993, data from G. Allen)

The 1991 data (figure 2.10) demonstrates no clear correlation between sill density and tidal range. The period of best fit is after day 250 up to day 290, excluding the neaps around day 300 where there is no apparent reduction in sill density. The relationship is then visible from day 317 to 345.

Figure 2.11 gives the same data for 1993. During period 5 (day 109 to 145, 1993) the sill density data are missing. These data have been subsequently inferred in section 2.3.2. At times during 1993 there is a clear relationship between tidal range and sill density. Two brief periods exist during the winter (the first being in 1992, days -35 to -20) where the sill density changes have the greatest amplitude over the spring – neap cycle. Later in the year, from day 40 to 109, the changes are of smaller amplitude but clearly follow a pattern of higher density (1023 kgm^{-3}) at springs and less at neaps (< 1020kgm^{-3}).

There is also a relationship at other times in the 1993 data. After day 200 the density changes by less than 1kgm^{-3} over the spring neap cycle, but there is still an obvious fortnightly variation.

2.3 Period 5

To illustrate some of the many processes at work in this system, preferably in isolation from one another, further analysis and comparison with the models has been undertaken on a small portion of the data. The main temporal focus is shifted to what was termed period 5 in Allen and Simpson (1998b). This period of time runs from 20th April 1993 to 26th May 1993 (Yearday 109 to 145). The focus of interest is on the internal tide, its creation by topographic interactions, and its modification by density variations.

It can be seen from figure 2.5 that the maximum rainfall during this period did not exceed 20mm per day, a reduction from the maximum values earlier in the year of over 50mm per day. There was also a reduction in the variation of the River Lochy flow. Analysis of the river flow data is shown in table 2.2. This indicates that prior to period 5 the flow was on average nearly 3 times and the variation of the flow was approximately 4 times greater. This would suggest that during period 5 there should be a reasonably constant stratification regime.

Immediately prior to period 5 it can be seen from both figures 2.5, 2.6 and table 2.2 that a substantial amount of rain fell and fresh water flowed into the basin. Without the direct measurements of the salinity gradient from the 1991 fieldwork the only indicator of such a gradient is the derived gradients from timeseries presented in section 2.2.2. The estimates before and after period 5 (table 2.3) are in agreement, suggesting that the seaward horizontal salinity gradient did not change appreciably during period 5.

It is for the reasons outlined above that the rest of this study focuses on the events of period 5. Undoubtedly there are many differing processes present in other parts of this large and varied data set.

2.3.1 Tidal Range

The tidal ranges during period 5 are shown in detail in figure 2.12. This shows that spring tides occurred at or around days 113, 127 and 141 and neap tides occurred at days 120 and 134. The difference between the spring and neap ranges during this period of time was approximately a factor of 3, typical for this location but greater than other ports in NW Britain (table 2.5).

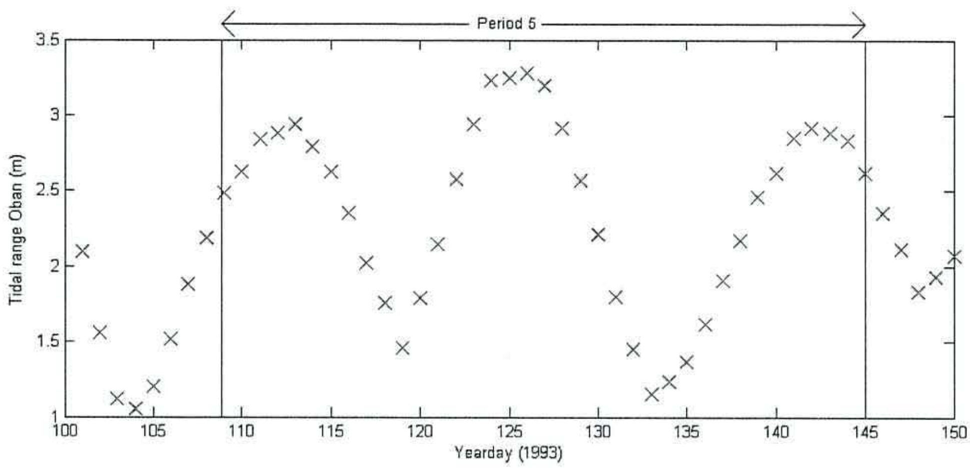

Figure 2.12 – Tidal range at Oban during period 5

2.3.2 Sinusoidal density variation

Unfortunately due to instrument failure the temperature and salinity sensor mounted on the seabed at the Corran sill was not recording during most of period 5, the timeframe of interest in this study. This has necessitated the estimation of this information from the set of spring tides centred about yearday 100, immediately before period 5. The data are needed as boundary forcing for the model, in order to investigate the influence of the inflowing density upon the circulation. The assumption that the along loch density gradient between the Upper Loch Linnhe basin and the basin seaward did not vary during this time has been investigated previously (section 2.2.2). The salinity gradient was found to vary by 5 % between days 100 and 161.

Harmonic analysis has been undertaken on the difference between the inflowing density at the sill and that recorded at 10m depth at the LL04 mooring site. The amplitude of this variation should be proportional to the tidal range if the along loch density gradient is assumed constant. If the short term variation is entirely attributed to the variation at the sill rather than at the LL04 mooring this gives a method of prediction of the sill density. The standard deviations for both timeseries of density are shown in table 2.6; this confirms that the sill density varies an order of magnitude more than that at the LL04 mooring. Figure 2.13 shows the density difference and the flood stream derived from the 1D model (Appendix1) starting from 09:00 on day 100 of 1993.

Table 2.6 – Mean density and standard deviation at LL04 and Corran sill

Location	Mean density (σ^t kgm^{-3})	Standard Deviation
LL04 (10m)	24.38	0.11
Corran Sill	23.59	1.30

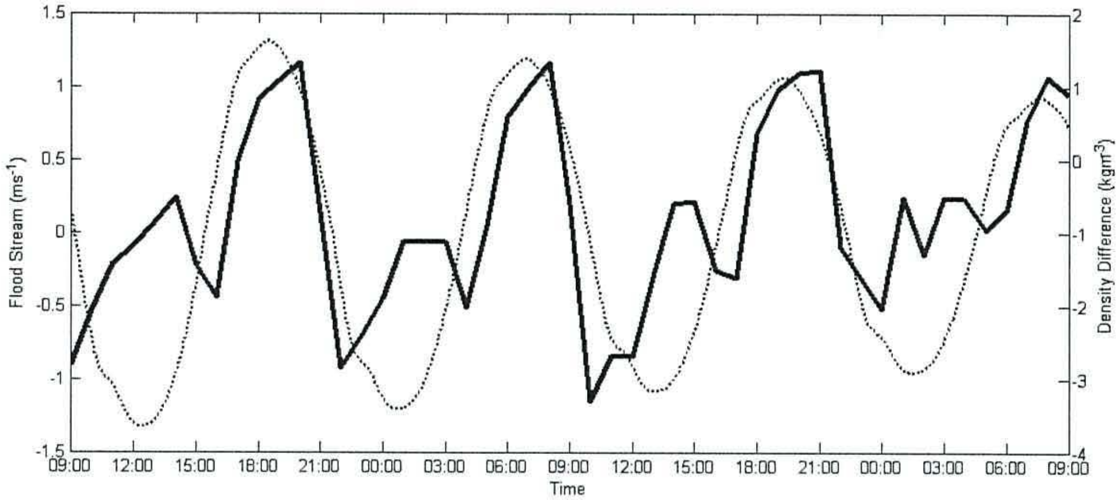

Figure 2.13 – Density difference between the sill and LL04 mooring (solid line) and flood stream (dotted line) starting day 100

It can be seen that during the majority of the time the density of the inflowing water was less than that at 10m depth at the LL04 site. (The zero point on the density axis of figure 2.13 is offset). There are fresh water sources at the Corran sill, however this density deficit can also be attributed to the water column over the sill being thoroughly mixed (Allen 1995). This mixing will mix the less saline surface waters down to sill depth, thus lowering the salinity.

The inflowing water had a greater density at and just after maximum flood. As the stream changed direction there was a dramatic fall in the density difference of up to 4kgm^{-3}. It can be seen that at maximum ebb there was also an increase in the density difference; however it still remained below zero during the entire ebb stream. This rise can be explained by aspiration taking place; the vertical advection of a stratified water column. The rise in the inflowing density during the ebb, while demonstrating aspiration, is of secondary interest to the prediction of the density during the flood; the boundary condition is not required during the ebb. With this in mind harmonic analysis has been undertaken for only the M2 variations. Relating the phase of the density variation to the phase of the flood stream gives equation 2.3. An appreciable M4 signal was found but this has not been included in this work.

$$\Delta\rho(t) = -0.78 + 1.18 \times \sin(\sigma t + 11^{o}) \qquad [2.3]$$

The uncertainty of the amplitude was $\pm 0.1 kgm^{-3}$ and the phase error was 5°.

2.3.3 Stratification

Despite being a period of time when the overall stratification of the system remained reasonably constant there are also periods of change evident from a closer inspection of the data. Figure 2.14 shows the density recorded at the 4 depths of the LL04 mooring. Between days 115 and 120 there was a significant change in the stratification of the loch. The density at 10m rose by over 1 while there were significant rises at all depths. This rapid increase in density is indicative of a renewal event taking place. In the analysis of Allen and Simpson (1998a) this event was identified as renewal event 9 on the 8^{th} May 1993.

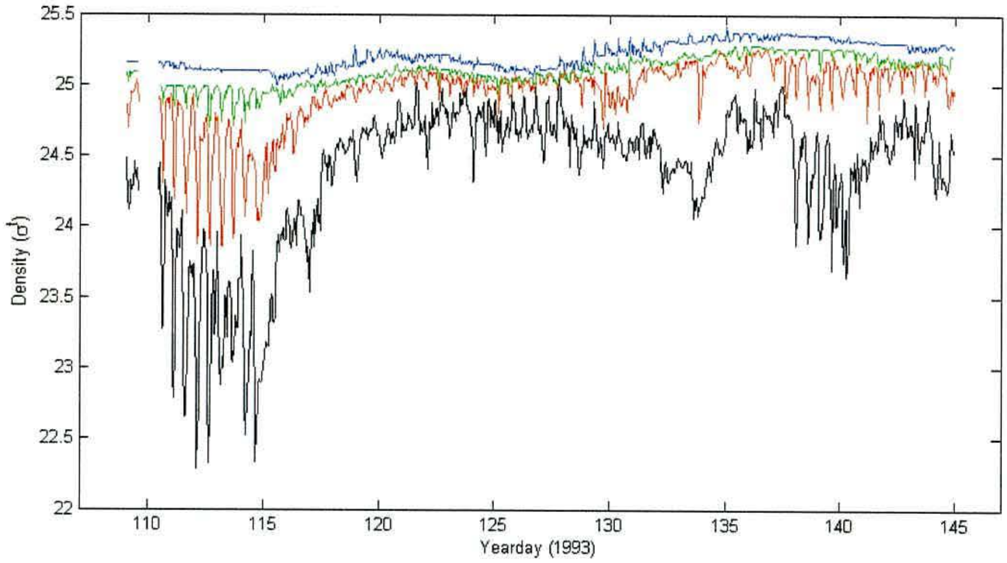

Figure 2.14 - Timeseries of density from the LL04 mooring during period 5. (10m black, 30m red, 60m green & 110m blue)

2.3.4 Mode 1 Internal Tide

From section 2.2.5 it was shown that there are 2 periods of spring tides and 2 periods of neaps during period 5. Figure 2.15 shows that the amplitudes of the streams are greater at all depths during springs. These were determined using the t-tide package (Pawlowicz *et al,* 2002). Time series of 50 hours, starting 5 hours apart, were separated from the current meter records and harmonic analysis was undertaken on each separate time series. This yields harmonic constants for the centre time of that series.

The results of this show the first set of springs, centred about day 113, have streams more than double the amplitude of the second set of springs centred about day 127. This is an inverse relationship with the tidal range. It is also evident from figure 2.15 that the two depths with the largest amplitudes were the surface and the bed, contrary to conventional channel flow where flows diminish toward the bed.

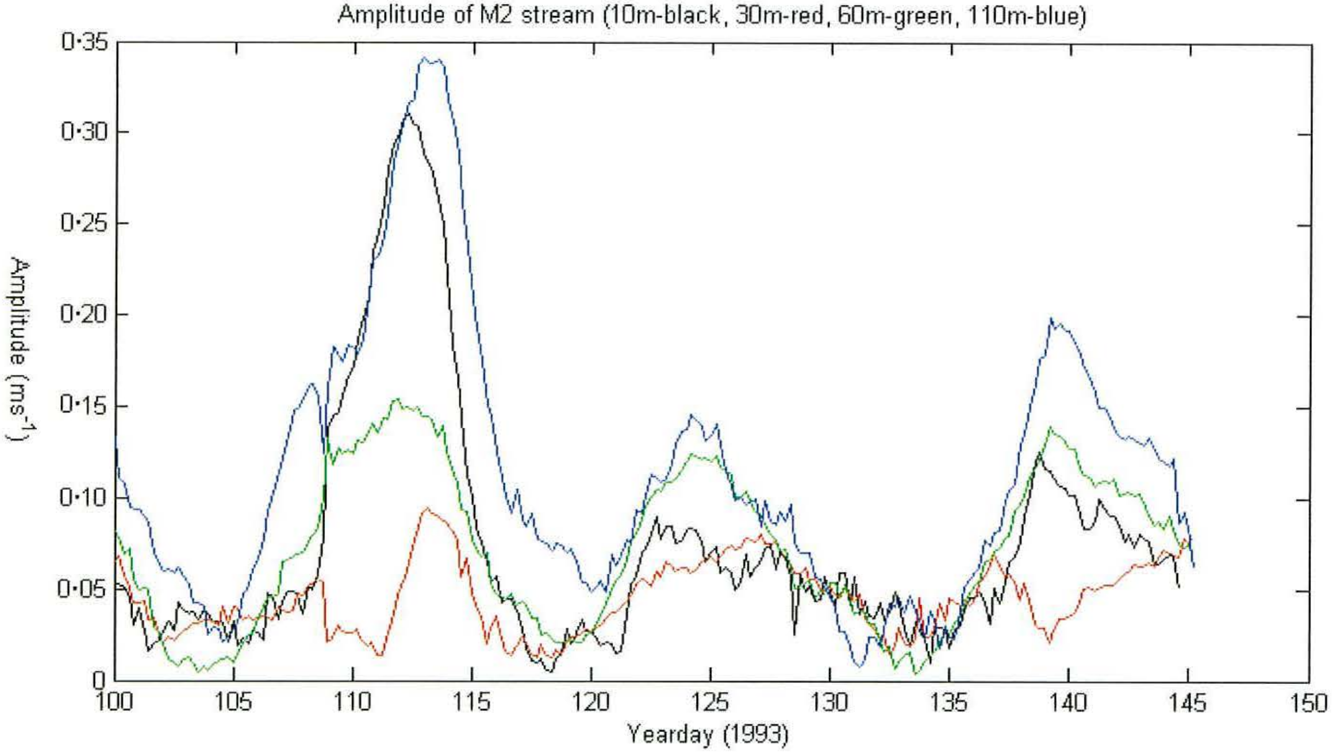

Figure 2.15 – Amplitudes of M2 streams at LL14 mooring during period 5

The reasons for these large tidal streams at 10m and 110m depth at this time are illustrated by a plot of the actual currents on day 113 (Figure 2.16). This shows that on day 113 the streams at 10m and 30m depth were approximately in phase, with the flows at 60m and 110m being shifted out of phase with the two surface measurements.

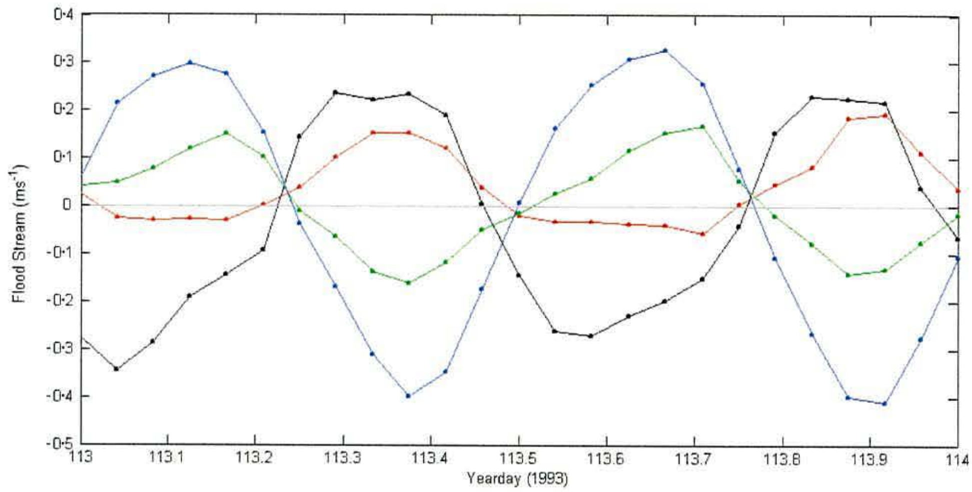

Figure 2.16 – Flood streams at LL14 mooring site on day 113
10m black, 30m red, 60m green & 110m blue.

To form a comparison with the data collected in 1991 by FRS, figure 2.17 shows the current meter data from station 1 (approximately co-incident with LL14) for two days in September. The depths of the current meters do not match exactly the configuration of the moorings of Allen (1995), but it is clear that the upper and lower streams are entirely out of phase with one another. The mid-depth stream does not show a clear semi-diurnal signal; a quarter diurnal signal is evident with maxima associated with maxima at both the 15m and 100m records, particularly on day 236.

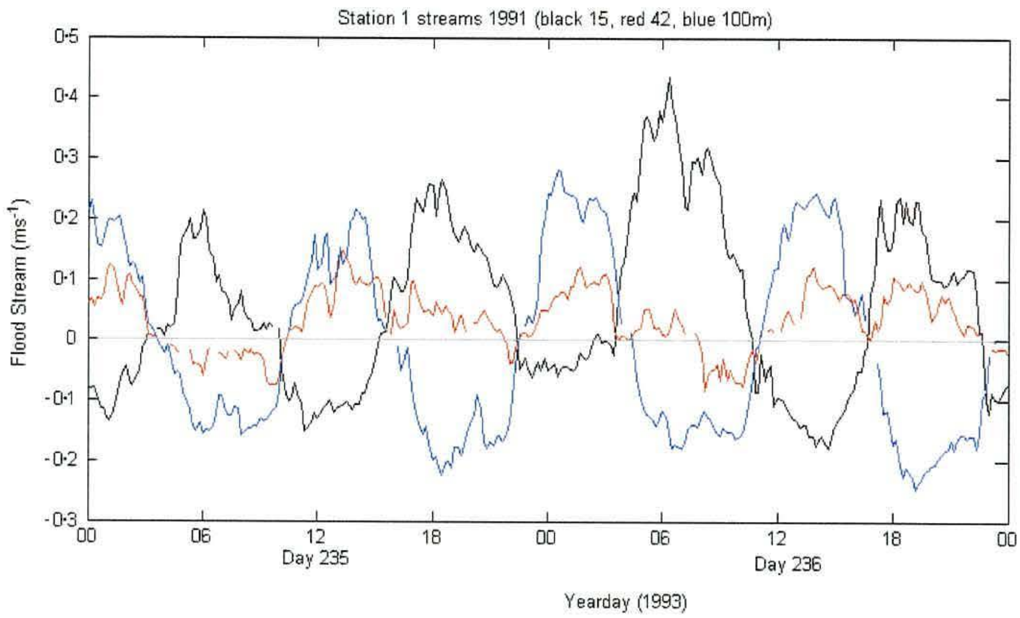

Figure 2.17 – Stream at LL14 site from FRS data 1991

In order to illustrate the phase shifts in the water column on day 113 harmonic analysis was undertaken on 2 days of data. The results of this are presented in figure 2.18. This shows that the surface flood begins at about the same time as the flood over the Corran sill. At 30m depth this flood stream is lagged by approximately a ½ hour or 15°. The streams at 60m and 110m depth are out of phase, some 200° after.

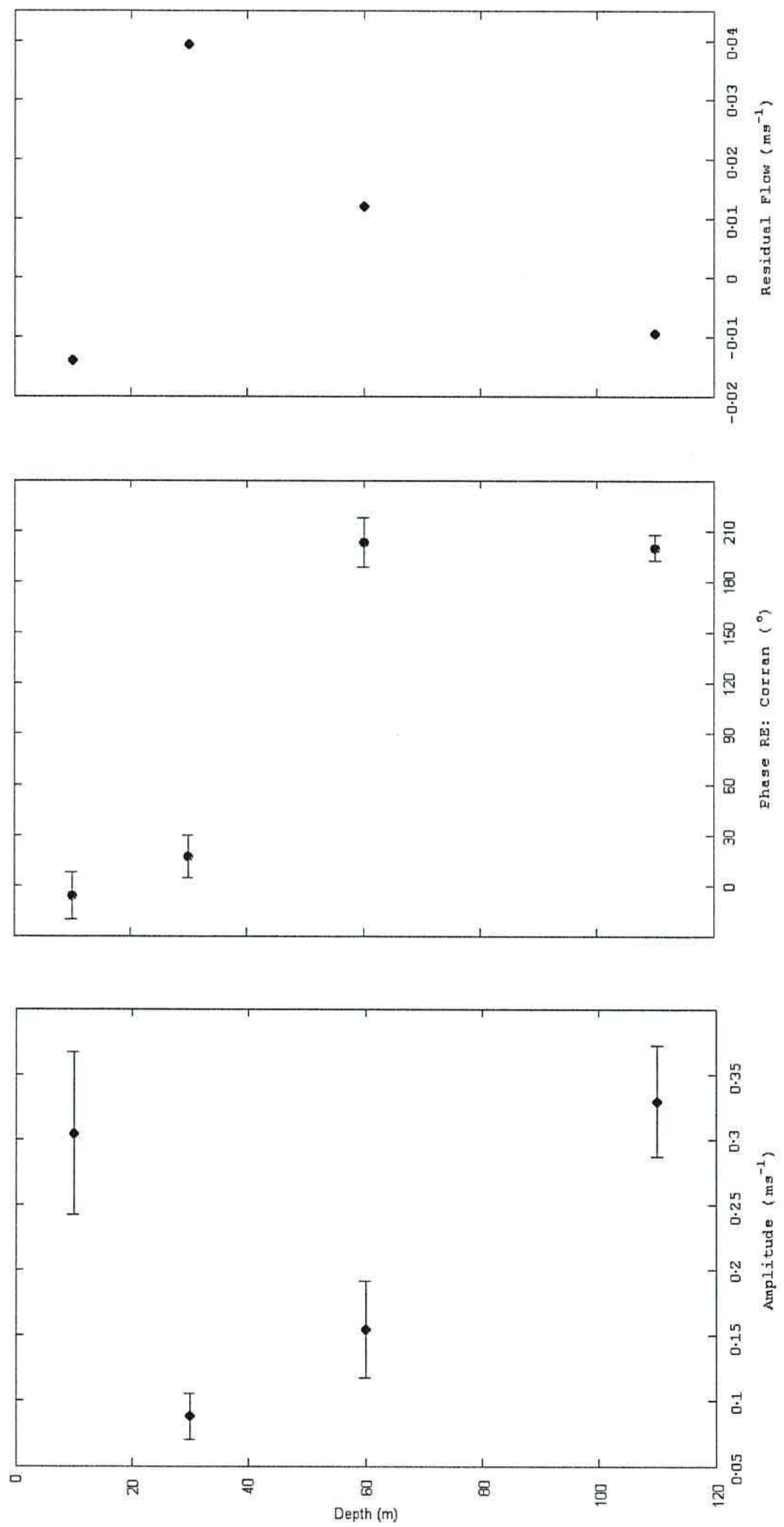

Figure 2.18 – Harmonic analysis of currents at LL14 on day 113

One section of the ADCP data is presented in figure 2.19. This shows the situation towards the end of the ebb stream. Clearly visible is the two layered nature of the flow at the northern end of the basin. The upper 25m of the water column is ebbing while below this depth the lower part of the water column is flooding, each layer has comparable but opposite velocities of up to $1 ms^{-1}$.

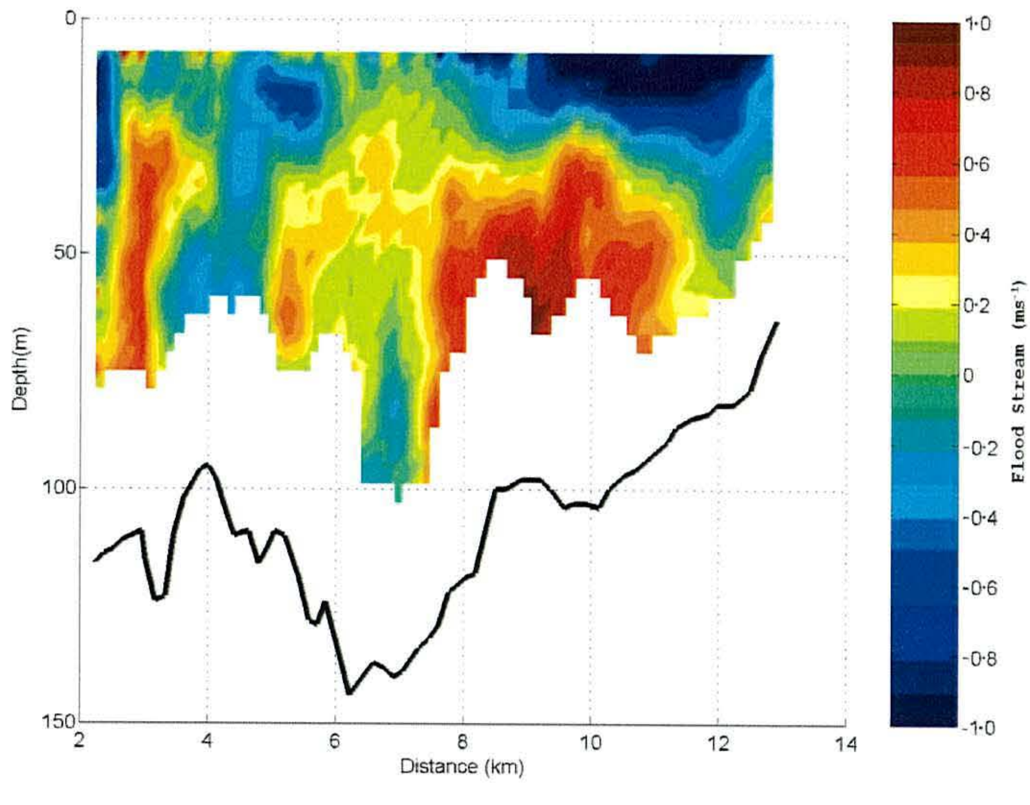

Figure 2.19 – ADCP section on day 131, (HW Oban +6¼ hours at 13km from the Corran sill to HW+7½ hours 2km from the sill)

2.3.5 Renewal Event Residual Flow

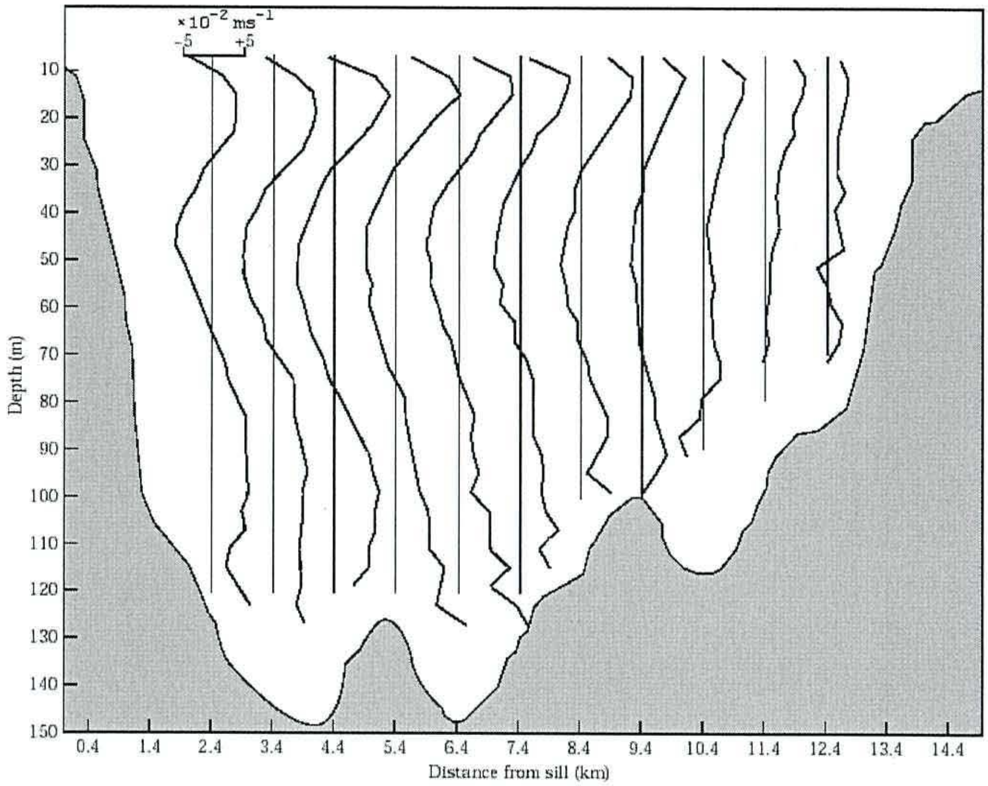

Figure 2.20 – Residual circulation from ADCP data (Allen and Simpson 1998a)

Figure 2.20 shows the residual flows calculated from ADCP data collected on day 12th May (yearday 131) by Allen and Simpson (1998a). This shows a multi-layer structure to the circulation. The surface layer, above sill depth flows seaward, at the Corran end of the basin. This probably continues along the length of the loch, however toward the Annat end of the basin this layer disappears above the reach of the ADCP. Immediately below this is a landward flow, which extends along the entire length of the basin, gaining depth up the loch. Between 30m and 70m depth there is a seaward flowing layer extending 10km up the basin. At the bed the flow is indeterminate until a point 4km up the basin, after which a predominantly landward flow is seen at depth.

This flow structure following a renewal event is comparable with that derived from the FRS data. During the 1991 data set, the longest period of sustained renewal occurred between days 147 and 167. This has been shown by a comparison of the density at Corran Narrows and that at 15m depth in the centre of the basin, shown in figure 2.20. (There was no equivalent to the LL04 mooring in this fieldwork).

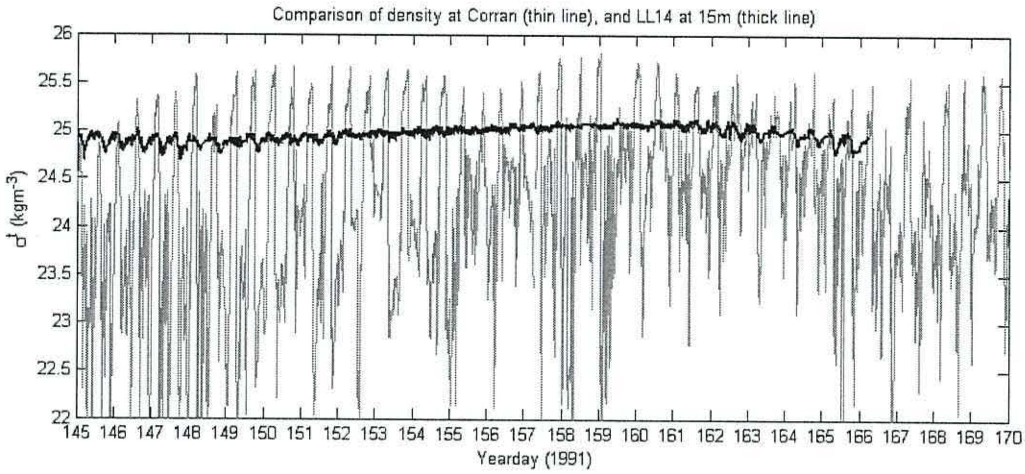

Figure 2.21 – Density at Corran sill and mid-loch location during renewal (1991)

The currents were recorded over 10 minute intervals, in order to evaluate this over a tidal cycle these currents were interpolated onto 5 minute intervals and then 4473 of these measurements were averaged to give a 30 tidal cycle mean flow. The results of this analysis are summarised below in table 2.7, the current meters at 80m and 140m were not recording at this time.

Table 2.7 – Residual flow between day 147 and 162.5 in 1991

Depth (m)	**Uploch flow (ms^{-1})**
15	1.5×10^{-2}
42	-4.0×10^{-3}
80	--
100	2.9×10^{-2}
140	--

The values of residual flow derived over such a long period of time from the FRS data compare favourably with the profile at x=7.4km in figure 2.20. This backs up the observation of a landward flow at the seabed and a landward flow in the layer 10 to 30m. Between these two layers exists a thick layer of seaward flow.

2.4 Summary of the Data

From the two years of data there is a common seasonal cycle of high rainfall and therefore riverflow in the spring and autumn. The summer is characterised by lower levels of rainfall. This pattern is reflected in the horizontal salinity gradient between Upper Loch Linnhe and the larger seaward basin Loch Linnhe itself.

During periods of strong horizontal salinity gradients there is a correlation between dense water flowing over the sill at Corran narrows and large tidal range. This is particularly pronounced in the spring if the reduction in riverflow occurs at about the same time as the spring equinox tides.

The stratification of the basin changed appreciably during the data collection. The analysis of internal wavelengths by Allen (1995) shows that at some times the mode 1 internal tide may become resonant; caused when the wavelength approximates the length of the basin. This is most noticeable around the spring tides of day 113 in 1993; however it would be expected to occur at other times.

The pattern of residual flow observed during periods of renewal has been recorded by both the ADCP survey of (Allen and Simpson 1998a) and a separate current meter deployment undertaken by FRS. The distinct layered pattern is evident in both sets of data suggesting it is consistent with the renewal process in general rather than a peculiarity of the flow regime at one instance in time.

Chapter 3 – Numerical Models

3.1 The hydrostatic approach

3.1.1 Development of hydrostatic width integrated slice models

2D slice models, where a vertical grid is arranged in the x-z plane (figure 3.1) were developed in the late 1960's and are based on original work by Leedertse (1967) and Heaps (1969). This followed a desire to model the theory and observations of density driven estuarine flows undertaken by many workers, most famously by Hansen and Rattray (1965).

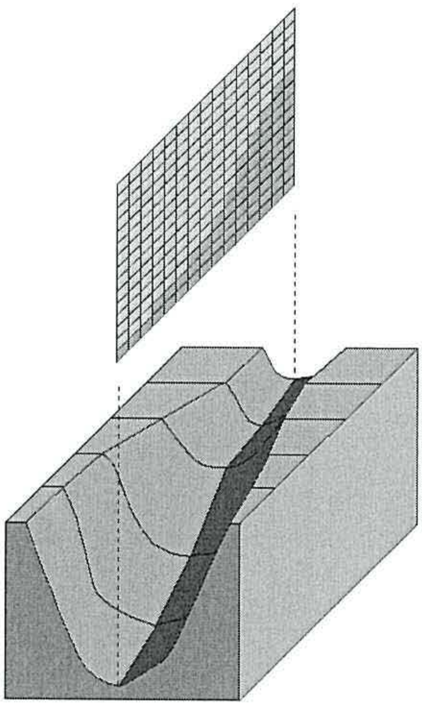

Figure 3.1 – Slice Model Domain

Hamilton (1975) presents a similar model of the Rotterdam Waterway. The governing equations are presented below; equations 3.1 to 3.4 represent the depth-averaged continuity, continuity, salt conservation and momentum balance equations respectively.

$$\frac{\partial \eta}{\partial t} + \frac{1}{B}\frac{\partial}{\partial x}\left[B \int_{-\eta}^{h} u dz \right] = 0 \qquad [3.1]$$

$$\frac{\partial}{\partial x}(Bu) + B\frac{\partial w}{\partial z} = 0 \qquad [3.2]$$

$$\frac{\partial s}{\partial t} + u\frac{\partial s}{\partial x} + w\frac{\partial s}{\partial z} - \frac{\partial}{\partial z}\left(K_v \frac{\partial s}{\partial z} \right) - \frac{1}{B}\frac{\partial}{\partial x}\left(BK_h \frac{\partial s}{\partial x} \right) = 0 \qquad [3.3]$$

$$\frac{\partial u}{\partial t} + u\frac{\partial u}{\partial x} + w\frac{\partial u}{\partial z} = -ag(z+\eta)\frac{\partial s}{\partial x} - g\frac{\partial \eta}{\partial x} + \frac{\partial}{\partial z}\left(A_v \frac{\partial u}{\partial z} \right) \qquad [3.4]$$

B is the channel width
u the width-integrated along channel velocity in the x direction
w the width-integrated vertical velocity, positive downwards in the z direction
s the salinity
η the surface elevation relative to the undisturbed level
g the acceleration due to gravity
a the rate of change of density with respect to salinity ($\approx 7.8 \times 10^{-4}$)
A_v the vertical eddy viscosity
K_h and K_v the horizontal and vertical components of eddy diffusivity

Of note here is the different treatment of width changes in the horizontal and vertical in equations 3.2 and 3.3. This reflects the model design of a rectangular channel, i.e. width (B) varies with horizontal distance but not with depth.

The advection of momentum in equation 3.4 is of the flow form, subsequent models have favoured the transport or flux form of these terms. The finite difference form of these terms uses upwind differencing to maintain stability. It has been reported that oscillations can be created by using centred difference approximations to gradients close to fronts (James 1986), however the upwind scheme, always stable and positive, creates massive numerical diffusion. Most models have combined centred and upwind differences for the advection of momentum, others have removed the advective term all together (Gillibrand, 1993).

A similar model was later applied to the same location, the Rotterdam Waterway, by Smith and Takhar (1981). The main aim was to test more advanced turbulence schemes that had been developed in atmospheric sciences during the 1970's, and apply them to a partially mixed estuary.

Dunbar and Burling (1987) applied a derivative of this model to a loch in British Columbia, finding that the generated internal tide was somewhat more complex than the analytical models of Stigebrandt (1976) might suggest. The use of implicit techniques was found to be of little advantage owing to the non-linear nature of the flows in Burrard Inlet. High values of horizontal diffusion coefficients were required to suppress high frequency oscillations that occurred in the solution. Values of horizontal diffusion were 10^6 higher than the corresponding vertical diffusion.

Stacey *et al.* (1995) applied a version of this type of model to Knight Inlet in British Columbia. This time the transport, or flux form, of advection was used, and an expression for friction at the sides of the channel introduced. In contrast to the model of Hamilton (1975) width was considered to vary in both the horizontal and vertical. The grid spacing in this model was allowed to vary in both the horizontal and vertical directions. The same model was used by Stacey and Gratton (2001) to investigate the tidal dynamics of Saguenay Fjord, also in British Columbia.

The most common restriction on the size of the timestep is that the Courant number should be less than unity. In words this dictates that any surface waves cannot travel more than the distance between successive grid points in one timestep. Surface waves travel faster than any internal waves. Mathematically it is expressed in equation 3.5. This shows that in general a fine horizontal resolution and deep water requires a small timestep.

$$C = \Delta t\sqrt{gh}\left(\frac{1}{(\Delta x)^2}+\frac{1}{(\Delta y)^2}\right)^{\frac{1}{2}} < 1 \qquad [3.5]$$

In order to remove this restrictive timestep the barotropic mode (surface wave) was separated out from the internal so that a short timestep was used on the barotropic mode, and a larger timestep was used on the more complex internal velocity field. This meant that for the application to Knight Inlet a timestep 20 times larger could be used for the internal dynamics. A different technique for undertaking the same task was presented by Wang and Kravitz (1980). Here the surface elevation (barotropic mode) has been calculated by evaluating the continuity equation implicitly. Subsequently the internal dynamics are calculated using explicit equations; both calculations are on a larger timestep, not constrained by the phase speed of surface waves.

3.1.2 Outline of the hydrostatic model used in this study

The model used here is in essence that of Wang and Kravitz (1980); the developments of Kerner (1985) and later work of Gillibrand (1993) are also included. The latter added variable grid spacing in the vertical and applied the hybrid advection scheme of James (1986) to scalars. The scheme of Hamilton was also added to allow the free surface to move through the grid points. With the large tidal ranges found in Scotland this removed the need for the near-surface grid spacing to be larger than the tidal range.

Dynamics

The governing equations for the horizontal momentum balance and scalar balance are given in equations 3.6 and 3.7 respectively. A rigorous derivation of these equations is given in the thesis of Kerner (1985), chapter 1. An overview can be found in Wang and Kravitz (1980) which details the application of the model to the partially mixed estuary of the Potomac River in North America. Equation 3.7 is posed in terms of a general scalar (ϕ) but has been applied to salinity, temperature and a passive tracer in the model.

$$\frac{\partial}{\partial t}(uB)+\frac{\partial}{\partial x}(uuB)+\frac{\partial}{\partial z}(uwB)-\frac{\partial}{\partial x}\left(BA_h\frac{\partial u}{\partial x}\right)-\frac{\partial}{\partial z}\left(BA_v\frac{\partial u}{\partial z}\right)$$
$$+C_D u|u|\frac{\partial B}{\partial z}+Bg\frac{\partial \eta}{\partial x}+\frac{Bg}{\rho_0}\frac{\partial}{\partial x}\int_{-\eta}^{h}\rho dz'=0 \quad [3.6]$$

$$\frac{\partial \phi B}{\partial t}+\frac{\partial \phi uB}{\partial x}+\frac{\partial \phi wB}{\partial z}-\frac{\partial}{\partial x}\left(BK_h\frac{\partial \phi}{\partial x}\right)-\frac{\partial}{\partial z}\left(BK_v\frac{\partial \phi}{\partial z}\right)=0 \quad [3.7]$$

Those symbols not previously defined are:

C_D the co-efficient of bottom friction
ρ and ρ_0 the density and depth mean density respectively
A_h the horizontal component of eddy viscosity (not considered in the model of Hamilton 1975)

Equations 3.6 and 3.7 are solved in conjunction with two continuity expressions, the first integrated over the width of the channel (B), the second also integrated over the water depth from the surface ($-\eta$) to the depth of the water column (h).

$$\frac{\partial}{\partial x}(uB)+\frac{\partial}{\partial z}(wB)=0 \quad [3.8]$$

$$\frac{\partial}{\partial t}(B\eta)+\frac{\partial}{\partial x}\int_{-\eta}^{h}(uB)dz=0 \quad [3.9]$$

The equations are solved on a staggered Arakawa C grid. The horizontal grid spacing is constant, while the vertical grid spacing is fixed but can vary spatially. This allows the surface layer to be well represented with a fine vertical grid spacing, while larger vertical intervals deeper in the water column reduce the computational requirement in areas where gradients are expected to be weak.

Density is assumed to vary linearly with salinity (S), a simplification commonly used in ocean models, using co-efficients α and β derived from a best-fit to the equation of state within the salinity range expected.

$$\rho=\rho_0(\alpha+\beta S) \quad [3.10]$$

Numerical scheme

The finite difference approximations to equations 3.6 to 3.9 are treated as centred in space and time. The centred time scheme requires the filter of Asselin (1972) to remove oscillations caused by the computation. The computation of the free surface is undertaken twice in each timestep, by differing methods. Initially the horizontal momentum equation (3.6) is integrated over the water depth and solved explicitly using Gausian elimination (Wang and Kravitz 1980). The new value of surface elevation is then used in the momentum equation (3.6) to describe the sea-surface slope term. Once the velocity field is calculated the surface elevation is then re-calculated using an explicit scheme to ensure that continuity is satisfied.

The semi-implicit scheme of Wang and Kravitz (1980) gave an eight-fold decrease in model runtime when applied to an estuarine system. When the same model was subsequently applied to sea lochs by Dunbar and Burling (1987) and Gillibrand (1993) there was no computational advantage. This was attributed to highly non-linear nature of the flow field over steep changes in topography found in sea lochs and not in estuaries. The inability of this type of model to cope with non-linear flows was further illustrated by Gillibrand (1993). The advective terms had to be removed from the computation all together in a study of Loch Sunart to maintain stability. In summing up he questions the applicability of using this model in the sea loch environment.

Turbulence Scheme

Based on initial work by Munk and Anderson (1948), numerous schemes relating vertical viscosity (A_v) and diffusivity (K_v) to the Richardson Number (Ri) have been presented (equation 3.11). The work of Bowden and Hamilton (1975) has been followed in this study. Relating the mixing coefficients to Ri allows the effects of stratification to reduce any vertical transfer of momentum and scalars. Various equations have been given for the relationship between A_v and K_v with Ri. They are generally of the form of equations 3.12 and 3.13 often using site-specific coefficients determined empirically from field data.

$$Ri = \frac{g}{\rho}\frac{\partial \rho}{\partial z}\left(\frac{\partial u}{\partial z}\right)^{-2} \qquad [3.11]$$

$$A_v = A_0(1+\alpha Ri)^p \qquad [3.12]$$

$$K_v = A_0(1+\beta Ri)^q \qquad [3.13]$$

Values for the constants α, β, p and q are given by Munk and Anderson (1948) to be 10, 3.3, -½ and -1½ respectively. The value of A_0 represents values for a non-stratified system. In a direct comparison of methods of parameterising eddy diffusion and viscosity, Bowden and Hamilton (1975) showed that the minimum values should vary as a function of both the mean flow multiplied by the water depth, and the local instantaneous Richardson number. In this case these minimum values have been prescribed as constants.

3.1.3 Modifications to the hydrostatic model used by Gillibrand

Sigma co-ordinates for the open boundary scalar profiles

Allowing the surface to move through the upper grid points in the model can cause problems where strong vertical salinity variations exist in the upper part of the water column. If each grid point is assigned a fixed salinity value on the open boundary, the surface salinity will vary depending upon which grid point is at the free surface. The refinement to the model of Gillibrand (1993) presented here stretches a boundary salinity profile between the free surface and the bottom salinity point such that the surface (and depth averaged) salinity does not jump as grid points are included and rejected by the surface moving through them.

The open boundary profile is specified as the salinity at an equally spaced number of depths on the open boundary. The surface point of the boundary profile is not the same as the uppermost model grid point which usually is some distance below the surface. The bottom point is used to give the salinity at the lowest model salinity point. This uses the assumption that there is little spatial gradient near the seabed and so the shift of ½.Δz is unimportant. A linear interpolation is used between the two 'sigma boundary' points above and below each model grid point on the open boundary. An outline of the scheme is shown in figure 3.2 and equation 3.14.

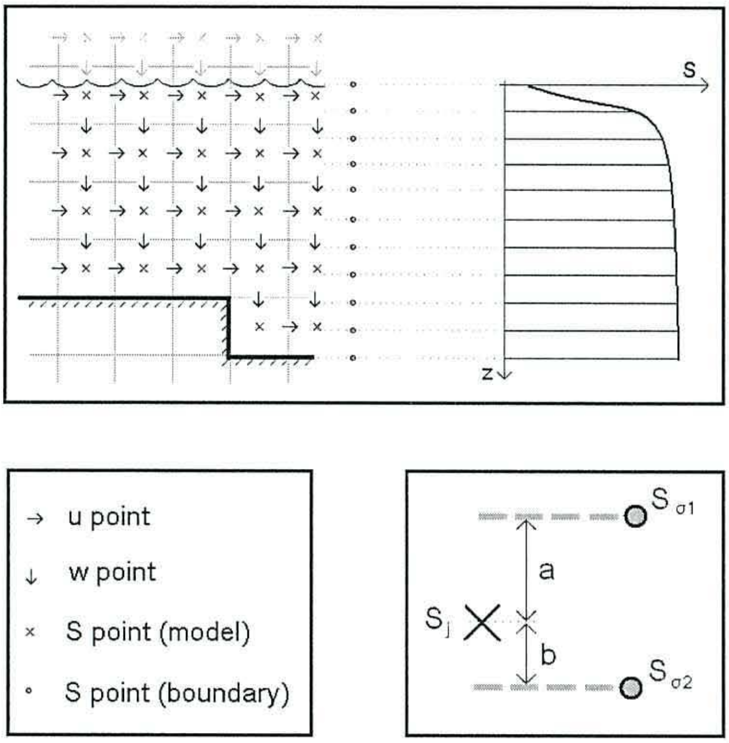

Figure 3.2 - Relationship between model grid and sigma co-ordinate boundary grid

The model grid salinity points are shown as crosses and the sigma co-ordinate boundary grid points are circles; the salinity at point S_j is therefore given by equation 3.14. In this case the nearest surface model grid point is used, the procedure is the same for the others.

$$S_j = S_{\sigma 1} + \left(S_{\sigma 2} - S_{\sigma 1} \cdot \frac{a}{a+b} \right) \qquad [3.14]$$

Spinup

Other modifications required were to hold the initial density structure fixed during a spinup period (T), which itself was introduced to reduce the level of surface seiching generated in the basins. During this time the amplitude of the tidal forcing was increased according to a sine wave between the limits $t/T \in [0, \pi/2]$.

3.2 Non hydrostatic models

The assumption that pressure in a fluid is hydrostatic and hence purely a function of depth, density structure and surface elevation has been widely used in oceanography to vastly simplify both numerical and analytical models. In this type of numerical modelling the vertical velocity equation is omitted and vertical acceleration is neglected; the vertical velocities are chosen to satisfy continuity. Therefore no account of vertical momentum is taken. By calculation of the pressure field, and the full use of equations to describe the momentum in both horizontal and vertical directions the non-hydrostatic model can resolve many more features of oceanographic flows.

3.2.1 Historical development of non-hydrostatic models

This group of models has developed out of engineering models aimed at small scale and complex flows. It is only recently that increases in computational power have made their application possible to oceanographic scale flows. Conceptually the only difference between a hydrostatic model and a non-hydrostatic model is the treatment of the spatial pressure derivatives. However, the hydrostatic model must calculate the vertical velocity by continuity alone and totally ignore the vertical momentum equation.

Complicating matters by introducing the compressibility of gas and Coriolis forces, Janjic, Gerrity *et al* (2001) propose an add-on computation of pressure to correct an initial hydrostatic system of equations for an atmospheric model. It is only recently that such methods have been applied to atmospheric simulations, however the underlying concept is not new. The first freely distributed code solving such a problem came out of work at the Los Alamos Labs (Hirt *et al.* 1975).

The SOLA code was a continuation of the Marker and Cell (MAC) approach where the Poisson Equation for pressure was first solved. With its extension to use the Volume of Fluid (VOF) method to compute the free surface the model is outlined in Hirt and Nichols (1981). It has a variable mesh size in both dimensions and the free surface can pass through any of the points such that the fluid can occupy any part of the model domain.

The computation of each timestep took three stages:

1. The momentum equations are solved without pressure gradient terms.
2. An iterative solution of the Poisson Equation is undertaken in conjunction with adjustments to the velocity field.
3. The fluid region and the surface is calculated.

Here the iterative approach adapts both the pressure and velocities simultaneously whereas the approach used in the model developed later in this study uses an iterative scheme to calculate a pressure correction that is later applied to the velocity field. This is the Projection method of Chorin (1968). The first calculation is of velocity, ignoring the non-hydrostatic pressure gradient terms, subsequently the non-hydrostatic pressure field is calculated and later a correction is applied to the velocity field.

Chorin (1968) investigates the merits of several iterative schemes that will yield a solution to the Poisson equation, recommending the Successive Over-Relaxation (SOR) scheme. It is pointed out by the author that this primitive equation scheme (3 equations, 2 velocity vectors and pressure) does not suffer from instabilities in the same way that the 2-dimensional vorticity - stream function calculation can.

Vlasenko *et al.* (2002) have used this vorticity - stream function form of the Navier - Stokes equations to give a non-hydrostatic laterally averaged model. This was applied to the Trondheimsfjord in Norway and reproduced residual transport due to non-linear internal waves.

3.2.2 The need for non-hydrostatic models in sea loch simulation

Marshall *et al.* (1997) give various conditions for the applicability of the hydrostatic approximation. In simple terms if the vertical acceleration is insignificant compared to the buoyancy (b in equation 3.15), then the hydrostatic approximation holds.

$$b = -g\left({}^{\delta\rho}\!\big/_{\rho_{ref}} \right) \qquad [3.15]$$

Posing the buoyancy in terms of the Brunt-Vaisala frequency leads to the following inequality, which if true, the hydrostatic approximation is valid. U is a characteristic velocity, L a characteristic length scale and N the Brunt Vaisala frequency.

$$\frac{U^2}{L^2 N^2} << 1 \qquad [3.16]$$

It follows from equation 3.16 that large velocities in small channels with little stable buoyancy will require a non-hydrostatic model. These conditions would be expected near to a sill in a loch where mixing would reduce stable density gradients.

It is also argued that when the horizontal length scales under consideration become similar in magnitude to the water depth hydrostatic equations break down (Marshall *et al.* 1997). The length scales at which the hydrostatic approximation breaks down is thought to lie in the range 1km to 10km in the open ocean, somewhere between the geostrophic and convective length scales.

Hydrostatic models cannot operate properly under conditions of density inversions, where denser water overlies less-dense water resulting in overturning motions.

Previous solutions to this problem have been to artificially mix such phenomena instantly. Such dense water cascades reported in the Gareloch by Ellis (2001) could therefore not be reproduced using such a scheme. They would be better modelled with a non-hydrostatic model capable of handling such unstable stratification and reproducing the density driven cascades they cause.

Modelling the Knight Inlet data has been undertaken by Cummins (2000) using the hydrostatic Princeton Oceanographic Model. The topography in the lee of the sill had to be artificially changed to mimic flow separation. While the steady state solution did match the observations, the evolution of flow up to that steady state did not. The model output shows a large breaking internal wave, absent from the data. When boundary layer separation was forced to take place by altering the topography the breaking internal wave was removed from the solution. He suggests future work should focus on a fine resolution non-hydrostatic approach that incorporates a high-order turbulence closure model.

Modelling dynamically similar flows, but on a far smaller scale, Johns and Xing (1993) presented two non-hydrostatic models. The inclusion of non-hydrostatic pressure effects was required in order to simulate flow separation on the lee flank of a bottom sandwave. Earlier hydrostatic work by the same author was criticised for being unable to reproduce this flow separation.

The non-hydrostatic approach of Vlasenko *et al* (2002) shows that non-linear lee waves, generated by sills, induce a residual circulation influencing the long term, large scale flow of these systems. Observational evidence of non-hydrostatic events such as flow separation and lee waves has been recently put forward by Inall *et al.* (2004) in Loch Etive.

The width averaged hydrostatic approach to sealoch modelling, taken by Bourgault and Kelley (2004) has the advantage of high resolution at less computational cost than a 3d model. In this model the grid spacing was reduced near to the sill and increased in the centre of the basin such that the small-scale, near-sill dynamics were accurately reproduced.

The two non-hydrostatic slice models in the literature (Vlasenko *et al.* 2002, Bourgault and Kelley 2004) differ fundamentally in the treatment of pressure. The former eliminates the pressure equation all together by using the stream function vorticity formulation of the Navier – Strokes equations. The latter introduces the width variation into the Poisson equation for pressure and subsequently solves this using the conjugate pressure gradient method. The model put forward in this study is essentially a simplification of the mathematics of Bourgault and Kelley (2004); the Successive Over Relaxation (SOR) method is used to solve the same width integrated Poisson equation.

It is an attempt to model the non-hydrostatic phenomena that have been shown to control the dynamics of other sill-basin systems, and the implication for basin scale circulation in the study area, that this non-hydrostatic model has been developed. Its performance will be compared against the model used by Gillibrand (1993) to assess the criticisms raised by the author of the applicability of an estuarine model to sea lochs.

3.2.3 The mathematical formulation of the Bourgault and Kelley model

The model equations presented in Bourgault and Kelley (2004) are shown overleaf. They are the width-averaged equations for horizontal and vertical momentum, continuity, depth-averaged continuity and the tracer (ϕ) transport equation. They have been solved on a variable spacing Arakawa C grid with the x direction along the channel and the z direction positive downwards with the origin at the undisturbed sea surface.

$$\frac{\partial u}{\partial t}+u\frac{\partial u}{\partial x}+w\frac{\partial u}{\partial z} = -\frac{1}{\rho_0}\frac{\partial P}{\partial x}+\frac{1}{B}\left[\frac{\partial}{\partial x}\left(BA_h\frac{\partial u}{\partial x}\right)+\frac{\partial}{\partial z}\left(BA_v\frac{\partial u}{\partial z}\right)-S_f u|u|\right] \quad [3.17]$$

$$\delta\left[\frac{\partial w}{\partial t}+u\frac{\partial w}{\partial x}+w\frac{\partial w}{\partial z}\right] = -\frac{1}{\rho}\frac{\partial P}{\partial z}+\frac{\rho}{\rho_0}g+\frac{\delta}{B}\left[\frac{\partial}{\partial x}\left(BA_h\frac{\partial w}{\partial x}\right)+\frac{\partial}{\partial z}\left(BA_v\frac{\partial w}{\partial z}\right)\right] \quad [3.18]$$

$$\frac{\partial Bu}{\partial x}+\frac{\partial Bw}{\partial z}=0 \quad [3.19]$$

$$\frac{\partial \eta}{\partial t}=-\frac{1}{B|_{z=0}}\frac{\partial}{\partial x}\int_{-\eta}^{H} bu\, dz \quad [3.20]$$

$$\frac{\partial \phi}{\partial t}+u\frac{\partial \phi}{\partial x}+w\frac{\partial \phi}{\partial z}=\frac{1}{B}\left[\frac{\partial}{\partial x}\left(BK_h\frac{\partial \phi}{\partial x}\right)+\frac{\partial}{\partial z}\left(BK_v\frac{\partial \phi}{\partial z}\right)\right] \quad [3.21]$$

Although similar to previous width-averaged models there are some notable differences. Firstly advection is here described in the flow form and not the flux or transport form as other workers have preferred. The formulation for side-friction is only applied to the horizontal momentum equation 3.17 and assumes a symmetrical channel. This is in contrast to the more complex formulation of Stacey *et al.* (1994) where both channel sides are described. The value of the side friction coefficient is thus given by equation 3.22; the constant S_0 is a tunable parameter from Lavelle *et al.* (1991).

$$S_f = S_0\left(1+\left|\frac{\partial B}{\partial z}\right|\right) \quad [3.22]$$

The pressure gradients in the horizontal and vertical momentum equations are expressed by two further equations, 3.23 and 3.24 respectively.

$$\frac{\partial P}{\partial x} = g\left(\rho_0 \frac{\partial \eta}{\partial x} + \rho_0 \frac{da_0}{\partial x} + \int_{-\eta}^{z} \frac{\partial \rho}{\partial x} dz\right) + \frac{\partial P'}{\partial x} \qquad [3.23]$$

$$\frac{\partial P}{\partial z} = \rho g + \frac{\partial P'}{\partial z} \qquad [3.24]$$

The variation of the mean water level with respect to the geoid (a_0) has been included in the horizontal pressure equation. The vertical pressure equation includes the hydrostatic pressure. The terms containing P' are the deviation of pressure due to non-hydrostatic effects. This pressure field is calculated by solving the width integrated Poisson equation for pressure (equation 3.25). The solution method used by Bourgault and Kelley (2004) was the preconditioned conjugate pressure gradient method as outlined in Marshall *et al.* (1997). The velocity field is subsequently 'corrected' for the effects of non-hydrostatic pressure, as undertaken in the original projection method of Chorin (1968).

$$\frac{\partial}{\partial x}\left(B \frac{\partial P'}{\partial x}\right) + \frac{\partial}{\partial z}\left(B \frac{\partial P'}{\partial z}\right) = \frac{\rho_0}{\Delta t}\left(\frac{\partial B\tilde{u}}{\partial x} + \frac{\partial B\tilde{w}}{\partial z}\right) \qquad [3.25]$$

Restrictions on the timestep are removed by the implicit treatment of the advective and diffusive terms in both the momentum and scalar equations. The surface wave speed restriction is also removed by the implicit method of Wang and Kravitz (1980) in the barotropic pressure gradient term. All terms were solved on a grid with variable grid spacing in both horizontal and vertical dimensions. The surface grid points were allowed to move with the free surface; meaning that the surface grid spacing must be larger than the tidal range.

This model includes a switch variable that allows the same code to be run in hydrostatic and non-hydrostatic modes. The vertical momentum equation (3.18) has this switch (δ) included which can vary between 0 (hydrostatic) and 1 (non-hydrostatic).

3.2.4 Outline of the non-hydrostatic model used in the current study

The model developed for use in this study has simplified the maths and numerics of the scheme of Bourgault and Kelley (2004). The computational grid, and the positions of the variables, is shown in figure 3.3. The grid is of fixed and constant spacing, and the rigid lid approximation is used such that the surface does not move (Vlasenko *et al.* 2002).

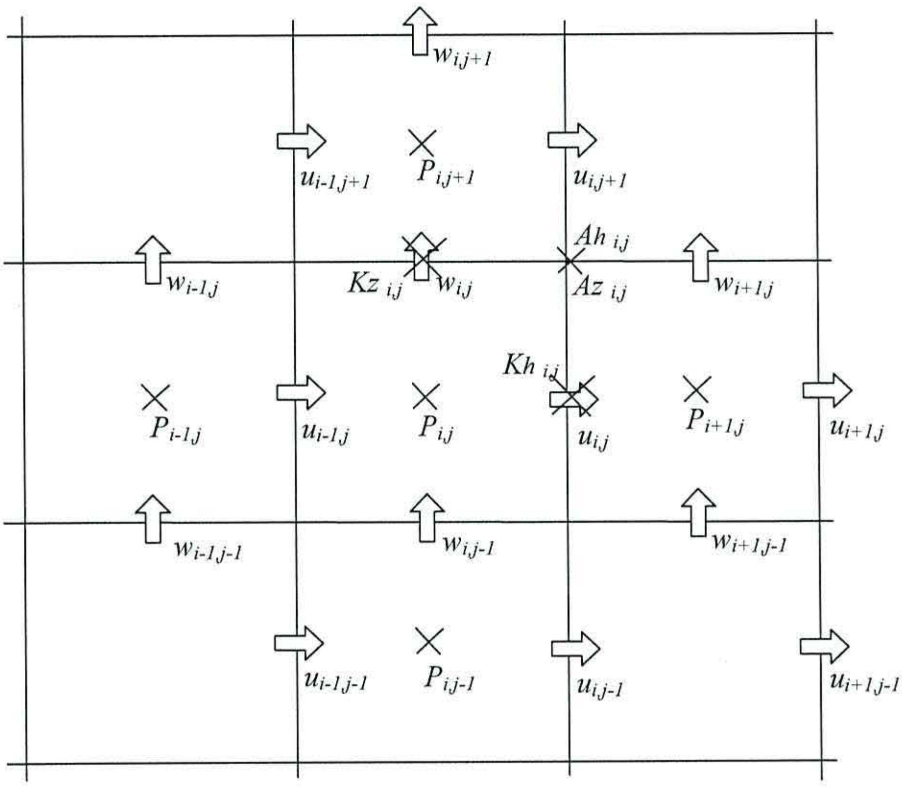

Figure 3.3 – The computational grid used in this study

The model equations are presented in equations 3.26 to 3.28. These are the horizontal and vertical momentum equations and the scalar transport respectively. Initially equations 3.26 and 3.27 are solved without the pressure gradient terms (the last terms in separate square brackets). This gives an initial estimate of the velocity components ($\widetilde{u}$ & $\widetilde{w}$ respectively). Subsequently the width-integrated Poisson equation for pressure is solved using these initial estimates. This gives the pressure gradient that augments the initial estimates of velocity.

Equation 3.28 gives the evolution of any scalar (Φ), in the current version of the model salinity is the only scalar. Temperature is the other state variable that can be modeled in this way. More complex turbulence schemes involve the transport of turbulent kinetic energy and dissipation that can use the same mathematics and code.

$$\frac{\partial u}{\partial t}=\left[\frac{1}{B}\left(\frac{\partial}{\partial x}\left(A_h B\frac{\partial u}{\partial x}\right)+\frac{\partial}{\partial z}\left(A_v B\frac{\partial u}{\partial z}\right)-S_f u|u|\right)-\frac{\partial\left(Bu^2\right)}{\partial x}-\frac{\partial\left(Buw\right)}{\partial z}\right] -\left[\frac{1}{\rho}\cdot\frac{\partial P}{\partial x}\right] \qquad [3.26]$$

$$\frac{\partial w}{\partial t}=\left[\frac{1}{B}\left(\frac{\partial}{\partial z}\left(A_v B\frac{\partial w}{\partial z}\right)+\frac{\partial}{\partial x}\left(A_h B\frac{\partial w}{\partial x}\right)-S_f w|w|\right)-\frac{\partial\left(Bw^2\right)}{\partial z}-\frac{\partial\left(Buw\right)}{\partial x}\right] -\left[\frac{1}{\rho}\cdot\frac{\partial P}{\partial z}\right]-g \qquad [3.27]$$

$$\frac{\partial \phi}{\partial t}=\frac{1}{\sigma_\phi\cdot B}\left[\frac{\partial}{\partial x}\left(K_h B\frac{\partial \phi}{\partial x}\right)+\frac{\partial}{\partial z}\left(K_v B\frac{\partial \phi}{\partial z}\right)\right]-\frac{\partial}{\partial x}(Bu\phi)-\frac{\partial}{\partial z}(Bw\phi) \qquad [3.28]$$

Advection

The advection of momentum has been handled using the flux or transport form rather than the advective form. The two schemes can be shown identical but the flux form is often favoured for its conservative properties (Xue and Lin 2001). The integration of this term over the width of the channel differs from the more common depth integration (George KJ, Pers. Comm.) in that the length over which integration is undertaken cannot vary with time. The numerical treatment of this term is centred in space scheme.

Note that this scheme differs from that given by Griebel *et al.* (1998) in that the centred difference is not combined with an upwind difference to maintain stability. A weighted averaged of a centred and upwind scheme is often used, the weighting factor (γ) can be chosen arbitrarily (Griebel *et al*, 1998) or calculated in relation to the local gradients (James, 1986). The use of the upwind term is kept to a minimum to reduce numerical diffusivity. This step was not required in the sealoch simulations, although the model can use an upwind weighting factor if required.

By contrast the advection of scalars, identical to equation 3.21 of Bourgault and Kelley (2004), is handled with a TVD advection scheme as described in James (1996) and Souza and James (1996). This is compared against a centred difference / upwind scheme in the next chapter.

<u>Momentum Coefficients</u>

The velocity distribution across a channel varies from the mean value. Therefore the non-linear terms in the equations of motion will, if posed in terms of the mean velocity, be in error. The inclusion of the co-efficient (β) in the advective term (equation 3.29) allows for this effect. This situation was first addressed in 1877 by Boussinesq (Xia and Yen, 1994) who proposed equation 3.30 for the momentum coefficient (β).

$$(2\beta - 1)U\frac{\partial U}{\partial x} \qquad [3.29]$$

$$\beta = \frac{\int_A u^2 dA}{\overline{U}^2 A} \qquad [3.30]$$

If a velocity profile is considered to vary sinusoidally across a channel, equation 3.30 gives a value for $\beta = 1.23$. A parabolic profile yields a value of 1⅓, although in turbulent flow it can be as large as 2 (Chadwick and Morfett, 1998). The maximum velocity found in a cross section of open channel flow is slightly beneath the free surface. The ratio of the sectionally averaged mean velocity to the maximum is 0.64 and 0.67 for the sinusoidal and parabolic distributions respectively; similar quantities have also been quoted in the literature. Armaly *et al* (1983) found a value of ⅔ in a laboratory flume while Campbell *et al* (1998) relate the sectionally averaged velocity to the depth mean velocity in the centre of the Menai Strait with a co-efficient of 0.87. Including the influence of variations of velocity with depth, Tinis and Pond (2001) related the maximum recorded velocity over a sill in Sechelt Inlet with the sectional average by a factor of 0.24.

Clearly across channel variations of the velocity field are significant. Xia and Yen (1994) include the momentum co-efficients in the advective term as shown in equation 3.29. The same paper also includes modifications to the non-hydrostatic pressure terms to account for cross channel variations. This has not yet been explored with the current model.

Methods to solve the Poisson Equation

A brief discussion of the various methods used to solve this type of equation is outlined here, showing the development of the method chosen for this study, Successive Over Relaxation (SOR).

The matrix method involves writing equations for each point in space and solving one large matrix problem. In one dimension the Poisson equation can take the form of equation 3.31, discretised in equation 3.32 using a centred difference.

$$\frac{\partial^2 P}{\partial x^2} = \tilde{u}(x) \qquad [3.31]$$

$$\frac{P_{i+1} - 2P_i + P_{i-1}}{\Delta x^2} = \tilde{u}_i \qquad [3.32]$$

By specifying the boundary values for U at $i = 0$ *and* $i = n + 1$ this can be written in the matrix form $A \times P = \tilde{u}$ (equation 3.33). Solving for P involves inverting the sparse matrix (A) which when n is large can be inefficient to implement even in one dimension.

$$\frac{1}{\Delta x^2}\begin{bmatrix} -2 & 1 & & & \\ 1 & -2 & 1 & & \\ \cdots & \cdots & \cdots & \cdots & \cdots \\ & & 1 & -2 & 1 \\ & & & 1 & -2 \end{bmatrix} \times \begin{bmatrix} P_1 \\ P_2 \\ \cdots \\ P_{n-1} \\ P_n \end{bmatrix} = \begin{bmatrix} \tilde{u}_1 - U_0 \\ \tilde{u}_2 \\ \cdots \\ \tilde{u}_{n-1} \\ \tilde{u}_n - U_{n+1} \end{bmatrix} \qquad [3.33]$$

Iteration involves an initial approximation of a solution across the entire computational domain. A series of steps are undertaken whereby the values are modified according to a formula across the entire domain. Each successive step gives a better approximation to the solution to the problem than the last. As the approximations converge on the correct answer the differences between each successive answer becomes less. The process is stopped when this difference falls below a pre-determined threshold ($10^{-9}\overline{P}$, where $\overline{P}$ is the mean pressure).

The simplest iterative method of solution is the Jacobi method. Re-arranging equation 3.32 for P_i gives equation 3.34. Starting with an initial estimate P^k the value of P at iteration $k+1$ can be approximated by;

$$P_i^{k+1} \approx -\frac{1}{2}\left(\Delta x^2 \tilde{u}_i - P_{i-1}^k - P_{i+1}^k\right) \qquad [3.34]$$

The Gauss-Seidel method uses the value previously estimated at i-1 in the current iteration (equation 3.35). Assuming we sweep across the calculation spatially from $i = 1$ to $i = n$.

$$P_i^{k+1} \approx -\frac{1}{2}\left(\Delta x^2 \tilde{u}_i - P_{i-1}^{k+1} - P_{i+1}^k\right) \qquad [3.35]$$

A refinement to this is to make the correction to the approximation larger by some factor, thus accelerating convergence to the correct solution. This is achieved by the parameter ω, which varies between the limits 1 and 2. Setting ω to unity gives the Gauss-Seidel method. The value of P_i^k has been added outside the brackets on the right hand side of equation 3.36, and subtracted inside giving the Successive Over Relaxation (SOR) equation;

$$P_i^{k+1} \approx P_i^k - \frac{\omega}{2}\left(\Delta x^2 \tilde{u}_i + 2P_i^k - P_{i-1}^k - P_{i+1}^{k-1}\right) \qquad [3.36]$$

In practice the optimum value for the relaxation parameter (ω) can be found by trial and error. Being purely a function of the computational grid a modest model run can be used as a test case and the number of iterations, required to bring the pressure field within the specified tolerance, reduced to an acceptable level. The optimum value needs to be found to 2 decimal places, (Bourgault D, Pers. Comm.) as varying the second digit can half the number of iterations required in some simulations. This numerical experiment is outlined in chapter 6.

Any convergent iterative system shows a decrease in the magnitude of the corrections applied at each successive iteration. Various methods for quantifying the errors all use the difference between successive approximations and relate this to an allowable error. In this model the allowable error has been scaled in proportion to the mean pressure across the computational domain.

The maximum magnitude of the correction is calculated at each iteration across the model domain. If this falls below a value typically of $1\times10^{-9}\overline{P}$ then the cycle is stopped.

P^+	P^-	P^+	P^-	P^+
i-2	i-1	i	i+1	i+2

Figure 3.4 – Grid scale pressure variation

The discretisation of the spatial gradient of pressure in the SOR algorithm (equation 3.36) requires the pressure at $i+1$ and $i-1$. The situation where pressure varies at grid scale as shown in figure 3.4 could arise, leading to the calculation that the pressure gradient is zero everywhere.

To remove the possibility of this occurring rather than sweeping the iteration across the domain one cell at a time, the computation is undertaken at every even numbered cell. Following this sweep the values at odd numbered cells are calculated. In two dimensions this produces a chessboard pattern, often referred to as 'chess board' or 'red-black SOR'.

Including width variation in the Poisson Equation

In this study the Poisson equation for pressure (equation 3.25) contains the channel width inside the derivatives on the left-hand side, which complicates its solution. The two examples of a non-hydrostatic slice model previously published use differing techniques here. Vlasenko *et al.* (2002) eliminates the pressure equation all together by the use of the stream function – vorticity formulation of the equations of motion. Bourgault and Kelley (2004) modify the conjugate pressure gradient method to allow for changes in channel width, although gives no details. The method of solution taken in this study is to modify the SOR algorithm to allow the total pressure to be solved. (equations 3.37 and 3.38). The next estimate of pressure at iteration $k+1$ is given by the SOR equation (3.37). The derivation of this in a width-varying channel is outlined in Appendix 2.

$$P_{i,j} = (1-\omega)P_{i,j}^{k} + \frac{\omega}{\left(\frac{B_{i+\frac{1}{2},j} + B_{i-\frac{1}{2},j}}{(\Delta x)^2}\right) + \left(\frac{B_{i,j+\frac{1}{2}} + B_{i,j-\frac{1}{2}}}{(\Delta z)^2}\right)} \times \left(\left[\frac{B_{i+\frac{1}{2},j} P_{i+1,j}^{k} + B_{i-\frac{1}{2},j} P_{i-1,j}^{k+1}}{(\Delta x)^2} \right] + \left[\frac{B_{i,j+\frac{1}{2}} P_{i,j+1}^{k} + B_{i,j-\frac{1}{2}} P_{i,j-1}^{k+1}}{(\Delta z)^2} \right] - RHS_{i,j} \right) \qquad [3.37]$$

where $RHS_{i,j}$ is the right hand side of the Poisson equation, evaluated at the point i,j at time level t and given by equation 3.38:

$$RHS_{i,j} = \frac{\rho_0}{\Delta t} \left(\frac{B_{i+\frac{1}{2},j} \widetilde{u}_{i,j}^{t} - B_{i-\frac{1}{2},j} \widetilde{u}_{i-1,j}^{t}}{\Delta x} + \frac{B_{i,j+\frac{1}{2}} \widetilde{w}_{i,j}^{t} - B_{i,j-\frac{1}{2}} \widetilde{w}_{i,j-1}^{t}}{\Delta y} \right) \qquad [3.38]$$

Boundary conditions

The surface is considered to be a rigid lid. This enables a simple boundary condition to be applied in that the pressure immediately above is zero. The influence of sea-surface slope is still retained, via the pressure gradient found by solving the Poisson equation. The influence of the change of channel cross section while the tide rises and falls is not included. Lochs and fjords have steep sides so this effect is reduced; this is not the case for many channels where this assumption could not be justified.

Boundary conditions for pressure at the remaining boundaries are that there is no gradient normal to the boundary. This follows from Newton's 2nd law that every force should have an equal and opposite reaction. The boundary exerts the same pressure to the fluid that the fluid exerts to it.

The vertical velocity at the surface is set to zero. Horizontally the free slip condition is used in that the velocity above the surface is set to the value below. For the small scale analytical proofs the bottom boundary uses a no-slip condition, assuming that the scale of the model enables the boundary layer to be resolved. This involves setting the value of velocity normal to the boundary but outside to –1 times the value inside. Interpolation of the two yields zero on the boundary.

For the larger sealoch scale simulations a free slip condition is applied at the bottom boundary, and a purely quadratic friction term is specified. This assumes that the boundary layer falls entirely between the lowest grid point and the wall. Neither the free-slip or no-slip condition will satisfy the boundary layer problem at all times at all locations in the model. The thickness of the boundary layer will change over time and space. However, as the velocity changes logarithmically the assumption that the lowest velocity is outside the boundary layer will only be a slight underestimate if it is inside the outer limits of this layer.

The TVD advection scheme uses a free-slip boundary condition for the advection term only. The outflowing boundary has a no-gradient condition.

As a consequence of the simplification at the surface the open boundary forcing must be undertaken using a velocity profile rather than specifying the boundary elevation as is done in the hydrostatic model. The profile used is given by equation 3.39 (Prandle, 1985). This assumes a constant viscosity and a bed stress co-efficient of 0.0025, both reasonable assumptions in the application. The consequence of this is that the open boundary must be at a point in the system where there is no baroclinic activity and the flow can be represented by this idealised profile, hence the use of the Corran sill as the seaward boundary.

$$u_z = 0.89\bar{u}\left\{\frac{-z^2}{2} + z + \frac{\pi}{4}\right\} \qquad [3.39]$$

Turbulence scheme

The turbulence scheme of Munk-Anderson (1948) outlined in section 3.1.2 has been trialed but yielded results little different from setting all mixing parameters to constants. This simple scheme where values for diffusion and viscosity are set as constants has been used with all the simulations presented in this thesis. Horizontal turbulent mixing parameters have been either calculated using the scheme outlined in Stacey *et al* (1995), a width-averaged adaptation of the original work of Smagorinsky (1963), or simply specified as a constant.

A more complex *K-L* scheme (Rodi, 1984) has been coded to calculate the vertical mixing parameters with this model but is not presented here. The turbulence models have been separated from the dynamical model such that they can be easily changed (see next section).

Coding

The non-hydrostatic model has been coded using a combination of the *C* and *C++* programming languages. The principal advantage of using this approach is that the computationally intensive time-stepping section has been written in *C*, optimising run-time speed. In the same code the model initialisation and input/output sections are written in a more objective way, making full use of the flexibility and adaptability of the object orientated techniques in *C++*. The classes CDataFile and CgridFile are examples of this where a stream object has had functionality added to read or output parameters.

The other main use for Objects has been the coding of the turbulence model as a separate object. Several versions of this object have been created, varying in complexity, however they all share a common interface with the dynamic model. This enables the turbulence scheme to be changed by using different header and class implementation files and re-linking with the model. The main model and the rest of the code don't require re-compilation.

To increase the flexibility of the code the size of the computational domain is chosen at run-time rather than at the compilation stage. The flexible memory allocation and array indexing systems in *C* remove the need to hard code maximum domain sizes and make possible the concept of spatial sweep lists.

Computational domains consist of fluid and non-fluid cells. Computations are only undertaken in the fluid section, cells outside this are ignored. Differentiating between fluid and non-fluid cells can involve time wasting tests. This has been overcome by the use of spatial sweep lists. At the initialisation stage lists are constructed of the i,j indices of cells where computations of velocity and pressure are to be undertaken. The spatial sweep across the computational domain inside the time-stepping routines is then a matter of reading the indices from the appropriate list one cell at a time. This means that the non-fluid cells are never interrogated by the model, saving more computational time in domains where the majority of the cells are non-fluid.

Optional parts of the code are selected at compile-time using pre-processor directives. This has been used in three cases;

1. To enable outputs to be selected without time consuming tests at run-time.
2. To switch between different equations, or to select different scientific options; e.g. buoyancy driven flow, radiation boundary conditions and inflow profiles.
3. To enable different sections to be selected depending upon which platform the code is being compiled for. This enables one piece of code to work across different platforms, making upgrading and maintenance a far simpler task. The current model compiles under Solaris, Linux and Windows.

3.3 Width Integrated Stream Function

The stream function of the resultant flow field has been calculated and is used in the presentation of the output. Contours of the stream function, streamlines, are curves that are parallel to the velocity vector at all points. The flux of mass perpendicular to two planes between two streamlines is a constant. Where the fluid is considered to be incompressible and density variations are ignored, the volume fluxes are also identical. In the width-averaged case the width of the channel needs to be included in the calculation to maintain continuity of volume.

The stream function (ψ) is said to satisfy the integrability condition (Griebel *et al.* 1998) in that the order of the derivatives can be changed (equations 3.42 and 3.43).

$$\frac{\partial^2 \psi}{\partial x \partial y} = \frac{\partial^2 \psi}{\partial y \partial x} \qquad [3.40]$$

$$\frac{\partial^2 \psi}{\partial x \partial y} - \frac{\partial^2 \psi}{\partial y \partial x} = 0 \qquad [3.41]$$

$$\frac{\partial}{\partial x}\left(\frac{\partial \psi}{\partial y}\right) - \frac{\partial}{\partial y}\left(\frac{\partial \psi}{\partial x}\right) = 0 \qquad [3.42]$$

A comparison of equation 3.42 with the expression for continuity (equation 3.43) reveals the equalities given in equations 3.44 and 3.45.

$$\frac{\partial}{\partial x}(B \cdot u) - \frac{\partial}{\partial y}(B \cdot w) = 0 \qquad [3.43]$$

$$\frac{\partial \psi}{\partial y} = B \cdot u \qquad [3.44]$$

$$\frac{\partial \psi}{\partial x} = B \cdot w \qquad [3.45]$$

The stream function is an optional output from the model and is calculated by fixing $\psi = 0$ at the bottom boundary and using the relationship in equation 3.44. The contour plot of the stream function shows the streamlines. The streamline at $\psi = 0$ is used to evaluate where the flow detaches and attaches itself to the bathymetry. This has been used in the backwards facing step example to establish the re-attachment length. Where the flow is complicated by reverse eddies it is useful to space the contour values out exponentially rather than linearly. If more contours are located in the bottom end of the range of stream function values, then areas of slow flow and reverse flowing eddies are better visualised. The computation of this width-integrated stream function has been added to the hydrostatic model and included in the development of the non-hydrostatic model.

Chapter 4 – Non Hydrostatic Model Validation

Presented in this chapter are test case scenarios used to investigate the performance of the non-hydrostatic model described in the last chapter. The model has been tasked with simulating a variety of small scale laboratory experiments that show its ability to re-produce processes important in this study. The fundamental processes include flow separation and density driven flows, the model's abilities and shortcomings are examined. This chapter concludes with a simulation of the Loch Etive data presented in Inall *et al* (2004). This high resolution data depicts a jet in the lee of a shallow sill. It is perhaps the best British data set for such purposes; similar in scope to the Knight Inlet data set so often the subject of numerical simulations in North America.

4.1 Backwards facing step

Flow through a narrow channel where a sudden increase in depth occurs has been the subject of flume and numerical experiment. A thorough experimental investigation has been undertaken by Armaly *et al* (1983) under a range of flow conditions from the purely laminar through to turbulent flow regimes. It has since been frequently used to validate computational fluid dynamics schemes (Zhu 1995).

A schematic of the experiment is given in figure 4.1; of primary interest here is the re-attachment length of the flow following the re-circulation zone behind the step. The estimation of this length from numerical simulation is taken from the point where the contour of $\psi = 0$ (dashed line in fig 4.1) intersects the lower boundary of the model.

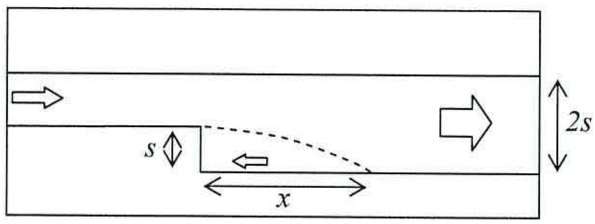

Figure 4.1 – Backwards facing step flow experiment

In the simulation the step height (s) was taken to be 0.75m and the re-attachment length was normalised to this (x/s). The grid consisted of 100 × 30 points representing a domain of 30m × 1.5m. The upper boundary and lower boundaries were given a no-slip condition and left and right boundaries were inflow and outflow respectively. The inflow velocity was set to 1ms^{-1} at all points on the open boundary, and had reached an equilibrium profile by the time it reached the top of the step at x = 7.5m. (see figure 4.4)

The Reynolds number is a measure of the inertial forces to the viscous forces. The definition given in Armaly *et al* (1983) uses the hydraulic diameter ($D=2h$) whereas subsequent works have used the depth of water (h) in the channel as a length scale (equation 4.1). Throughout this work the water depth has been used to define the Reynolds number

$$\text{Re} = \frac{Uh}{\nu} \qquad [4.1]$$

At a Reynolds number of 125 the re-attachment length, normalised to the step height was found by numerical means (Zhu 1995) to be within the range 5.08 to 5.29, dependant upon inlet length and grid size (The grid used was 640 × 64 points). The flume experiments of Armaly *et al* (1983) give a re-attachment length of approximately 6 from flume tank observations at this Reynolds number.

As previously discussed the upwind difference parameter (γ) allows the numerical diffusivity of the model to be '*tuned*'; at *Re* = 125 the value of γ was chosen to be 0.1 to give a re-attachment length of 4.9. The experiment was then repeated at *Re* = 250 and *Re* = 500, using otherwise identical input parameters; the results are tabulated in table 4.1 and the streamlines are shown in figure 4.2. The simulation was allowed to run for a maximum of 320 seconds (at *Re* = 500) and in each case a steady state was reached. This took considerably less time for the lower Reynolds number simulations.

Above *Re* = 500 the flow never reaches a steady state, eddies are shed into the stream and replaced with new ones (figure 4.3). Therefore the mean re-attachment length has been calculated by averaging the stream function over the time interval of 100 to 191 seconds; chosen to cover the generation of 20 eddies behind the step.

Table 4.1 – Re-attachment length vs. Reynolds number

	Reynolds number			
	125	**250**	**500**	**1000**
Armaly *et al* (1983)*	6	10	16	13.7
Griebel *et al* (1998)	-	5.8	8.3	-
Zhu (1995)	5.08 – 5.29	6	7	3.5
This study	4.9	8.9	15.9	8.1

* Reynolds number definition used in Armaly *et al* (1983) has been altered following Zhu (1995). Using channel height (*h*) rather than the hydraulic diameter (2*h*) reduces the reported *Re* of Armaly *et al* (1983) by a factor of 2. This has been taken into account here.

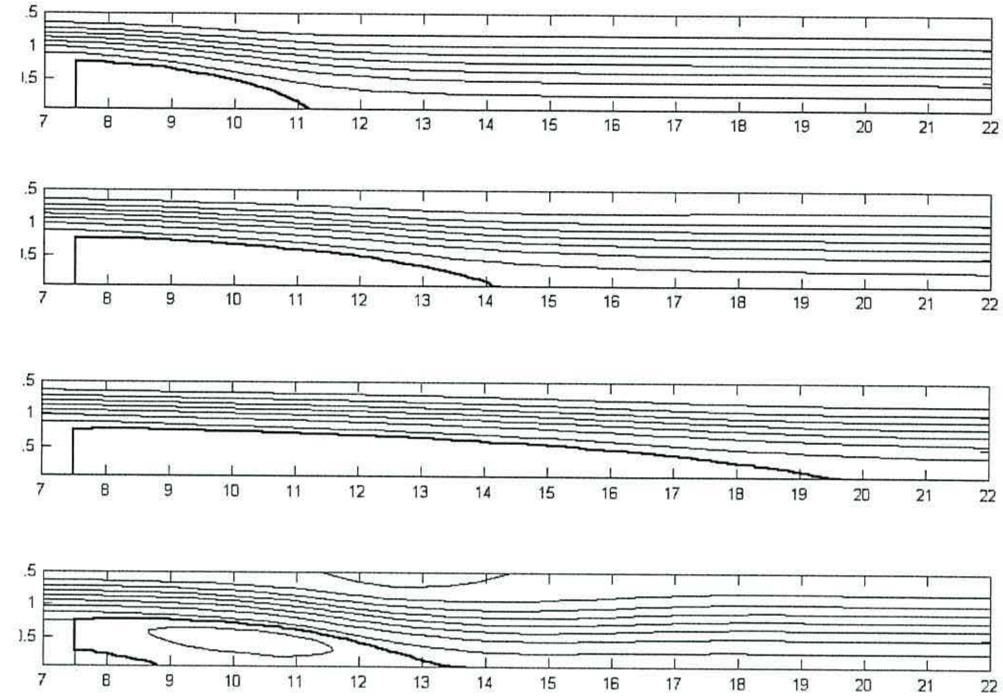

Figure 4.2 – Streamlines at Re = 125, 250, 500 & 1000 respectively, bold line indicates contour of $\psi = 0$

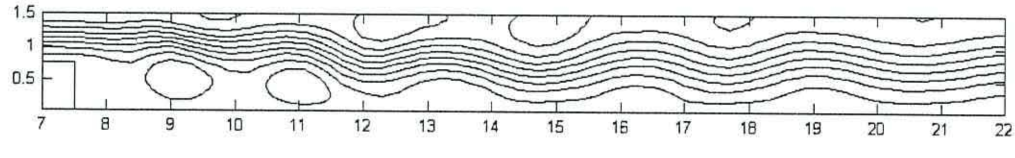

Figure 4.3 – Instantaneous streamlines at Re = 1000

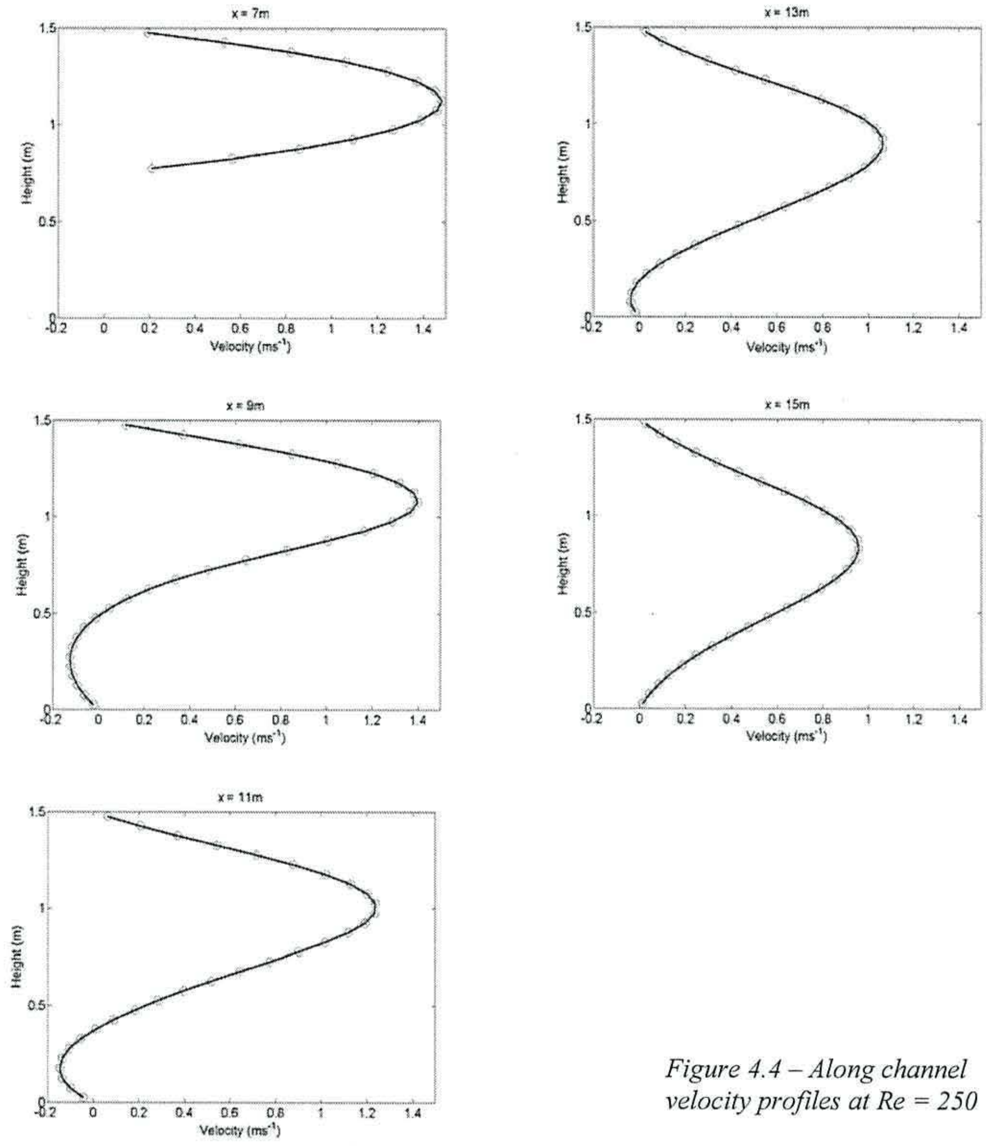

Figure 4.4 – Along channel velocity profiles at Re = 250

At higher Reynolds numbers the flow is no longer steady. Zhu (1995) concludes that this marks the point at which the flow is not laminar but transitional. There is a reduction in re-attachment length and a second re-circulating region is seen on the upper boundary immediately downstream of the first eddy behind the step.

Although this model has been tuned to give a reasonable answer at *Re* = 125, re-attachment lengths are reproduced throughout the laminar flow regime and into the transitional one. The reduction of re-attachment length at *Re* = 1000 is reproduced by the model, although an underestimate by a factor of 40%. The model results from this study are in closer agreement to the flume experiments of Armaly *et al* (1983) than either of the two numerical studies that form a comparison. Perhaps this may, in part, be due to the fact that the model of Zhu (1995) used no tuning and that of Griebel *et al* (1998) used a different advection scheme.

4.2 Flow along a channel of varying width

The model was set to calculate the flow along a channel of uniform depth but varying width. The dimensions of the channel were taken from the apparatus of experiments reported in Lane-Serff *et al.* (2000). The channel has a length of 1.16m and a depth of 0.29m; the width varies from 0.05m at the centre to 0.13m at either end. The width (B) is given by equation 4.2:

$$B = r - \sqrt{r^2 - x^2} + B_c \text{ when } |x| \le 0.29 \qquad [4.2]$$

otherwise $B = B_0$

$x = 0$ at the centre of the channel.

$B_0 = 0.13\text{m}$

$B_c = 0.05\text{m}$

$r = 0.5775\text{m}$ (the radius of the curved contraction)

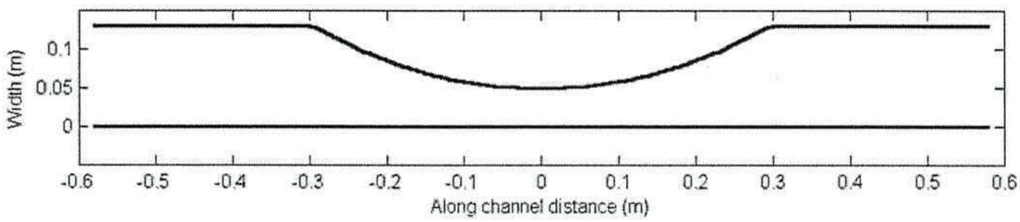

Figure 4.5 – Width variation in the Lane-Serff channel

Conservation of volume

A computational grid of 116 by 29 points ($\Delta x = \Delta y = 10^{-2}$m) was used, at one end a uniform inflow velocity was set to be 1ms^{-1} and at the other an outflow condition was set. A time step of 10^{-3} seconds was used; over the initial 5 seconds of simulation the inflow velocity was accelerated from rest and the output was examined after 10 seconds.

The cross sectional area of the channel is therefore 0.0377 m^2 at the ends and 0.0145 at the narrowest section in the centre. The current profiles at *x=0m* and *x=0.58m* are shown in figure 4.6. The depth averaged velocities and volume fluxes are given in table 4.2. From this the error of flux conservation can therefore be estimated to be 4.99×10^{-4}.

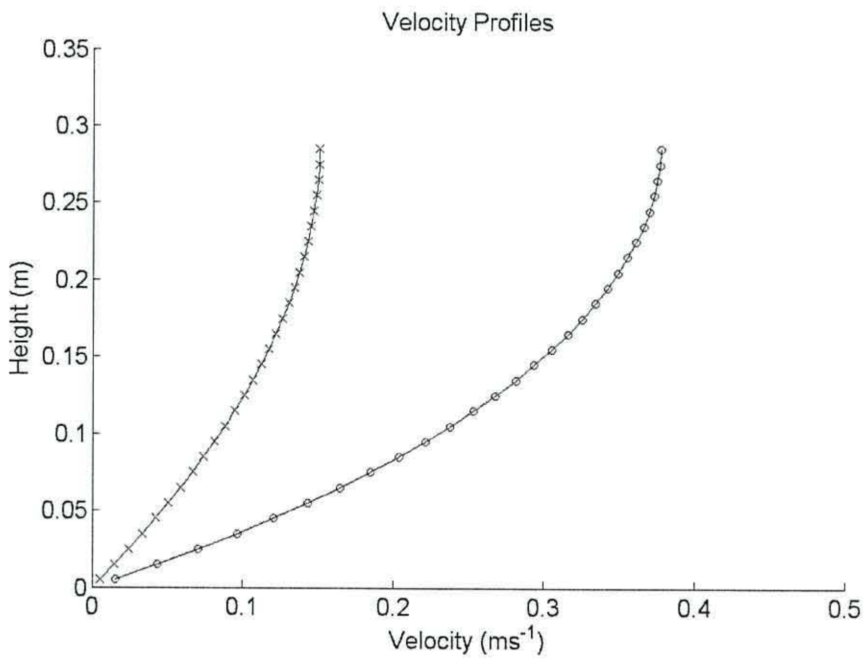

Figure 4.6 – Velocity profiles at the centre of the channel, x=0 (circles) and at the end of the channel, x=0.58m (crosses)

Location	Section (m^2)	Mean velocity (ms^{-1})	Volume flux (m^3s^{-1})
Centre (x=0)	0.0145	0.25987006897	0.00376811600006
End (x=0.58)	0.0377	0.09999996552	0.00376999870010

4.3 The lock exchange experiment

The study of flows created by a horizontal density gradient has often been used to draw parallels to estuarine circulation. In this standard fluid dynamics experiment a long narrow channel is divided into two sections by a lock gate as shown in figure 4.7. To the left is an unstratified fluid of density ρ . To the right is a stratified region where the lower fluid has the same density ρ and the upper has a density ρ . The lock gate is opened and the flow caused by the horizontal density gradient in the upper layer is modelled.

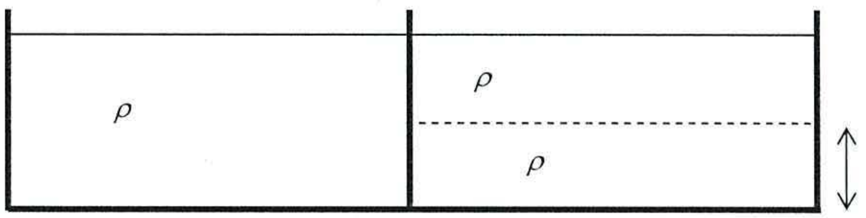

The model domain used was 5.0 metres in length and 1.0 metres deep. The computational grid was 50 by 10 giving both horizontal and vertical resolutions of 10^{-1}m. Salinities were specified to be 34 and 28 giving densities of ρ and ρ as 1026.26 kgm^{-3} and 1021.57 kgm^{-3} respectively.

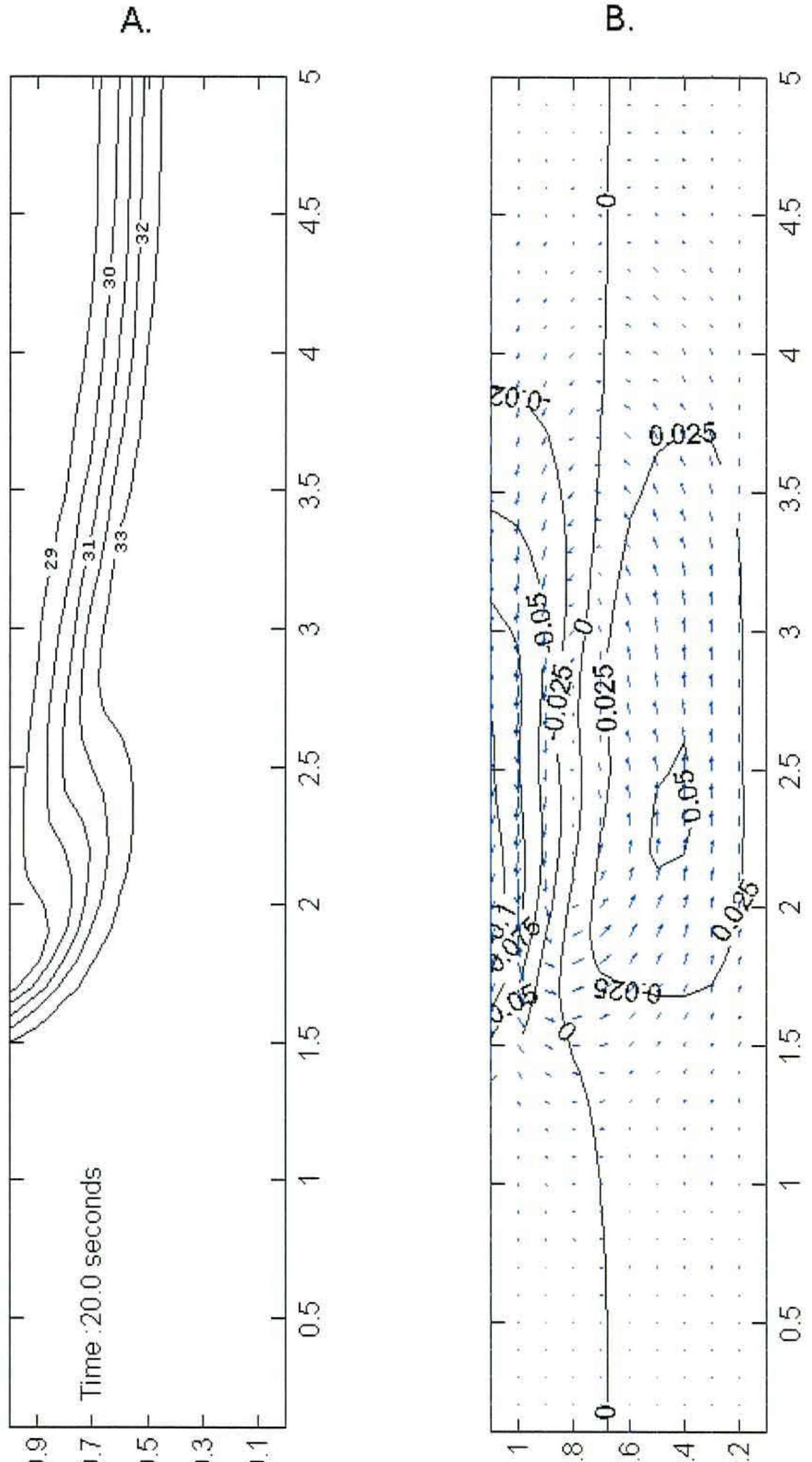

Figure 4.8 – (a) Contours of salinity and (b) velocity (ms^{-1}) after 20 seconds

Equating the change in potential energy from the stratified to the mixed system to a change in kinetic energy yields an expression for the speed of the gravity head (U) shown in equation 4.3 (Simpson, JH. lecture notes).

$$\Delta PE = -\frac{1}{2}\Delta\rho g h^2$$

$$\Delta KE = \rho h U^2$$

$$-\frac{1}{2}\Delta\rho g h^2 + \rho h U^2 = 0$$

$$\therefore U = \sqrt{\frac{g'h}{2}} \qquad [4.3]$$

where g' is the reduced gravity given by $g\left(\Delta\rho/\rho\right)$.

Using the parameters of the experiment a value of U can be calculated to be $0.106\mathrm{ms}^{-1}$.

The maximum value of horizontal velocity can be seen from figure 4.8 to be located at the head of the brackish intrusion at the surface as it flows over the denser water. From the model data the maximum is $0.118\ \mathrm{ms}^{-1}$, in close agreement with but slightly larger than the value derived from energy considerations. This increase in velocity may be due to the isohalines being locally inclined the other way (figure 4.8 a, from x=2.0 to x=2.2m), providing an extra density driven component to the surface flow.

4.3.1 Comparison of advection schemes

To form a comparison of the effectiveness of the two scalar advection schemes outlined in chapter 3, identical simulations were run with the TVD (case A) and transport form (case B). Contours of salinity are shown after only 3 seconds of simulation in figure 4.9. Case B, the transport form, uses an equal mixture of upwind and centred differences. As can be seen case B shows a grid scale pattern caused by the classic centred difference overshoot problem. The TVD scheme (case

A) does not exhibit any of this pattern and has not diffused the sharp gradient any more than case B.

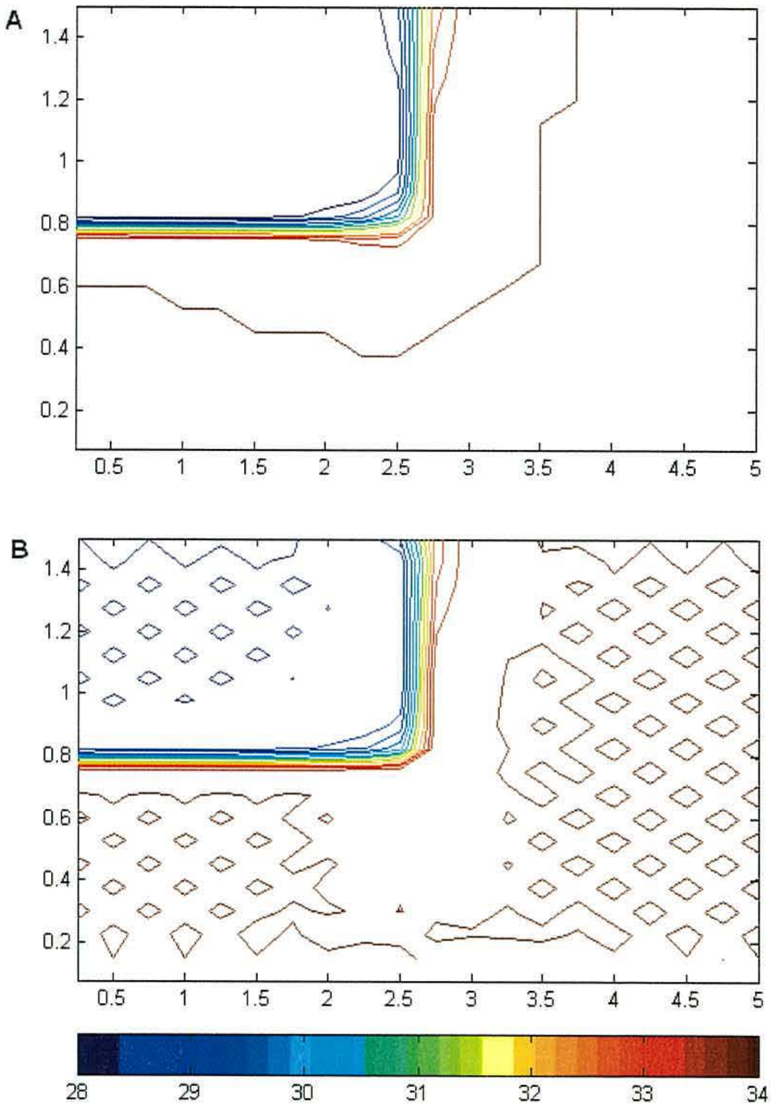

Figure 4.9 – Contours of salinity from lock exchange using TVD (A) and transport form (B) of the advection equation for salinity

4.4 Density Driven flow through a constriction

In order to investigate the exchange through the Bab al Mandab Strait between the Red Sea and the Gulf of Aden, Lane-Serff *et al* (2000) made use of a laboratory flume experiment using the flume already described in section 4.3. In this case both ends were sealed and three fluids of different densities were introduced at rest, and then allowed to move due to density driven flows once a barrier was removed. The initial conditions are shown in figure 4.10 *A & B*; the depths of the fluids (y_{1-} and y_{1+}) are varied to produce 3 experiments outlined in table 4.3.

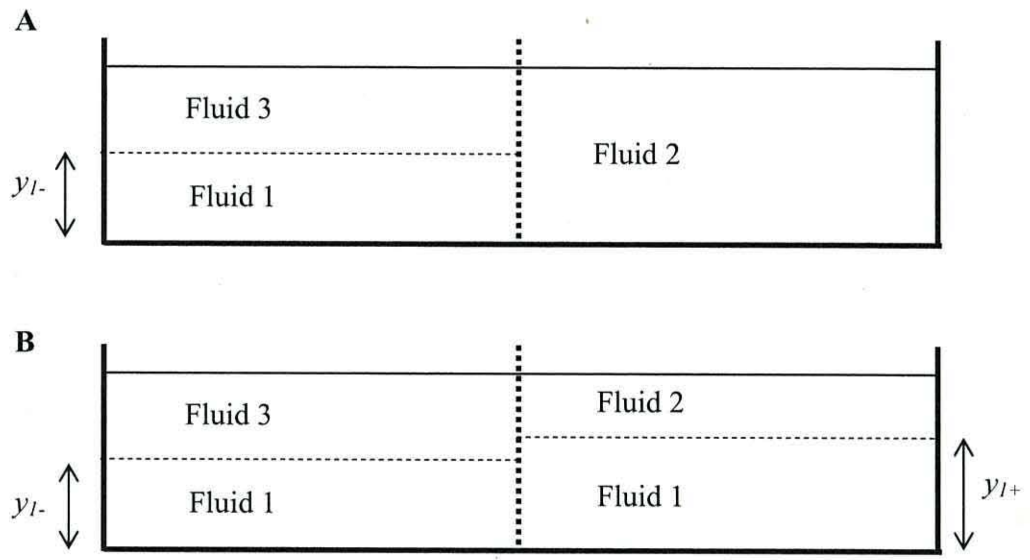

Figure 4.10 – The initial density structure of the Lane-Serff experiments

Experiment 1 coincides with case A (figure 4.10) with the depths of fluids 1 and 3 equal. Experiment 2 is an example of case B where fluid 1 occupies the lower half of the flume on both sides of the barrier. Experiment 3 is another case B set-up, this time with the depths of fluid 1 different each side of the barrier.

Table 4.3 –Relative Fluid depths for the Lane-Serff experiments

Experiment	y_{1-}	y_{1+}
1	0.5	-
2	0.5	0.5
3	0.5	0.25

Although the salinities in table 4.4 are outside the ranges used to calculate the linear approximation to the equation of state (chapter 3) they yield the densities of the original experiment. The model domain used is the same as that used for the '*Flow along a channel of varying width*' simulation except the spatial resolution was doubled to $\Delta x = \Delta y = 5mm$ over a computational domain measuring 1.16m long by 0.29m high.

Table 4.4 – Density and Salinity of the Lane-Serff fluids

Fluid	**Density** (kgm^{-3})	**Salinity**
1	1150	19.6
2	1075	9.5
3	1000	0.0

When released the intermediate layer (fluid 2) moves through the curved constriction in the centre of the channel and interleaves fluids 1 and 3. In experiment fluid 1 also pushes a density driven current towards the right, a similar but less dense intrusion occurs at the surface where fluid 3 moves towards the right. The shear created causes interfacial waves to appear on both of the fluid boundaries in experiment 1 and on the upper boundary in experiments 2 and 3 (Figure 4.11).

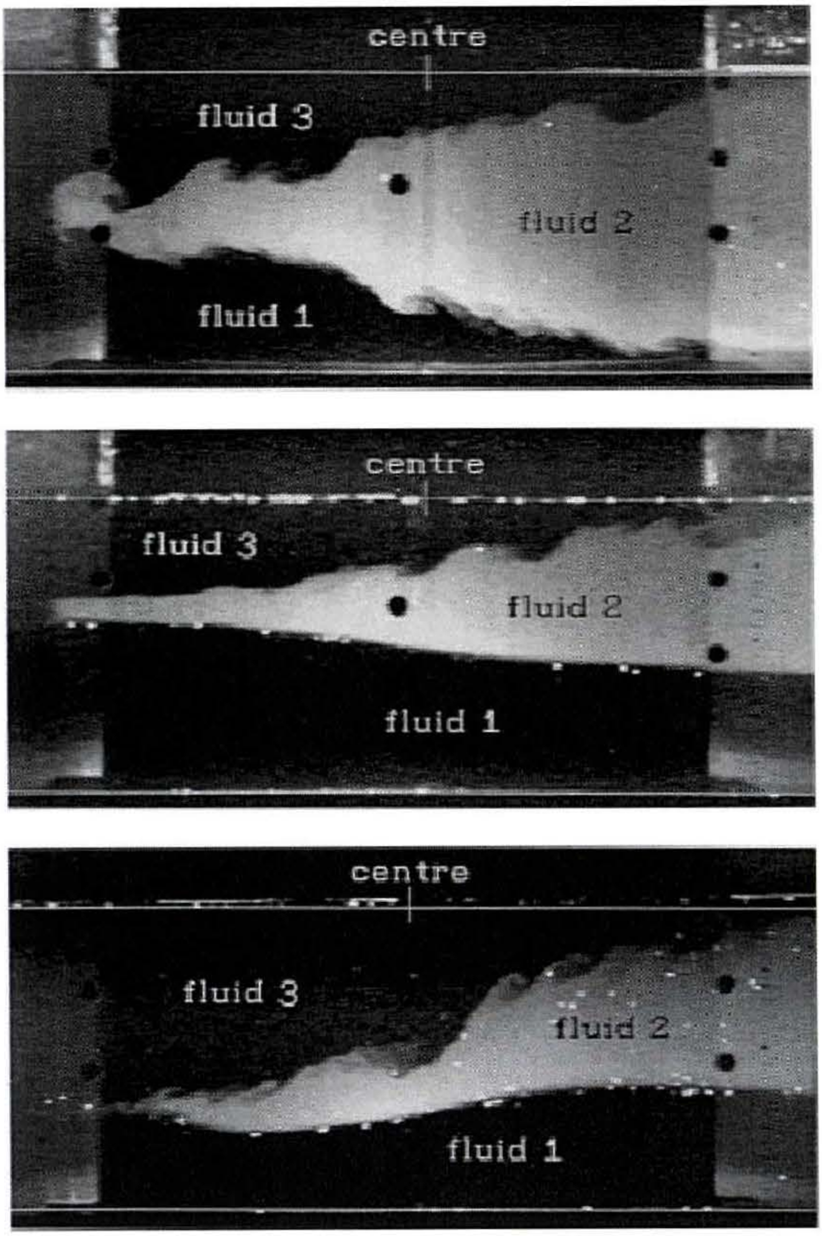

1

2

3

Figure 4.11 – The results of the Lane-Serff experiments 1, 2 and 3 (Lane-Serff et al. 2000)

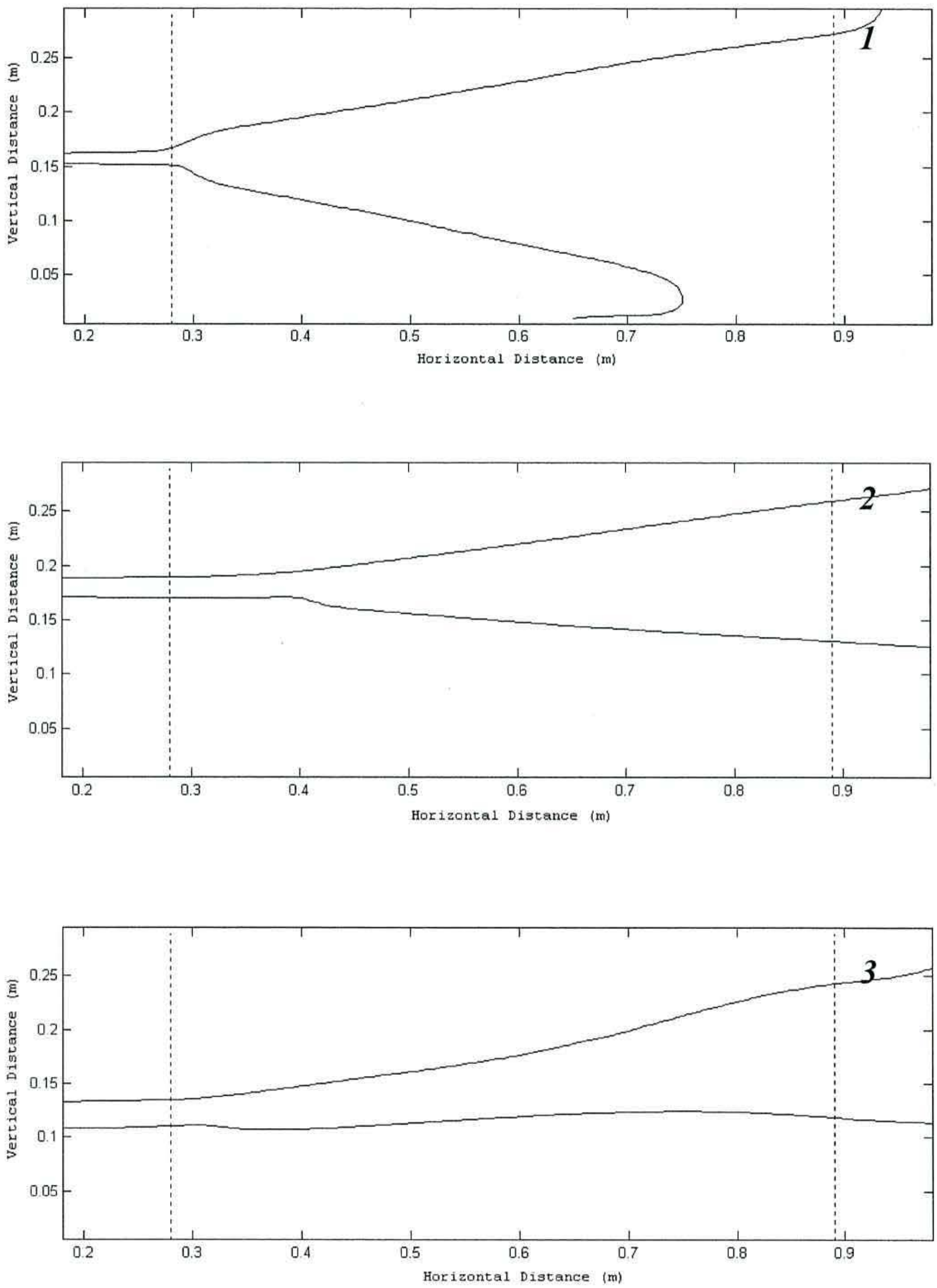

Figure 4.12 – Model interface positions for the 3 experiments

The extent of the photos in figure 4.11 is an exact match for the scale of the plots of model output in figure 4.12 so a direct comparison can be made. Only the centre section of the experimental flume is shown, there is another 0.18m at either end not shown. The extent of the curved contraction is visible in the photos and is shown in the plots as a vertical dashed line.

In general the interface positions match well with the experiment. However the small scale instabilities present on both interfaces in experiment 1 and on the upper interface in the other two experiments are not reproduced. Not shown is the level of diffusion of the initial sharp interface. By the end of the simulation, after 18 seconds, the interface has spread to approximately 15 mm wide. This would have the effect of spreading the velocity shear over this distance, and so locally reducing it to a level where the production of shear instabilities was not possible. This numerical diffusion is a product of the large grid resolution (5mm) necessary to run the simulation in an acceptable time. Another possible explanation for the missing shear instabilities is that the grid resolution itself may be too coarse to resolve waves of this scale. The other major deficiency in this work is the resolution of the bottom boundary layer in experiment 1. Again the coarse resolution of the grid is the likely cause.

Experiments 2 and 3 have been reproduced by the model simulation. In experiment 2 the rise of the interface to the left of the constriction, coupled with a fall to the right produces the same interface slope on the lower layer. The kink in the lower interface at 0.4m from the left of the tank is sharper in the model than in the experiment, but present in both. At the same time the less dense fluid from the left has spread across to the right. Experiment 3 shows a wave on the lower interface in both model and flume tank, similar in length to the constriction. Lane-Serff *et al* (2000) also note a '*small hydraulic jump on the lower interface to the left of the constriction.*' This is also reproduced by the model (the remnants of it are visible at $x=0.4m$); it is the remains of the step in the lower interface at startup (figure 4.10).

4.5 Loch Etive Sill

A small, high resolution model has been constructed of a section of Loch Etive in order to form a comparison with the data published in Inall *et al* (2004) and collected as a part of the Northern Seas Programme at SAMS. The grid used consisted of 333 by 69 points covering a domain of 3.33km long by 138m deep giving a horizontal resolution of $\Delta x = 10m$ and $\Delta z = 2m$. The location is shown in figure 4.13 (depth contours in fathoms). The origin of the model is at the sill to the upper basin in Loch Etive, the other open boundary is approximately 1km southwest of Glenoe Bay. The extent of the model is shown in red. The bathymetry data were taken from Admiralty chart 2814[B], a survey undertaken in 1861; the area around the sill has been taken from more recent surveys. The channel widths used for the model domain are shown in figure 4.14.

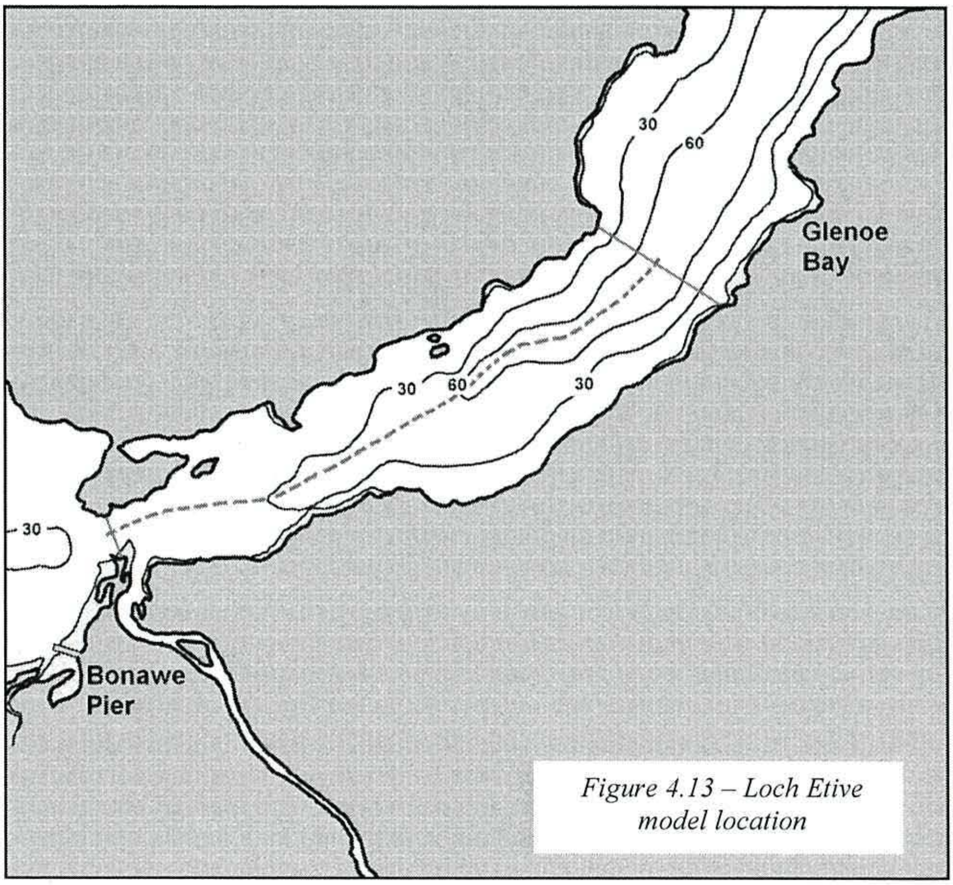

Figure 4.13 – Loch Etive model location

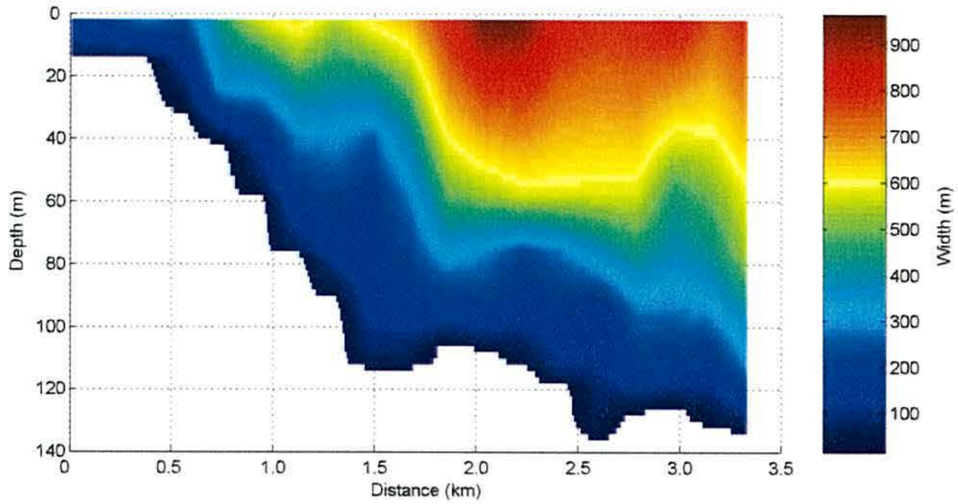

Figure 4.14 – Loch Etive model widths

Forcing

Open boundary velocity has been taken from Inall *et al.* (2004), where a bed mounted ADCP recorded velocity profiles at the sill. These have been depth averaged and give a maximum cross-sill jet speed at the sill of 1.3 ms^{-1}. A sine wave has been used as the forcing with this amplitude and a period of the M2 tide.

The stratification data was not available so a constant salinity gradient was assumed. It was found by trial and error that provided the gradient remained in the range $0.01 \leq \partial S / \partial z \leq 0.0589$ the simulation was little influenced. The upper limit is coincident with the buoyancy frequency quoted in Inall *et al.* (2004) as the stratification above sill level. Toward the upper end of this stratification range the size of the areas of flow separation were reduced.

The observations ran over a tidal cycle, however the transect presented (figure 4.15) illustrates the situation. Maximum flood occurred at 15:40 so this is ½ hr before. The flow detachment was at 35m depth, the wavelength of the leewaves was estimated to be of the order of 100m and their maximum amplitude was 15m (Inall *et al.* 2004). The model streamline output is shown in figure4.16 for the same time (LW slack + 2hrs 35mins).

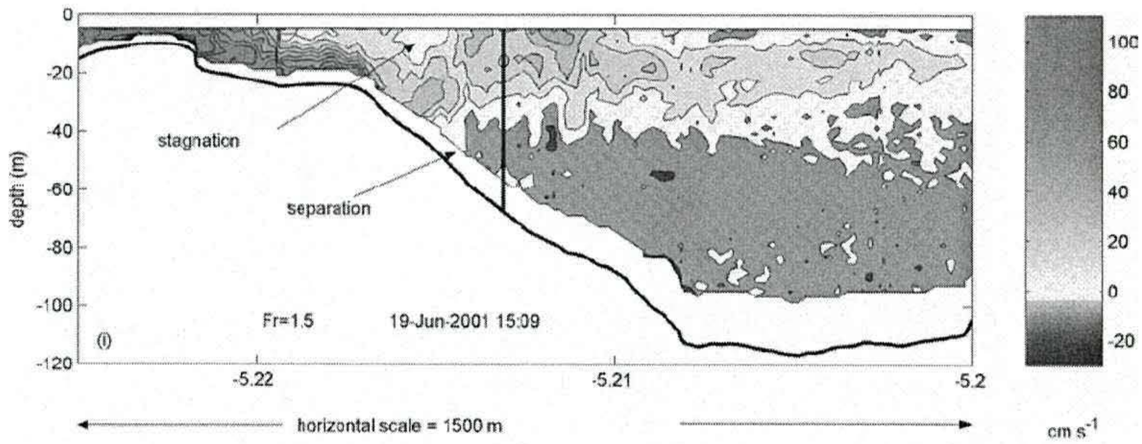

Figure 4.15 – ADCP data in the lee of the Loch Etive sill (Inall, et al. 2004)

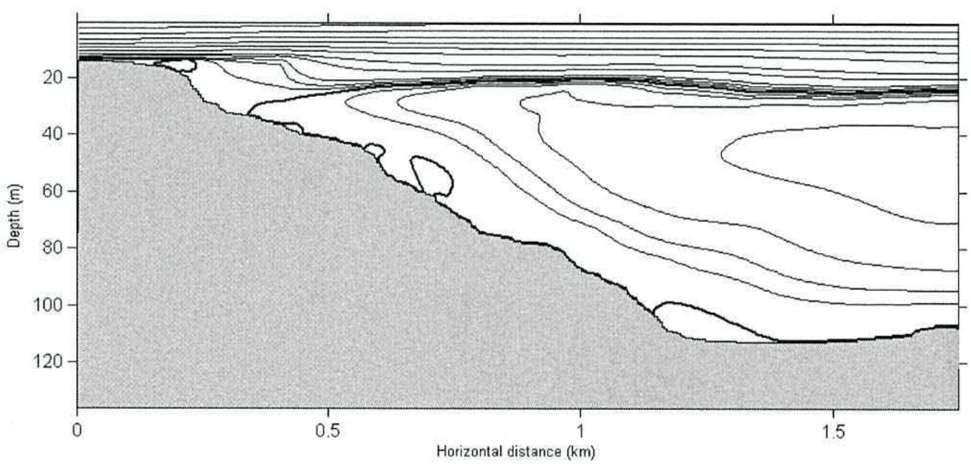

Figure 4.16 – Model streamlines in the lee of the Loch Etive sill

It can be seen from a comparison of figures 4.15 and 4.16 that the modelled point of separation is slightly shallower than the data at approximately 30m. The lee waves observed downstream of the separation are not reproduced by the model. The bold streamline represents the point of separation so it is of interest to note that towards the bottom right corner of the figure there is a flow separation of the reverse flow from the unseen shoal to the right of the data. This is suggested in the ADCP data as areas of light near to the bottom blanking zone of the data.

The underestimate of the depth of the flow separation point may in part be due to the omission from the model output of the stagnant patch. This process has been described for the flow over Knight Inlet by Farmer and Armi (1999). A wedge of stagnant water is produced by entrainment of water from the lower layer. The effect of this stagnant patch is to confine the flow toward the seabed and to push the separation point down the lee of the sill (Lamb 2004). Here the lack of a stagnant patch may be contributing to the separation point being too shallow.

Two theories regarding the processes leading up to the creation of the stagnant patch have been proposed, either lee wave breaking or entrainment of water from the lower layer. Both would require the reproduction of small scale shear instabilities and mixing on scales less than the grid scale of this model. Without a high order turbulence scheme the model is not capable of simulating this mixing.

The same simulation is presented in Stashchuk *et al* (In Press.), shown in figure 4.17. This model is that presented in Vlasenko *et al* (2002), and in this instance has a horizontal interval of 2½ m and a vertical grid spacing of between 0.07m and 1m in the deepest parts of the domain. The output suggests that two separate regions of flow separation are produced, whereas the simulation from the present model shows these two regions merged into one. The model output immediately prior to figure 4.16 is included (figure 4.18) covering the region of the Stashchuk *et al* (In Press.) plot. The far higher grid resolution of the comparative model is the likely cause for this discrepancy, and for the lack of lee waves in this coarser model. Both models show two distinct regions of flow separation with a hydraulic jump between.

Lamb (2004) concludes that the accurate simulation of a bottom boundary layer is a prerequisite for the accurate modelling of flow separation from the Knight Inlet sill. He uses a model with a fine vertical grid spacing of 0.5m over the sill. This, and the model forming this comparison would suggest that the simulation provided by the present model may not fully capture the subtleties of the bottom boundary layer as a quadratic friction formulation has been used.

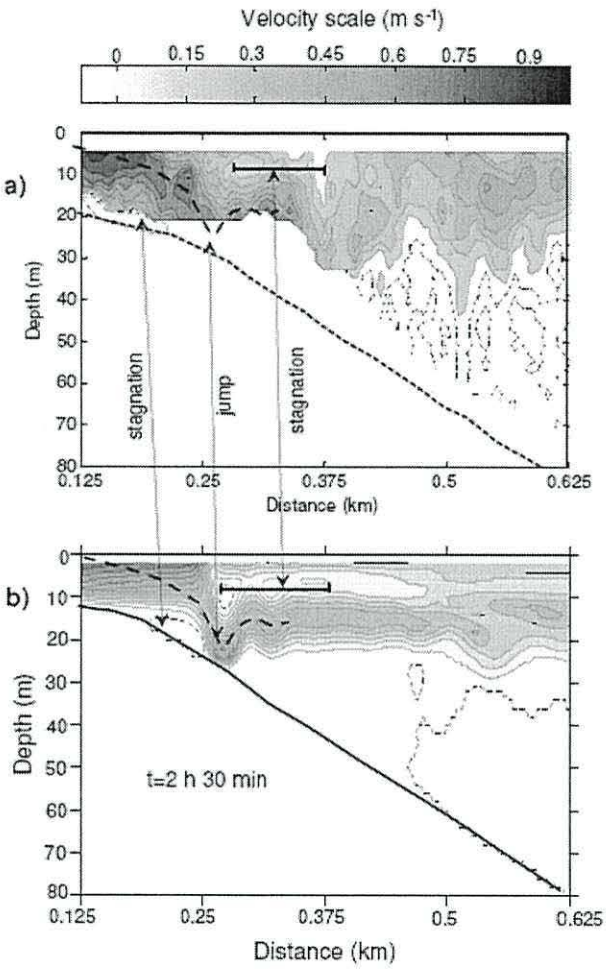

Figure 4.17 – Simulation of Etive Sill by Stashchuk et al (In Press.). a) data, b) model output

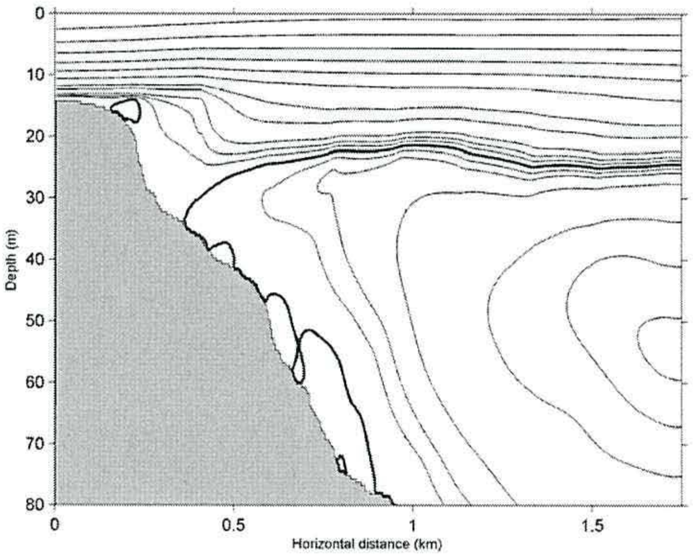

Figure 4.18 – Streamlines over the Etive sill from the current model

4.5 Summary

The model has been assessed against standard test cases. It reproduces the backwards facing step problem as well as any other numerical scheme that forms part of the comparison. It has been shown that the model conserves volume through a channel that changes widths. It also reproduces density driven flows in a rectangular tank (lock exchange) and through more complex geometry (Lane-Serff 2004).

Finally the model has been compared with observations and numerical simulation of flows over a sill in a Scottish sealoch. In view of the simplifications involved in this model the major processes are well reproduced. The model ignores any horizontal density gradients. It also has only a simple turbulence scheme and so viscosity is poorly related to the dynamics of the flow. The simulation of flow separation and areas of reverse flow is therefore proof of concept for the model.

Chapter 5 – Non Hydrostatic Model Application to Upper Loch Linnhe

This chapter describes the results from the non-hydrostatic model developed in chapter 3. The velocity forcing has been derived from the 1D model (Appendix 1) and the salinity data has been taken from measurements by Allen (1995). In this chapter the application to a horizontally uniform density structure is first presented. The model has then been used to simulate renewal situations; the results of these experiments are discussed in chapter 7.

5.1 The model domain, parameters & initial conditions

The model domain is shown in figure 5.1; this covers a region from Corran Point (56°43'.28N, 005°14'.38W) landward to include Upper Loch Linnhe and Loch Eil. The widths and depths of the channel have been taken from Admiralty chart 2380 at ½ cable intervals, and then subsequent interpolation has been undertaken to arrive at the required spatial interval.

The domain was covered with a grid of 289 horizontal points and 77 vertical points; $\Delta x = 100m$ and $\Delta z = 2m$. The horizontal grid interval required that the maximum pressure error be 10^{-9} times the mean pressure. The propagation of the tide along a channel of this length is driven by changes in sea surface slope. In this type of model the variation of pressure simulates this process so that any errors, or unresolved gradients, will introduce an error. Reducing dx means that there becomes a need to resolve ΔP between adjacent grid points to a higher level of accuracy. This introduces a new limit on the grid scale imposed by the nature of the iterative solution of the pressure field. Thus the horizontal resolution of the model could not be further reduced without incurring a disproportionate increase in computational load.

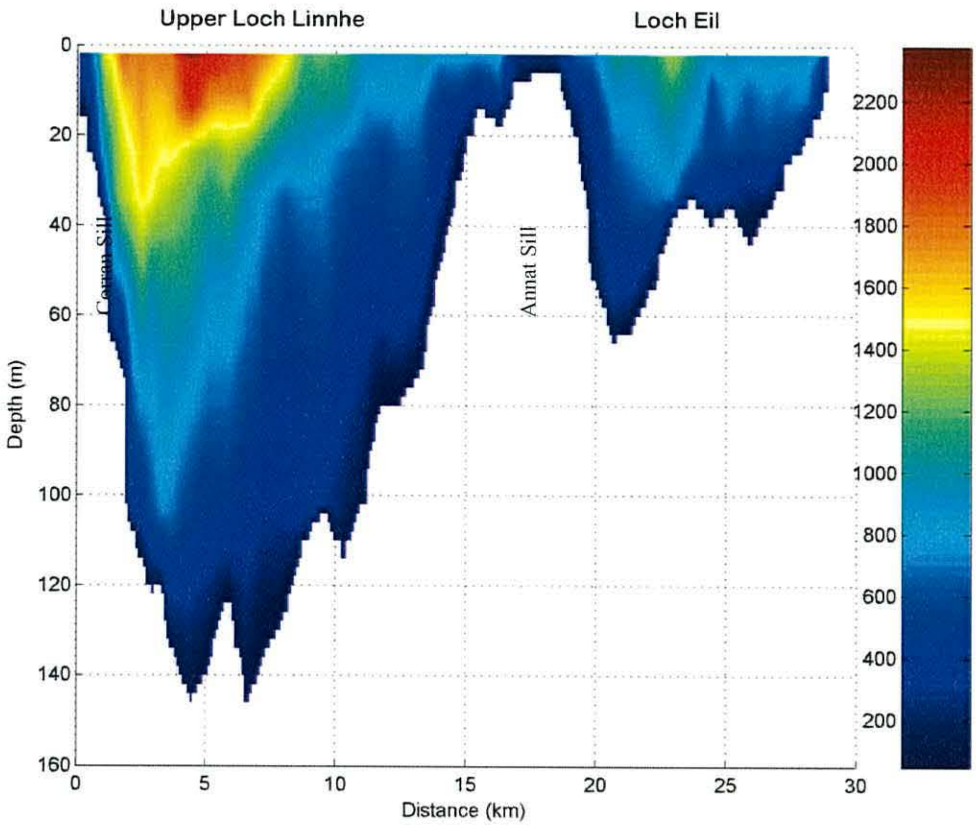

Figure 5.1 – Model Domain Section showing channel width

A modification to the topography was necessary to account for the horizontal gyre found by Allen (1995) immediately north of Corran Narrows. Here, due to the sill being offset to the axis of the loch, the flow separates from the Northern shore and forms a significant horizontal gyre. The effect of this gyre is to cause the inflowing jet to be longer than if the flow spread to the entire loch width. From the ADCP data of Allen (1995), shown in figure 5.2, the centre of this gyre was estimated to be 3.5km from Corran. The cross loch component significantly reduced 4.5km from Corran. Therefore the topography was modified as follows. The maximum width up to 3.5km from the sill was set to that at the northern end of Corran Shoal (56°43'.6N, 005° 14'.8W). Between 3.5 and 4.5km the width was increased linearly to the full width of the loch. This is referred to as the 'thinjet' topography in the rest of this work.

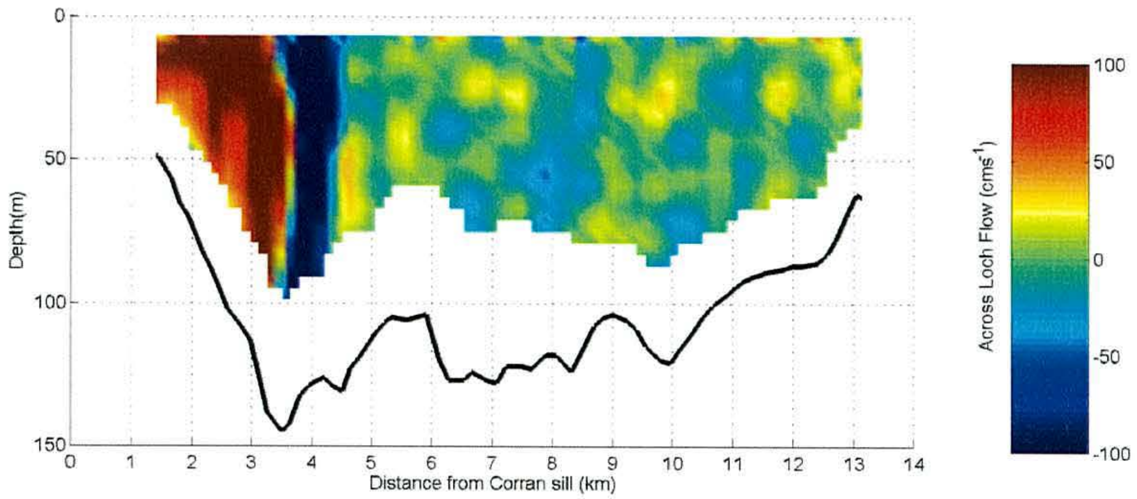

Figure 5.2 – Cross loch flow from ADCP data showing horizontal gyre

5.1.1 Optimising the SOR acceleration

As outlined in chapter 3 the optimum value for the acceleration or relaxation parameter in the SOR algorithm is grid dependent. So for each application either one of the expressions involving the Jacobi Radius needs to be evaluated or a series of numerical experiments performed to determine the optimum value.

The model grid was used in a simulation from rest for the first 30 minutes of the flood stream. The time step used was 0.5 seconds. The total number of pressure iterations was totalled and the value of the acceleration parameter was varied between 1.5 and 1.9. The results are shown in figure 5.3.

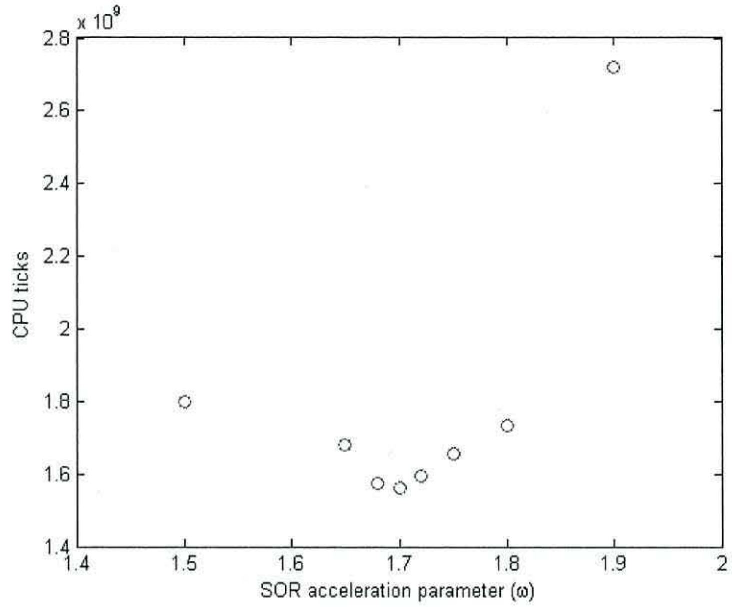

Figure 5.3 – The influence of the acceleration parameter

A figure of 1.7 is often quoted in the literature (Griebel *et al.* 1998) and has been shown to be suitable in this case. The advantage of the SOR scheme over the Gauss-Siedel iteration scheme ($\omega=1$) is approximately a five times increase in speed.

It is worth noting here that in this configuration the upper boundary condition is that pressure is zero above the surface. This enables real values for pressure to be calculated. If this boundary condition is changed for a no-gradient condition the absolute values of the pressure can vary enormously. However if only the gradient of the pressure is of interest the real values need not be calculated. Using this system of pressure the SOR cycle requires less iterations to arrive at an acceptable solution within the error bounds. This has not been implemented in this study.

5.1.2 Choice of turbulence parameters

Values of the background levels of the turbulence parameters (Eddy viscosity and diffusivity) have traditionally been used to tune numerical models to fit a particular data set. Theoretical investigations by Buitenhuis (2003) give values for vertical eddy viscosity in a large Norwegian Fjord in the range 5×10^{-3} to 2.5×10^{-2} m^2s^{-1}. Analysis of data from Puget Sound gave Cannon *et al.* (1990) values of vertical eddy diffusivity (*Az*) between 1.74×10^{-2} to 4.6×10^{-2} m^2s^{-1}. The mean value of 2.84×10^{-2} was subsequently used in theoretical arguments. Chapter 3 outlines the turbulence schemes coded for the model. In this application the turbulence parameters have been held constant for simplicity at a value of 1×10^{-2} m^2s^{-1}. This undoubtedly underestimates mixing near the sills and overestimates it in other areas.

The value of horizontal turbulence parameters applied to slice models has been previously undertaken in an arbitrary fashion, usually to maintain stability (Stacey *et al.* 1991). Values quoted there are $10m^2s^{-1}$. Values from the non-hydrostatic model of Vlasenko *et al* (2002) are between 10 and $22m^2s^{-1}$.

There is no need to control stability in this application and hence resort to excessive horizontal viscosity; however it is likely that this parameter does vary significantly between the turbulent sills and relatively calm basins of lochs. The parameterisation of Smagorinky used in Stacey *et al* (1995) and by Bourgault and Kelley (2004) has been coded for this model but is not included here.

5.1.3 Choice of time step

The maximum horizontal velocity in the model domain is 2.4 ms^{-1} located in the Annat Narrows at maximum flood; the maximum vertical velocity is 0.105 ms^{-1}, a downwelling against the slope of the Annat sill. Given the model resolution of 100m in the horizontal and 2m in the vertical these velocities can be used to estimate minimum timesteps from equation 5.1, the Courant-Friedrichs-Lewy (CFL) condition.

$$|u|\Delta t \leq \Delta x \qquad [5.1]$$

Assuming equality, i.e. a CFL number of unity, the limiting timestep for horizontal and vertical motions is 41.6 and 19.0 seconds respectively. However, the stability of the vertical diffusion equation must also be satisfied. The simple explicit diffusion scheme used in this model dictates that:

$$\Delta \leq \frac{1}{2 \quad (\Delta \ )^{2}} \qquad [5.2]$$

Given a typical value for $A_v = 0.01\ m^2s^{-1}$ this limiting timestep would be of the order of 1¼ seconds. It is therefore this criterion that limits the timestep, and also the vertical resolution of the model.

In order to relax this constraint an implicit treatment of vertical diffusion would speed up the computation. The semi-implicit Duffort-Frankel method is the most obvious; however this would require centred time differences rather than the forward time discretisation used currently.

5.1.4 Stratification

Initial conditions for the model run corresponding to the SeaRover and ADCP data collection were taken from the SeaRover data itself. Allen and Simpson (2002) give the salinity section at LW +¼ hours. This data describes the situation in the centre section of the basin down to 70m depth. There is a region 1.3 NM long near to the sill where there is no information, along with a further 3 NM at the northern end of the model. Both the northern and southern sections of missing data were filled by assuming there to be no horizontal salinity gradient. In the case of the southern section data does exist; the salinity given by the seabed mounted CTD at the Narrows was 31.955 at low water. This corresponds well with the surface layer salinity of 32 so it is a good approximation to assume no horizontal gradient, at least in the surface layer at slack water. The SeaRover salinity data was then interpolated onto a grid matching the model scalar points.

During the flood stream the salinity measured at the seabed mounted conductivity sensor on the sill increased, suggesting a seaward horizontal salinity gradient. This variation of salinity has been simulated using the harmonics derived from timeseries of sill salinity (section 2.3.2).

Density profiles presented in Allen and Simpson (1998b) have been averaged over periods of approximately 30 days. These are based on long term measurements at 5 depths at two mooring sites (LL04 and LL14 sites shown in chapter 2). These are complemented by CTD casts and show good agreement. Therefore this profile has been used across the entire model domain. Little data exists north of the LL14 mooring in the centre of Upper Loch Linnhe, and none has been found for Loch Eil. The assumption that stratification does not change landward cannot be assessed without further fieldwork.

The profile for Period 5 (days 109 to 145 of 1993) is shown if figure 5.4, taken from Allen and Simpson (1998b). With the assumption of a constant temperature of 10°C this has been converted to a salinity profile.

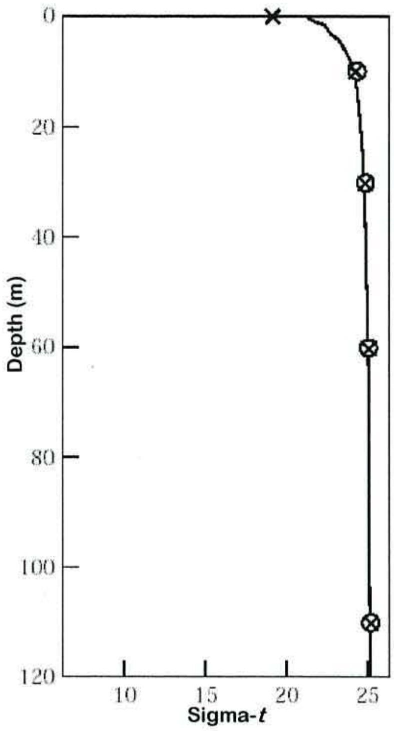

Figure 5.4 – Density profile for period 5, LL04 (O) and LL14 (×), CTD profiles (line) (Allen and Simpson 1998b)

The conversion from density to salinity is the reverse of the linear approximation to the equation of state (chapter 3). If density can be expressed as a linear relationship with salinity (equation 5.3) then equation 5.4 represents the reverse. Coefficients of ρ_0 = 1024 kgm^{-3}, S_0=34.05 and a=7.6×10^{-4} have been used which is a good approximation at 10°C (see figure 5.5).

$$\rho = \rho_0 + a(S - S_0) \qquad [5.3]$$

$$S = S_0 + \frac{(\rho - \rho_0)}{a} \qquad [5.4]$$

This creates a field of 'effective' salinity that yields the original density pattern created by both temperature and salinity variations. The approach has been used previously by Lavelle e*t al.* (1991) amongst others, and should introduce little error location where the cross sectional area changes rapidly, there will undoubtedly be anomalies between the cross sections and hence velocities.

To overcome this possibility, and to include the effects of the free surface changing the channel cross section over the tidal cycle, the volume flux from the 1D model was used instead of the raw velocity output. The volume flux was outputted from the 1D model (at point 40 in the Loch Linnhe branch) corresponding to Corran Narrows. This flow was then divided by the cross sectional area of the non-hydrostatic model at this point to obtain velocity time series for forcing.

During the initial 5 minutes of simulation a 'soft forcing approach' was taken. Over the entire model run a radiation condition was applied to the boundary velocities to allow short period waves to escape. The velocity profile was assumed to follow that described by the work of Prandle (1985) (chapter 3).

5.2.2 Salinity

This follows the assumption that the water column is fully mixed over the sill. The boundary value has been taken from the modified current meter installed on the bed of the sill in 5m of water. Clearly the river Lochy influences the density by continuous addition of fresh water immediately south of the Annat sill. The mean tidal flux at the point where the River Lochy joins Upper Loch Linnhe is approximately 2×10^3 m^3s^{-1}. From Chapter 2 the mean river flow during period 5 is approximately 10% of the tidal flux. This would suggest a reduction of salinity by the same amount at this location. There are many other sources of fresh water over the model domain. With no salinity data from the Northern end of the loch, the influence of fresh water cannot be assessed. This is perhaps the single largest source of discrepancy and the dynamics associated with this residual flow and any horizontal density gradients cannot be assessed without further fieldwork.

5.3 Model runs

Firstly the model has been applied to the situation of no horizontal variation of the density field. This simulation uses the tidal forcing present on day 113 and has been undertaken with this model, and in chapter 6 with the hydrostatic model. The comparison of these two simulations can be found in chapter 7.

Subsequently the non-hydrostatic model has been applied to conditions of renewal. Three model runs were undertaken, all using the initial conditions of the Searover density slice (Allen and Simpson 2002) at LW +¼ hour. Firstly this initial state was forced without introducing any new horizontal density variation. The inflowing water was given the same density profile as exists in the model. The other two simulations used increasing density at the inflow. The first had an equilibrium depth of 40m, and the second was slightly denser than the densest water found in the basin. The results from this group of simulations are compared with the data in chapter 7.

5.4 Results

The results of the model simulation using a horizontally uniform density field are presented here. The flow field is visualised every hour over the 13 hours of the tidal cycle starting at LW slack and continuing for a further 12 hours until approximately ½ hour before the next LW slack.

5.4.1 Flow Field

The figures on the following pages show current vectors describing the flow field every hour. The horizontal axis measures distance from the Corran sill (at $x=0$) to the Annat sill ($x=16km$) at the North Eastern end of the Upper Loch Linnhe basin. The vertical velocity component has been scaled by a factor of approximately 10^2 to maintain the aspect ratio of the plots. Therefore the large vertical velocities should be placed in the context that they appear roughly 100 times larger than the horizontal.

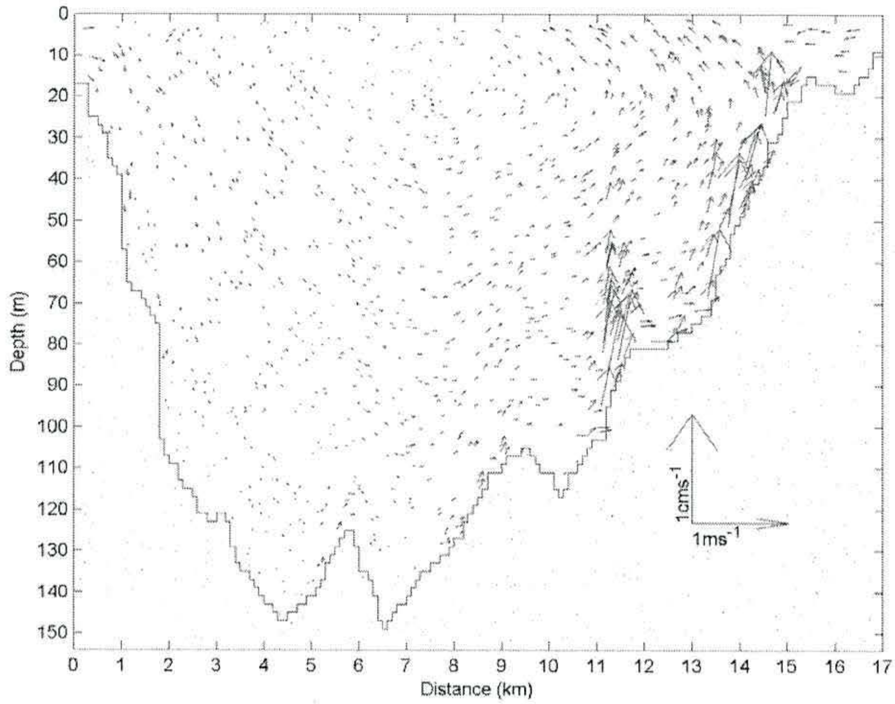

Figure 5.6a – Current field at LW slack

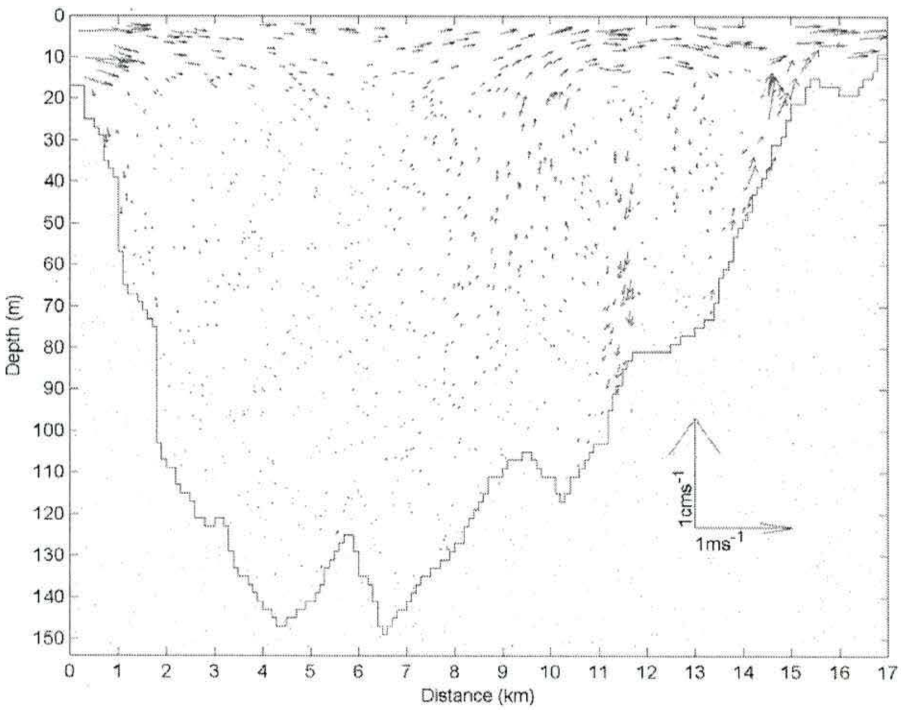

Figure 5.6b – Current field at LW slack +1 hour

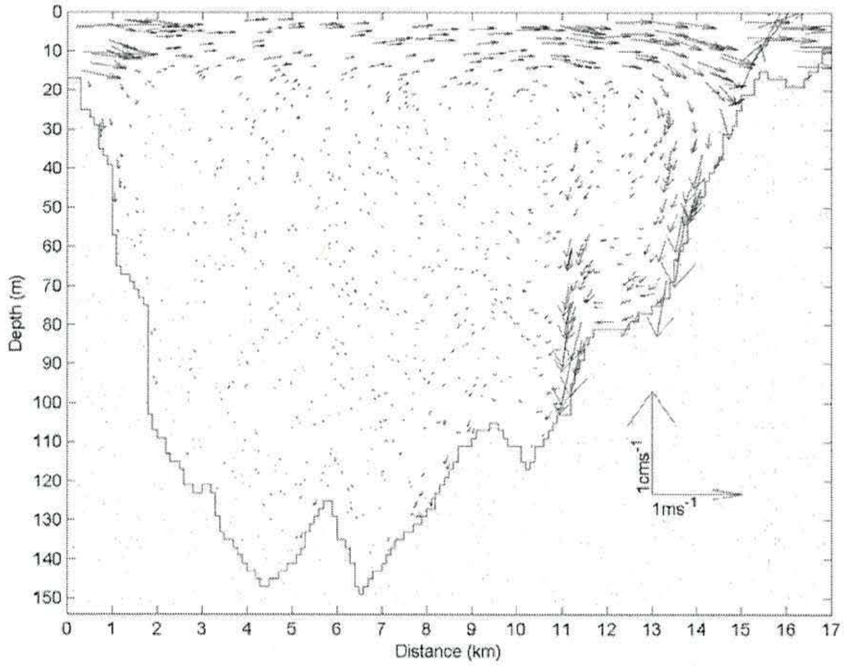

Figure 5.6c – Current field at LW slack +2 hours

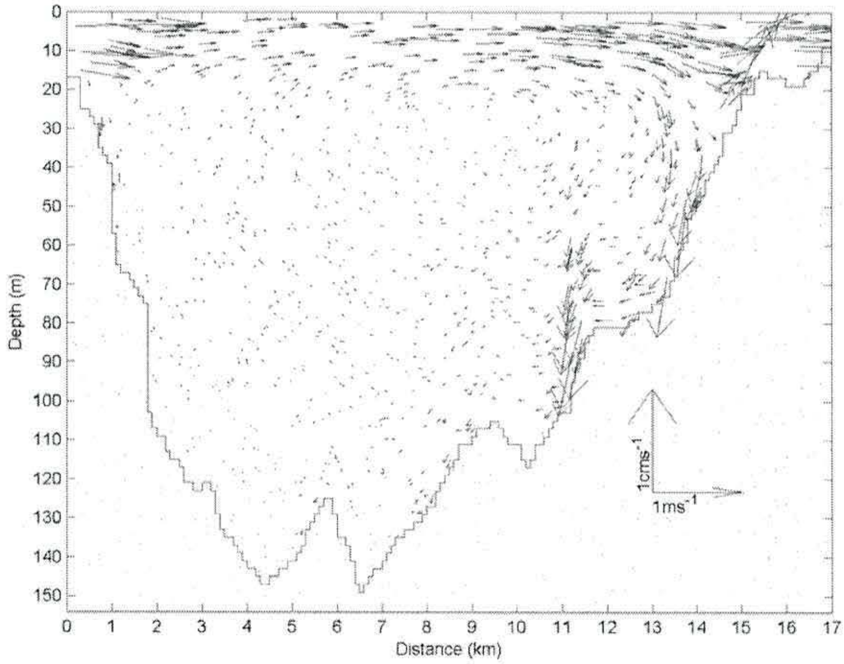

Figure 5.6d – Current field at LW slack +3 hours

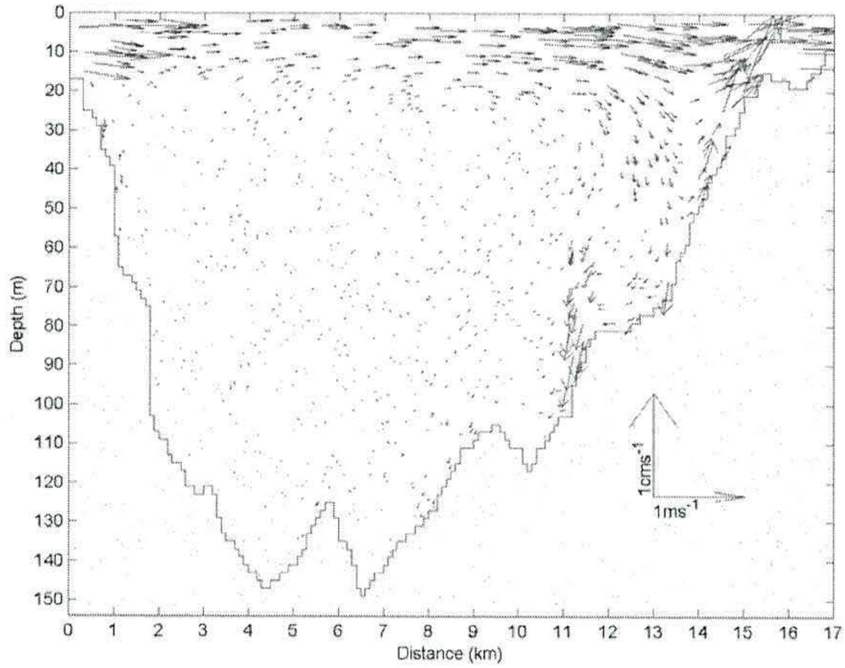

Figure 5.6e – Current field at LW slack +4hours

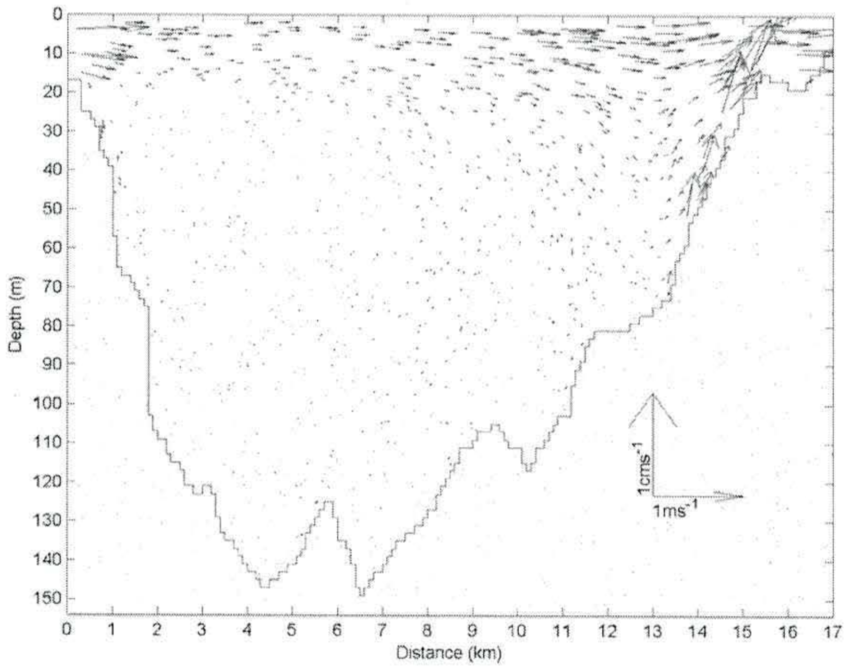

Figure 5.6f – Current field at LW slack +5 hours

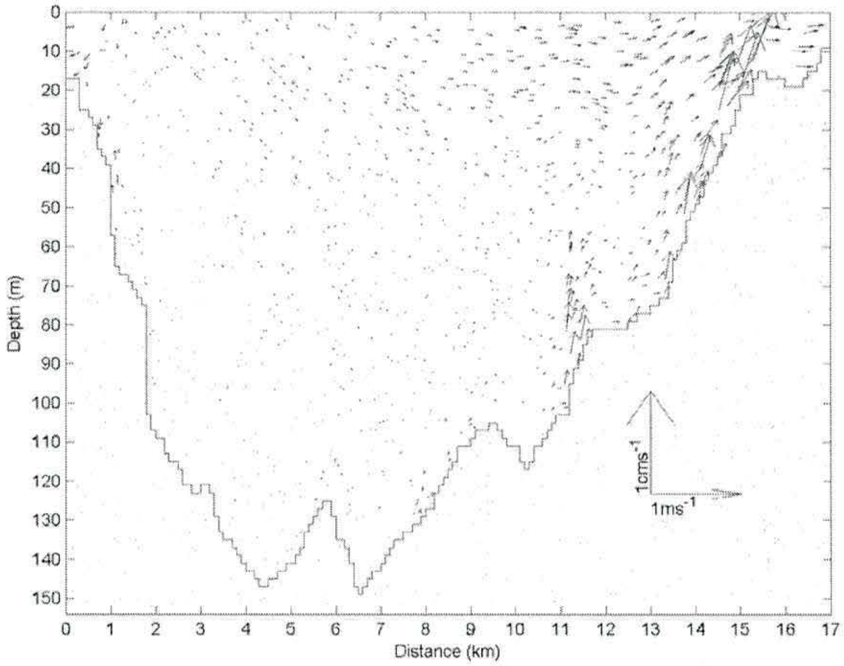

Figure 5.6g – Current field at LW slack +6 hours

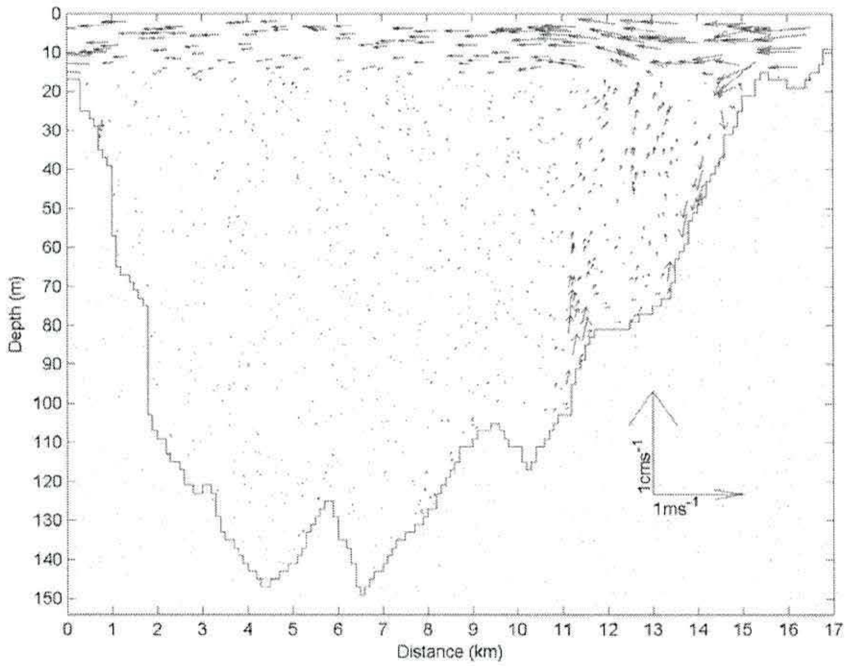

Figure 5.6h – Current field at LW slack +7 hours

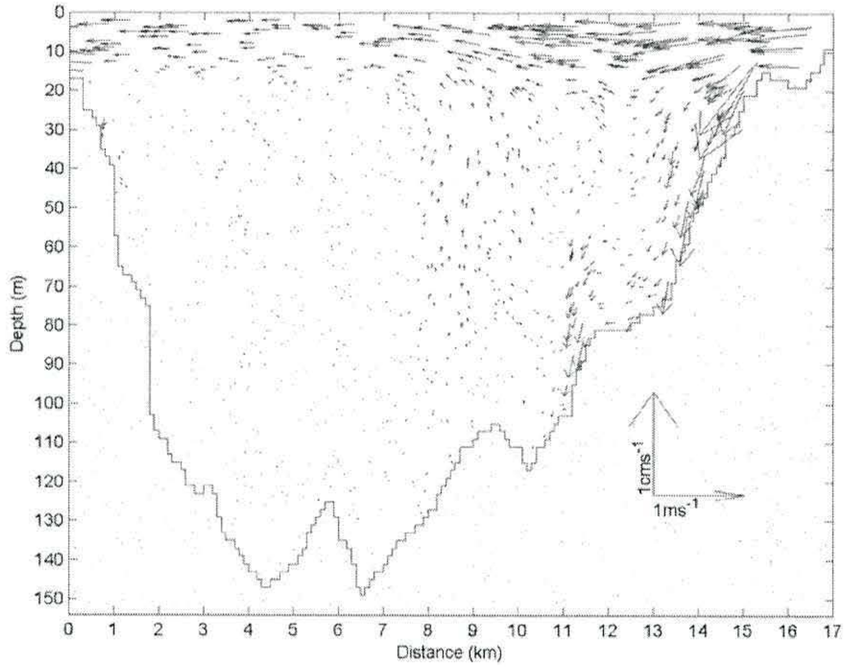

Figure 5.6i – Current field at LW slack +8 hours

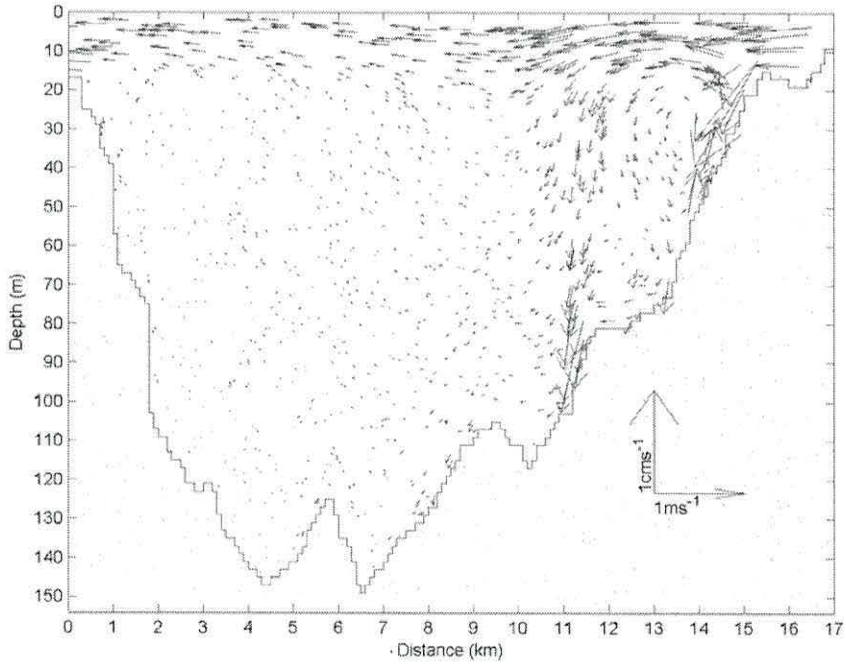

Figure 5.6j – Current field at LW slack +9 hours

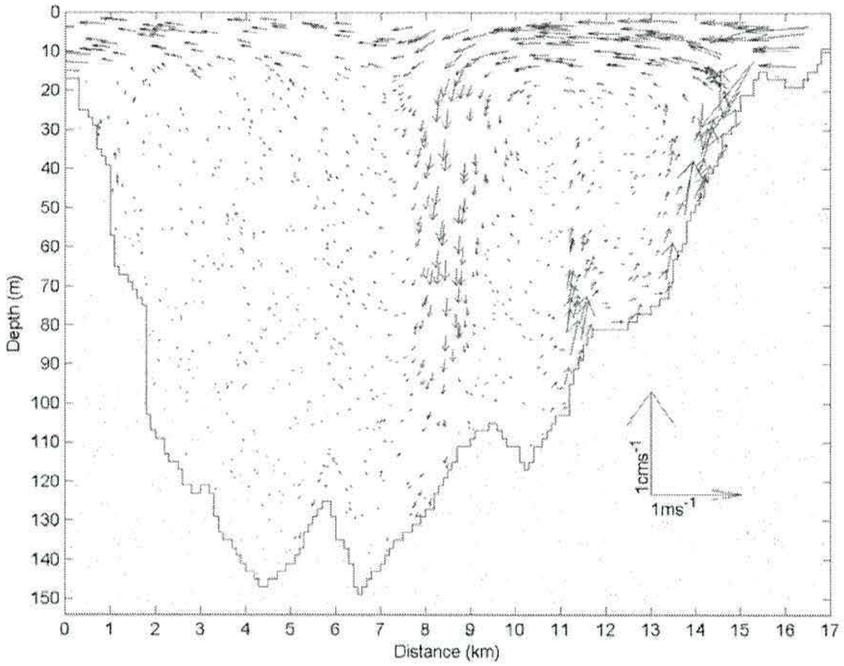

Figure 5.6k – Current field at LW slack +10 hours

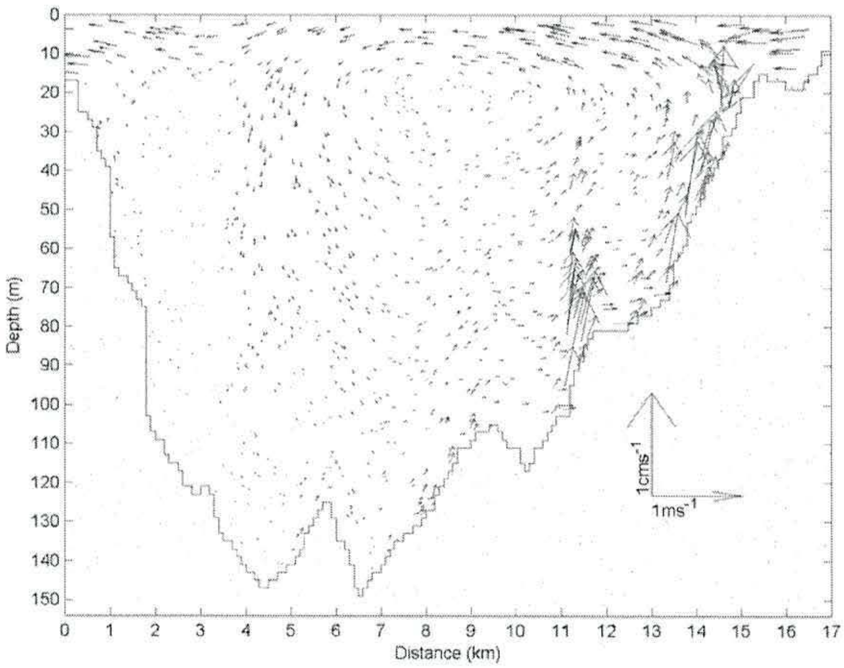

Figure 5.6l – Current field at LW slack +11 hours

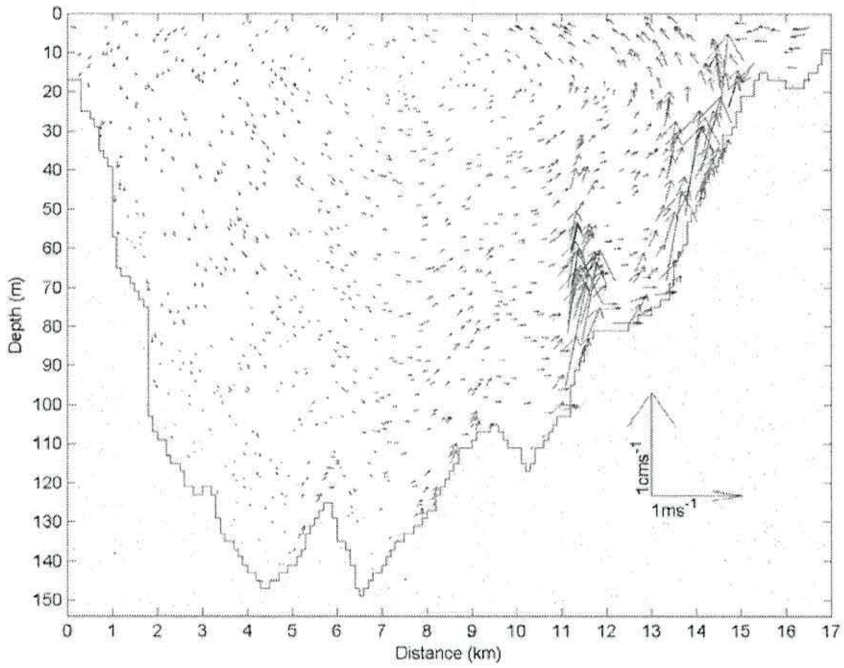

Figure 5.6m – Current field at LW slack +12 hours

The sequence of flow shown in figures 5.6*a* to 5.6*m* show that 1 hour after the commencement of the flood stream the flow has detached itself from the topography and formed an area of re-circulation 4km long in the lee of the Corran sill. Two hours after LW slack this re-circulation encompasses the entire basin, causing a strong downwelling against the slope of the Annat sill. The flood stream then begins to reduce in speed and causes the re-circulation to reduce in extent, so by LW slack +4 hours the downwelling at the Annat sill has turned to an upwelling. At LW slack +6 hours, shortly before the start of the ebb stream, 2 distinct waves, characterised by vertical eddies, are visible at the Annat end of the basin.

The ebb stream has started in figure 5.6*h*, LW slack +7 hours. However at this time the stream is still flooding out of the basin at the Annat end. The waves upstream of the Annat sill have grown in amplitude. Another hour into the ebb stream shows the ebb flowing strongly over the Annat sill. At the surface and at the bed there are strong streams, separated by a region of weaker flow at mid-depth. At LW slack +10 hours a region of flow separation and reverse flow appears; subsequently this expands to fill the basin by LW slack +12 hours.

5.4.2 Flows at mooring sites

Time series of the currents extracted at the two mooring sites are presented below in figures 5.7 and 5.8. The mooring closer to the sill (LL04) shows a jet above sill level on both phases of the tide. This flows above a relatively stagnant lower layer.

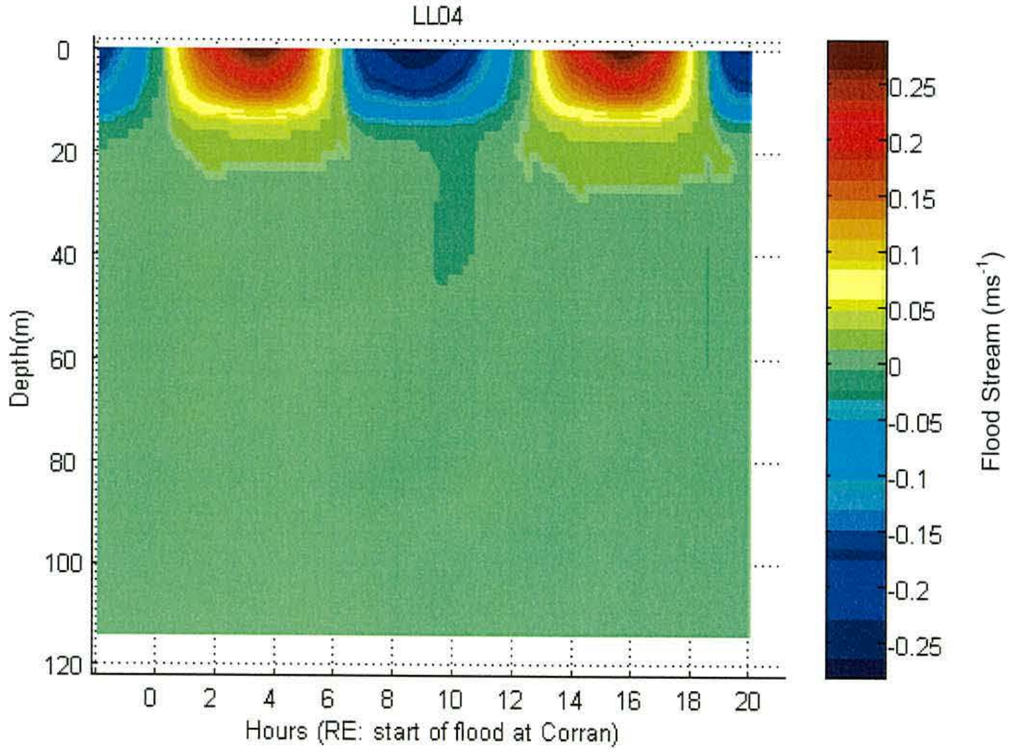

Figure 5.7 – Current time series at LL04 mooring site

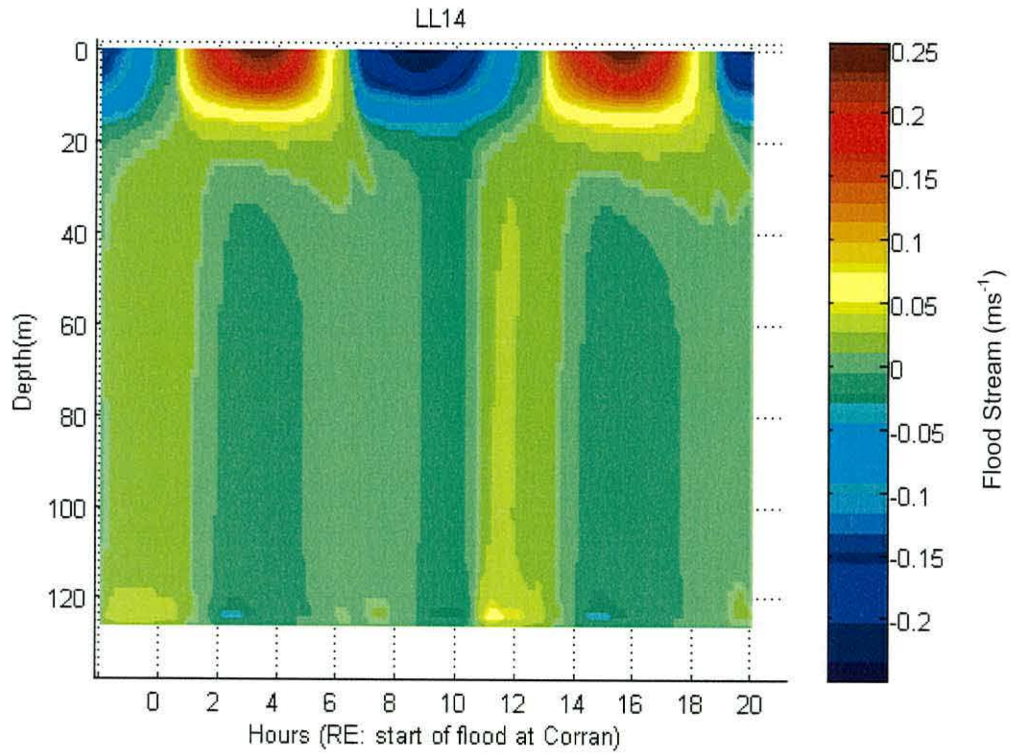

Figure 5.8 – Current timeseries at the LL14 mooring site

The modelled timeseries for the LL14 site in the centre of the basin shows a jet in the upper 15m of the water column, similar to that at the near-sill mooring site. In the lower part of the water column there is evidence of a weak reverse flow, stronger at 120m depth.

5.4.3 Harmonic Analysis

In order to undertake harmonic analysis of the modelled velocities the barotropic component was removed by subtracting the depth-mean velocity at each column. Harmonic analysis was undertaken using the t-tide package (Pawlowicz *et al.* 2002) and only the M2 signal has been examined. This analysis was conducted for each grid point in the model domain; in this section only the columns corresponding to the LL04 (near sill) and LL14 (mid-basin) mooring locations are shown.

The plot of the residual flow at the LL04 mooring site (figure 5.9) shows a seaward flow above the sill depth of 10m. Immediately below this there is an equal and opposite landward flowing layer down to a depth of 30m. The phase shift and the amplitudes of the flow at this location are broadly similar to those at the LL14 mooring site (figure 5.10).

Residual flows at the mid-loch mooring are at their strongest in the upper 10m, a maximum value of $5mms^{-1}$ is found at the surface. The depth of phase change coincides with a landward residual flow; however below 40m depth this is reduced to approximately zero. This landward flowing layer is far weaker than that shown in figure 5.9 for the LL04 mooring.

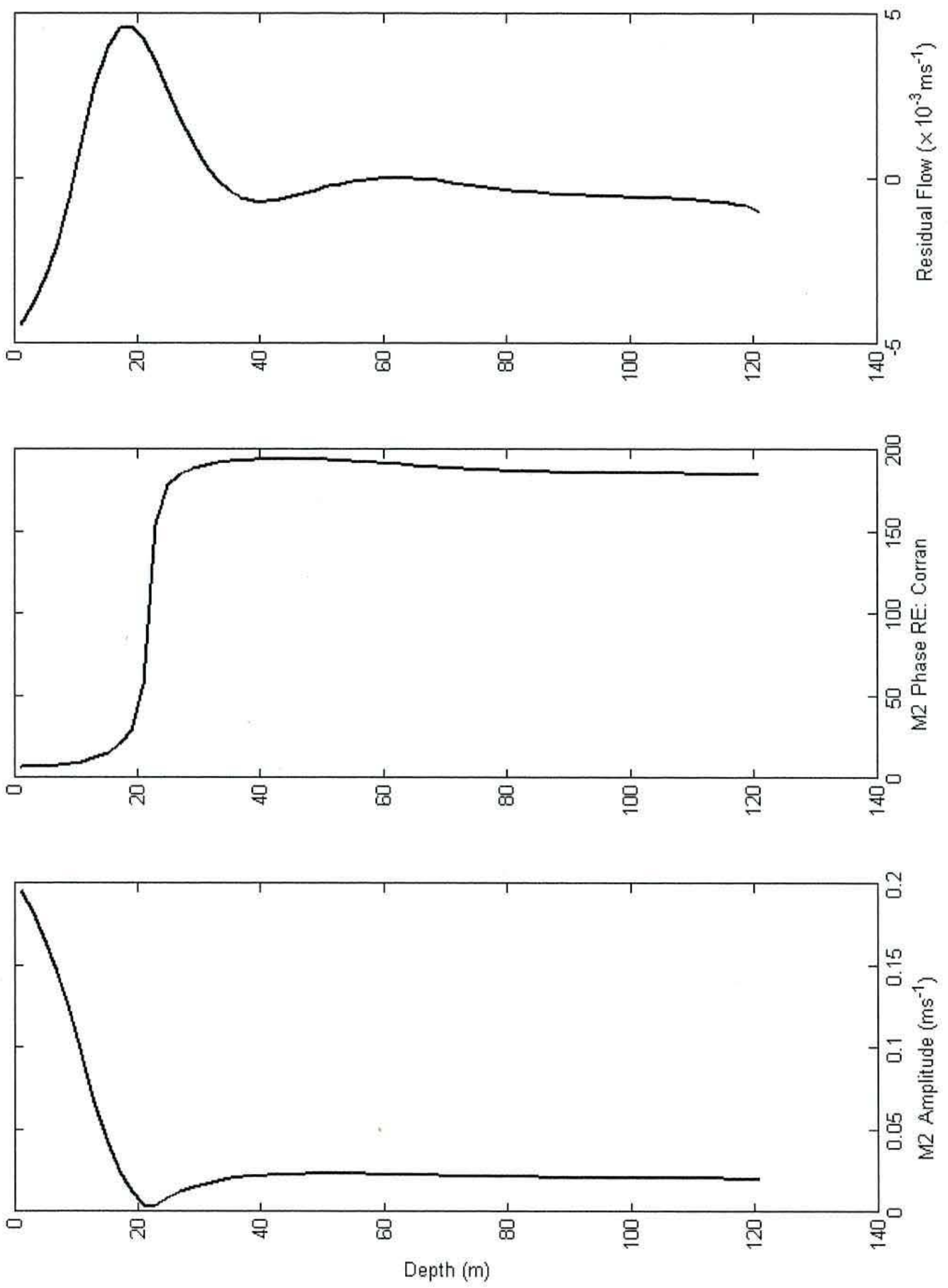

Figure 5.9 – Harmonic analysis of the LL04 profile

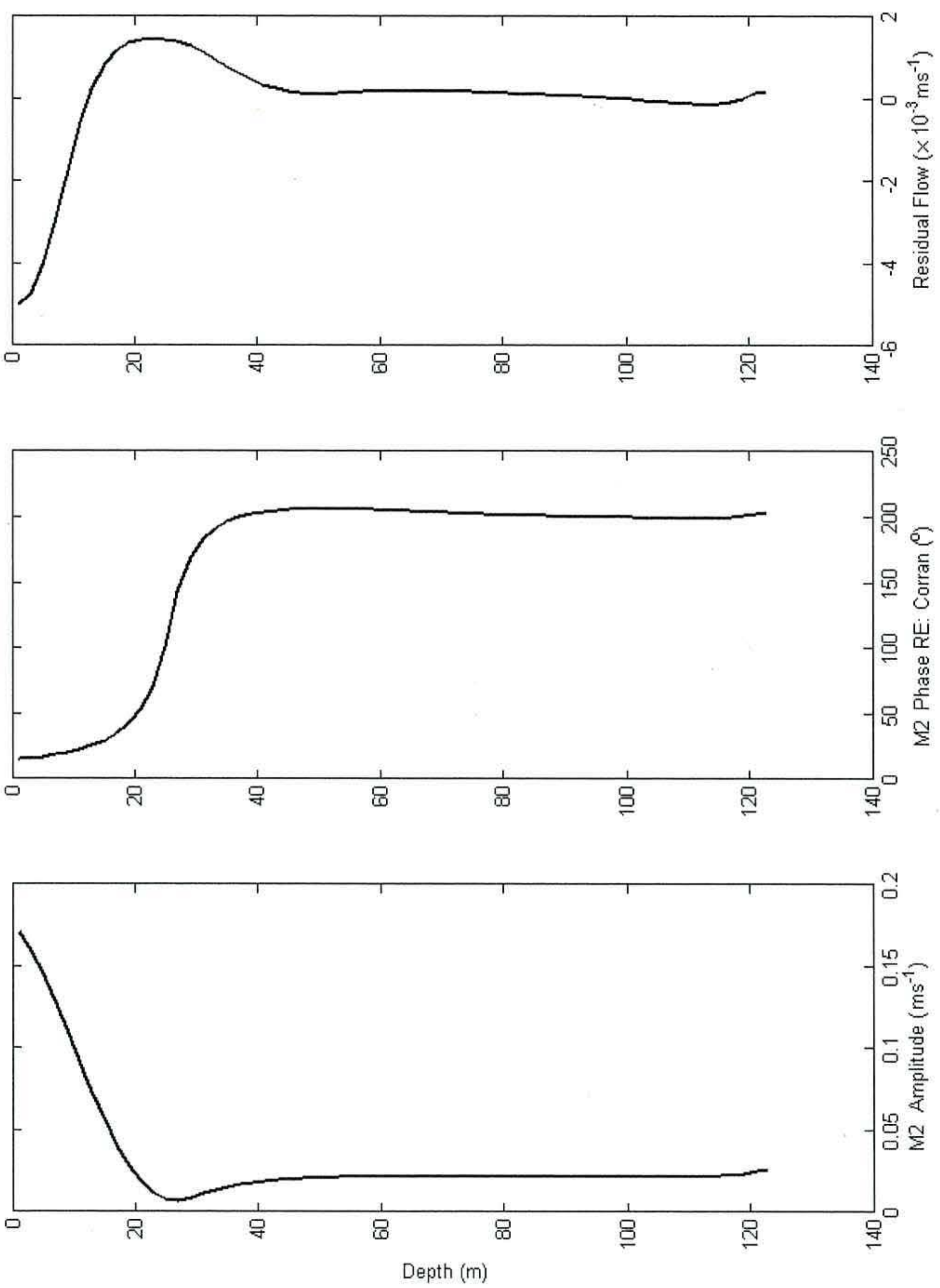

Figure 5.10 – Harmonic analysis of the LL14 profile

Figure 5.10 shows a distinct 2-layer structure to the flows at the mid-loch location. The upper 20m of the water column are lagged approximately 20° to the inflowing stream over the sill. Between 20m and 30m depth there is an abrupt change in the phase, below this point the flood stream is lagged a little over 200°. This shows two layers completely out of phase, the classic mode 1 internal tide. At the depth of phase change there is a velocity minimum with the amplitude of the M2 stream as little as $0.01ms^{-1}$. The maximum amplitude is found at the surface, a value of $0.17ms^{-1}$, values in the lower layer are typically $0.02ms^{-1}$ showing a slight increase near to the bed.

5.5 Summary of results

The harmonic analysis and the sequence of sections through the flow show the presence of a mode 1 internal tide. The surface and bottom waters flow in separate directions throughout much of the tidal cycle. There is, however, a marked asymmetry to this response. Following the start of the flood stream the reverse flow is established within one hour. At the other end of the tide, and the other end of the basin, there is a three hour delay before recirculation takes hold in the lower layer. Thus the flow in the lower layer will deviate from the purely sinusoidal.

Chapter 6 - Hydrostatic Model Application to Upper Loch Linnhe

The model used by Gillibrand (1993), outlined in the first part of chapter 3, is here applied to the study area. The modifications made in chapter 3 have been implemented in the code. In order to form a comparison both with the hydrostatic model and the data, this simulation covers day 113 of 1993. The comparable data is presented in section 2.3.4; the comparable non-hydrostatic simulation was shown in sections 5.3 and 5.4.

6.1 The Model Domain and forcing

The extent of the model domain for this hydrostatic model was necessarily greater than that used in the previous chapter for the non-hydrostatic model. This is partly due to the need to keep the open boundary distant from the Corran sill, which in trial simulations caused instabilities to grow. The landward boundary is the head of Loch Eil such that the modelled channel only has one open end. The horizontal grid spacing was 50m (finer than the non-hydrostatic model). A cross section of the model domain, including the non-uniform vertical grid spacing, is shown in figure 6.1. The positions of the two moorings LL04 and LL14 are indicated.

The use of the non-uniform vertical grid spacing is well illustrated in figure 6.1. The 47 vertical grid points vary their spacing from 1m near to the surface to 10m in the deepest parts of the loch. This allows the near surface layer to be well resolved while at the expense of the boundary layer in the deepest parts of the loch.

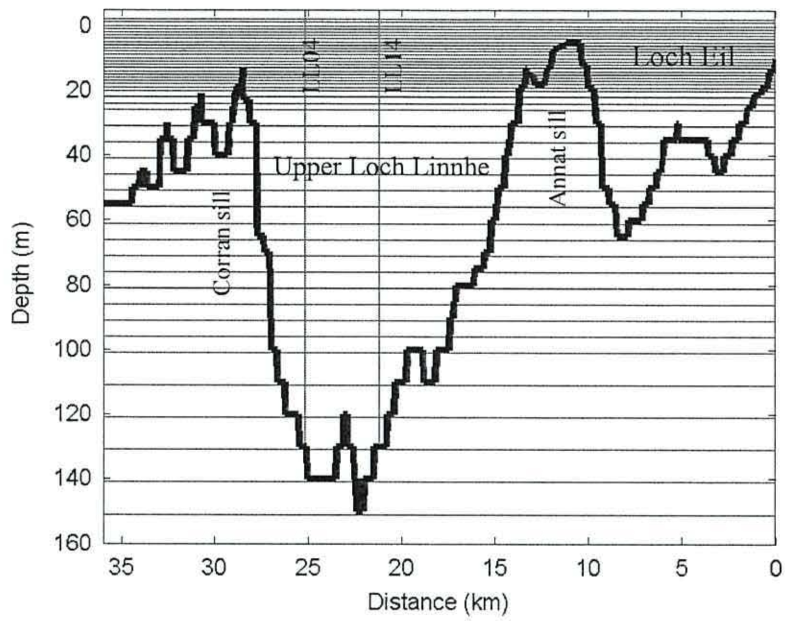

Figure 6.1 – Cross section through model domain

The modified 'thinjet' topography (section 5.1), where the widths in the lee of the Corran sill have been reduced to account for horizontal flow separation from the Northern shore was tried with this model. The model failed to run. It is assumed that the nature of the fast flowing jet could not be reproduced by the mathematics of this model.

6.1.1 Choice of Turbulence Parameters

Gillibrand (1993) chose a value of background vertical eddy viscosity of 1×10^{-3} m^2s^{-1} for his simulation of Loch Sunnart. Values derived from observations are discussed in chapter 5, but tend to be around 2.5×10^{-3} m^2s^{-1}. In order to keep this model stable higher values had to be used. By trial and error the minimum value that would allow the model to run was found to be 2×10^{-3} m^2s^1.

The value for horizontal eddy viscosity has been chosen to prevent the model becoming unstable rather than from any observations or theoretical work. The model of Gillibrand (1993) multiplies this parameter by a factor of 10^5 in the program code which means that in this model run a value of 2×10^4 m^{2}s^{-1} is used. Using values less than this causes the model run to be interrupted by the formation of absurdly strong currents around the both sills. The value quoted in Gillibrand (1993) for the Loch Sunnart simulation was 10^4 m^{2}s^{-1}, chosen to maintain stability rather than from observational evidence.

6.1.2 Stratification

The salinity profile for the entire model domain has been assumed to follow that shown in Allen and Simpson (1998b) for period 5. The process of creating this 'effective' salinity profile assuming that the temperature uniform was outlined in chapter 5.

6.1.3 Open Boundary Forcing

This model uses the sea surface elevation at the open boundary as the driving force, in contrast to the model outlined in the previous chapter where the boundary velocity is specified.

In order to simulate the rise and fall of the tide at the open boundary the output of the 1D model has undergone harmonic analysis using the t-tide package (Pawlowicz *et al.* 2002). The harmonic constants obtained from this are shown in table 6.1. The same 5 harmonic frequencies have been used that were used in the 1D model forcing from original measurements and harmonic analysis of Allen (1995).

Table 6.1 – Tidal harmonics used to force the open boundary

Harmonic	Amplitude (m)	Phase lag RE: equilibrium tide (^{o})
M_2	1.1884	168.57
S_2	0.5030	205.90
N_2	0.2408	149.11
MM	0.1682	222.70
MSF	0.1116	299.52

A comparison of the data collected by Allen (1995) and these harmonic constants show they are remarkably similar. The location of this site is approximately 4.4km landward of the tide gauge deployment. The phase lag for the M_2 tidal elevation is ½ degree, or approximately 1 minute. The amplitudes of the harmonic constants derived from this point are slightly larger than those used to force the 1D model with. The M_2 amplitude is 8mm larger, (± 1mm) so significant in the harmonic analysis but insignificant in terms of tidal forcing.

The method of deriving an 'effective' salinity profile from a published density profile has been outlined previously in chapter 5. The sigma co-ordinate open boundary profile spacing was 1m with the surface elevation at mean sea level, covering the open boundary depth of 58m. The period 5 profile was applied at this open boundary such that no horizontal salinity gradients existed.

6.2 Model Results

The inflowing salinity was set as equal to the profile used across the model domain (period 5 stratification). The tidal forcing was taken from day 113 in 1993, a spring tide with a range of 3m.

6.2.1 Flow Field

The flow field over a complete tidal cycle is shown in figures 6.2a to 6.2m at hourly intervals. The flow vectors are plotted at random intervals rather than on the model grid, which due to its variable nature is not suited to visualisation.

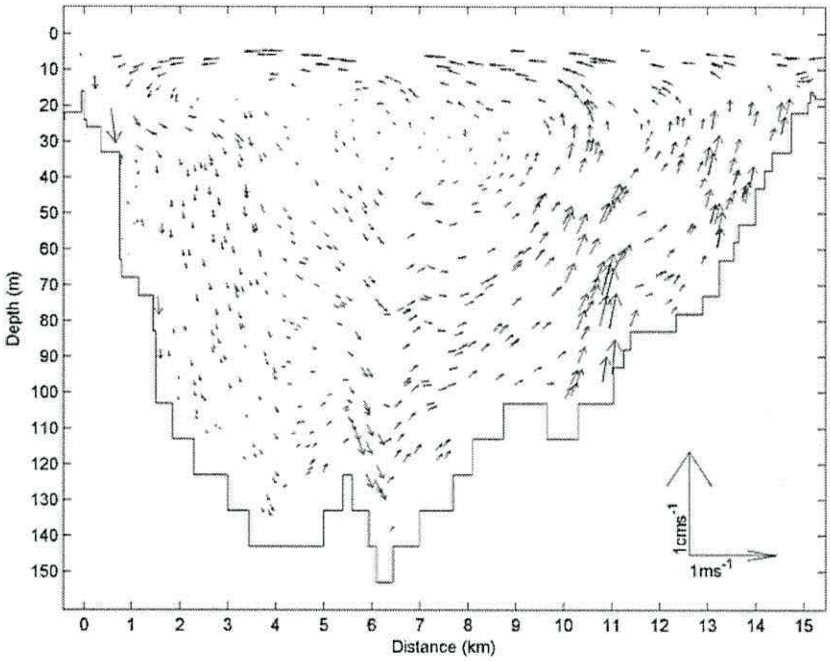

Figure 6.2a – Current field at LW slack

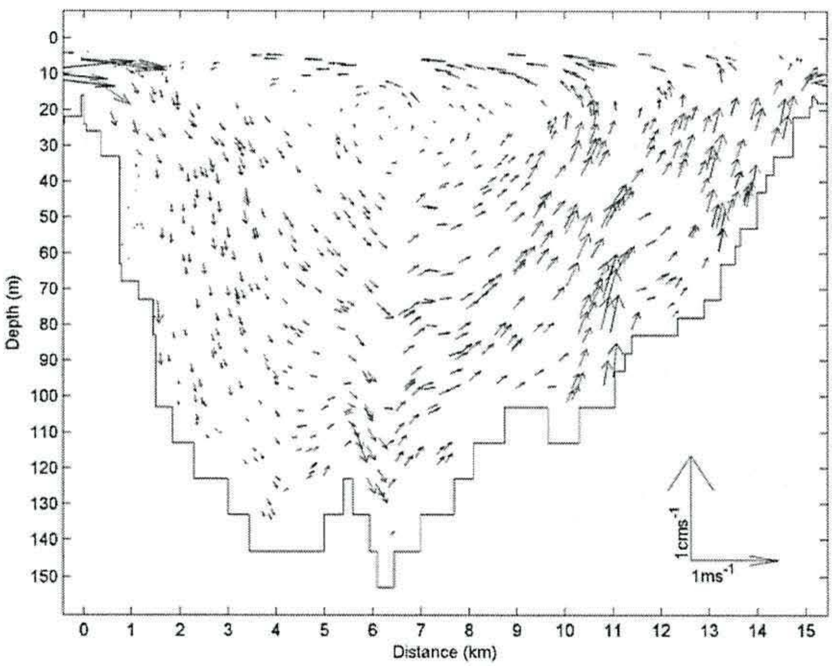

Figure 6.2b – Current field at LW slack +1hour

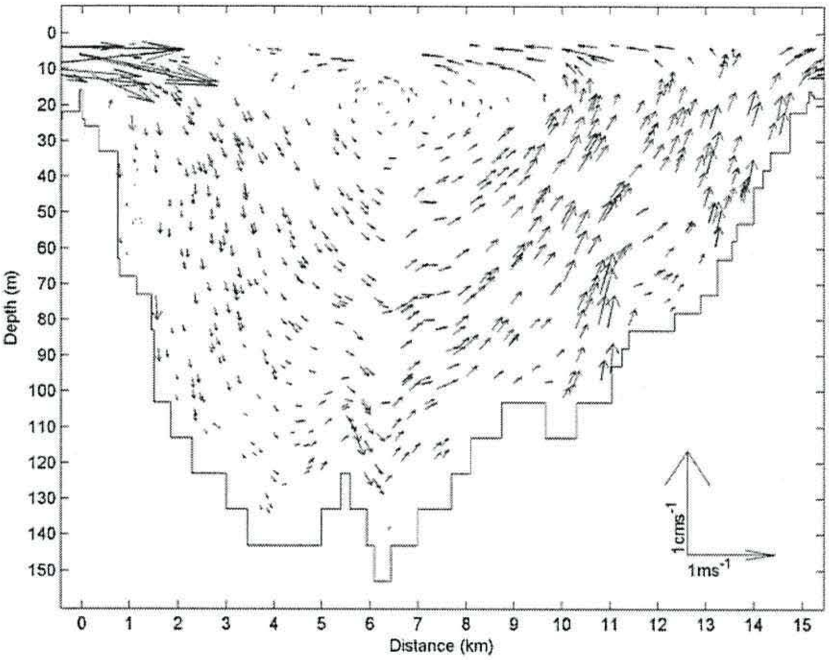

Figure 6.2c – Current field at LW slack + 2 hours

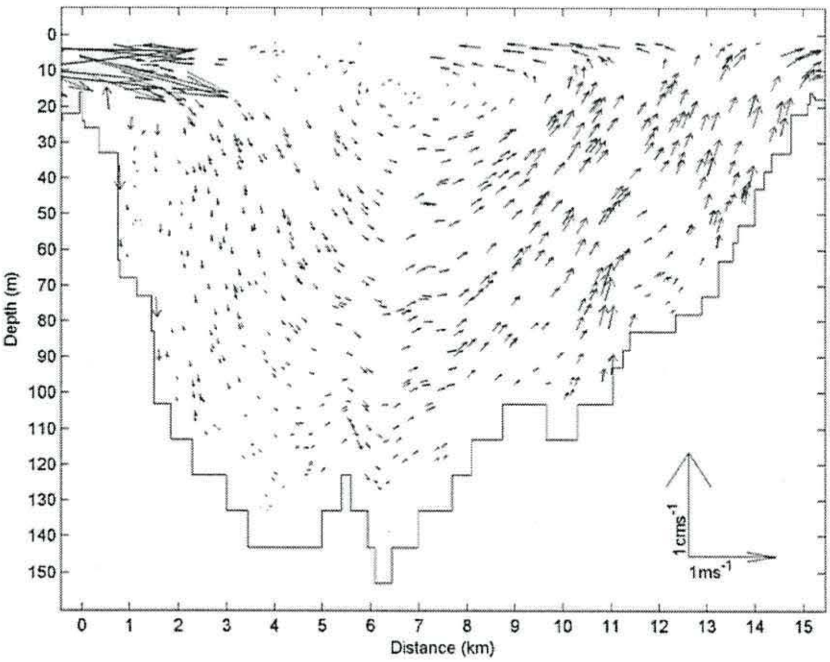

Figure 6.2d – Current field at LW slack + 3 hours

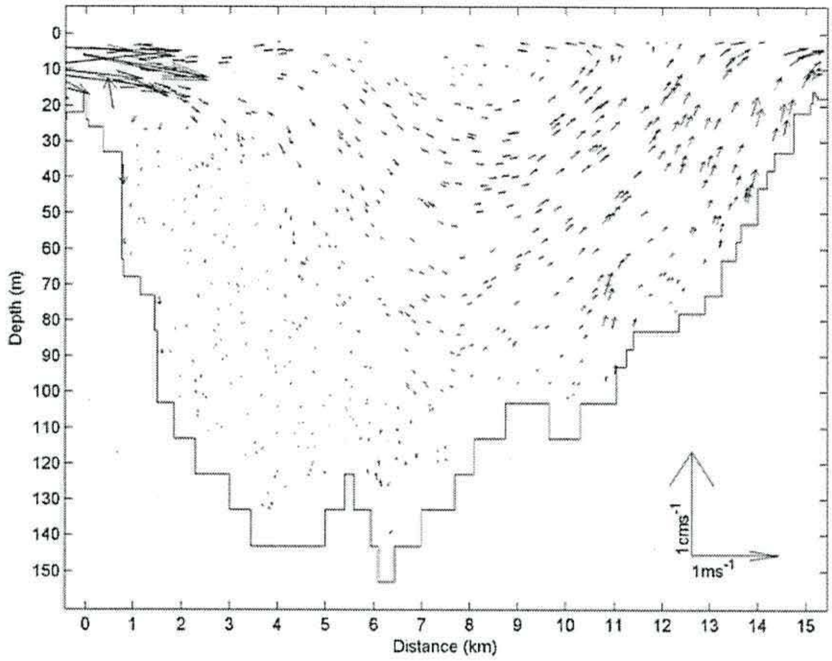

Figure 6.2e – Current field at LW slack + 4 hours

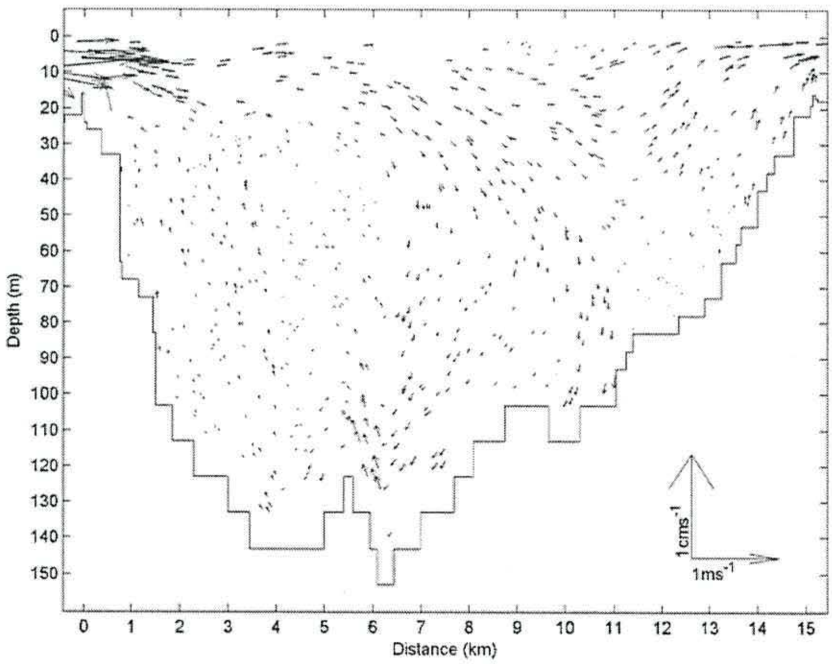

Figure 6.2f – Current field at LW slack + 5 hours

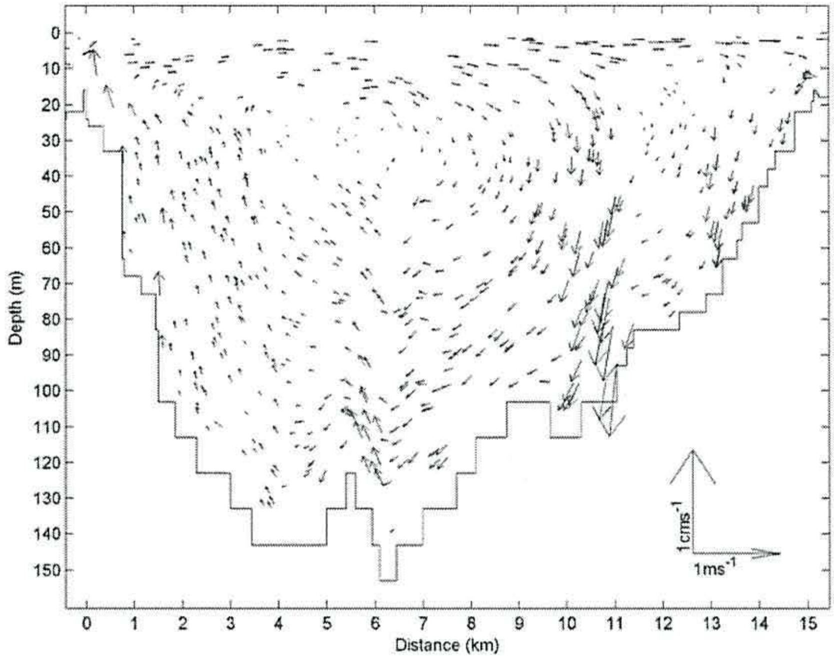

Figure 6.2g – Current field at LW slack + 6 hours

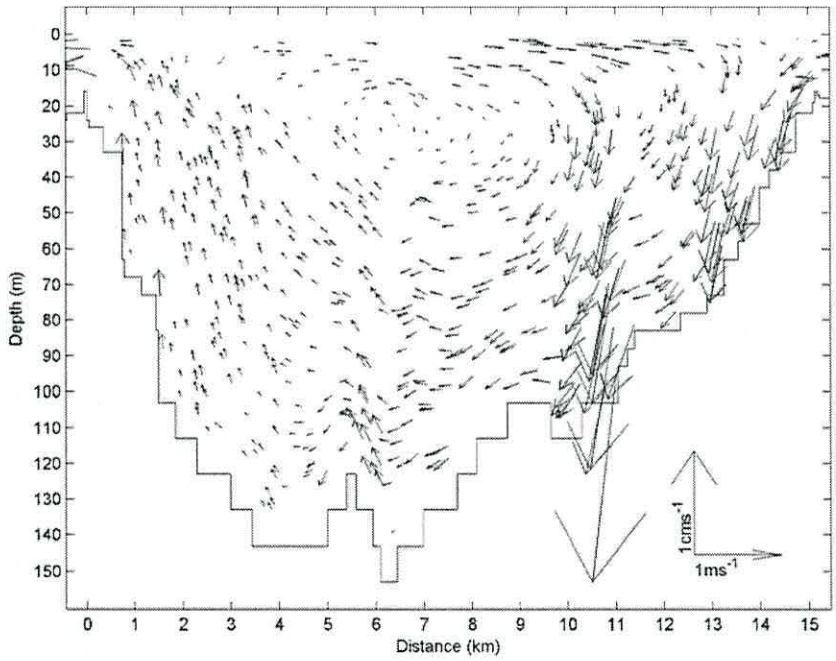

Figure 6.2h – Current field at L W slack + 7 hours

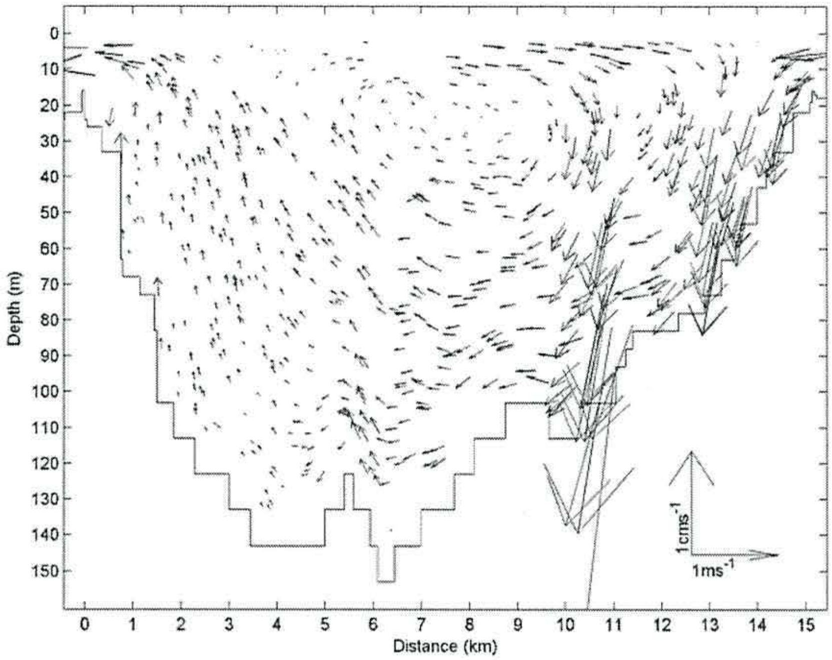

Figure 6.2i – Current field at LW slack + 8 hours

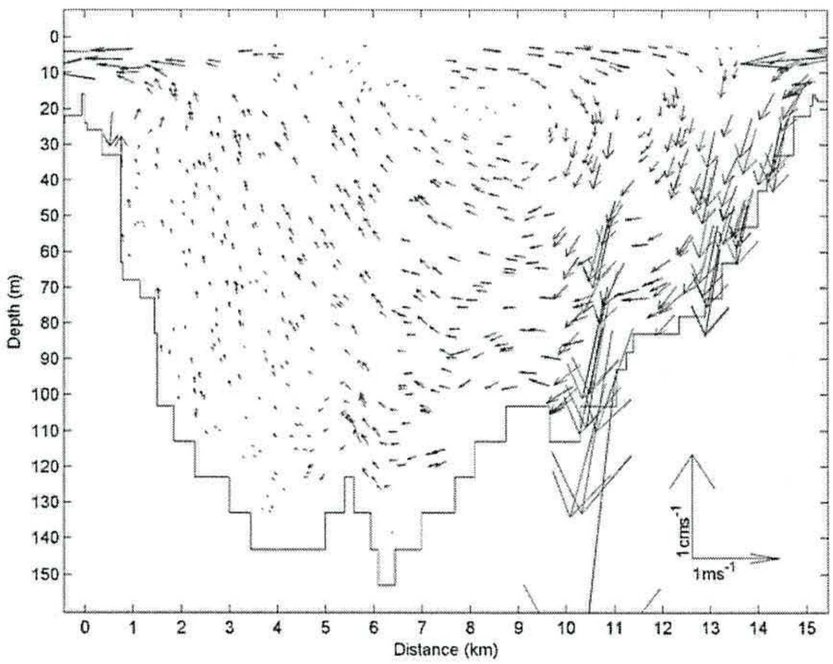

Figure 6.2j – Current field at LW slack + 9 hours

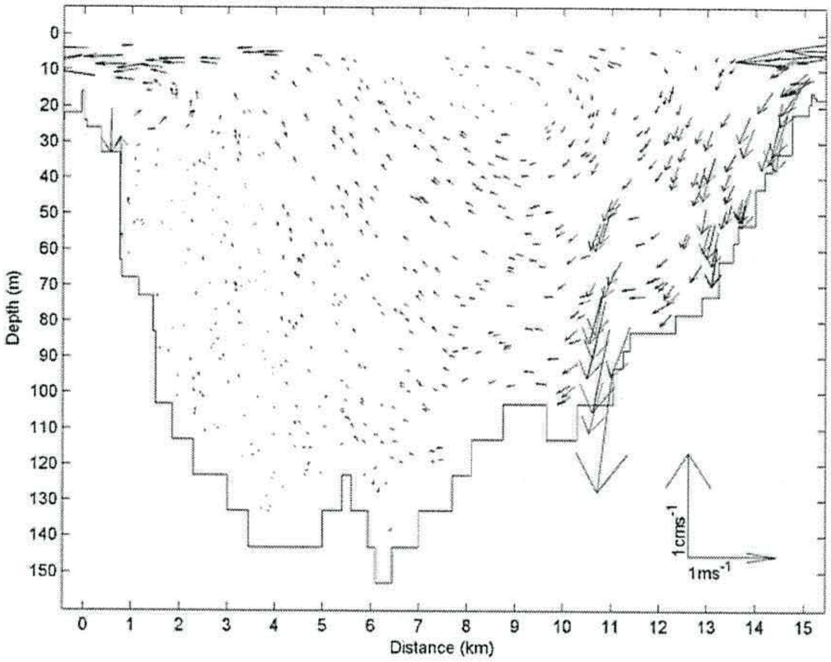

Figure 6.2k – Current field at LW slack + 10 hours

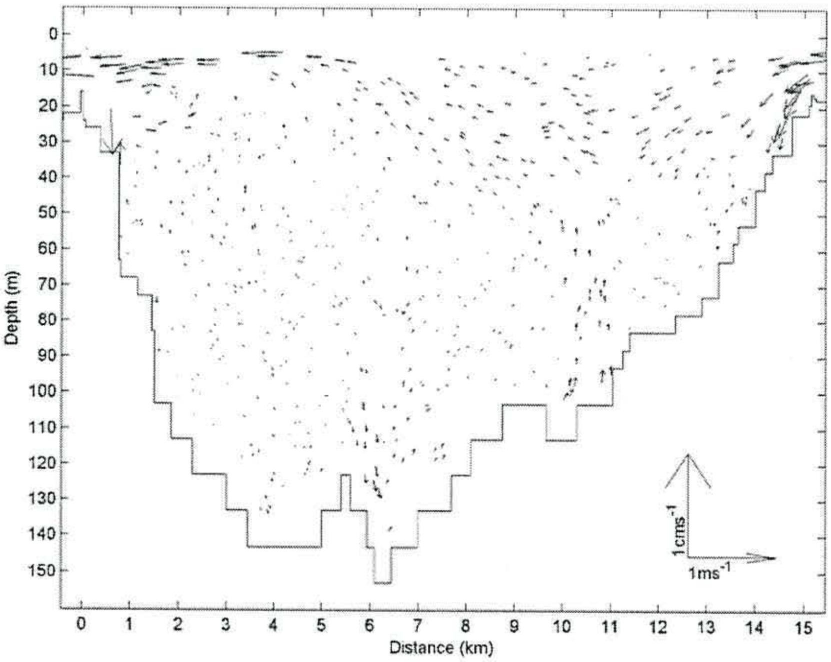

Figure 6.2l – Current field at LW slack + 11 hours

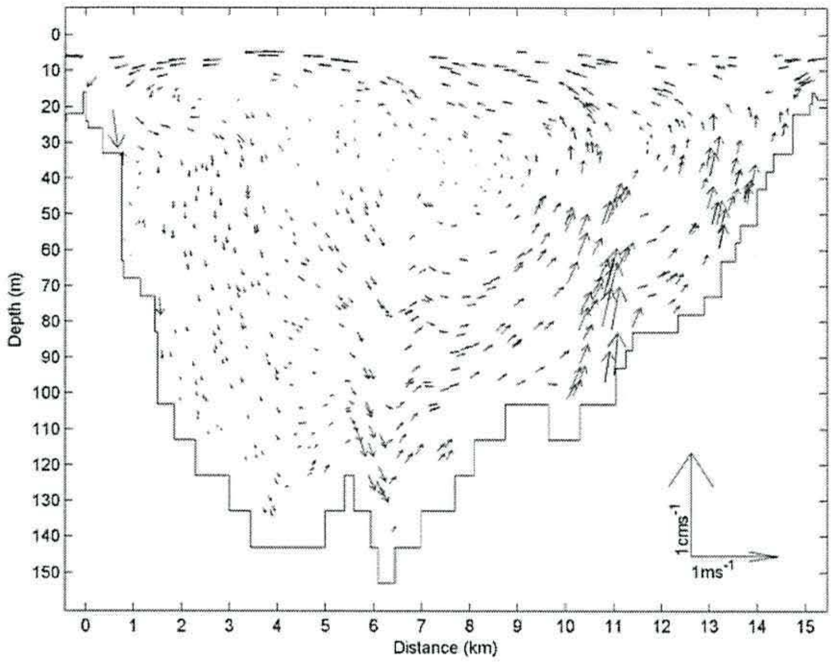

Figure 6.2m – Current field at LW slack + 12 hours

The sequence of current vectors over the tidal cycle show the flood stream entering over the Corran sill, and following the topography to depth. It plunges underneath the ambient basin water forming an area of convergence approximately 4km from the sill. This pattern continues until LW slack +4 hours when the area of surface convergence is shifted uploch and the small area of flow separation immediately inside the sill grows to fill the basin (LW slack +5 hours). The flow pattern on the ebb follows a similar pattern except that no flow separation is visible from the slope of the Annat sill. At some point between LW slack +11 and LW slack +12 the basin flow reverses again.

The flows co-incident to the LL04 and LL14 moorings are shown in figures 6.3 and 6.4. The sign of the horizontal component has been reversed to make uploch flows positive, matching the data analysis of Allen (1995).

The timeseries of currents at the LL04 mooring site (figure 6.3) shows that flood and ebb streams mainly confined to the upper 20m of the water column. Below this depth the lower layer was quite stagnant, with velocities below 0.025 ms^{-1}. The exception to this is the start of the flood stream that occurred at about 30m depth up to 1 hour after the commencement of flood at the sill. At the same time the surface waters were still ebbing strongly. After this time the flood stream appeared at the surface until approximately high water when the ebb stream began.

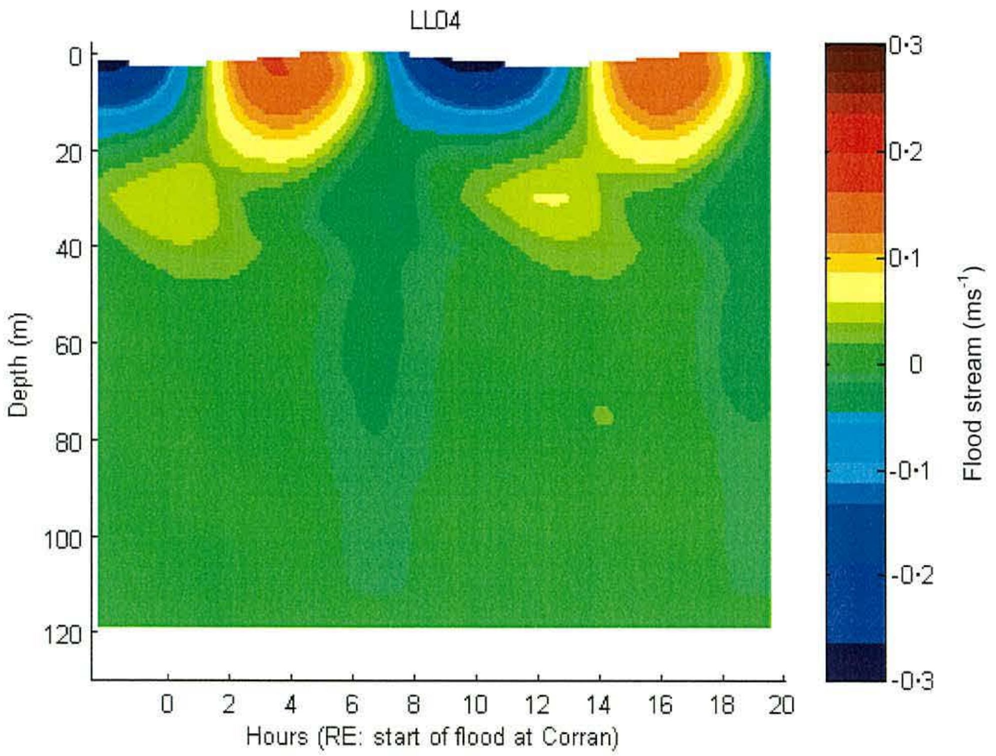

Figure 6.3 - Velocity time series from LL04 mooring site on day 113

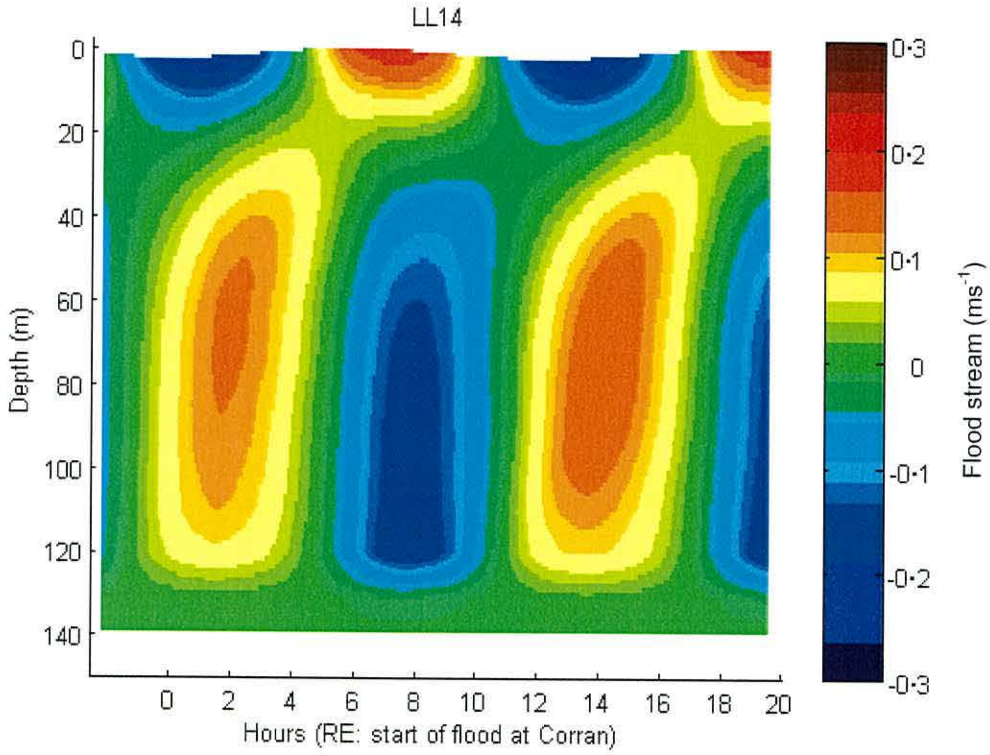

Figure 6.4 – Velocity time series from LL14 mooring site on day 113

The similar timeseries at mooring site LL14 (figure 6.4) shows a clear semi-diurnal internal tide with the surface and lower layers flowing in completely different directions. At the start of the flood stream it is the lower layer (below 25m) that flows landward, while the surface waters are shown to ebb strongly. During the ebb stream over the sill (starting at t = 6¼ hours) it is the lower layer that ebbs, with the strongest streams found at depth. The extent of the lower layer reaches to within 10m of the seabed where velocities reduce dramatically.

6.2.2 Harmonic Analysis

The velocity field was analysed for the mooring sites LL04 and LL14 (1¼ NM and 3¼ NM north of Corran Narrows respectively). The timeseries of velocity profiles at each site was first interpolated onto a regular vertical spacing of 1m.

Subsequently harmonic analysis was undertaken for each depth after the barotropic component had been removed by subtracting the depth-mean velocity. The behavior of the M_2 component was eluded using the t-tide package (Pawlowic, *et al.* 2002). The phase of the M_2 stream is plotted relative to the phase of the flood stream at the Corran sill. This in turn has been calculated from the 1-D model output (Appendix 1) and found to be 183° ±10°.

The results of the harmonic analysis are shown in figure 6.5 and 6.6 for the two mooring sites. Each figure shows the amplitude, phase relative to the flood stream at Corran narrows, and residual flow varying over the profile.

The amplitude of the semi-diurnal stream at LL04 (figure 6.5) reduces from a value of 0.2 ms^{-1} at the surface to less than 1×10^{-2} ms^{-1} at 20m depth. Below this there is a small increase up to a maximum of 8×10^{-2} ms^{-1} at 30m, however generally the amplitudes of the semi-diurnal oscillations in the lower layer were less than 1×10^{-2} ms^{-1}.

The phase of the flood stream at LL04 relative to that at the Corran sill is approximately 30° behind in the upper 20m of the water column, below this depth there is a sudden change of phase with depth such that at 25m the phase is 120° before. In the lower layer there is a fairly uniform change of phase from this value of 120° at 25m to 180° at 120m.

The residual flows are strongly seaward from the surface maximum of 4×10^{-2} ms^{-1} down to 10m where there is no net flow. There is a landward maximum residual flow at 20m depth of 1.5×10^{-2} ms^{-1}, which continues down to 40m where the flows are again predominantly seaward. From about 80m depth down to the seabed at 120m there is no residual flow.

At the LL14 mooring in the centre of the basin also show the largest amplitudes near the surface, 0.25 ms^{-1} that reduces by an order of magnitude at 30m depth.

There is then a steady increase in amplitude down to 90m where a maximum of 0.1 ms^{-1} is located. The value is only slightly diminished to approximately 0.07 ms^{-1} at 120m.

The surface layer, down to approximately 30m, has a phase lag of a little over 120° relative to the flood stream at Corran. Below this there is a smooth transition of phase to a lower layer between 60m and 120m where the phase ranges from 30° before to 60° before Corran respectively.

The residual flows at this site are seaward above 20m depth, below this they are landward with a maximum at 40m depth of 1×10^{-2} ms^{-1} and extend landward to a depth of 80m. The lowest layer exhibits seaward flows increasing with depth to a value of 2×10^{-2} ms^{-1} at 120m.

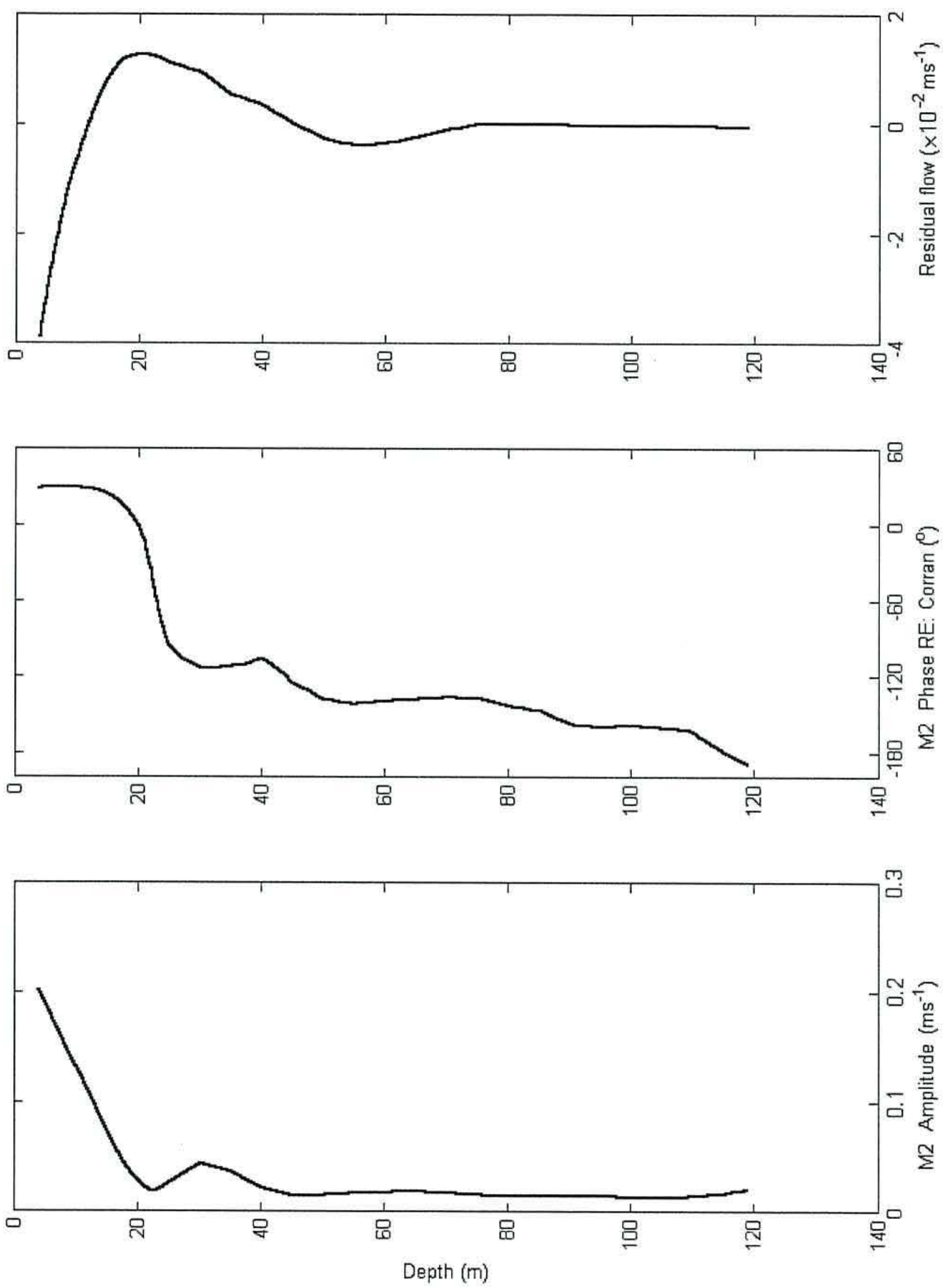

Figure 6.5 – Harmonic analysis of LL04 profile

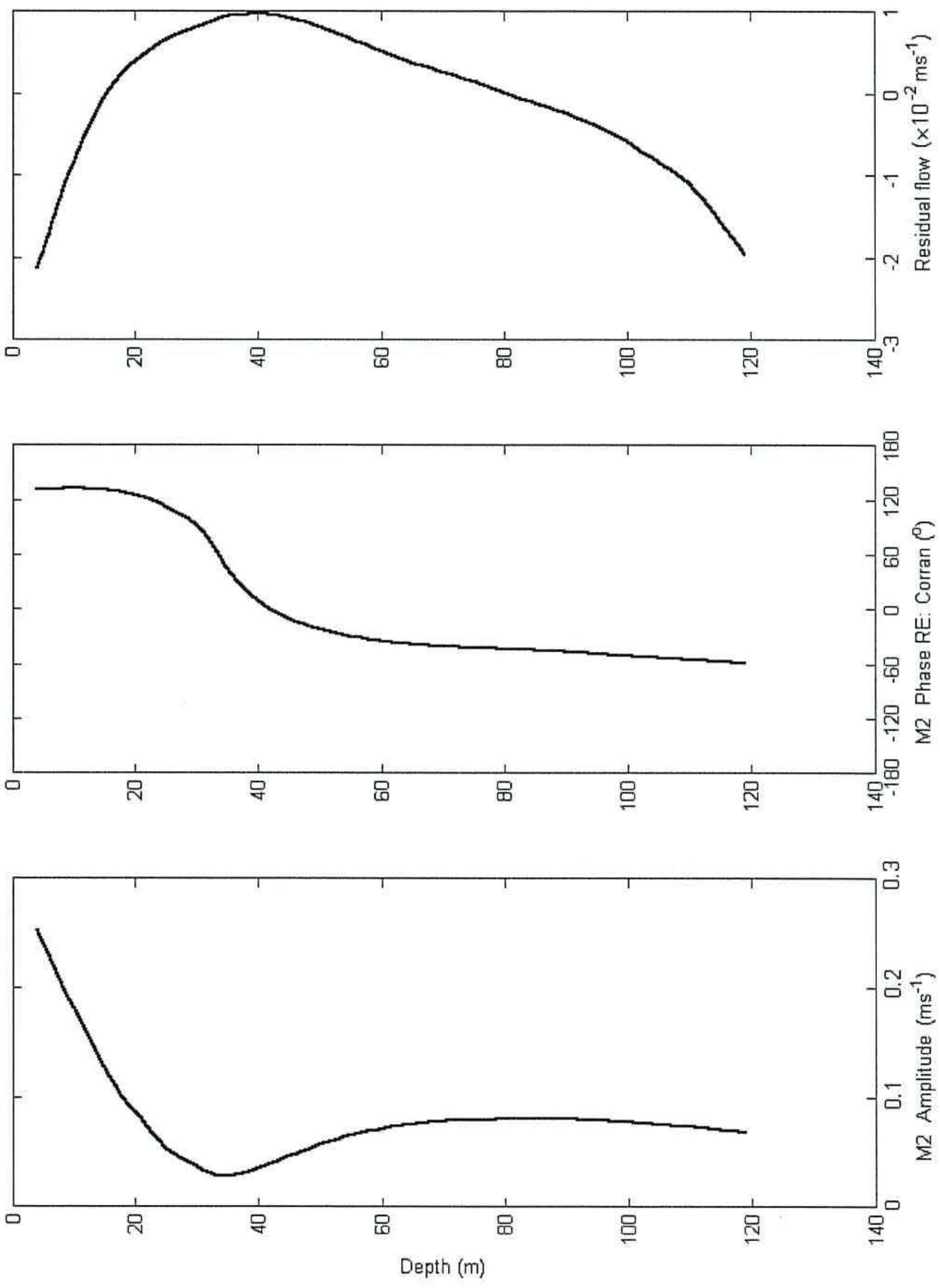

Figure 6.6 - Harmonic analysis of LL14 profile

6.2.3 Summary of Results

From the harmonic analysis of the stream at LL04 mooring site the flood stream is shown to commence at the surface approximately 1 hour (30°) after the flood stream at the Corran sill. This is also evident from the velocity plot (figure 6.3) showing that the flood stream began at 30m depth for the first hour of the flood. The flow field at LW slack +1 hour (figure 6.2b) shows the flood stream flowing under the outflowing surface stream from the previous ebb.

At the LL14 mooring site in the centre of the basin a clear mode-1 internal tide is evident. The flood stream commences in the lower layer approximately 2 hours before that at Corran, being the result of the return flow in the lower layer during the previous ebb stream. This is evident from the flow field at LW slack + 11 hours (approximately 1½ hours prior to the next LW slack). The surface layer at this location is approximately 30m thick, this depth being the site of the smallest amplitude streams.

Similarly during the ebb stream, starting at LW slack + 7 hours (figure 6.2h), the surface ebb from the Annat sill (northern end of the basin) meets the uploch flowing surface layer and dives underneath it. This causes strong flows down the slope into the Upper Loch Linnhe basin. In the upper layer the uploch stream is maintained until LW slack +10 hours until re-circulation at the Corran end of the basin commences and the flows reverse such that the surface ebbs and the lower layer floods.

The residual flows in the centre of the basin are seaward at the surface and seabed, and a compensating landward flow is shown in the centre of the water column. The same seaward surface residual is found at the mooring site near to the sill, however the deeper residual flow is found in the 20 to 40m depth range.

Chapter 7 – Synthesis and Comparisons of Models with Data

This chapter covers the comparison of the data with the two numerical models for the situation of the flood stream being of equal density to the ambient basin water. Subsequently the data for a period of time when dense water flows into the loch is compared with the non-hydrostatic model.

Processes for the generation of an internal response to the tidal forcing are elucidated from the non-hydrostatic model output and the data. It is proposed that there are several processes involved in creating an internal response in this system.

7.1 Comparison of the two models with the data

The model runs to re-produce the events of day 113 of 1993 can now be compared with the data from chapter 2. The data demonstrates that the set of spring tides around yearday 113 of 1993 produce a strong mode 1 internal tidal response. Both the non-hydrostatic and hydrostatic models have been set to simulate this situation; the results for each model are outlined in chapters 5 and 6 respectively as a series of 13 hourly slices showing current vectors.

7.1.1 Barotropic flow over Corran sill

To form a direct comparison of the models' ability to reproduce the tidal flows requires the forcing to be comparable. The two models are forced in different ways; the hydrostatic model is forced by a time series of sea-surface elevation while the non-hydrostatic model is forced with a specified velocity profile. The two models have their open boundaries in different locations; the open boundary of the hydrostatic model had to be moved south of Corran narrows to maintain stability.

Presented in figure 7.1 are time series of depth-averaged velocity over the Corran sill from both models. The amplitudes are identical; however there is more distortion of the sine wave evident in the non-hydrostatic timeseries. This shows up as an inequality between the length of the flood and ebb phases. The hydrostatic model has phases of approximately equal duration.

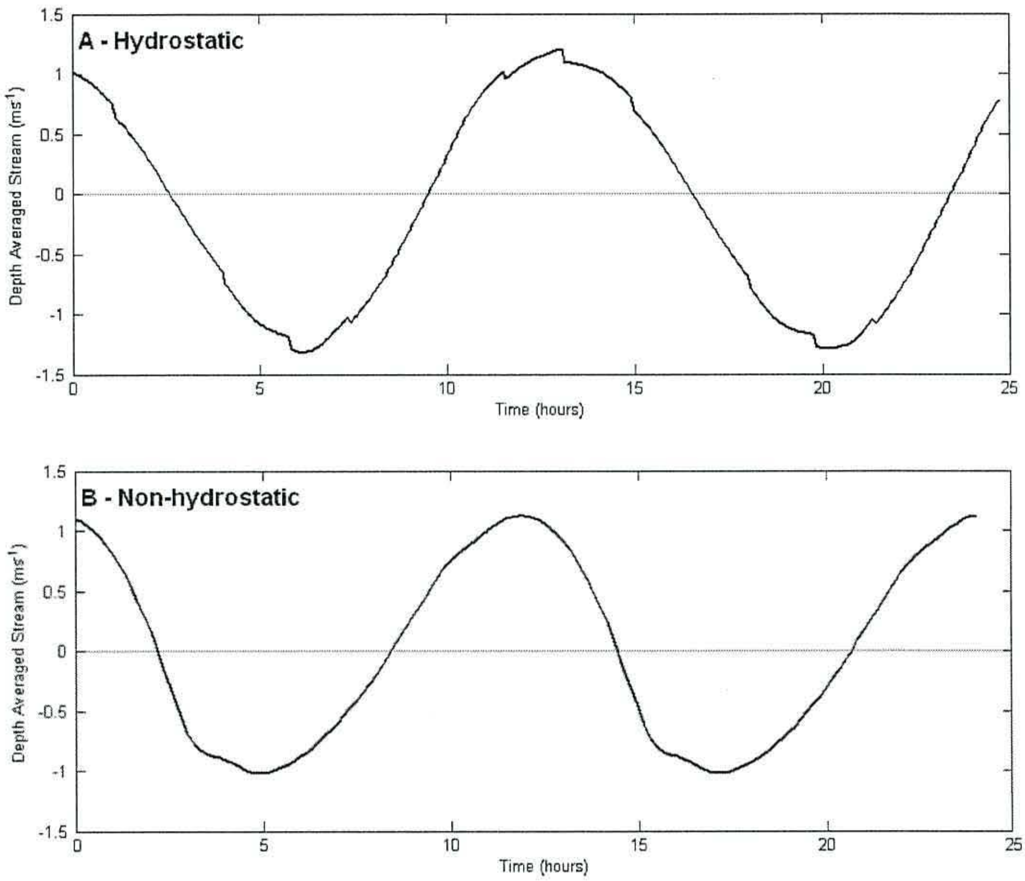

Figure 7.1 – Depth averaged flow over the Corran sill from the hydrostatic (A) and non-hydrostatic (B) models.

At maximum flood and ebb oscillations are evident in the output of both models. These are far greater in the output of the hydrostatic model, and are ultimately the cause of the model's instability without high levels of viscosity.

7.1.2 Phase of the flood stream at LL14 mooring site

Output from both numerical models has been used to produce profiles of velocity at the mooring location in the centre of the loch basin. Harmonic analysis of this data is presented in sections 5.4.3 and 6.2.2 for the non-hydrostatic and hydrostatic models respectively. The phases on day 113 (when no renewal was taking place) have been taken from the data at 10m, 30m, 60m and 110m depths. A comparison of both models and the data is presented in figure 7.2.

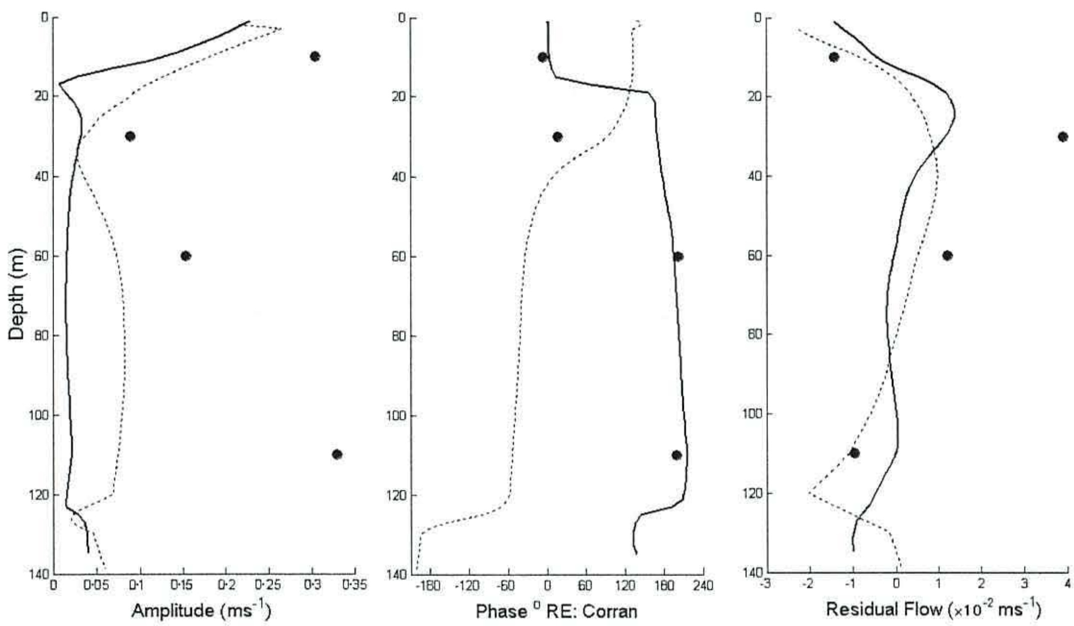

Figure 7.2 – Harmonic comparison of models and data at LL14 mooring
Data (circles), hydrostatic model (dotted line) and non-hydrostatic model (thick line)

Both models show a reduction of the amplitude of the M2 motions from a maximum at the surface to a minimum at 20 to 30m depth. Both models then fail to reproduce the increase in amplitude below this depth towards the seabed. The hydrostatic model does give a small increase with depth, approximately 20% of that observed. The residual flows show that both models approximate the flow regime. Neither model uses riverflow as an upstream forcing, which may account for the underestimate of seaward transport near the surface and landward transport immediately beneath the surface layer.

It is the phase comparison that shows the greatest disagreement between the models. At 10m depth the hydrostatic model shows that the flood stream starts approximately 4 hours after that at Corran narrows. In the lower layer there is a almost 180° shift between the observations and the model output. The non-hydrostatic model does mostly reproduce the phases of the observations. The only exception is at 30m depth. The upper layer thickness is clearly underestimated by the non-hydrostatic model.

The reasons for the marked disagreement in phases between the two models can be seen from a comparison of the timeseries of flows presented in figures *5.6a* to *5.6i* for the non-hydrostatic model and in figures *6.2a* to *6.2i* for the hydrostatic case.

The hydrostatic model shows the incoming flood following the slope of the basin and plunging to depth while the upper part of the water column, between the surface and 20m, ebbs. On the other hand the non-hydrostatic model suggests the flood stream occurs in the surface layer, and two hours after LW slack the lower part of the water column ebbs. This process starts by the flow detaching from the slope of the basin. This region of flow separation steadily increases in size to cover the entire length of the basin by LW slack +2 hours. By contrast the hydrostatic model does indeed reproduce a region of detachment and flow reversal, but this is confined to the immediate area behind the sill.

The lack of flow separation evident from the hydrostatic model is the ultimate cause of the lack of agreement with the data. The reasons for the inability of such models to allow the flow to separate from a boundary are discussed in the chapter 8.

7.2 The simulation of renewal

7.2.1 Vertical velocity

In order to demonstrate the link between inflowing salinity variation and the nature of the internal tide a pair of simulations were undertaken with the non-hydrostatic model only. The topography used was the 'thinjet' variant, taking into account flow separation from the north western shore as described in chapter 5 section 5.1. Both simulations used velocity forcing for a tide equal to the Mean Spring Range, and an initial stratification equal to the period 5 mean profile (section 5.1.4). Simulation *A* used an inflowing salinity profile that did not vary, and matched the initial conditions. Simulation *B* used a time varying inflow salinity, based on the harmonic analysis presented in section 2.3.2.

Figure 7.3 shows the results of harmonic analysis of the vertical velocity at 25m depth along the length of the basin. This depth was chosen as it was found to be the depth of the maximum vertical velocity by analysis of the normal modes undertaken by Allen (1995) and Allen and Simpson (1998a). Case A, the constant inflowing density profile, is shown as a dashed line and the time varying inflowing density (case B) is shown as a solid line.

Both simulations show an increase in the amplitude of the M2 motions toward the North Eastern end of the basin. Including the time varying salinity forcing gives vertical motions approximately an order of magnitude larger than the simulation without salinity variation. Spatially the main difference is the amplitude maximum at x = 4km present in simulation B and absent in simulation A. This point is coincident with the end of the jet.

The phases of the vertical variations vary with distance in both instances; changing by approximately 180° over the length of the basin. The differences are slight; the errors in the analysis of case A are proportionately larger due to the smaller amplitude of the M2 motions in this case. In both cases the phases are not related to any particular time, however there is a phase shift between the two simulations, simulation B is approximately 90° later.

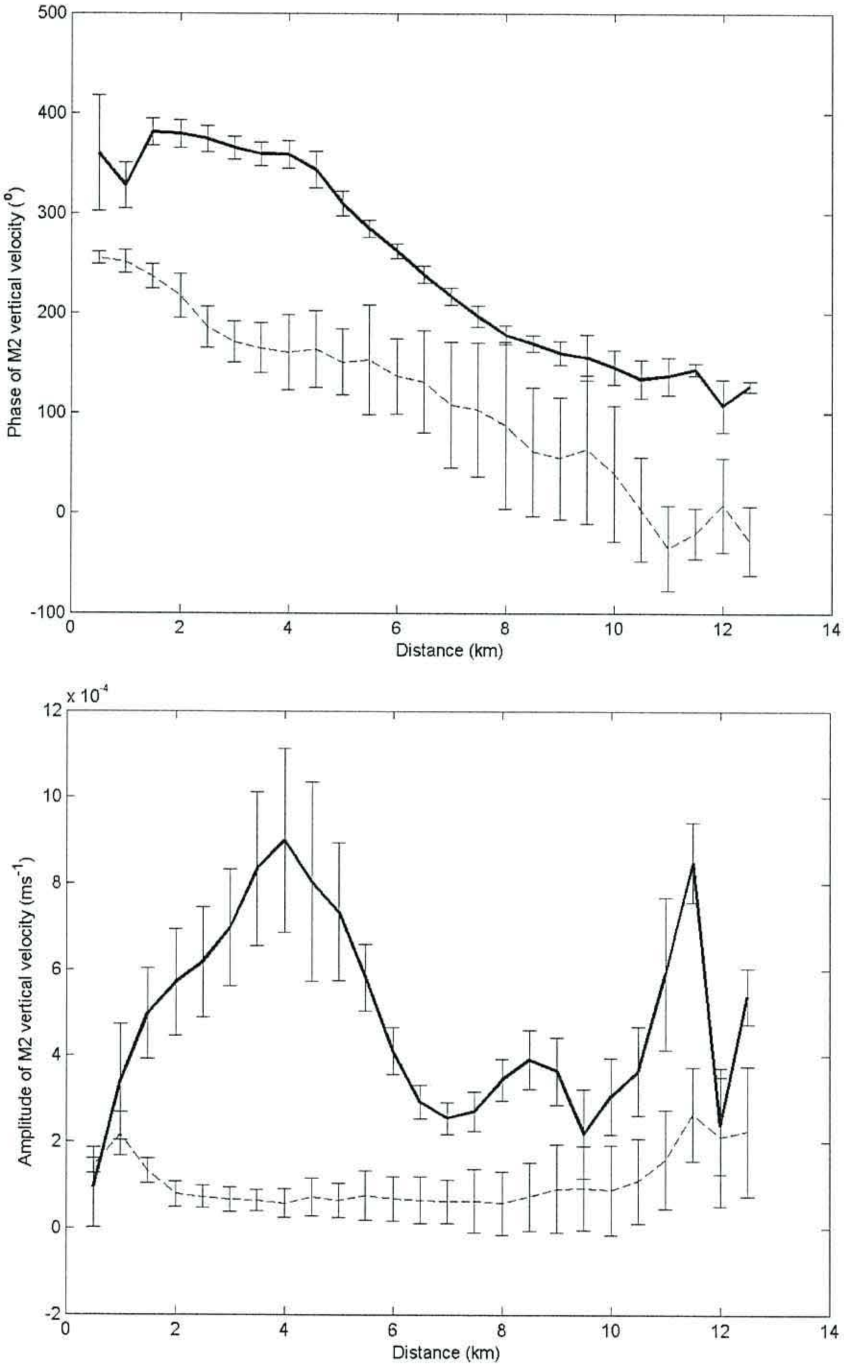

Figure 7.3 – Phases and amplitudes of M2 vertical motions, constant inflowing density (dashed line) & time varying density (solid line)

The spatial distribution of vertical motions was derived from salinity sections by Allen and Simpson (1998a). Figure 7.4 shows the analysis of the vertical displacement of an isopycnal centred about 25m depth.

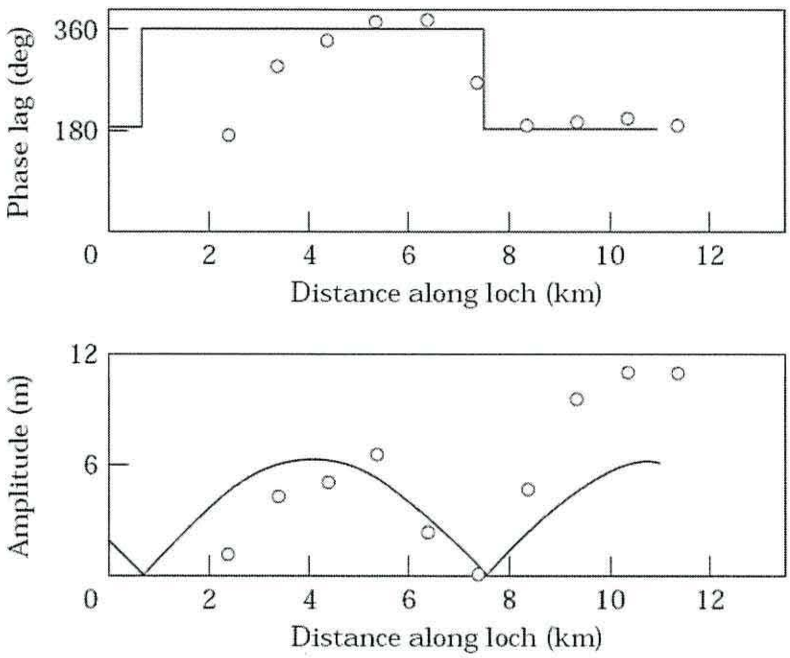

Figure 7.4 – Harmonic analysis of the vertical displacement at 25m depth observations (circles) and from theory (line) (Allen and Simpson 1998a)

The reduction of amplitude in the centre of the basin at about x=7km is present in both the data of Allen and Simpson (1998a) and the model simulation including time varying salinity. From theory the 180° phase change is abrupt and centred at x=7km; the data shows a more gradual phase change over 2km. The model output from simulation B gives this phase change over approximately 3km, and centred further seaward.

A timeseries of the vertical motions from simulation B is shown in figure 7.5 for a tidal cycle. This provides an overview of the situation, showing upwelling as a positive velocity. It can be seen that sinking occurs at the Corran end of the basin from the commencement of flood for 10 hours of the tidal cycle. The exceptions to this are two times of upwelling close to the sill, firstly at the start of the flood and subsequently at the start of the ebb. During the first 10 hours there is predominantly an upwelling at the North Eastern end of the basin. The region from 13½ km to Annat sill is not shown, and is a region of intense upwelling. The opposite signs of the velocities at both ends, indicative of a mode-1 response, is most evident from this plot.

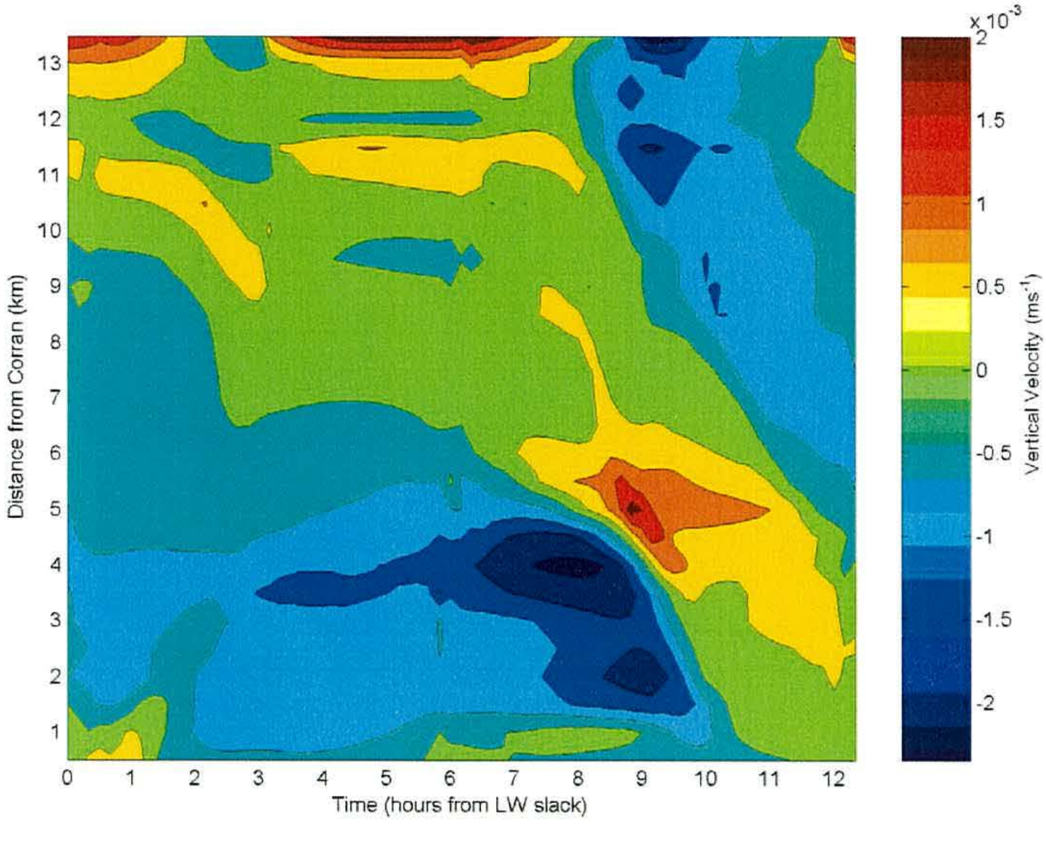

Figure 7.5 – Vertical velocity at 25m depth (ms^{-1})

7.2.2 Residual Flow

The harmonic analysis of the model output also reveals the residual flows. This enables a comparison with the data derived from ADCP observations co-incident with the CTD sections reported in Allen and Simpson (2002). For comparison 3 scenarios are discussed, non-renewal, partial renewal and full renewal.

The data (figure 7.6) shows a complex 4-layer structure to the circulation, reviewed and compared with other data in chapter 2. The surface layer, above sill depth flows seaward; below this a landward flow is observed at between 10m and 30m depth. This is confined to the southern end of the basin in the lee of the sill. Between 30m and 70m depth there is a seaward flowing layer extending 10km up the basin. At the bed the flow is indeterminate until a point 4km up the basin, after which a predominantly landward flow is seen at depth.

The computed non-renewal residual circulation pattern also exhibits this layered structure. Figure 7.7 shows that above sill depth the flow is seaward. Without the influence of river flow in the model this seaward circulation is a consequence of asymmetry in the tidal response. The seaward flowing layer between 30m and 60m depth is resolved, however its horizontal extent is only 4km landward of Corran, rather than the 10km Observed. The landward flow at the bed 4km north of Corran is reproduced in this simulation, along with its absence seaward of this point. The situations for the partial and full renewal are shown in figures 7.8 and 7.9.

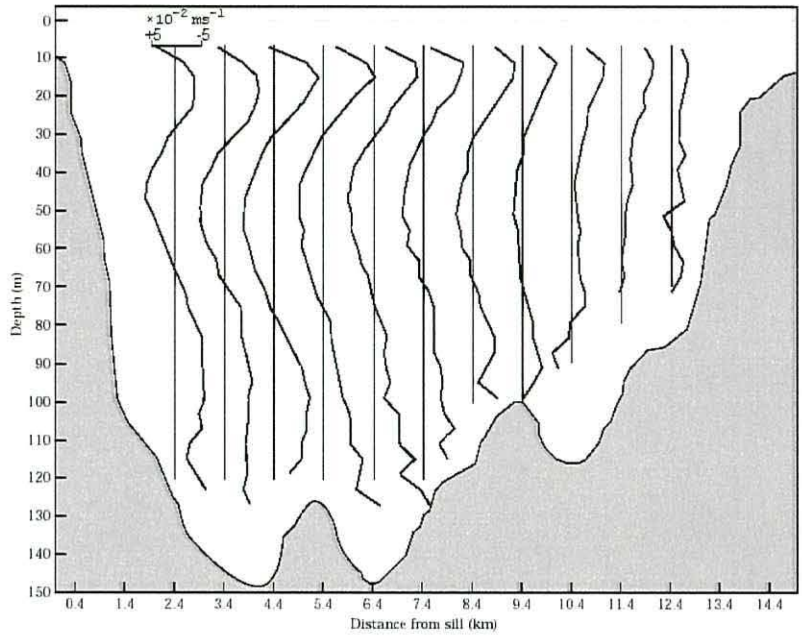

Figure 7.6 – Residual flow derived from ADCP data

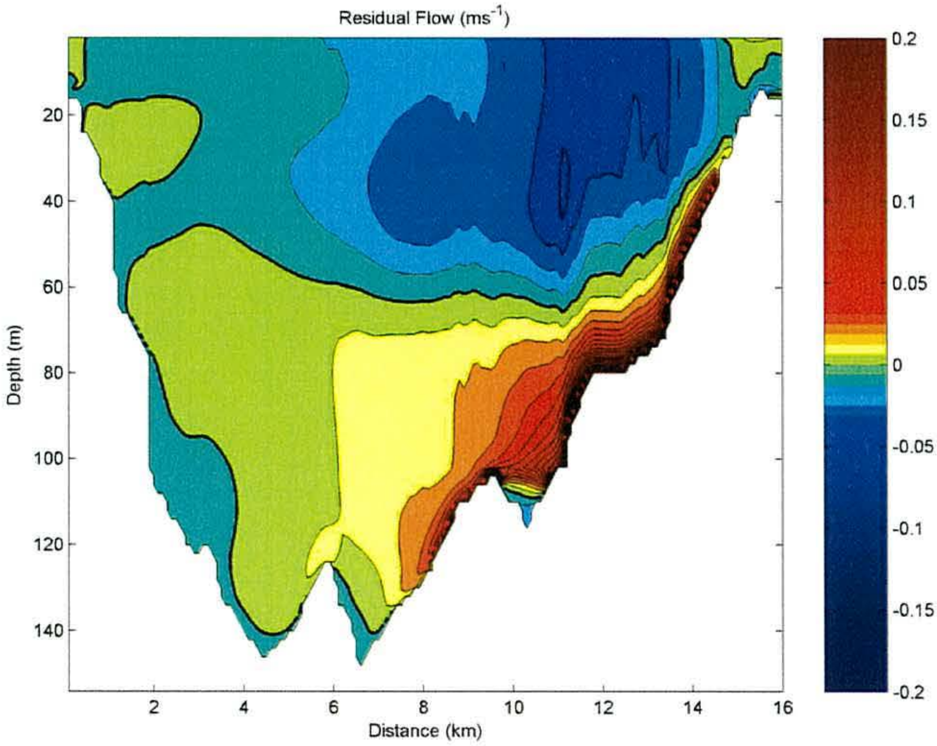

Figure 7.7 – Residual flow from model output for non-renewal scenario

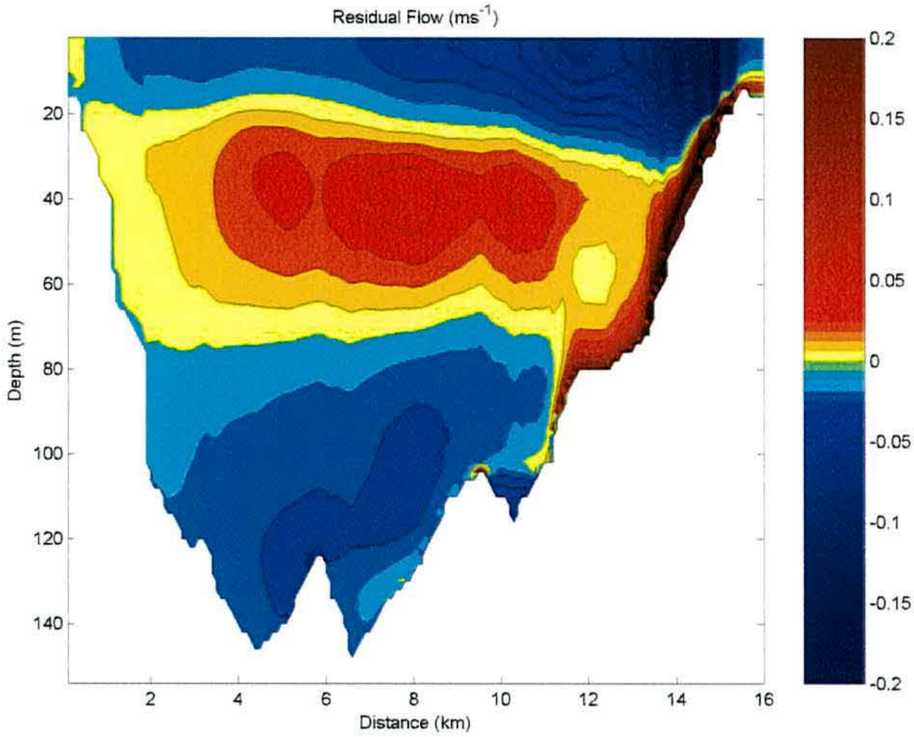

Figure 7.8 – Residual flow from model output for partial renewal

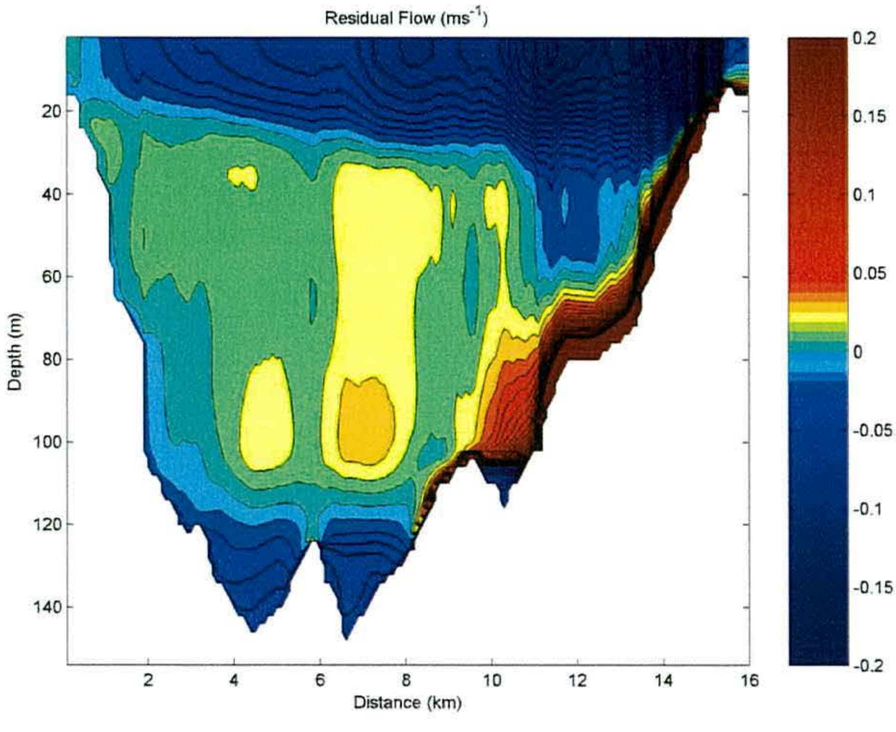

Figure 7.9 – Residual flow from model output for a full renewal

As can be seen from a comparison of the ADCP derived residual flows and those of the two renewal event simulations, while simulating renewal at depth, the simulations fail to resolve the upper layers of the residual structure. The most likely explanation for this discrepancy is the forcing used. The time series of sill density (figure 2.20) shows a distinct variation of density over the tidal cycle. This is consistent with the spatial gradients calculated in chapter 2. The forcing used in this study assumes that the denser water flows into the basin over the entire flood stream. In reality it is only the last part of the flood that brings in the denser water. The first stages of the flood stream will be of comparable density and therefore force the basin in the same manner as the non-renewal simulation shown in figure 7.7.

It is of great interest that all three of the simulations above show a strong residual landward flow up the slope of the Annat sill. It is suggested in the ADCP data only at the very bottom of the profile for x = 12.4 km. Its appearance in all of these simulations would suggest that it is related to the asymmetry of the internal forcing mechanisms and not any density forced flows. Its position, at the seabed, in conjunction with the implied strength of flow of up to $0.2 ms^{-1}$, would have implications for both sediment and pollutant transport if this were to be backed up with observations.

7.3 Baroclinic Adjustment in response to a dense jet

The 30m dip of the isopycnals found in the Searover density profiles (figure 7.10) has been attributed to two processes. Initially it was thought to be associated with an internal hydraulic jump (Allen and Simpson, 1998b); this view was later revised by Allen and Simpson (2002) who attribute this to a baroclinic density driven response to the strong horizontal density gradients. This density gradient occurs as denser water enters the basin over the Corran sill, having sufficient momentum to hold the seaward flowing brackish layer back. Then, as the momentum reduces and HW slack is approached, the density gradients force a motion to re-establish equilibrium. This has been simulated using the harmonic variation of inflowing density into a basin of horizontally uniform density. The results of the simulation are shown in figure 7.11. The dip of isopycnals is reproduced at 5km from Corran. At the other end of the basin uplifting of the isopycnals is also reproduced, centred about 11km from Corran.

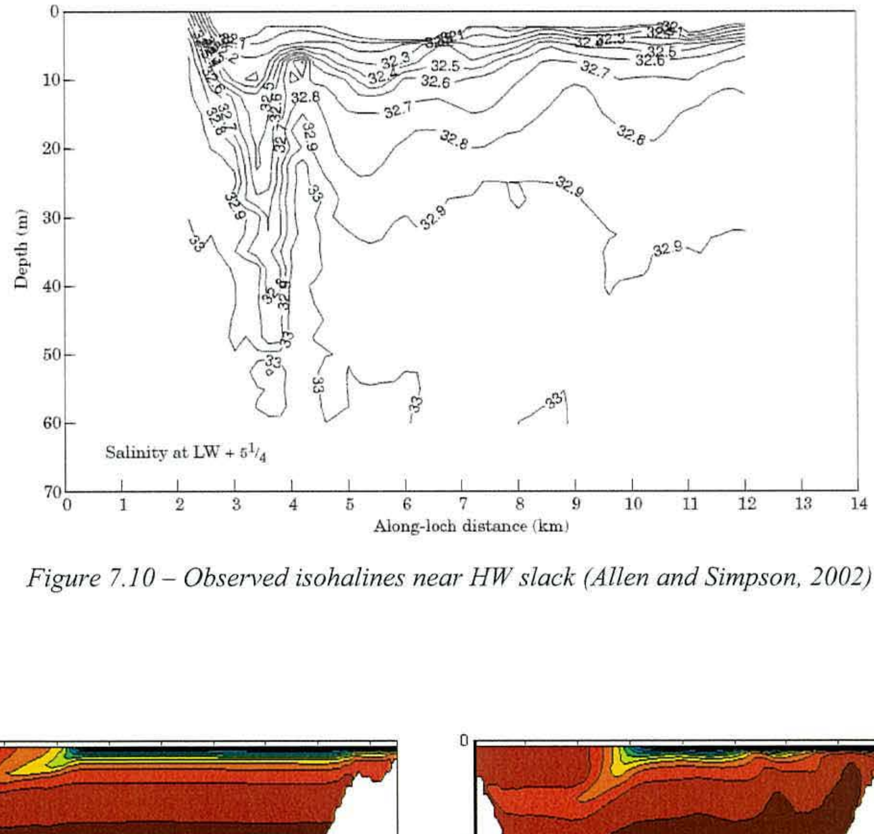

Figure 7.10 – Observed isohalines near HW slack (Allen and Simpson, 2002)

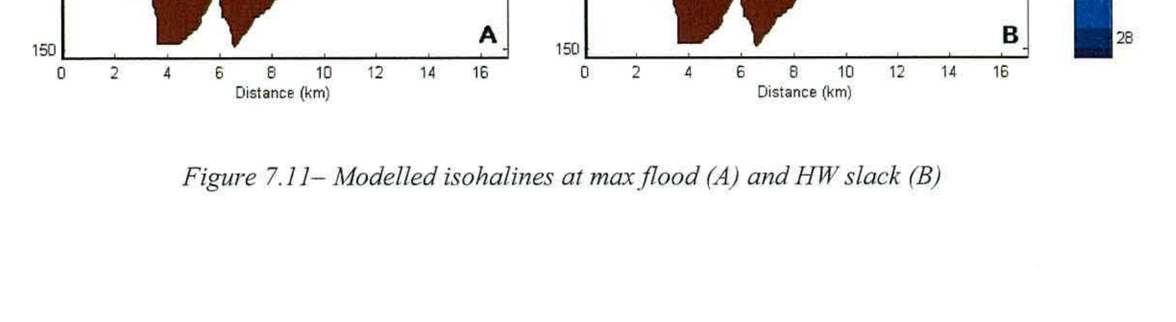

Figure 7.11– Modelled isohalines at max flood (A) and HW slack (B)

The initial flood stream is less dense than the ambient basin water. However at maximum flood (figure 7.11 A) the water flowing over the sill has become more saline due to the advection of the horizontal density gradient (see section 2.3.2). At HW slack the dense water begins to sink as the water column is unstable. This sinking produces the kink in the isopycnals at x = 5km as observed by Allen and Simpson (2002) (figure 7.10).

7.4 Processes generating the internal responses

It can be seen from the non-hydrostatic model output presented here and in chapter 5 that there are three possible processes leading to the generation of an internal response to the tidal forcing. Each process is sumarised below, and an assessment of their role in the tidal response of the Upper Loch Linnhe basin is given.

7.4.1 Bernoulli Forcing

The backwards facing step simulation shows how a reversed stream can be created at depth downstream of a sudden expansion of the channel. Prior to the generation of the area of flow reversal the flow must detach from the channel bed. This creates a jet of fast moving fluid which according to the theory of Bernoulli exerts a lower pressure. The pressure gradient thus generated forces water beneath the jet upstream, at the same time viscous coupling at the lower boundary of the jet forces fluid downstream. The reverse eddy is then generated (section 4.1).

In the context of the Upper Loch Linnhe basin this process takes place at both ends of the basin at opposite ends of the tide. The reverse flowing eddy is produced landward of the Corran sill during the flood stream, (excluding the obvious effects of the horizontal gyre) and seaward of the Annat sill during the ebb (evidenced by the ADCP section, figure 2.19). Model output for the flood and ebb streams (LW+3 and LW+11 hours respectively) is shown in figure 7.12. A schematic of the process is shown in figure 7.13.

It should be evident from figures 7.12 and 7.13 that the phase shift of velocity created in the centre of the basin at depth should be 180°. In practice it is slightly less; there is a delay in flow separation taking place and extending to the centre of the basin following the start of the tidal streams.

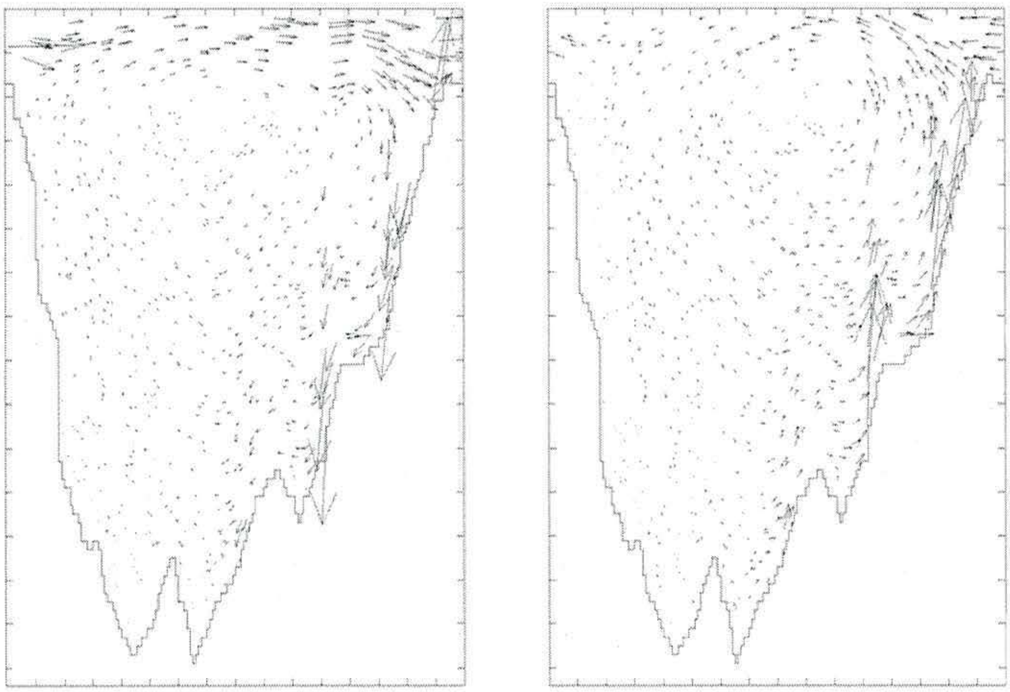

Figure 7.12 – Model current flows (LW+3 and LW+11 hours)

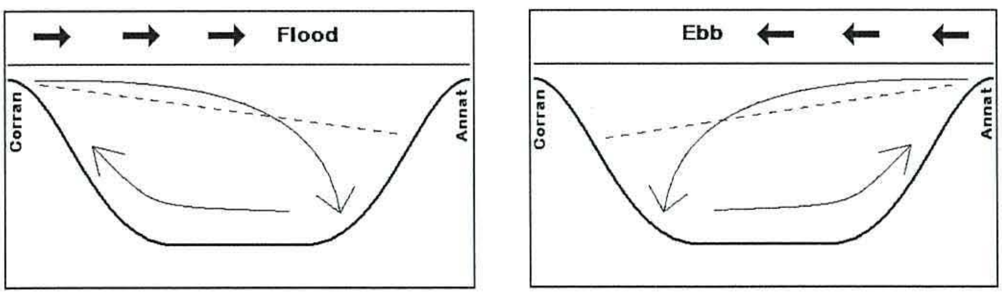

Figure 7.13 – Internal forcing via the Bernoulli Effect (interface shown as dashed line)

From the Bernoulli equation, the term for the kinetic head of water is given by $u^2/2g$ (Chadwick and Morfett, 1998). Therefore the situation over the Corran sill, approximated by the flow slowing from $1ms^{-1}$ to $0.1ms^{-1}$ will be balanced by an increase of head of water of 49mm. However were this loss of kinematic head to be balanced by the movement of a pyncnocline the reduced gravity would replace the acceleration due to gravity. In this case $g' = 0.002 \times g$, therefore the vertical displacement of the interface would be 24.75m.

The preceding estimate of interface deflection assumes that the entire pressure deficit was made up by the movement of the interface. In reality it would be expected that both surface and pycnocline would adjust (Hill and Foda, 1988). This theory does, however, show that the internal tide can be accounted for by the theory of Bernoulli.

7.4.2 Aspirational Forcing

The process of aspiration has been previously observed in Scottish sealochs (Inall *et al.* 2004), water of twice the sill depth was seen to cross the entrance sill to the upper basin of Loch Etive. Horizontal forcing of a stratified fluid up a slope results in a vertical component to the forcing and a lifting of any density gradient. The vertical displacement is related to the speed of the horizontal forcing, therefore at maximum flow there is maximum vertical displacement. When this flow slackens (or reverses in the case of a tidal stream) gravity restores the dense water to an equilibrium position in the water column. This is an example of the linear internal tide being forced by a non-separating flow over a sloping seabed.

The model output in figure 7.14 illustrates this process which is summarised in figure 7.15. The waves created in the upper third of the basin are comparable with those found in the Searover section presented in figure 7.11.

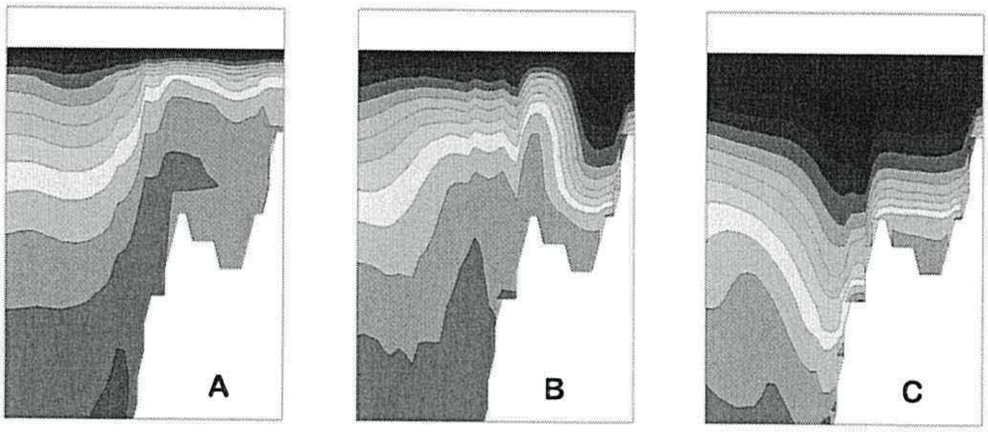

Figure 7.14 –Salinity contours from the non-hydrostatic model (A= LW+6½, B=LW+8, C=LW+9½ hours)

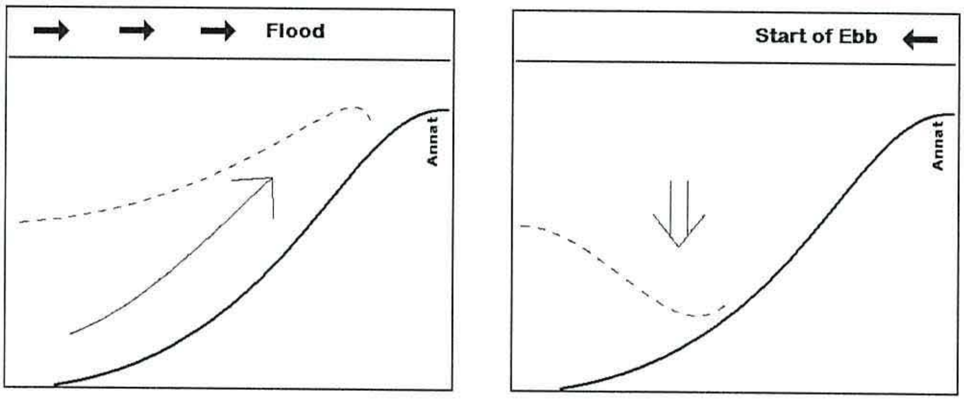

Figure 7.15 – Schematic of internal forcing by Aspiration (isopycnal shown as dashed line)

The created waves are therefore associated with the turn of the tidal stream. They would not be expected to be entirely symmetric. The process lifting the water increases gradually over the increasing tidal flow. The restoring force due to gravity is supplemented by a change in the direction of the tidal flow, and so this part of the wave would exhibit rapid changes.

It can be seen from figure 7.14*B* that a short wave is created as the stratified water is forced by the ebb stream. The behavior of such a short, steep wave in shallow water would depend upon the nature of the stratification; it may propagate as a bore either broken or purely undular.

7.4.3 Time-varying density

The horizontal density gradient between the Upper Loch Linnhe basin and the seaward basin causes the density of the flood stream to increase with time. This effect is greater at springs when the horizontal advection is greater, and vertical advection of a vertical gradient outside Corran is possible. The local effects of this change in salinity are the feature discussed in section 7.3.1 and in Allen and Simpson (2002). The basin scale effects of the time varying inflow density has been simulated by the model and discussed in section 7.2.1. There was an order of magnitude increase in vertical motions when the inflowing salinity varied over the flood stream. A graphical summary of how time-varying density causes an internal response is given below (figure 7.16).

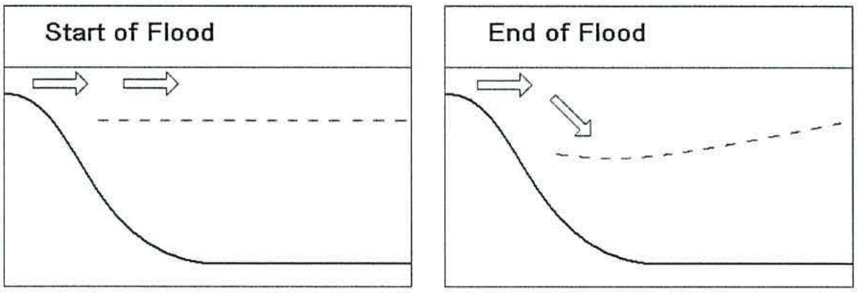

Figure 7.16 – Time varying inflow density

7.5 Summary of comparisons

The hydrostatic model cannot simulate the flow in the basin corresponding to a mode 1 internal tide due to its failure to simulate flow detachment. The non-hydrostatic model does reproduce this internal tide, along with the process of flow separation.

Post renewal the non-hydrostatic model qualitatively reproduces the interface position at the northern end of the basin well. The internal waves of shorter length than the tide are found in the data and the simulation. The mechanism for their generation is thought to be the forcing of dense water up a slope by aspiration.

The other mechanism proposed for the generation of the internal tide is via the Bernoulli Effect in the lee of the sill. The re-circulation formed should give rise to a 180° shift of phase from the surface to the bed. This phase shift is reproduced by the non-hydrostatic model during a period of non-renewal; however the amplitude, especially in the lower part of the water column, is underestimated considerably.

The effects of an inflowing jet of greater density than the ambient basin water have been reproduced by the model. This creates a sharp drop in the isopycnals as the water column returns to an equilibrium state at HW slack. This downwelling process is an important process leading to the formation of an internal tide under these conditions.

A comparison of the residual flows observed post renewal show that the model reproduces the layered flows but underestimates the extent of the seaward flowing layer immediately below the inflow. All of the residual flow situations show a net landward, and therefore upslope flow, at the northern end of the basin.

Chapter 8 - Discussion and Conclusions

The major features of the flow identified by the model output are discussed in relation to other pertinent studies. The ability of the two models to reproduce the flow is put into context with recent numerical studies, and with boundary layer theory previously applied to the flow of air over an aerofoil section. This chapter concludes with a proposed plan for future work and model development.

8.1 Mode 1 internal response

The exact mechanism by which jet fjords show internal tides has yet to be fully understood. It was Stigebrandt (1999) who, citing the data of Allen and Simpson (1998b) used in this thesis, proposed that a different mechanism for the generation of internal tides by jets must exist. Recent numerical investigations by Stashchuk *et al.* (In Press.) provide a clue to just such a mechanism in Loch Etive. They suggest that on the flood stream a jet is created over the sill (Chapter 4); on the ebb the flow is subcritical at the sill and therefore the linear internal tide can be created at this time. They point to the asymmetry of the internal motions and suggest that they are only forced for half the tidal cycle, during the ebb stream.

Upper Loch Linnhe differs from the upper basin of Loch Etive in that both ends are open and so the flood stream can leave via the Annat Narrows. Therefore the mechanism proposed by Stashchuk *et al* (In Press.) could occur in Loch Linnhe on both phases of the tide.

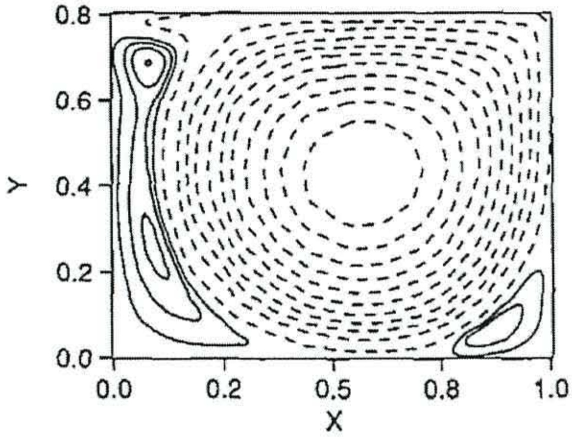

Figure 8.1 – Streamlines from lid driven cavity flow (Poliashenko and Aidun, 1995)

The re-circulation in the backwards facing step example is not reliant upon the far end of any basin; the re-circulation is driven by a need to maintain continuity in the lee of the step following flow separation. This is borne out by the correct simulation of the flow over the Loch Etive sill. The recirculation was simulated with an outflow boundary condition downstream; thus demonstrating that it is the low pressure in the lee of the sill that drives the recirculation. It is not caused by interaction of the flow with the far end of the basin as is the case with lid-driven cavity flow test cases (figure 8.1).

The lack of amplitude of the internal tidal motions produced by the non-hydrostatic model is evident compared against the 110m current meter record from the LL14 mooring. While the phase of this internal tide is accurately produced the amplitude is not. The mechanism by which this vertical recirculation is maintained may not be entirely described by the model. A schematic of this process is shown in figure 8.2.

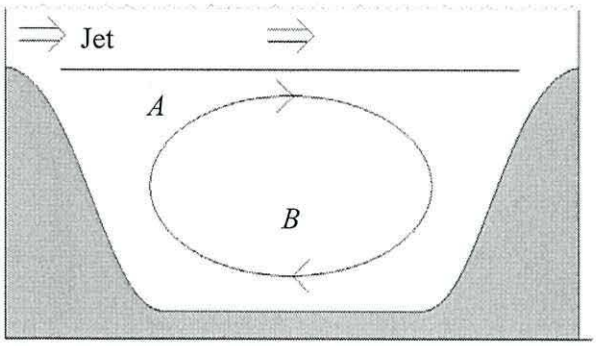

Figure 8.2 – Schematic of basin gyre

Figure 8.2 shows that beneath the inflowing jet at point *A* horizontal momentum is imparted to the waters below sill depth by viscous forces. This creates a return flow in the lower part of the water column and helps to drive the recirculation gyre. Viscous forces at point *B*, together with frictional forces against the seabed will reduce the amplitude of the velocities in this gyre.

It should be apparent that greater viscous coupling at point *A* than at point *B* will encourage the formation of this gyre. Any higher order turbulence schemes relating the vertical eddy viscosity to the turbulent kinetic energy in the water column should reproduce this inequality of viscosity. The lack of a turbulence scheme in this model could be the cause of this deficiency. It may also explain the seemingly thin upper layer, shown by the lack of agreement of the phases at 30m depth. An increase in the vertical mixing of momentum should deepen the upper layer.

It was Cummins (2000) who suggested the use of more complex turbulence schemes in sealochs; in that case to encourage the accurate simulation of the boundary layer and its separation. This study provides another compelling reason to relate the mixing parameters to the turbulent energy in the water column.

The mode 1 internal response of the Upper Loch Linnhe basin has been thoroughly investigated by the originator of the data (Allen, 1995; Allen and Simpson, 1998a&b; Allen and Simpson, 2002). Observations of a similar mode 1 internal response have been made recently in the Gareloch (Ellis, 2001). Previously the data of Farmer and Osborne (1976) is suggestive of an internal response generated at the head of a loch.

The mechanism proposed in this study, the vertical advection of a density gradient by horizontal forcing up a slope, would account for these observations. It has also been shown to generate the undulations of the isopycnals near the Annat end of the Loch Linnhe basin. The streams are strong in this area due to the connection of Loch Linnhe to Loch Eil. These strong tidal streams will generate a far greater internal response than if the basin were closed at the head.

The variation of inflowing density over the flood stream has been shown to reinforce the internal response; in the area centred about 5km from Corran this accounts for an order of magnitude increase in vertical velocity. The author has been unable to find a similar process described in the literature, although it should by no means be confined to Upper Loch Linnhe.

8.2 Hydrostatic – non-hydrostatic model comparisons

The model of Bourgault and Kelley (2004), while similar to the model presented here, has one unique feature not seen in other non-hydrostatic models. The same code can be run in a hydrostatic format by modifying the fundamental equations with a '*switch variable*'. This enables a direct compassion to be made between hydrostatic and non-hydrostatic models. In the hydrostatic mode this model has produced flow separation over the Knight Inlet sill. A comparison with the non-hydrostatic model shows that the hydrostatic version produces only one small lee wave rather than the train of lee waves from the non-hydrostatic simulation. The hydrostatic model did reproduce flow separation, however to a lesser extent than either the data or the non-hydrostatic model. In a basin scale context this difference between the hydrostatic and non-hydrostatic my account for the discrepancy between model and data in Loch Sunnart by Gillibrand (1993). The model was unable to reproduce the internal tide, showing a 90° phase shift between observations and model. A later version of the same model has been more recently compared against long term salinity data (Gillibrand, 2001); however the absence of any comparison with velocity data would suggest it also reproduces the dynamics poorly. The comparison here reinforces the conclusion of Gillibrand (1993) that his model was '*not entirely suitable for the sealoch environment.*'

There is clearly a difference in the ability of various models to reproduce flow separation. A comparison can be made between the hydrostatic work of Cummins (2000) and the non-hydrostatic work of Lamb (2004). These two papers recount the simulation of the flow over Knight Inlet, both with purely 2-dimensional models. The limitations of this approach are discussed in Klymak and Gregg (2001) where the 3-dimensional nature of the flow is discussed. Both these simulations suffer comparably from the 2d approach.

The hydrostatic model compared favorably at maximum flow but the acceleration phase of the tidal cycle was poorly modelled. In order to achieve a satisfactory end state the topography was modified to mimic flow separation. The bathymetry downstream of the sill was cut off at 80m (dashed line in figure 8.3) and a no-slip condition was introduced in order to match the observations in the upper part of the water column. To demonstrate the flow field the streamlines are shown in figure 8.3 for maximum ebb. Upstream of the sill there is a vertical eddy above the seabed, however in the lee of the sill the flow remains attached and rapidly descends the leeward slope.

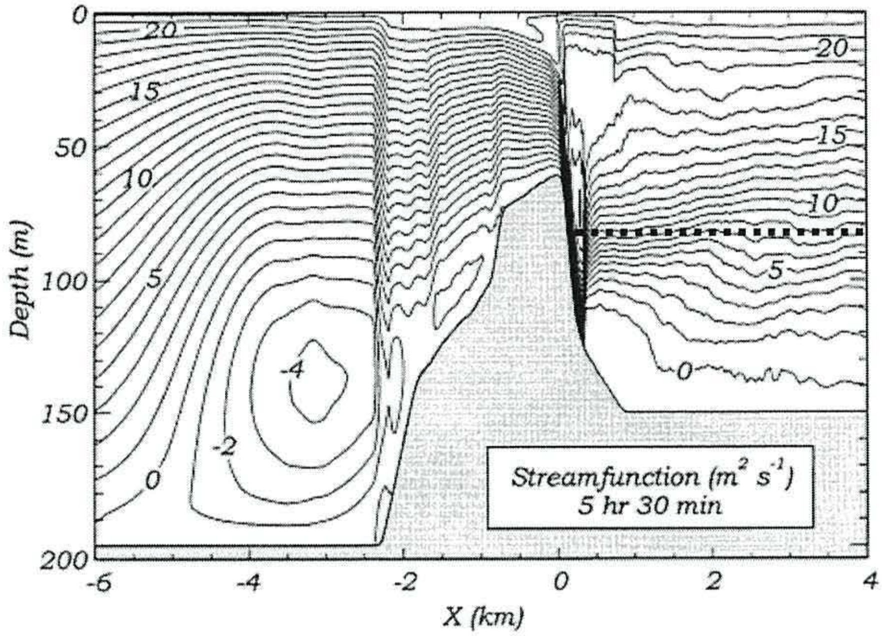

Figure 8.3 – Streamfunction from Knight Inlet simulation (Cummins 2000)
Flow is left to right

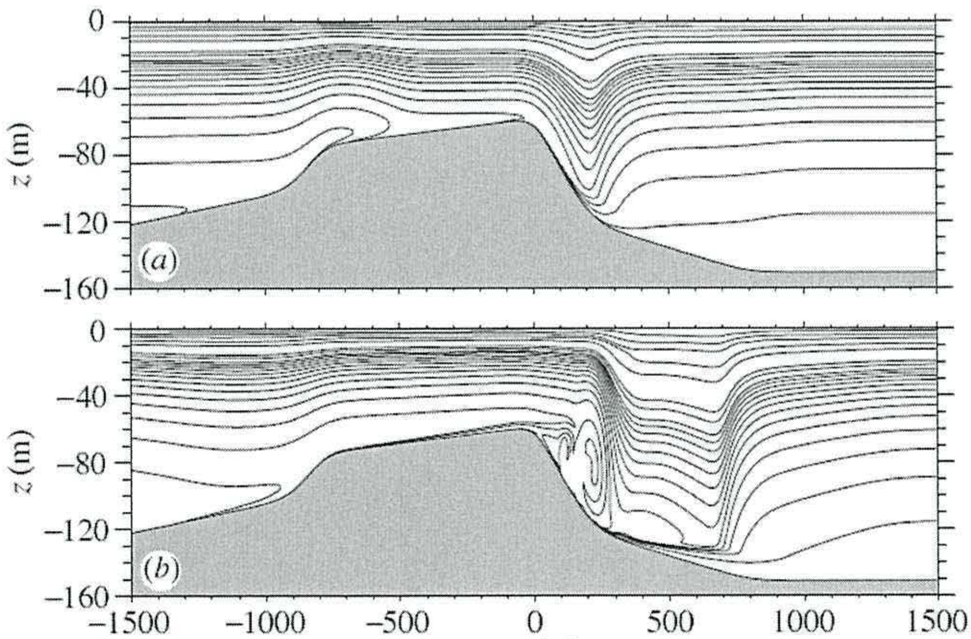

Figure 8.4 – Density Contours from (Lamb 2004) (1hr and 1.5 hrs after slack)

The model output of Lamb (2004) shown in figure 8.4 suggests that flow separation takes place approximately 1hr after slack at a point 20m below the crest of the sill. Half an hour later this point of separation has moved towards the crest at some 7m beneath it.

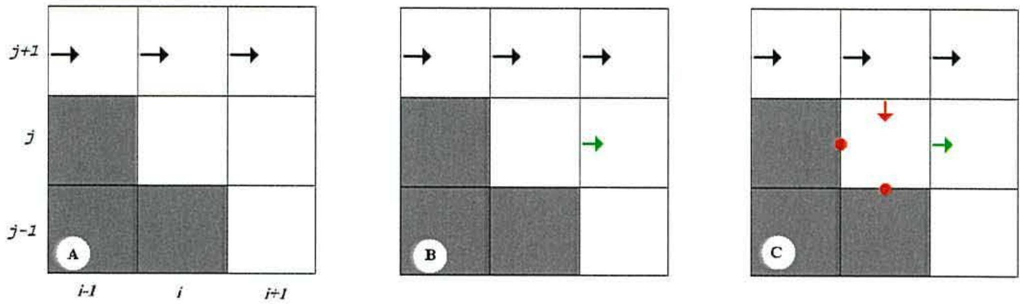

Figure 8.5 – Schematic of hydrostatic model flow

The hydrostatic model approach is outlined in figure 8.5. Step *A* shows a horizontal flow, forced from an open boundary to the left. In step *B* the flow at $u_{(i+ \frac{1}{2},j)}$, shown in green, has been caused by vertical viscous coupling to the velocity above. Step *C* shows the boundary conditions for the cell (i,j) as red circles. Velocities at these points are set to zero, being perpendicular to the boundary. Therefore there is a net negative flux in cell (i,j) which must result in a downwards vertical velocity $w_{(i,j+\frac{1}{2})}$, shown as the red arrow, to maintain continuity. This continues along such a stepped boundary such that the vertical flow is always downward and the flow cannot separate.

8.3 Flow separation

This fundamental process can be modified by any density difference across a sill. Density forced flow separation was suggested by Klymak and Gregg (2003) where a buoyant jet was encouraged to separate. The reverse process, density induced flow attachment, was observed in Loch Etive by Inall *et al.* (2004), here a dense layer flows over the sill and detaches from a point some way down the slope. The current study agrees with these mechanisms in that the tendency for flow separation to take place can be modified by any density difference between the sill flow and basin waters. This is especially evident from the residual flow simulations of the partial and full renewal.

To form a comparison with analytical theory a simple expression to describe situations when flow detaches from the lee of an obstacle (for example an aerofoil or expanding channel) is taken from Schlichting (1960). The apparent simplicity of equation 8.1 belies its derivation, based on the theory of laminar flows against a pressure gradient.

$$\sigma = \frac{\left[U\dfrac{\partial^2 U}{\partial x^2}\right]}{\left[\dfrac{\partial U}{\partial x}\right]^2} = 11.13 \qquad [8.1]$$

For no separation $\sigma > 11.13$ and for separation to occur $\sigma < 11.3$

The derivatives of U can be put in terms of the depth profile of a sill if we assume continuity is maintained. In this instance changes in width are ignored. Inall *et al* (2004) show that the width of the Loch Etive jet increased little with distance from the sill, it separates from the side of the channel and maintains a constant width. They observed flow separation from the shore creating horizontal gyres similar to those in Klymak and Gregg (2001). In Loch Linnhe the horizontal gyre shows flow separation from the northern shore and a horizontal gyre (figure 5.2). The depth profile has been obtained between the Corran sill and a point 1km uploch from the high resolution model domain (Δx = 50m). A quadratic (equation 8.2) has been fitted to this profile (figure 8.6).

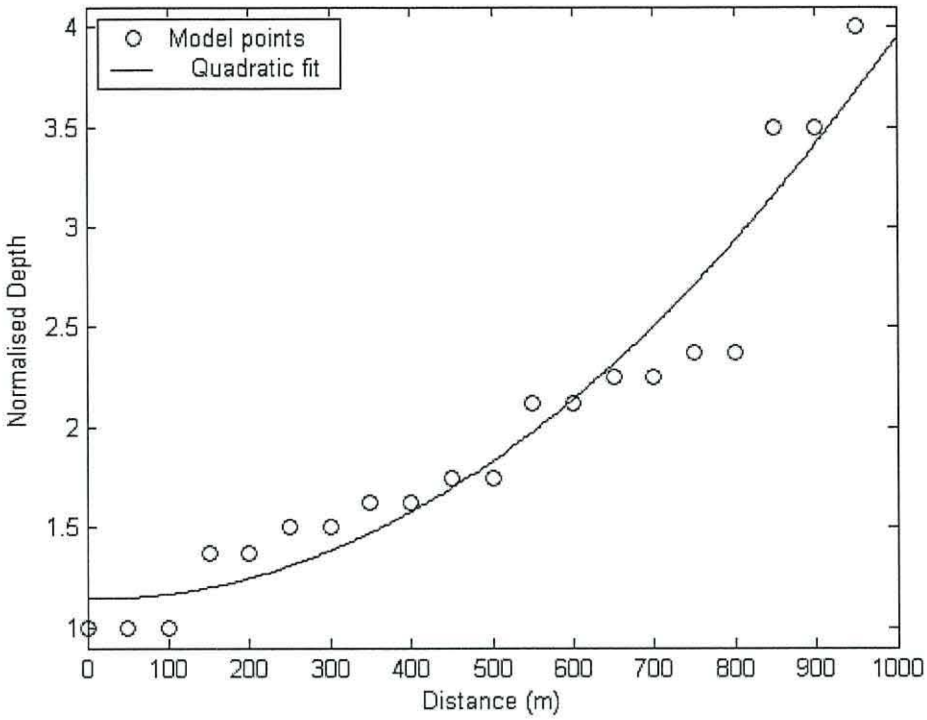

Figure 8.6 – Bathymetry of the lee slope of the Corran sill

$$d = 2.9\times10^{-6}x^2 - 6.6\times10^{-5}x + 1.1 \qquad [8.2]$$

Using continuity arguments (Equations 8.3 and 8.4) we can obtain an expression for the change in depth averaged velocity with respect to x in terms of the sill velocity (U_s) and the bathymetry.

$$U_x = U_s \times \frac{1}{\left[\frac{\partial d}{\partial x}\right]} \qquad [8.3]$$

$$\frac{\partial U}{\partial x} = U_s \times -\frac{\partial d}{\partial x} \qquad [8.4]$$

Substituting these expressions derived from the quadratic fit to the bathymetry into equation 8.5 allows the calculation of σ over this region for various sill velocities.

This is essentially a re-write of equation 8.1 (Schlichting 1960) in terms of these variables.

$$\sigma = \frac{U_s}{\left[\frac{\partial d}{\partial x}\right]} \times \frac{\left[\frac{\partial^2 U}{\partial x^2}\right]}{\left[\frac{\partial U}{\partial x}\right]^2} \qquad [8.5]$$

Including the bathymetry of this particular problem equation 8.5 can be quantified by;

$$\sigma = \frac{U_s}{2.9\times10^{-6}x^2 - 6.6\times10^{-5}x + 1.1} \times \frac{U_s \times -5.8\times10^{-6}}{3.4\times10^{-11}x^2U_s^2 - 7.7\times10^{-10}xU_s + 4.4\times10^{-9}} \qquad [8.6]$$

A plot of equation 8.6 over the 500m in the lee of the sill, varying the sill velocity up to 1ms^{-1}, is presented in figure 8.7. The grey area represents $\sigma > 11$, i.e. attached flow. The reasons for the apparent flow detachment over the entire slope at very low current speeds remains unclear. It may be that some of the assumptions used in deriving this theory regarding the behavior of boundary layers do not hold true at such low speeds. This theory is after all applied to the flow of air over an aerofoil (Schlichting 1960), a different problem entirely.

It can be seen from figure 8.7 that the flow detaches at 450m from the sill crest when current speeds reach 0.03ms^{-1}. The point of detachment then rapidly moves to 175m from the crest as the current rises to 0.20ms^{-1}. As current speeds increase from this point there is only a small change in the point of flow separation. Referring back to the original quadratic for depth the point x=150m is 18.5m. This compares favorably with the flow field presented in figure 5.5c. It is worth noting that this analytical theory, ignoring the effects of the turbulent boundary layer, will cause the flow to apparently separate earlier than it otherwise would. The agreement between this theory and the model may serve to demonstrate the lack of accurate simulation of a turbulent boundary layer by the numerical model.

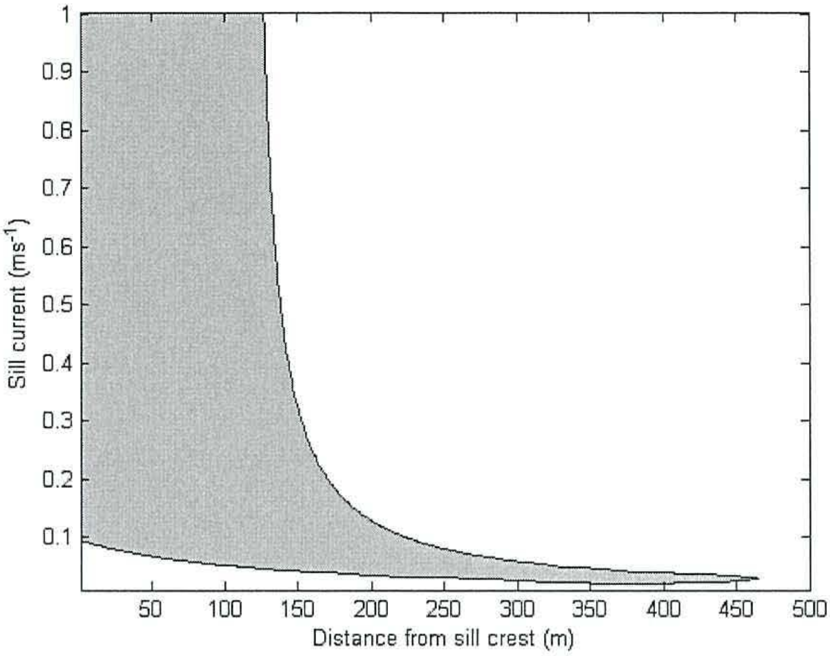

Figure 8.7 – Regions of flow attachment and detachment from theory (Grey area represents attached flow)

Flow separation has been demonstrated at every sill considered in this study. The data (Inall *et al*, 2004) and the model simulations presented by Stashchuk *et al.* (In Press.) both show the jet separating from the Loch Etive sill. In Loch Linnhe the ADCP data (figure 2.19) shows flow separation of flow from the Annat sill on the ebb stream. Complicated by the presence of a horizontal gyre, there are no direct observations of flow separation from the Corran sill. The theory of Schlichting (1960) has been used to show that the flow should separate from the topography at this location, over almost the entire flood stream. The non-hydrostatic model agrees with this theory.

8.4 Renewals

While many studies have concentrated on the identification of renewal events from density data, and the environmental factors thought to control them, very little study has been undertaken into their dynamics. The occurrence of renewal is often controlled by unpredictable forcing so it is co-incidence when observations can be made. The ADCP survey of Allen and Simpson (1998a) was fortunate in that it occurred immediately post renewal. The observations of a density driven component to an intruding jet in the Gareloch (Ellis 2001) were possible because fortuitously renewal was taking place at the time.

Observations by Liungman *et al.* (2001) of a renewal event in a Swedish fjord were used to develop theoretical arguments for water entrainment by a plume. They show that the volume of entrained water was double that of the original inflow, a comparable finding to that of Edwards and Edelsten (1977). Therefore they conclude that this type of mixing is more important in determining the deep water density than mixing by vertical diffusion. It follows that the timing of future renewal events must be controlled by this process and so its simulation is vital to any such work. The simulation of complete renewal by the current model illustrates this mixing. The inflowing water had a density of 0.2kgm^{-3} greater than that at the deepest part of the basin; the residual flows suggest that the uploch flowing layer does not flow along the bottom. The assumption is that it is no longer denser after mixing has taken place during the inflow down the slope. The simple turbulence scheme employed in this application would be expected to underestimate this mixing. The data of Liungman *et al* (2001) would therefore provide a good test of a more complex turbulence scheme.

8.5 Future work

The further development of the non-hydrostatic model presented here is the next logical step in this work. The goal would be to improve its performance and robustness to a point where it can be used as an operational model. In order to achieve finer resolution and therefore model some of the processes deficient in these simulations, gains in model efficiency must be made. The important features currently un-resolvable are the bottom boundary layer and the small scale instabilities that cause the stagnant patch observed in Knight Inlet (Farmer and Armi 1999) and Loch Etive (Inall *et al*, 2004).

The diffusive terms need to be treated in an implicit way to enable the timestep to be increased or grid resolution to be decreased. A non-uniform grid has been used in other simulations to increase computational economy in areas away from small scale processes (Bourgault and Kelley 2004). This step would necessitate the development of a technique other than SOR to solve the Poisson equation as the optimal acceleration parameter is grid scale dependant. The simplest efficiency gains can be obtained by treating the surface boundary as a free-surface, calculating the surface position, and therefore any slope, by the solution of a continuity equation. This establishes the depth averaged pressure gradient and therefore the computationally expensive SOR algorithm only need find the non-hydrostatic component. Preliminary experiments with this system show an order of magnitude decrease in processing time; however it suffers from reflected surface waves at the boundary.

Since iterative schemes were first used in the solution of Poisson equations at the Los Alamos laboratories in the late 1960's, computers have changed remarkably. Large, fast memory and parallel processors are no longer restricted to supercomputers. The reasons for choosing iterative schemes over methods involving inverting sparse matrices may be no longer apply. Iteration is an inherently linear method that cannot be efficiently undertaken in parallel. Inverting a matrix can be distributed over a parallel machine far more effectively. Future non-hydrostatic modellers therefore need to evaluate methodologies on the architecture of modern and future computers.

The turbulence scheme used in the current study is another major cause of discrepancies with the observations. If the grid resolution is increased to allow the simulation of a bottom boundary layer, a higher order turbulence scheme must also be incorporated to this end. The object orientated structure of the model code can be exploited to allow experimentation with more than one of the group of turbulence closure schemes that relate mixing coefficients to turbulence, reviewed in Rodi (1984) and more recently in Burchard (2002).

Future observations should include the accurate measurement of the boundary layer over a sill, and details of flow separation. It is only by the accurate simulation of such phenomena that the dynamics of these systems can be modelled. There is a bias of turbulence observations towards the measurement and simulation of vertical mixing parameters at the expense of their horizontal equivalents. It has been shown in the review of similar models that the horizontal eddy viscosity is often used simply to maintain computational stability. The most complex mathematical formulation for this parameter is that used by Stacey *et al* (1995). The extensive use of higher order turbulence schemes in the vertical (Burchard, 2002) has no equivalent in the horizontal. It will only be by observations, perhaps using horizontal acoustic Doppler techniques in channels, coupled with models, that this knowledge gap can be filled.

8.6 Conclusions

The non-hydrostatic model presented in this thesis shows that the accurate simulation of the internal tide in Upper Loch Linnhe (and similar lochs bounded by shallow sills) can only be accomplished with a non-hydrostatic model. The process of flow separation, and its accurate simulation, is vital to the formation of an internal tide by water flowing over a sill in this system.

The lack of agreement using the hydrostatic model of Gillibrand (1993) with the data necessitated the creation of a new model free from the constraints of the hydrostatic approximation. This model has been validated by its ability to recreate processes important in the dynamics of sealochs. This includes the effects of density cascades and internal waves. Provided the flow is considered constant across the channel, this model reproduces the dynamics at far less computational cost than a 3-dimensional non-hydrostatic model.

The model output suggests that there are three possible processes in Upper Loch Linnhe that contribute to the formation of an internal tide in a jet-fjord. They are:

1. The Bernoulli Effect in the lee of the sill.
2. Aspiration of a vertical density gradient up a slope at the opposite end of the basin to the jet.
3. Time varying inflowing density causing a downwelling at toward the end of the flood stream.

Processes 2 and 3 can reinforce one another causing a mode-1 internal tide if conditions are suitable.

Appendix 1 - One Dimensional Channel Model

In order to give tidal boundary conditions for models of Upper Loch Linnhe a branching channel model was developed. This was validated against data from the Admiralty tide tables and a tidal diamond.

Methodology

1D Equations of Motion

The momentum equation for flow in a one-dimensional channel can be written as shown in equation A1.1. The two terms on the left are the temporal and advective accelerations respectively. These accelerations are balanced by three terms on the right, the sea-surface slope, friction due to stress on the seabed, and viscous forces due to turbulent eddies.

$$\frac{\partial U}{\partial t} + U\frac{\partial U}{\partial x} = -g\frac{\partial \eta}{\partial x} - g\frac{U|U|}{C^2 R} - A_h\frac{\partial^2 U}{\partial x^2} \qquad \text{[A1.1]}$$

The seabed friction term has been parameterised using Manning's equation for the Chézy coefficient (C), given by $C = R^{1/6}n^{-1}$. Where R is the hydraulic radius of the channel and n is Manning's roughness co-efficient.

Continuity dictates that;

$$\frac{\partial \eta}{\partial t} + \frac{\partial (UA)}{\partial x} = 0 \qquad \text{[A1.2]}$$

where A is the cross sectional area, and, assuming the channel to be triangular in section, is given by $A = ½.B.d$

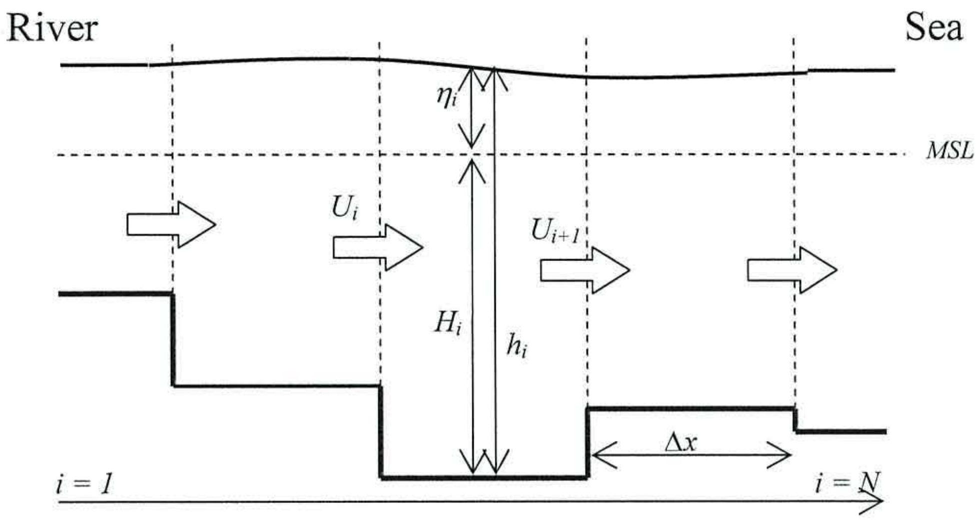

Figure A1.1 – Numerical grid for the 1D model

Equations A1.1 and A1.2 are subject to the boundary conditions $U_1 = 0$ (or U_1 = river flow) and $\eta_{i=N}$ is specified over time from tidal harmonics. The channel width (B) and the depth relative to Mean Sea Level (H) are specified at η points, half way between U points, and have been estimated from Admiralty Chart number 2380.

The parameters n (Manning's roughness coefficient) and A_h (the horizontal eddy viscosity) are specified across the model domain and have been used to tune the model.

The finite difference approximation to the equations use centred time differences with an Asselin filter (Asselin, 1972). The friction terms are lagged one time step and the advective term is a combination of centred and upwind differences. The other terms are entirely centred differenced in space.

Friction term

Values for Manning's roughness coefficient (n) are outlined for rivers in table A1.1 (Chadwick and Morfett, 1998).

Table A1.1 – Values for Manning's roughness coefficient

Channel type	**Manning's n**
Earth, straight	0.02 – 0.025
Earth, meandering	0.03 – 0.05
Gravel (75-150mm), straight	0.03 – 0.04
Gravel (75-150mm), winding or braided	0.04 – 0.08

Expressions for the hydraulic radius of square, trapezoidal and circular channels have been given by Chadwick and Morfett (2002). In this study a V shaped channel has been assumed; therefore the hydraulic radius, the cross sectional area divided by the wetted perimeter, is given by equation A1.3.

$$R = \frac{Bh}{4\sqrt{h^2 + \left(\frac{1}{2}B\right)^2}} \qquad \text{[A1.3]}$$

The assumption often used in estuaries and tidal channels that the water depth is small in comparison to the width enables the friction term to be simplified to Equation A1.4 (Bowen and Pinless, 1977).

$$\frac{-C_D \cdot U|U|}{h^{4/3}} \qquad \text{[A1.4]}$$

This type of friction term was originally used with the model, along with the assumption that the channel was square in cross section with a width equal to the mean width of the section. Tuning the model to reproduce the lag of high water required the co-efficient of friction (C_D) to be over an order of magnitude higher than the accepted value of $\cong 2.5\times10^{-3}$. This also gave a smaller tidal range at Loch Eil Head than at the open boundary. I have concluded from this that the simplifications used in deriving this friction term cannot be applied to channels of the geometry of sea lochs, where it is better to use Manning's full equation.

Branching Scheme

Side branches are assumed to join perpendicular to the main channel flow such that there is no transfer of momentum between the branch and the main channel. The connection is made via the continuity equation by evaluating the flux from the branch to the main channel. This involves adding a term to the continuity equation (A1.2) to account for a change of depth due to flux of water from the branch. The discretised continuity expression is given by equation A1.5, the final term is only evaluated at a cell in the main channel where a branch connects. The index j is the final cell in the branch.

$$\begin{aligned} h_i^{t+1} = h_i^{t-1} &- \frac{2\Delta t}{\Delta x}\left(u_{i+1}^{t}\frac{\left[B_i h_i^t + B_{i+1} h_{i+1}^t\right]}{2} - u_i^t \frac{\left[B_{i-1} h_{i-1}^t + B_i h_i^t\right]}{2}\right) \\ &- \frac{2\Delta t}{\Delta x \cdot B_i}\left(u_{j+1}^{t}\left[\frac{B_j + B_{j+1}}{2}\cdot\frac{h_j^t + h_i^t}{2}\right]\right) \end{aligned} \qquad [A1.5]$$

Open Boundary Forcing

Harmonic analysis of tide gauge data was undertaken by Allen (1995); 5 harmonic constants have been extracted from a time series of approximately one month. The location is approximately 10km south of Corran narrows; table A1.2 gives the harmonic constants. The sea level relative to chart datum (*Zo*) was inferred for this location by a linear interpolation of the values given for Corpach and Port Appin (data supplied by the Proudman Oceanographic Laboratory).

Table A1.2 – Harmonic constants used to force open boundary

Constituent	Amplitude (m)	Phase Lag (°)
M_2	1.18	168.0
S_2	0.50	206.6
N_2	0.24	148.8
MM	0.16	222.7
MSF	0.11	297.6

The phase of each constituent relative to the equilibrium tide has been taken from Admiralty data, along with the nodal factors for the middle of each year. A linear interpolation of the nodal factors between years is undertaken by the model when calculating the boundary elevation.

Comparison with data

Times of high and low waters

The model has been tuned by varying the co-efficient of bottom roughness such that the lag of high water is reproduced across the model domain. For the purposes of this tuning exercise the model was forced using harmonic data from GLA tide gauge, and a tidal cycle of the same amplitude of mean springs was chosen. This amplitude is the sum of M_2 and S_2 from table A1.2 (1.68m) giving a mean spring tidal range of 3.36m.

Table A1.3 – Delays of High and Low waters

***RE* Oban**	**Times (min)**	
	HW	LW
Corran	+07	+04
Corpach	+20	+40
Loch Eil Head	+45	+65
Loch Leven Head	+45	+45

The delay of high and low waters between Corran and Loch Eil head has been determined from model output (figure A1.2) to be 35 minutes for high water and 65 minutes for low water. From Admiralty data the lag should be 38 minutes for high water and 61 minutes for low water. The small discrepancy can be attributed to the fact that the width of the modelled loch is not permitted to change over the tidal cycle. While this holds true for the majority of the system, with steep sides, it is not true for the area immediately seaward of Corran Point, where the channel width changes appreciably between high and low water.

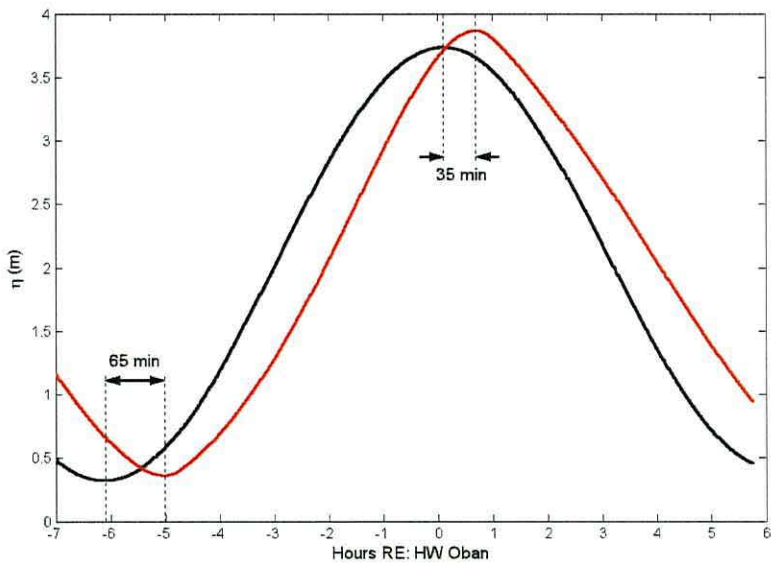

Figure A1.2 – Sea surface elevation Corran Narrows (black) & Loch Eil Head (red) from model output

A comparison of times of the tidal elements in the Loch Leven branch of the model shows poor agreement. The model gives the delay of LW relative to Oban as 37 minutes, an underestimate by 8 minutes. The arrival of HW at the head of Loch Leven should be 45 minutes after HW Oban; the model gives 5 minutes. The reason for this disagreement is again geometric simplification of the channel at Caolas nan Con, the sill between the upper and central basins of Loch Leven. In places the width of the Channel at HW is double that at LW. During the high part of the tidal cycle a significant proportion of the flow would be over these extremely shallow mud flats, resulting in a large amount of bed friction not accounted for in the model formulation. The small volume of this upper basin coupled with the large distance from the area of immediate interest in this study reduces the impact of this upon the tidal streams in Upper Loch Linnhe.

Tidal diamond data for Corran Narrows

The tidal diamond data published on chart 2380 describes the stream over the Corran Narrows sill. The principal axis of the velocities has been calculated as 024.5°T. At maximum flood and ebb the stream deviates from this towards the east, however by less than 12 degrees, allowing along loch components to be taken about the principal axis for comparison against the model.

A comparison of seaward velocity derived from the model and from the tidal diamond data for Corran Narrows is presented in figure A1.3. The ratio of the scales of the two axes is 1:1.4; this accounts for the relationship between the sectionally averaged velocity outputted by the model, and the surface velocity measured in the centre of the channel.

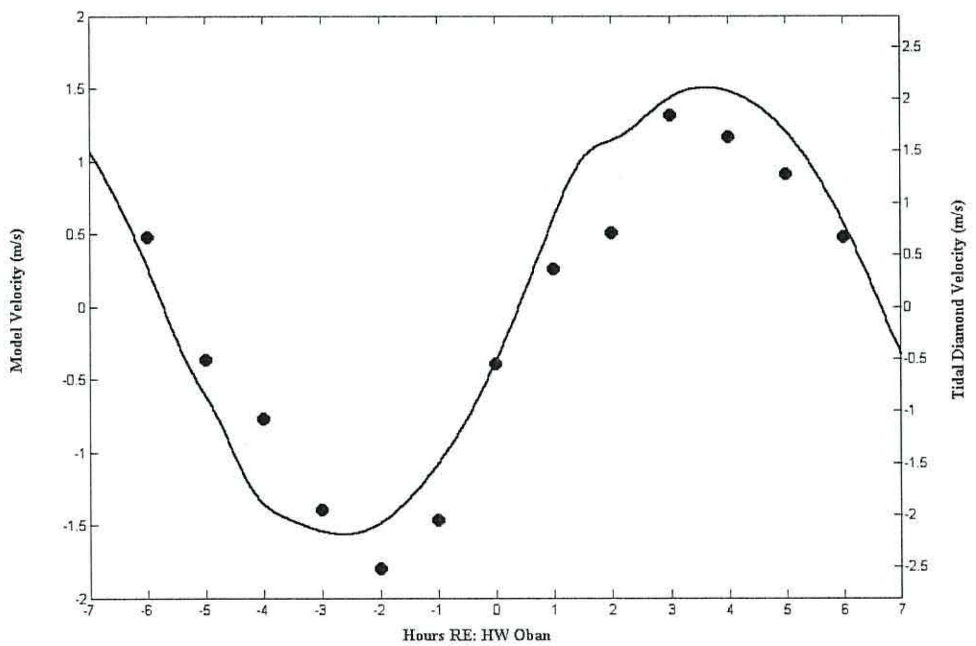

Figure A1.3 – Stream at Corran Narrows derived from model (line) and tidal diamond (dots)

The model and tidal diamond data are out of phase during the flood, (HW -6 to HW), the time of maximum flood being given by the model as HW -2:30 while the tidal diamond gives HW-2. However, the reduction in the acceleration of the ebb stream 2 hours after HW Oban is reproduced by the model, although an underestimate. There is a similar reduction on the flood phase, however less pronounced, 4 hours before HW.

Summary

This simple channel model has been calibrated against the available data to give sectionally averaged velocities and sea-surface elevations across the model domain. While the assumptions involved in 1-D models cannot capture the full physics of the problem it is an acceptable description, at least in the Upper Loch Linnhe branch of the system.

Appendix 2 - Solution of a 2-D Poisson equation modified to account for width variation

The Poisson equation for pressure (equation A2.1) has the channel width introduced (equation A2.2) from Bourgault and Kelley (2004).

$$\frac{\partial^2 P}{\partial x^2}+\frac{\partial^2 P}{\partial z^2}=F \qquad \text{[A2.1]}$$

$$\frac{\partial}{\partial x}\left(B\frac{\partial P}{\partial x}\right)+\frac{\partial}{\partial z}\left(B\frac{\partial P}{\partial z}\right)=F \qquad \text{[A2.2]}$$

This equation has been solved on the grid shown in chapter 3, figure 3.3; the discrete expression for the second derivative in the x direction is then given by;

$$\frac{\left[\dfrac{B_{i+\frac{1}{2},j}\left(P_{i+1,j}-P_{i,j}\right)}{\Delta x}-\dfrac{B_{i-\frac{1}{2},j}\left(P_{i,j}-P_{i-1,j}\right)}{\Delta x}\right]}{\Delta x} \qquad \text{[A2.3]}$$

Expanding the brackets (equation A2.4) and collecting terms together (equation A2.5) yields equation A2.6.

$$\frac{B_{i+\frac{1}{2},j}P_{i+1,j}-B_{i+\frac{1}{2},j}P_{i,j}-B_{i-\frac{1}{2},j}P_{i,j}+B_{i-\frac{1}{2},j}P_{i-1,j}}{(\Delta x)^2} \qquad \text{[A2.4]}$$

$$\frac{-P_{i,j}\left(B_{i+\frac{1}{2},j}+B_{i-\frac{1}{2},j}\right)+B_{i+\frac{1}{2},j}P_{i+1,j}+B_{i-\frac{1}{2},j}P_{i-1,j}}{(\Delta x)^2} \qquad [A2.5]$$

$$\frac{-P_{i,j}+\left[\dfrac{B_{i+\frac{1}{2},j}P_{i+1,j}+B_{i-\frac{1}{2},j}P_{i-1,j}}{\left(B_{i+\frac{1}{2},j}+B_{i-\frac{1}{2},j}\right)}\right]}{\left[\dfrac{(\Delta x)^2}{\left(B_{i+\frac{1}{2},j}+B_{i-\frac{1}{2},j}\right)}\right]} \qquad [A2.6]$$

Including the term for the 2nd derivative in the y direction the full Poisson equation becomes;

$$\left(\frac{-P_{i,j}+\left[\dfrac{B_{i+\frac{1}{2},j}P_{i+1,j}+B_{i-\frac{1}{2},j}P_{i-1,j}}{\left(B_{i+\frac{1}{2},j}+B_{i-\frac{1}{2},j}\right)}\right]}{\left[\dfrac{(\Delta x)^2}{\left(B_{i+\frac{1}{2},j}+B_{i-\frac{1}{2},j}\right)}\right]}\right)+\left(\frac{-P_{i,j}+\left[\dfrac{B_{i,j+\frac{1}{2}}P_{i,j+1}+B_{i,j-\frac{1}{2}}P_{i,j-1}}{\left(B_{i,j+\frac{1}{2}}+B_{i,j-\frac{1}{2}}\right)}\right]}{\left[\dfrac{(\Delta z)^2}{\left(B_{i,j+\frac{1}{2}}+B_{i,j-\frac{1}{2}}\right)}\right]}\right)=F_{i,j} \qquad [A2.7]$$

The first two terms can be re-arranged and split into four terms such that the pressure at cell i,j is separated giving;

$$\frac{-P_{i,j}}{\left[\dfrac{(\Delta x)^2}{B_{i+\frac{1}{2},j}+B_{i-\frac{1}{2},j}}\right]}+\frac{-P_{i,j}}{\left[\dfrac{(\Delta z)^2}{B_{i,j+\frac{1}{2}}+B_{i,j-\frac{1}{2}}}\right]}+\frac{\left[\dfrac{B_{i+\frac{1}{2},j}P_{i+1,j}+B_{i-\frac{1}{2},j}P_{i-1,j}}{B_{i+\frac{1}{2},j}+B_{i-\frac{1}{2},j}}\right]}{\left[\dfrac{(\Delta x)^2}{B_{i+\frac{1}{2},j}+B_{i-\frac{1}{2},j}}\right]}+\frac{\left[\dfrac{B_{i,j+\frac{1}{2}}P_{i,j+1}+E^{S}P_{i,j-1}}{B_{i,j+\frac{1}{2}}+B_{i,j-\frac{1}{2}}}\right]}{\left[\dfrac{(\Delta z)^2}{B_{i,j+\frac{1}{2}}+B_{i,j-\frac{1}{2}}}\right]}=F_{i,j} \qquad \text{[A2.8]}$$

The first two terms are re-arranged for $P_{i,j}$ and the last two terms are simplified by cancelling the double-decker fractions giving;

$$-P_{i,j}\left(\frac{B_{i+\frac{1}{2},j}+B_{i-\frac{1}{2},j}}{(\Delta x)^2}+\frac{B_{i,j+\frac{1}{2}}+B_{i,j-\frac{1}{2}}}{(\Delta z)^2}\right)+\left[\frac{B_{i+\frac{1}{2},j}P_{i+1,j}+B_{i-\frac{1}{2},j}P_{i-1,j}}{(\Delta x)^2}\right]+\left[\frac{B_{i,j+\frac{1}{2}}P_{i,j+1}+B_{i,j-\frac{1}{2}}P_{i,j-1}}{(\Delta z)^2}\right]=F_{i,j} \qquad \text{[A2.9]}$$

subtracting $F_{i,j}$ gives

$$-P_{i,j}\left(\frac{B_{i+\frac{1}{2},j}+B_{i-\frac{1}{2},j}}{(\Delta x)^2}+\frac{B_{i,j+\frac{1}{2}}+B_{i,j-\frac{1}{2}}}{(\Delta z)^2}\right)+\left[\frac{B_{i+\frac{1}{2},j}P_{i+1,j}+B_{i-\frac{1}{2},j}P_{i-1,j}}{(\Delta x)^2}\right]+\left[\frac{B_{i,j+\frac{1}{2}}P_{i,j+1}+B_{i,j-\frac{1}{2}}P_{i,j-1}}{(\Delta z)^2}\right]-F_{i,j}=0 \qquad \text{[A2.10]}$$

This can then be re-arranged for $P_{i,j}$ to give equation A2.11, an expression for the Gauss-Seidel iterative method.

$$P_{i,j} = \left(\frac{(\Delta x)^2}{B_{i+\frac{1}{2},j} + B_{i-\frac{1}{2},j}} + \frac{(\Delta y)^2}{B_{i,j+\frac{1}{2}} + B_{i,j-\frac{1}{2}}} \right) \times \left(\left[\frac{B_{i+\frac{1}{2},j} P_{i+1,j} + B_{i-\frac{1}{2},j} P_{i-1,j}}{(\Delta x)^2} \right] + \left[\frac{B_{i,j+\frac{1}{2}} P_{i,j+1} + B_{i,j-\frac{1}{2}} P_{i,j-1}}{(\Delta z)^2} \right] - F_{i,j} \right) \qquad [A2.11]$$

The Successive Over Relaxation (SOR) algorithm requires the correction to be multiplied by the acceleration parameter. This is achieved in equation A2.12, the method of solution of the Poisson equation in the non-hydrostatic model developed in this thesis.

$$P_{i,j} = (1-\omega) P_{i,j} + \frac{\omega}{\left(\frac{B_{i+\frac{1}{2},j} + B_{i-\frac{1}{2},j}}{(\Delta x)^2} + \frac{B_{i,j+\frac{1}{2}} + B_{i,j-\frac{1}{2}}}{(\Delta z)^2} \right)} \times \left(\left[\frac{B_{i+\frac{1}{2},j} P_{i+1,j} + B_{i-\frac{1}{2},j} P_{i-1,j}}{(\Delta x)^2} \right] + \left[\frac{B_{i,j+\frac{1}{2}} P_{i,j+1} + B_{i,j-\frac{1}{2}} P_{i,j-1}}{(\Delta z)^2} \right] - F_{i,j} \right) \qquad [A2.12]$$

The solution sequence is outlined in the flow diagram overleaf in figure A2.1

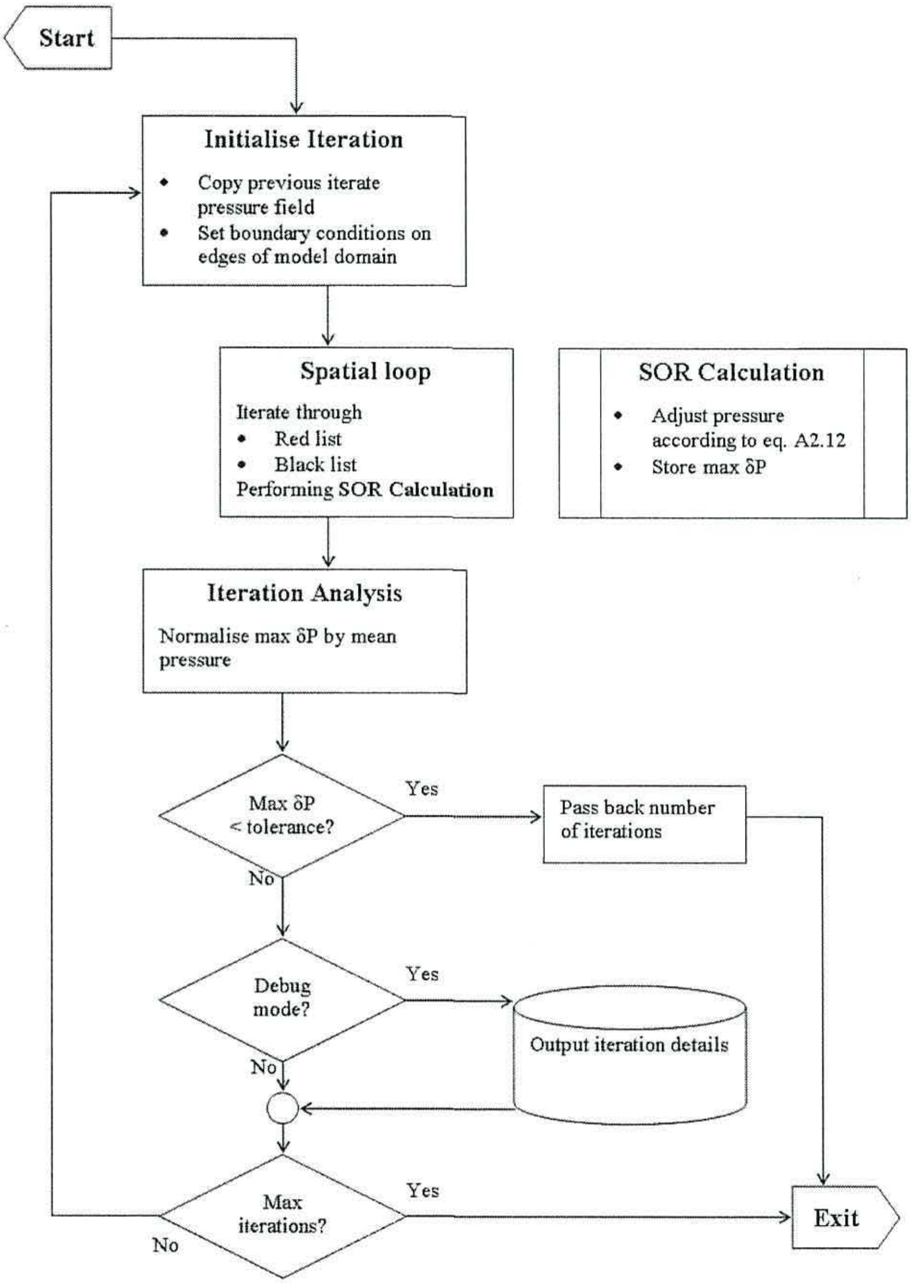

Figure A2.1 – SOR Solution sequence

References

Allen, G., 1995: Inflows, mixing and the internal tide of upper Loch Linnhe, School of Ocean Sciences, University of Wales, 125.

Allen, G. L. and J. H. Simpson, 1998a: Deep water inflows to upper Loch Linnhe. *Estuarine Coastal and Shelf Science*, **47,** 487-498.

——, 1998b: Reflection of the internal tide in upper Loch Linnhe, a Scottish fjord. *Estuarine Coastal and Shelf Science*, **46,** 683-701.

——, 2002: The response of a strongly stratified fjord to energetic tidal forcing. *Estuarine Coastal and Shelf Science*, **55,** 629-644.

Armaly, B. F., F. Durst, J. C. F. Pereira, and B. Schonung, 1983: Experimental and theoretical investigation of backward-facing step flow. *Journal of Fluid Mechanics*, **127,** 473-496.

Armi, L., 1986: The hydraulics of 2 flowing layers with different densities. *Journal of Fluid Mechanics*, **163,** 27-&.

Asselin, 1972: Frequency filter for time integration. *Monthly Weather Review*, **100**, 487-490.

Baines, P. G., 1984: A unified description of 2-layer flow over topography. *Journal of Fluid Mechanics*, **146,** 127-167.

Booth, D. A., 1987: Some consequences of a flood tide front in Loch Creran. *Estuarine Coastal and Shelf Science*, **24,** 363-375.

Bourgault, D. and D. E. Kelley, 2004: A laterally averaged non-hydrostatic ocean model. *Journal of Atmospheric and Oceanic Technology*, **21,** 1910-1924.

Bowden, K. F. and P. Hamilton, 1975: Some experiments with a numerical-model of circulation and mixing in a tidal estuary. *Estuarine and Coastal Marine Science*, **3,** 281-301.

Bowen, A. J. and S. J. Pinless, 1977: The response of an estuary to the closure of a mobile barrier; Richmond barrier on the upper Thames Estuary. *Estuarine and Coastal Marine Science*, **5**, 197-208.

Brandt, P., A. Rubino, D. Quadfasel, W. Alpers, J. Sellschopp, and H. Fiekas, 1999: Evidence for the influence of Atlantic–Ionian stream fluctuations on the tidally induced internal dynamics in the strait of Messina. *Journal of Physical Oceanography*, **29,** 1071-1080.

Buitenhuis, 2003: The velocity structure of estuarine circulation in fjords, University of Bergen, 74.

Burchard, H., 2002: *Applied turbulence modelling in marine waters. Lecture notes in Earth sciences*, Springer, 212 pp.

Campbell, A. R., J. H. Simpson, and G. L. Allen, 1998: The dynamical balance of flow in the Menai Strait. *Estuarine Coastal and Shelf Science*, **46,** 449-455.

Cannon, G. A., J. R. Holbrook, and D. J. Pashinski, 1990: Variations in the onset of bottom-water intrusions over the entrance sill of a fjord. *Estuaries*, **13,** 31-42.

Chadwick, A. and J. Morfett, 1998: *Hydraulics in civil and environmental engineering.* 3rd ed. Spon Press.

Chorin, A., 1968: Numerical solution of the Navier-Stokes equations. *Mathematics of Computation*, **22,** 745-762.

Cummins, P. F., 2000: Stratified flow over topography: Time-dependent comparisons between model solutions and observations. *Dynamics of Atmospheres and Oceans*, **33,** 43-72.

Dunbar, D. S. and R. W. Burling, 1987: A numerical-model of stratified circulation in Indian Arm, British-Columbia. *Journal of Geophysical Research-Oceans*, **92,** 13075-13105.

Dyer, K., 1996: *Estuaries a physical introduction*. John Wiley.

Edwards, A. and D. J. Edelsten, 1977: Deep water renewal of Loch Etive: A three basin Scottish Fjord. *Estuarine Coastal and Shelf Science*, **5**, 575 - 595.

Edwards, A. and F. Sharples, 1986: *Scottish sea lochs: A catalogue*. Scottish Marine Biological Association, 110 pp.

Ellis, K. M., 2001: Aspects of the tide in the Gareloch, University of Wales, 68.

Farmer, D. M. and L. Armi, 1999: Stratified flow over topography: The role of small-scale entrainment and mixing in flow establishment. *Proceedings of the Royal Society of London Series a-Mathematical Physical and Engineering Sciences*, **455,** 3221-3258.

Farmer, D. M. and H. J. Freeland, 1983: The Physical Oceanography of Fjords. *Progress in Oceanography*, **12**, 147-220.

Farmer, D. M. and L. Armi, 1986: Maximal 2-layer exchange over a sill and through the combination of a sill and contraction with barotropic flow. *Journal of Fluid Mechanics*, **164,** 53-&.

Farmer, D. M. and T. Osborne, 1976: The influence of wind on the surface layer of a stratified inlet: Part 1. Observations. *Journal of Physical Oceanography*, **6,** 931 - 940.

Farmer, D. M. and J. D. Smith, 1980: Tidal interaction of stratified flow with a sill in knight inlet. *Deep-Sea Research Part a-Oceanographic Research Papers*, **27,** 239-&.

Gillibrand, P. A., 1993: Circulation and mixing in a Scottish sealoch, School of Ocean Sciences, University of Wales, 133.

——, 2001: Calculating exchange times in a Scottish fjord using a two-dimensional, laterally-integrated numerical model. *Estuarine Coastal and Shelf Science*, **53,** 437-449.

Gillibrand, P. A. and W. R. Turrell, 1997: The use of simple models in the regulation of the impact of fish farms on water quality in Scottish sea lochs. *Aquaculture*, **159,** 33-46.

Gillibrand, P. A., W. R. Turrell, D. C. Moore, and R. D. Adams, 1996: Bottom water stagnation and oxygen depletion in a Scottish sea loch. *Estuarine Coastal and Shelf Science*, **43,** 217-235.

Griebel, M., T. Dornseifer, and T. Neunhoeffer, 1998: *Numerical simulation in fluid dynamics. Siam monographs on mathematical modelling and computation*, SIAM.

Hamilton, P., 1975: Numerical-model of vertical circulation of tidal estuaries and its application to Rotterdam-waterway. *Geophysical Journal of the Royal Astronomical Society*, **40,** 1-21.

Hansen, D. and M. Rattray, 1966: New dimensions in estuary classification. *Limnology and Oceanography*, **6,** 319-326.

Hill, D. and M. Foda, 1988: Subharmonic resonance of oblique interfacial waves by a progressive surface wave. *Proceedings of the Royal Society of London Series a-Mathematical Physical and Engineering Sciences*, **454,** 1129-1144.

Hirt, C. W. and B. D. Nichols, 1981: Volume of fluid (VOF) method for the dynamics of free boundaries. *Journal of Computational Physics*, **39,** 201-225.

Hirt, C.W., Nichols B.D., and N. Romero, 1975: SOLA – A numerical solution algorithm for transient fluid flows. Technical report LA-5852, Los Alamos National Laboratory, USA.

Inall, M., F. Cottier, C. Griffiths, and T. Rippeth, 2004: Sill dynamics and energy transformation in a jet fjord. *Ocean Dynamics*, **54,** 307-314.

Inall, M., T. Rippeth, C. Griffiths, and P. Wiles, 2005: Evolution and distribution of TKE production and dissipation within stratified flow over topography. *Geophysical Research Letters*, **32**.

James, I. D., 1986: A front-resolving sigma coordinate sea model with a simple hybrid advection scheme. *Applied Mathematical Modelling*, **10,** 87-92.

——, 1996: Advection schemes for shelf sea models. *Journal of Marine Systems*, **8,** 237-254.

Janjic, Z. I., J. P. Gerrity, and S. Nickovic, 2001: An alternative approach to non-hydrostatic modelling. *Monthly Weather Review*, **129,** 1164-1178.

Johns, B. and J. X. Xing, 1993: 3-dimensional modelling of the free-surface turbulent-flow of water over a bedform. *Continental Shelf Research*, **13,** 705-721.

Kerner, J., 1985: Documentation and verification of a finite-difference approximation of a laterally averaged estuarine model, State University of New York, 243.

Klymak, J. and M. C. Gregg, 2001: Three-dimensional nature of flow near a sill. *Journal of Geophysical Research*, **106,** 22295-22311.

——, 2003: The role of upstream waves and a downstream density pool in the growth of lee waves: Stratified flow over the knight inlet sill. *Journal of Physical Oceanography*, **33,** 1446-1461.

Lamb, K. G., 2004: On boundary-layer separation and internal wave generation at the knight inlet sill. *Proceedings of the Royal Society of London Series a-Mathematical Physical and Engineering Sciences*, **460,** 2305-2337.

Lane-Serff, G. F., 2002: Overview of topographic and boundary effects. 2nd Meeting on the Physical Oceanography of Sea Straits, Villefranche.

Lane-Serff, G. F., D. A. Smeed, and C. R. Postlethwaite, 2000: Multi-layer hydraulic exchange flows. *Journal of Fluid Mechanics*, **416,** 269-296.

Lavelle, J. W., E. D. Cokelet, and G. A. Cannon, 1991: A model study of density intrusions into and circulation within a deep, silled estuary - Puget Sound. *Journal of Geophysical Research-Oceans*, **96,** 16779-16800.

Liungman, O., L. Rydberg, and C. G. Goransson, 2001: Modeling and observations of deep water renewal and entrainment in a Swedish sill fjord. *Journal of Physical Oceanography*, **31,** 3401-3420.

Marshall, J., C. Hill, L. Perelman, and A. Adcroft, 1997: Hydrostatic, quasi-hydrostatic, and non-hydrostatic ocean modelling. *Journal of Geophysical Research-Oceans*, **102,** 5733-5752.

Masson, D. and P. F. Cummins, 2000: Fortnightly modulation of the estuarine circulation in Juan de Fuca strait. *Journal of Marine Research*, **58,** 439-463.

McIntosh, A., C. Moffat, G. Packer, and L. Webster, 2004: Polycyclic aromatic hydrocarbon (PAH) concentration and composition determined in farmed blue mussels (*mytilus edulis*) in a sea loch pre- and post-closure of an aluminium smelter. *Journal of Environmental Monitoring*, **6,** 209-218.

Munk, W. and E. Anderson, 1948: Notes on a theory of the thermocline. *Journal of Marine Research*, **8,** 276-295.

Overnell, J., 2002: Manganese and iron profiles during early diagenesis in Loch Etive, Scotland. Application of two diagenetic models. *Estuarine Coastal and Shelf Science*, **54,** 33-44.

Overnell, J., A. Edwards, B. Grantham, S. Harvey, K. Jones, J. Leftley, and D. Smallman, 1995: Sediment–water column coupling and the fate of the spring phytoplankton bloom in Loch Linnhe, a Scottish fjordic sea-loch. Sediment processes and sediment–water fluxes. *Estuarine Coastal and Shelf Science*, **41,** 1-19.

Overnell, J. and S. Young, 1995: Sedimentation and carbon flux in a Scottish sea loch, Loch Linnhe. *Estuarine Coastal and Shelf Science*, **41,** 361-376.

Pawlowicz, R., B. Beardsley, and S. Lentz, 2002: Classical tidal harmonic analysis including error estimates in Matlab using t-tide. *Computers and Geosciences*, **28.**

Pond, S. and G. Pickard, 1998: *Introductory dynamical oceanography*. 2nd ed. Butterworth-Heinemann.

Prandle, D., 1985: On salinity regimes and the vertical structure of residual flows in narrow tidal estuaries. *Estuarine Coastal and Shelf Science*, **20,** 615-635.

Reed, M., O. Johansen, P. Brandvik, P. Daling, A. Lewis, R. Fiocco, D. Mackay, and R. Prentki, 1999: Oil spill modelling towards the close of the 20th century: Overview of the state of the art. *Spill Science & Technology Bulletin*, **5,** 3-16.

Rodi, W., 1984: Turbulence models and their application in hydraulics - a state of the art review, Technical Report, International Association for Hydraulic Research, Delft, The Netherlands.

Schlichting, H., 1960: *Boundary layer theory*. 4th ed. McGraw-Hill.

Smith, R. B., 1985: On severe downslope winds. *Journal of the Atmospheric Sciences*, **42,** 2597-2603.

Smith, T. J. and H. S. Takhar, 1981: A mathematical-model for partially mixed estuaries using the turbulence energy equation. *Estuarine Coastal and Shelf Science*, **13,** 27-45.

Souza, A. J. and I. D. James, 1996: A two-dimensional (*x-z*) model of tidal straining in the Rhine ROFI. *Continental Shelf Research*, **16,** 949-966.

Stacey, M. W., 2005: Review of the partition of tidal energy in five Canadian fjords. *Journal of Coastal Research*, **21,** 731-750.

Stacey, M. W. and Y. Gratton, 2001: The energetics and tidally induced reverse renewal in a two-silled fjord. *Journal of Physical Oceanography*, **31,** 1599-1615.

Stacey, M. W., S. Pond, and A. N. Cameron, 1991: The comparison of a numerical-model to observations of velocity and scalar data in Burrard Inlet and Indian Arm, British-Columbia. *Journal of Geophysical Research-Oceans*, **96,** 10777-10790.

Stacey, M. W., S. Pond, and Z. P. Nowak, 1995: A numerical-model of the circulation in knight inlet, British-Columbia, Canada. *Journal of Physical Oceanography*, **25,** 1037-1062.

Stacey, M. W. and A. Valle-Levinson, 2006: Simulation and energy partition of the flow through Paso Galvarino, Chile. *Journal of Marine Research*, **64,** 249-266.

Stashchuk, N., M. Inall, and V. Vlasenko, In Press: Analysis of supercritical stratified tidal flow in a Scottish fjord.

Stigebrandt, A., 1976: Vertical diffusion driven by internal waves in a sill fjord. *Journal of Physical Oceanography*, **6,** 486-495.

——, 1979: Observational evidence for vertical diffusion driven by internal waves of tidal origin in the Oslofjord. *Journal of Physical Oceanography*, **9,** 435-441.

——, 1981: A mechanism governing the estuarine circulation in deep, strongly stratified fjords. *Estuarine Coastal and Shelf Science*, **13,** 197-211.

——, 1999: Baroclinic wave drag and barotropic to baroclinic energy transfer at sills as evidenced by tidal retardation, seiche damping and diapycnal mixing in fjords. Aha Huliko, Manoa, Hawaii.

Stigebrandt, A. and J. Aure, 1989: Vertical mixing in basin waters of fjords. *Journal of Physical Oceanography*, **19,** 917-926.

Syvitski, J., D. Burrell, and J. Skei, 1987: *Fjords: Processes and products*. Springer - Verlag.

Tinis, S. and S. Pond, 2001: Tidal energy dissipation at the sill of Sechelt inlet, British Columbia. *Journal of Physical Oceanography*, **31,** 3365-3373.

Tkalich, P., 2006: A CFD solution of oil spill problems. *Environmental Monitoring & Software*, **22,** 271-282.

Vlasenko, V., N. Stashchuk, and K. Hutter, 2002: Water exchange in fjords induced by tidally generated internal lee waves. *Dynamics of Atmospheres and Oceans*, **35,** 63-89.

——, 2005: *Baroclinic Tides: Theoretical modelling and observational evidence*, Cambridge University Press.

Wang, D. P. and D. W. Kravitz, 1980: A semi-implicit two-dimensional model of estuarine circulation. *Journal of Physical Oceanography*, **10,** 441-454.

Watts, L. J., T. P. Rippeth, and A. Edwards, 1998: The roles of hydrographic and biogeochemical processes in the distribution of dissolved inorganic nutrients in a Scottish sea-loch: Consequences for the spring phytoplankton bloom. *Estuarine Coastal and Shelf Science*, **46,** 39-50.

Xia, R. and B. Yen, 1994: Significance of averaging coefficients in open channel flow equations. *Journal of Hydraulic Engineering*, **120,** 169-190.

Xue, M. and S. J. Lin, 2001: Numerical equivalence of advection in flux and advective forms and quadratically conservative high-order advection schemes. *Monthly Weather Review*, **129,** 561-565.

Zhu, J. Y., 1995: The 2nd-order projection method for the backward-facing step flow. *Journal of Computational Physics*, **117,** 318-331.